The aggregation of alpha-synuclein and its disaggregation by the Hsp70 disaggregation machinery

The aggregation of alpha-synuclein and its disaggregation by the Hsp70 disaggregation machinery

Jim Emilien Jacques Monistrol

Thesis presented for the degree of Doctor of Philosophy

Birkbeck College, University of London

Declaration

I, Jim Emilien Jacques Monistrol, declare that the work presented in this thesis is my own. Where information has been obtained from other sources, I confirm that this has been clearly indicated in the thesis.

To my parents and Maï-Carmen,

Acknowledgements

There are several people that I would like to thank for their advice and their support during my PhD. First, I am very grateful to my supervisor Helen Saibil for her dedication. She was always available over these four years, despite her busy schedule. She was also very attentive and supportive over the different scientific as well as covid-related challenges encountered during my PhD. I would also like to thank my secondary supervisors Alan Lowe and Bart Hoogenboom. They brought many interesting and useful suggestions for additional experiments to tackle issues which initially looked insurmountable. I would also like to address my special thanks to Anthony Roberts, not only for being the chairman of my thesis committee but also for taking time in training me on the fluorescence microscope and the analysis of the data.

I would like to specially thank Natasha Lukoyanova and Shu Chen who trained me on the different electron microscopes (and were very patient with me while I was learning!), Claire Bagnéris who was always available and helpful when I conducted my biochemical experiments and Dave Houldershaw who fixed the countless IT issues that I faced.

In Helen's group, I would like to thank in particular Joe and Guen for their help in experiment optimisation and data processing, but also for our many interesting conversations and the very funny moments that we shared. I really enjoyed their company in the group (and I deeply missed them when they left). I would like to thank all the present and past members of Helen's group for their support as well: Erin, Ya, Jesus, Scott, Becca, Giles, Marina, Trishant, Claudine, Celia, Natasha B and Tom P.

I would also like to thank Tom F, Josh, Kat, Tyan, Ramteen, Mamata and Alex for their assistance for very specific issues related to sample preparation, data collection and processing.

A special thanks to my friends in France, in particular Thibault, as well as Alexandre and Clément who both experienced the adventure of a PhD. Our endless online conversations in the evenings were a great source of distraction. Thank you also to Claire, Thomas and Stéphane for making my PhD-related issues seem less overwhelming.

I would also like to thank Kaoru and Diego for their encouragement and support over the last few years.

I would like to express a heartfelt thanks to my parents for their inexhaustible support at each step of my life (I am finally done with my studies!)

Lastly, I have shared the most intense and enjoyable moments of my PhD with Maï-Carmen, who is also submitting her thesis this week. Thank you for your unconditional support and I am eager to start a new adventure with you after the PhD.

Abstract

Neurodegenerative disorders are characterised by the deposition of proteinaceous aggregates in the brain. In the case of synucleinopathies, such as Parkinson's disease, the aggregates are mainly composed of α-synuclein (αSyn). The aggregation process of αSyn is toxic for neurons but the cause of the toxicity remains elusive. *In vitro*, the constitutively expressed cytosolic heat shock 70 protein, Hsc70, together with two cochaperones, the J-domain protein DNAJB1 and the nucleotide exchange factor Apg2, can disassemble αSyn amyloid fibres and small oligomers. However, the model is incomplete, lacking structural as well as mechanistic details. To address these two issues (αSyn aggregation in cells and the incomplete model of αSyn disaggregation *in vitro*), I have used electron and fluorescence microscopy and biochemical assays.

Correlating fluorescence images and cryo tomograms, I have investigated the structure of αSyn aggregates in a yeast model. αSyn colocalises at the plasma membrane and forms cytosolic inclusions rich in vesicles and lipid droplets. Using cryo electron microscopy (cryo-EM) and tomography, I have shown that recombinant αSyn does not form large oligomers on the surface of tubulated liposomes.

Using single particle cryo-EM, I have studied the complex formed of αSyn amyloid fibres and a mutant of DNAJB1 lacking the J-domain and G/F linker (ΔJ-DNAJB1). A low-resolution reconstruction of the complex was generated in which horseshoe-like densities, identified as ΔJ-DNAJB1, surrounded the fibre. I also produced a high-resolution map of the αSyn fibre showing a new conformation.

Lastly, using cryo-EM, fluorescence microscopy and biochemical assays, I have investigated the function of Apg2 in disaggregation. Unexpectedly, Apg2 enhances Hsc70 recruitment to the fibres, preferentially at one end. This Apg2-induced recruitment regulates the disaggregation activity.

The work in this thesis provides new information about αSyn aggregation, its toxicity and its disaggregation by the Hsc70 system.

Contents

List of Figures

List of Tables

List of Abbreviations

2D: Two-dimensional

3D : three-dimensional

Å: Angstroms

αSyn: alpha-synuclein

Aβ : Amyloid β protein

ADP: Adenosine diphosphate

AFM: Atomic force microscopy

ATP: Adenosine triphosphate

BSA: Bovine serum albumin

CCD: Charge-coupled device

CEMOVIS: Cryo electron microscopy of vitrified sections

CLEM: Correlative light and electron microscopy

CMOS: Complementary metal-oxide semiconductor

Cryo-EM: Cryogenic electron microscopy

Cryo-ET: Cryogenic electron tomography

CTD: C-terminal domain

CTF: Contrast transfer function

CV: Column volume

ΔJ-DNAJB1: DNAJB1 lacking the J-domain and the G/F linker

DEDs: Direct electron detectors

DLB: Dementia with Lewy Bodies

DIC: Differential Interference Contrast

DNA: Deoxyribonucleic acid

DnaJ: Bacterial J-domain protein

DNAJ: J-domain proteins

DnaK: Bacterial Hsp70

DOPC: 1,2-dioleoyl-sn-glycero-3-phosphocholine

DOPE: 1,2-dioleoyl-s*n*-glycero-3-phosphoethanolamine

DOPS: 1,2-dioleoyl-s*n*-glycero-3-phospho-L-serine

DQE: Detective Quantum Efficiency

DTT: Dithiothreitol

EM: Electron microscopy

ER: Endoplasmic reticulum

FAIM: Fas apoptosis inhibitory molecule

FEG: Field emission gun

FIB: Focused ion beam

FRET: Fluorescence resonance energy transfer

FSC: Fourier shell correlation

FT: Fourier Transform

G/F: Glycine-phenylalanine rich

GFP: Green fluorescent protein

HEPES: 4-(2-hydroxyethyl)-1-piperazineethanesulfonic acid

Hsc70: Constitutively expressed cytosolic Hsp70

Hsp: Heat-shock protein

HSPs: Heat-shock proteins

IMAC: Immobilized metal ion affinity chromatography

IPTG: Isopropyl β-D-1-thiogalactopyranoside

KO: Knockout

LBs: Lewy Bodies

MSA: Multiple system atrophy

min: minutes

µm: micrometres

NAC: Non-amyloid component

NBD: Nucleotide-binding domain

NEF: Nucleotide exchange factor

n: refractive index of a medium

nm: nanometres

NMR: Nuclear magnetic resonance

OD_{600}: Optical density measured at 600 nm

PAGE: Polyacrylamide gel electrophoresis

PD: Parkinson's disease

PEP: Phosphoenolpyruvate

PG: Phosphatidylglycerol

PEG: Polyethylene glycol

RELION: Regularised Likelihood Optimisation

s: Second

SBD: Substrate-binding domain

SBDα: Substrate-binding domain rich in β-strands

SBDβ: Substrate-binding domain rich in α-helices

SD: Synthetic dropout

SDS: Sodium dodecyl sulphate

SEC: Size exclusion chromatography

SEM: Scanning electron microscope

SIRT: Simultaneous iterative reconstruction technique

TCEP: Tris-(2-carboxyethyl)phosphine

TEM: Transmission electron microscope

ThT: Thioflavin-T

TIRF: Total internal reflection fluorescence

UK: United Kingdom

USA: United States of America

WT: Wild type

ZFLR: Zinger-finger-like region

1. Introduction

1.1 The aggregation of alpha-synuclein and its toxicity

1.1.1 The formation of amyloid fibres: an incomplete model

Proteins in their physiological environment can adopt *de novo* their functional conformation. Indeed, Anfinsen's principle stipulates that, in their physiological environment (pH, ionic strength, temperature), proteins can fold into a state of minimal energy. This native state is determined by the amino acid sequence of the protein (Anfinsen, 1973). However, a type of assembly challenges this principle. Notably, proteins can misfold and self-assemble to form stable amyloid aggregates (figure 1.1A, Jahn and Radford 2005). Therefore, native conformations correspond to a locally minimal energy state whereas amyloid aggregates are the most stable assemblies. But how are those amyloid aggregates defined? What are their common features?

Amyloid aggregates are insoluble and ordered aggregates rich in β-strands. Amyloid fibrils consist of two or more protofilaments running along the fibril axis. The core of each protofilament adopts a common, cross-β conformation in which the β-strands are perpendicular to the fibril axis. Each cross-β repeat within a protofilament is separated by 4.7-4.8 angstroms (Å). Usually, hydrogen bonds govern intramolecular and intermolecular interactions of the β-strands. Also, the core of the protofilaments is often hydrophobic. Remarkably, this global architecture is shared between all the different amyloid fibrils, regardless of the original protein sequence (Iadanza et al., 2018). Although incomplete, a mechanism for the formation of amyloid fibrils has been proposed. The process of amyloid fibre formation would follow a "nucleation-polymerisation" model. Soluble monomeric proteins misfold and self-assemble to form

the amyloid fibrils in three stages: the nucleation phase, the elongation phase and the stationary phase (figure 1.1B, Arosio et al., 2015; Iadanza et al., 2018). The nucleation phase corresponds to the formation of soluble small oligomers from unfolded or partially folded monomers. The native conformation can also self-polymerise to form these first oligomers. However, this is less frequent because of the thermodynamic stability of the native state. The oligomers then self-assemble to form larger oligomers. Some of them are stable enough to stop the process at this point. Other oligomers continue polymerising until a fibril nucleus is formed, which marks the end of the first phase. This nucleation phase is the critical step of the process and is also called the lag phase. Indeed, the formation of the first oligomers requires monomers to change their conformation to form a nucleus, which is considered as the most unstable state with the highest associated energy. Then, during the elongation phase, the fibril nucleus extends by incorporating new monomers to create amyloid fibrils by exponential growth. During this step, amyloid fibrils can be fragmented. Fibril fragments then act as seeds to form new amyloid fibrils, accelerating the whole process. Moreover, secondary nucleation can occur during which fibrils trigger oligomer formation. Last, the stationary phase corresponds to the presence of fibrils. It is an equilibrium state in which the fibrillization and depolymerisation rates counterbalance one another. The kinetic characteristics of this model (slow nucleation step, fast fibril growth) were partially explained by Sawaya et al. in 2007. They studied amyloid fibril formation by combining bioinformatic and experimental studies of peptides forming amyloid fibres. They were able to identify eight different classes of amyloid fibrils (Sawaya et al., 2007). The classes were distinguished according to i) the contact surface between the two protofilaments (same residues in contact between each protofilament or different residues), ii) the orientation of the contact surface of each protofilament (parallel or

antiparallel orientations), and iii) the orientation of the monomers within a protofilament (parallel or antiparallel monomers within a protofilament).

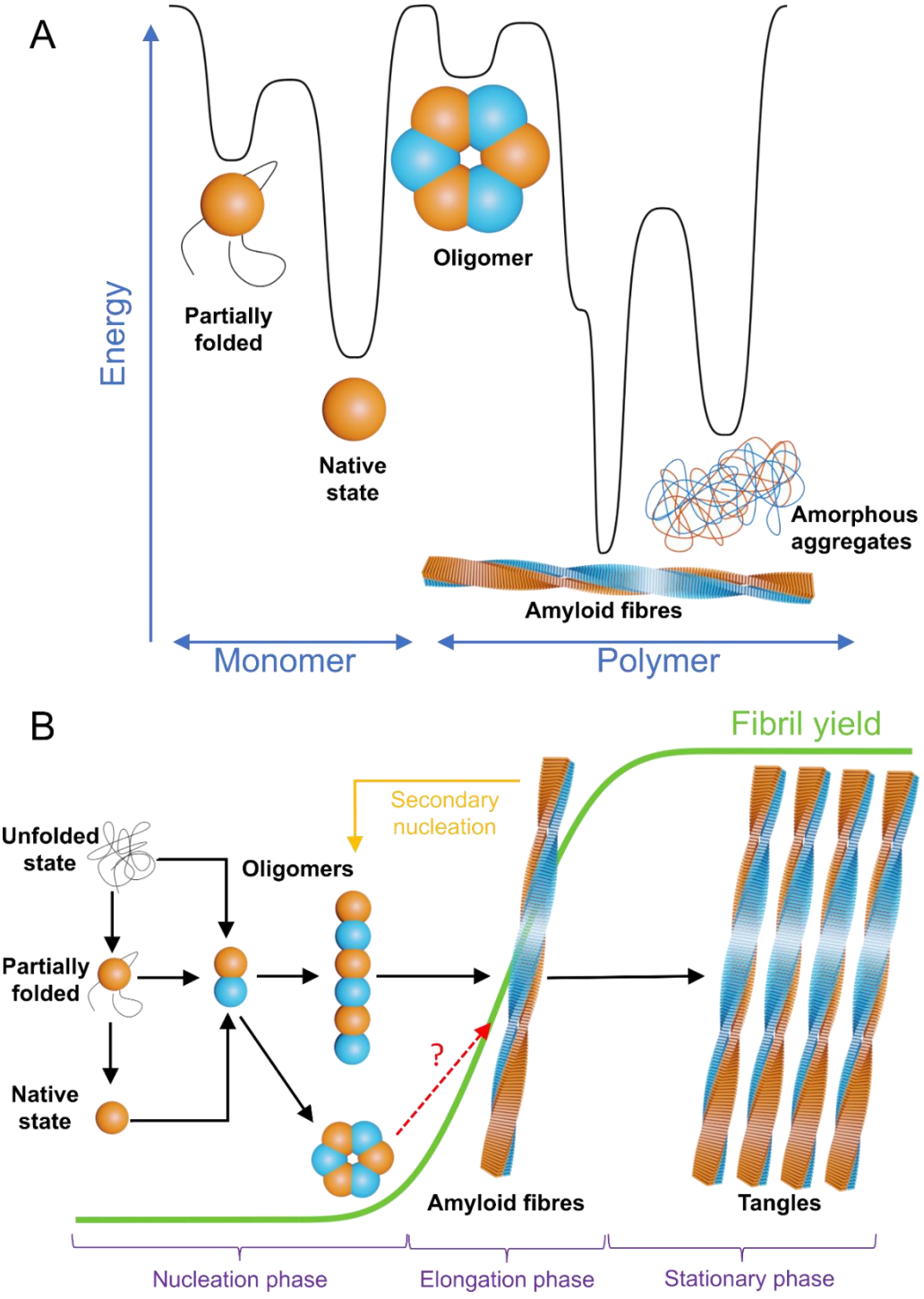

Figure 1.1: General information on amyloid fibres.

(A) A schematic figure representing the energy landscape for protein folding and aggregation. The figure was adapted from Jahn and Radford, 2005. (B) A schematic figure of the three stages leading to amyloid formation in vitro. The figure was adapted from Iadanza et al., 2018.

Notably, all the different classes share a common feature. The contact surface between the protofilaments is dehydrated with the residues of each protofilament intertwining with each other to form a “steric zipper”. Therefore, they suggested that the formation of these steric zipper interfaces would require several subunits which must adopt a new conformation (the nucleation phase). This whole process would need time and energy. On the contrary, extending preformed amyloid fibres would only require addition of one molecule at a time, rendering this process much faster (the elongation phase).

Even if the mechanism of amyloid fibre formation is broadly understood, the existence of amyloid fibres still challenges Anfinsen’s principle since their formation does not entirely depend on their amino acid sequence. Baldwin et al. performed *in vitro* experiments to explain why some proteins form amyloid fibres by comparing the free energy of the native state and the free energy of the amyloid state of different proteins as a function of the polypeptide length (Baldwin et al., 2011). They concluded that for short peptides (smaller than 150 residues), the free energy of the amyloid state is significantly lower than the free energy of the native state. In contrast, proteins longer than 150 residues did not display any free energy difference between the two states. This study suggested that i) amyloid fibres are often composed of small proteins shorter than 200 residues and ii) one reason for the evolution to generate large proteins would be the low probability to form amyloid fibres.

Thus, although the general mechanisms of amyloid fibre formation and the proteins involved in it are known, a certain number of questions remains unanswered. Critically, amyloid aggregates have been found in cellular inclusions associated with aging-related disorders. It is currently estimated that around 50 proteins or peptides can assemble into amyloid aggregates related to diseases such as neurodegenerative disorders and type II diabetes (Sipe et al., 2016). Therefore, a detailed understanding of the factors triggering

amyloid fibre formation, their structures, and the mechanisms underlying their disassembly is crucial.

1.1.2 Parkinson's disease and alpha-synuclein

Neurodegenerative diseases such as Alzheimer's disease, Parkinson's disease (PD), and Huntington's disease are characterised by the accumulation of cellular inclusions which are proteinaceous aggregates. All these disorders share a common mechanism: cellular inclusions lead to cellular dysfunction starting in a specific area of the brain depending on the disorder. The aggregates also activate a chronic inflammatory response via the involvement of astrocytes and microglia. The mechanism is still unclear but the inflammatory response triggers the production of reactive oxygen species which lead to mitochondria dysfunction, progressive neuronal death and gradual inhibition of synaptic transmission between neurons (Amor et al., 2010; Soto and Pritzkow, 2018). In Parkinson's disease, dopaminergic neurons involved in body movements are affected. Neuronal death can trigger different symptoms according to the stage of the disease. In the early stage, physical symptoms such as muscular rigidity, slow and imprecise body movements, or tremors are observed. In the late stages, cognitive symptoms such as sensory disturbances, tiredness, and depression appear (Meade et al., 2019). In the late 1960s, PD patients' post-mortem brain tissues were observed by electron microscopy: well-ordered proteinaceous filaments were present in cellular inclusions (Roy and Wolman 1969). However, it was only in 1997 that two different studies successfully identified the protein involved in PD. Spillantini et al. examined the composition of the cellular inclusions called Lewy Bodies (LBs). They found that LBs are mainly composed of alpha-synuclein (αSyn) (Spillantini et al., 1997) and more recently, Shahmoradian et al. found that LBs are mainly composed of amorphous aggregates of αSyn as well as vesicles and distorted mitochondria (Shahmoradian et al., 2019). In

parallel, Polymeropoulos et al. showed that familial PD, which represents 10-15% of the cases, can be caused by the single-point mutation A53T of the *SNCA* gene which expresses αSyn (Polymeropoulos et al., 1997). Results from these two articles led to the consensus that αSyn plays a critical role in PD progression. The role of αSyn was then confirmed by the discovery of other PD familial forms involving the duplication or the triplication of the *SNCA* gene or various single-point mutations (figure 1.2A, Appel-Cresswell et al., 2013; Chartier-Harlin et al., 2004; Kruger et al., 1998; Lesage et al., 2013; Pasanen et al., 2014; Singleton et al., 2003; Yoshino et al., 2017; Zarranz et al., 2004).

Other familial forms of PD were discovered that were not associated with protein aggregation. For instance, the genes *PARK2* and *PARK6*, encoding Parkin and PINK1 respectively, can cause early onset of the disorder (Kitada et al., 1998; Valente et al., 2004). Both proteins target defective mitochondria for degradation to regulate oxidative stress (Pickrell and Youle, 2015). Mutations in their genes prevent mitochondria degradation and trigger a higher production of reactive oxygen species, leading to neuronal cell death (Amo et al., 2011; Wang et al., 2011).

In the last two decades, researchers have studied αSyn to understand its physiological function as well as its pathological role in the synucleinopathies, this last term referring to all the αSyn-involved disorders such as PD, Dementia with Lewy Bodies (DLB) and Multiple System Atrophy (MSA).

αSyn is a short protein (140 residues, 14.4 kDa) which is widely expressed in the brain and localises at the pre-synaptic termini (Maroteaux et al., 1988). αSyn is composed of three different domains: a lysine-rich N-terminal region (residues 1-60), a hydrophobic nonamyloid-β component (NAC) region (residues 61-95), and an acidic C-terminal

region (residues 96-140; figure 1.2A, Fusco et al., 2014). The physiological role of αSyn remains unclear. Because of its localisation at presynaptic termini, αSyn is presumably involved in synaptic activity (Murphy et al., 2000). More precisely, αSyn regulates the pool of synaptic vesicles and their trafficking during synaptic transmission, via a potential role in the formation of the SNARE complex (Auluck et al., 2010; Burré et al., 2010; Lautenschläger et al., 2017). Upon binding, αSyn stimulates vesicle clustering and *in vitro* experiments confirmed αSyn affinity for liposomes and vesicles (Diao et al., 2013; Fusco et al., 2016; Lautenschläger et al., 2018). αSyn can also interact with other lipid membranes since αSyn can localise at mitochondrial membranes and can influence the vesicle trafficking between the endoplasmic reticulum (ER) and the Golgi apparatus (Cooper et al., 2006; Ramezani et al., 2019). All these different functions involve the ability of αSyn to bind to lipid membranes. This distinguishing feature is attributed to the presence of seven imperfect repeats (KTKEGV) present in the N-terminus and NAC domains of αSyn (figure 1.2A, Auluck et al., 2010; Maroteaux et al., 1988). The repeats intervene in the formation of an amphipathic α-helical structure with opposing polar and nonpolar surfaces (figure 1.2B-C, Chandra et al., 2003; Ulmer and Bax, 2005). Therefore, the positively charged polar surface can interact with the negatively charged lipid headgroups. In parallel, the nonpolar surface is inserted into the hydrophobic acyl chains of the lipid bilayer (figure 1.2B). When αSyn adopts this conformation, the C-terminal domain remains unfolded (Auluck et al., 2010). Interestingly, the helical structure of αSyn is quite flexible since it can change according to the curvature of the lipid bilayer. If the lipid bilayer is weakly curved (for plasma membrane and large vesicles), αSyn adopts a so-called “extended helical structure” (Georgieva et al., 2008). In this conformation, αSyn helix extends to residue 95. On the contrary, if the lipid bilayer is highly curved, αSyn adopts a hairpin

structure formed of two antiparallel helices called the “broken α-helix” (residues 1 to 42 and residues 45 to 98; Chandra et al., 2003). In these two different conformations, the N-terminal domain acts as an anchor via electrostatic interactions while the NAC domain modulates the binding affinity to the vesicles (Fusco et al., 2014). Recently, a physiological function has been suggested for the “broken α-helix” conformation: each helix would bind to different lipid bilayers up to a distance of 150 Å, triggering thus the clustering of vesicles or their docking at the plasma membrane via a “double anchor” mechanism (Fusco et al., 2016). By total internal reflection fluorescence (TIRF) microscopy, Man et al. showed that αSyn thermodynamically and kinetically stabilises the docking of synaptic vesicles on the plasma membrane *in vitro* (Man et al., 2021).

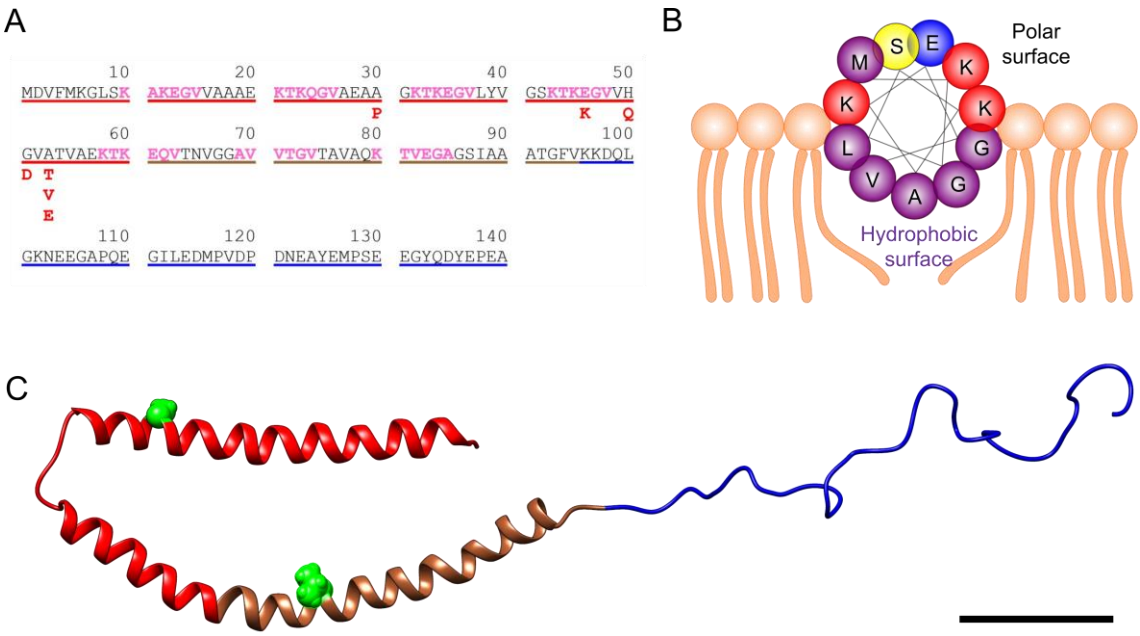

Figure 1.2: αSyn protein.

(A) The sequence of αSyn. The N-terminus, NAC and C-terminus domains are underlined in red, brown and blue, respectively. The seven KTKEGV imperfect repeats are written in pink. The single-point mutations involved in familial forms of Parkinson’s disease are written in red. (B) The axial view highlights the polar and non-polar surfaces of the helical conformation. The figure was adapted from Auluck et al., 2010. (C) αSyn broken-helical structure. Green spheres display the alanine at position 30 and the valine at position 70. The N-terminus, NAC and C-terminus domains are represented in red, brown and blue, respectively. PDB: 1XQ8 (Ulmer and Bax, 2005). Scale bar, 20 Å.

1.1.3 Alpha-synuclein amyloid fibres and toxicity

The aggregation of αSyn has been well studied *in vitro*. *In vitro*, αSyn can also form amyloid fibres via the involvement of the NAC domain in αSyn misfolding and aggregation. More precisely, residues 71-82 are sufficient to self-aggregate and their deletion from the αSyn sequence prevents αSyn aggregation (Giasson et al., 2001). By using NMR and mutations, it was shown both *in vitro* and in *C. elegans* that a 7-residue sequence (residues 36-42) controls the aggregation of αSyn (Doherty et al., 2020). The remarkable improvements in cryo-electron microscopy (cryo-EM) and nuclear magnetic resonance (NMR) in recent years enabled near atomic structure determination of several αSyn amyloid cores. Tuttle et al. were able to solve the structure at 4.8 Å by NMR (Tuttle et al., 2016). Two years later, similar structures were solved at 3.4 Å and 3.1 Å using cryo-EM (Guerrero-Ferreira et al., 2018; Y. Li et al., 2018, respectively). In these cryo-EM solved structures, fibrils have 2-fold rotational symmetry along the fibril axis, are 10 nm wide and composed of two 5-nm-wide protofilaments. Each αSyn subunit is planar, perpendicular to the fibril axis and adopts a β-strand-rich conformation displaying a general Greek key topology (types 1a and 1b in figure 1.3). In type 1a polymorph, αSyn β-strands interact with each other via hydrogen bonds and are spaced 4.7-4.8 Å apart. As shown previously, this structure highlights the key role of residues 71-82 which are part of the Greek key. However, another region composed of residues 45-57 is also essential for the stability of the fibres. This region stabilizes the structure via intramolecular (residues E46-K80 and E61-K58) as well as intermolecular salt bridges (residues K45/H50-E57). N-terminal (residues 1-40) and C-terminal (103-140) domains remain flexible. The protofilament interface is mainly hydrophobic (G51, A53, V55) and adopts a steric zipper conformation. Type 1b is very similar to type 1a. The main differences are: i) in type 1b, the N-terminus is more rigid with an additional

ordered β-strand (residues 38-40) and ii) a small region of the C-terminus adopts a β-strand secondary structure (residues 96-98) in type 1b polymorph (figure 1.3).

Four other *in vitro* WT αSyn fibre structures, or "strains", were solved by cryo-EM (figure 1.3; Guerrero-Ferreira et al., 2019; B. Li et al., 2018). Strains were called type 2a, type 2b, rod polymorph and twister polymorph. Type 2a and 2b structures were solved at 3.1 Å and 3.5 Å respectively. The most striking difference is that strains 1a and 1b display compact hydrophobic steric zippers whereas strains 2a and 2b display a "hydrophobic cleft" stabilised by a couple of intermolecular salt bridges (figure 1.3, K45-E57 and K45-E46 for types 2a and 2b, respectively). The rod polymorph is very similar to type 1b polymorph (figure 1.3). The twister polymer is slightly different: although the "Greek key" topology is present, the protofilament interface is at a different position in the NAC domain (residues 68-78) and is exclusively governed by hydrophobic interactions (figure 1.3).

Interestingly, some of the discovered strains suggested important roles for the mutants found in familial PD. Most of the mutations (residues 46, 50, 51 and 53) tend to destabilise the fibre structures described above by inhibiting critical electrostatic or hydrophobic interactions at the protofilament interface. Only the twister and the type 2a polymorphs are not influenced by the mutations. This observation let the authors who found the twister polymorph to draw the conclusion that the mutants of αSyn will favour the twister conformation (B. Li et al., 2018). Moreover, Guerrero-Ferreira et al., who found the type 2a polymorph, determined the cross-section of the E46K mutant and found that it was similar to the cross-section of type 2a polymorph (Guerrero-Ferreira et al., 2019).

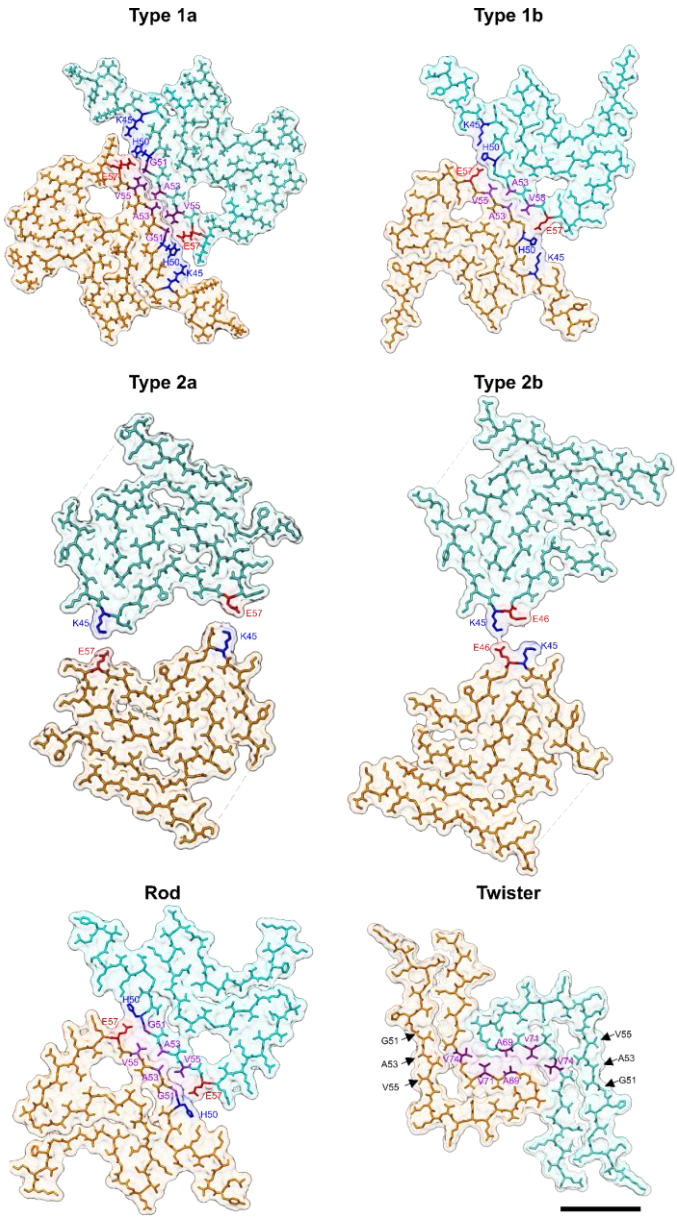

Figure 1.3: The structures of type 1a and WT αSyn amyloid fibres solved by cryo-EM.

Atomic representations of a cross-section showing two αSyn subunits (orange and cyan) for the different solved structures. Hydrophobic residues localised at the protofilament interface are represented in purple. Electrostatic interactions stabilising the structure are represented by colouring the positively charged residues in blue and the negatively charged residues in red. Orange and cyan dashed lines represent unresolved linkers. PDB files: 6H6B for type 1a (Guerrero-Ferreira et al., 2018), 6A6B for type 1b (Y. Li et al., 2018), 6SSX for type 2a (Guerrero-Ferreira et al., 2019), 6SST for type 2b (Guerrero-Ferreira et al., 2019), 6CU7 for rod strain (B. Li et al., 2018), and 6CU8 for twister strain (B. Li et al., 2018). Scale bar, 20 Å.

These results were surprising since E46K, H50Q and A53T mutants are known to have faster aggregation kinetics (Flynn et al., 2018). Therefore, they should adopt different strains that would favour their aggregation. This is why solving the structures of those mutants was critical for understanding the aggregation process of αSyn. H50Q was the first mutant whose amyloid structure was determined (figure1.4B, Boyer et al., 2019). Two conformations were solved: an asymmetric conformation displaying two different protofilaments whose interface encompassed residues 58 to 61 (KTKE) and a second conformation, which was the majority strain, displaying a stable single protofilament. Solving these structures helped explain why the H50Q mutant has faster aggregation kinetics and why it is more cytotoxic (Khalaf et al., 2014). Since a single protofilament is stable and can form H50Q amyloid fibres, the energy required to form this conformation is lower, and therefore the nucleation phase is shorter. The increased toxicity could come from the new conformation displaying a different surface for interaction with cellular components. The same structure was solved for the A53T mutant (figure 1.4B, Sun et al., 2020). Two groups also solved the structure of the E46K mutant (figure 1.4B, Boyer et al., 2020; Zhao et al., 2020). In both structures, the E46-K80 electrostatic interaction is disrupted. Because of this, the Greek key conformation is not adopted. But the conclusions drawn from the 2 structures differ. In the first structure (PDB: 6UFR), there are more interacting residues than in the WT conformations, which renders this conformation more stable (Boyer et al., 2020). That might explain why the E46K mutation leads to higher levels of aggregation *in vitro* and in cells (Choi et al., 2004; Pandey et al., 2006). On the other hand, in the other solved structure (PDB: 6L4S), the authors found that the fibres formed with the E46K mutant are less stable than WT fibres under severe denaturing conditions or protease cleavage (Zhao et al., 2020a). They then suggest that this lower stability would explain why the

seeding capacities of the E46K mutant are enhanced. It should be noticed that a potential explanation for these differences could be the N-terminus acetylation of αSyn in one of the studies (Zhao et al., 2020a) since αSyn is frequently acetylated at the N-terminus *in vivo* (Burré et al., 2013). Lastly, the structure of the G51D mutant was solved and was identical to the structure of the N-terminally acetylated E46K mutant (Sun et al., 2021). Another common post-translational modification of αSyn found in LBs is its C-terminal truncation (Li et al., 2005). That is why Ni et al. studied the effect of C-truncation on N-terminally acetylated WT αSyn (figure 1.4C, Ni et al., 2019). They found that the fibres are more twisted when the C-terminus is shorter and that truncated fibres can also act as seeds for WT monomeric αSyn. This result confirmed that although the C-terminus is not ordered in the different strains of αSyn amyloid fibres, it still influences αSyn aggregation as previously reported (Flynn et al., 2018; Van Der Wateren et al., 2018; Yap et al., 2011). Another post-translational modification of αSyn is the N-terminal truncation (Kellie et al., 2014). McGlinchey et al. truncated the N-terminus (residues 1-40), resulting in a structure of αSyn fibril with two asymmetric protofilaments (McGlinchey et al., 2021). Lastly, the phosphorylation of tyrosine 39 is a common post-translational modification found in LBs (Zhao et al., 2020b). It leads to the formation of a more stable fibre structure characterised by 100 ordered residues, a trimer fibril and the phosphorylated tyrosine 39 interacting with 8 residues of the N-terminus (Zhao et al., 2020b).

These recent solved structures provide new insights into the aggregation of αSyn. But do they reflect the *in vivo* aggregation process of αSyn? Schweighauser et al. studied αSyn amyloid fibres extracted from the brains of patients suffering from MSA and DLB (Schweighauser et al., 2020). Two asymmetric assemblies were solved for MSA-related αSyn fibres, leading to the discovery of four new conformers, called PF-IA, PF-IB, PF-

IIA, and PF-IIB (figure 1.4D). Although the structures display the “Greek key” topology, the N-terminus is much more ordered in these new structures and a non-proteinaceous density was also observed. It was suggested that this density would correspond to a phosphate ion based on its size and the charges of the residues surrounding it. This density was proposed to play a crucial role in the arrangement of the N-terminus. Using two-dimensional classification, it was shown that fibres extracted from the brains of patients with DLB differ from the fibres of the fibres with MSA (Schweighauser et al., 2020), suggesting that different conformers are involved in distinct synucleinopathies. The fact that different structures were solved for the assemblies produced *in vitro* and those extracted from post-mortem brain is challenging, suggesting that the reported *in vitro* structures may not be relevant to the aggregation process *in vivo*. This difference is all the more striking as similar observations were found for *in vitro* tau filaments and those extracted from post mortem brain tissue (Fitzpatrick et al., 2017; Zhang et al., 2019).

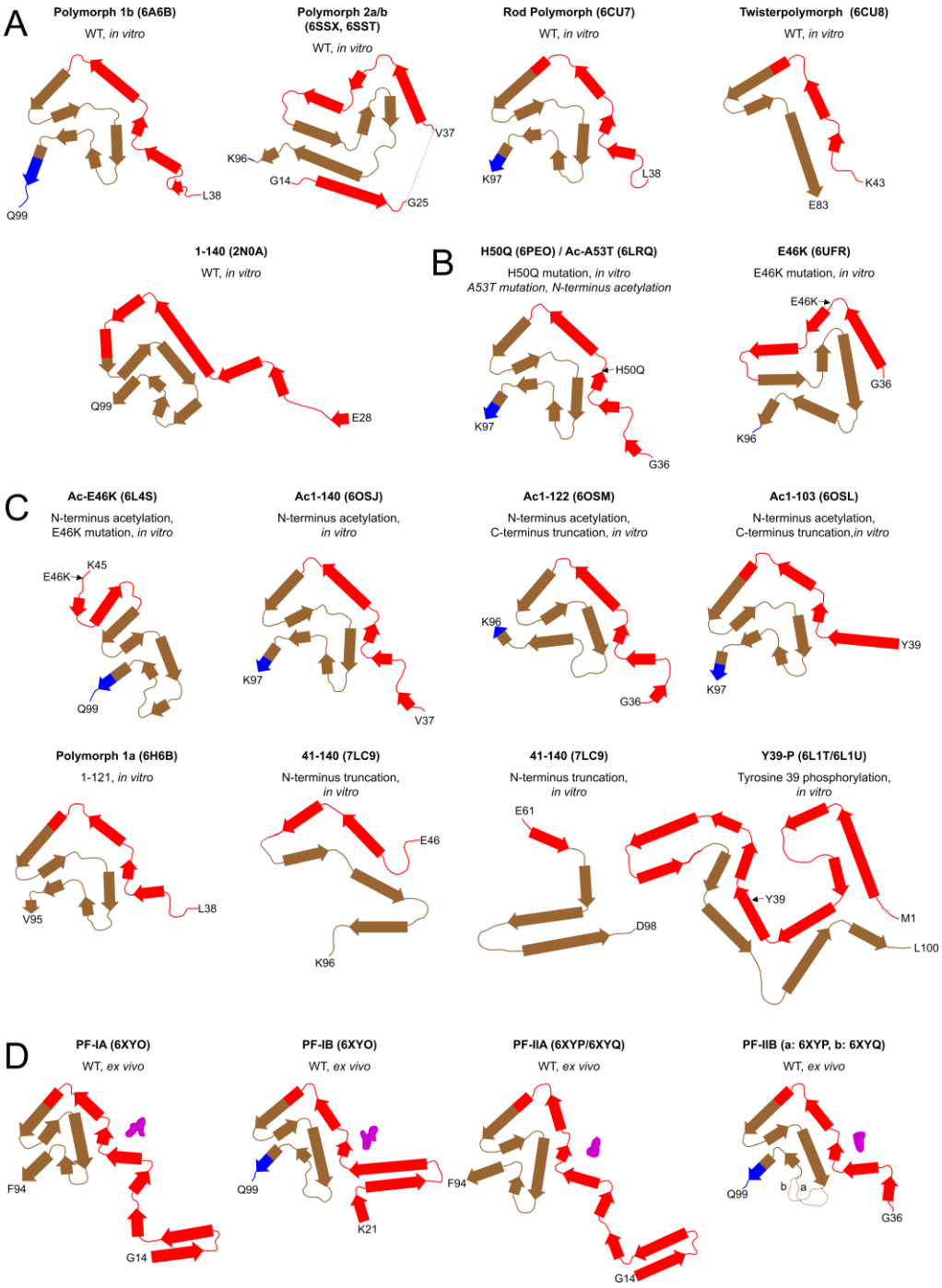

Figure 1.4: Secondary structures of the cross-sections for the WT αSyn (A), mutant (B), post-translationally modified (C), and *ex vivo* amyloid fibres (D). For each cross-section, the header indicates the name of the polymorph, the PDB number, the sequence (WT, truncated, mutation, post-translational modification) and the protocol used to obtain the fibres (reproduced *in vitro* or extracted from post-mortem brain tissue). Arrows represent β-strands. In magenta are extra non-proteinaceous densities. The figure was adapted from Schweighauser et al., 2020. PDB files: 6A6B (Y. Li et al., 2018); 6SSX/6SST (Guerrero-Ferreira et al., 2019); 6CU7/6CU8 (B. Li et

al., 2018); 2N0A (Tuttle et al., 2016); 6PEO (Boyer et al., 2019); 6LRQ (Sun et al., 2020); 6UFR (Eisenberg et al., 2020); 6L4S (Li et al., 2020); 6OSJ/6OSM/6OSL (Ni et al., 2019); 6H6B (Guerrero-Ferreira et al., 2018); 7LC9 (Xiaodan et al., 2021); 6L1T/6L1U (Zhao et al., 2020); 6XYO/6XYP/6XYQ (Schweighauser et al., 2020).

Lipids, which are associated with the physiological function of αSyn, also intervene in its aggregation. Surprisingly, synaptic vesicles can trigger αSyn aggregation *in vitro* by stimulating primary nucleation (Galvagnion et al., 2015). Also, the seven residues (residues 36-42) that control αSyn aggregation are also required for vesicle fusion (Doherty et al., 2020). These two studies indicate an ambiguous mechanism between the physiological function of αSyn related to lipids and its pathological aggregation. Singh et al proposed a model explaining the transition from a physiological helical structure to the pathological amyloid fibres (Singh et al., 2011). This model suggests an equilibrium between amphipathic and 3_{10} helices, which favours the former. However, the 3_{10} helices, which are more elongated and less compressed than amphipathic helices, can self-polymerise to form intermediate helical aggregates. These helical aggregates would further elongate to form β-strands due to the higher thermodynamic stability of the latter. The β-strands would then self-assemble to form amyloid fibres.

1.1.4 Are small oligomers of alpha-synuclein the toxic species?

The reconsideration of amyloid fibril toxicity started in 2002 when Bucciantini and co-workers studied the toxicity of different assemblies (Bucciantini et al., 2002). By looking at a protein containing an SH3 domain which is known to self-aggregate, they showed that annular or spherical species formed in the early stages of the aggregation process are more cytotoxic than amyloid fibres. They suggested that the presence of amyloid fibres in inclusions is not the sign of a toxic event but, on the contrary, the sign of a protective cell response since αSyn subunits are now trapped in a less dynamic

assembly. This hypothesis was further supported by other studies showing that pre-fibrillar aggregates are more toxic than amyloid fibres (Winner et al., 2011). It was also suggested that different types of soluble oligomers present a common structure and share a common toxic mechanism that requires the permeabilization of lipid bilayers (Kayed et al., 2004, 2003). The issue is that studying these preformed oligomers is challenging because of their high instability. Thus, αSyn oligomers were kinetically trapped by lyophilising the protein in order to study them (Chen et al., 2015). Structures of two different oligomers were partially solved in 2015 using cryo-EM. The flexibility of the oligomers limited them to low resolution, but the general shape was observable. These oligomers, called 10S and 15S, consist of 18 and 29 αSyn subunits respectively. These two assemblies share a common conformation with a cylindrical shape. The structure displays a hydrophobic surface exposed to the solvent, suggesting a potential role as a plasma membrane pore. More recently, Fusco et al. studied the membrane disruption caused by two oligomers called type A* and type B* (Fusco et al., 2017). In contrast to type A*, type B* is extremely neurotoxic. Using NMR, Fusco et al. found that the toxicity originated from the ability of αSyn to disrupt lipid membrane in type B* oligomers. Indeed, type A* oligomers remain mainly unfolded at the lipid surface. On the contrary, type B* oligomers have the ability to anchor at the lipid bilayer. Owing to the folding of the N-terminal domains into amphipathic helices which stabilise the binding to the lipid bilayer, the NAC domains adopt conformations rich in β-strands which can insert into the lipid bilayer and destabilise it.

Thus, although the story is still incomplete, there is some rationalisation for αSyn toxicity *in vitro*. The αSyn aggregation process is toxic, although the cause of the toxicity is unknown, and the toxicity suggests the interactions of αSyn with lipids and vesicles. However, does this theory match the *in vivo* observations?

1.1.5 Does *in vivo* observation of alpha-synuclein aggregation support *in vitro* results?

As mentioned above, amyloid fibres have already been observed in LBs of post mortem brain sections (Roy and Wolman, 1969). However, reproducing this observation in animal models to study αSyn toxicity is challenging. Only two studies displayed the presence of αSyn amyloid fibres. The first animal model was developed in *Drosophila* (fruit fly). Overexpression of human αSyn triggered cytosolic inclusions composed of an amorphous core with filaments at the periphery (Feany and Bender, 2000). An αSyn knockout (KO) mouse model also displayed fibrillar inclusions of human αSyn (Fares et al., 2016). Interestingly, human αSyn only formed amyloid fibres when the physiological mouse αSyn protein was knocked out. The seeding and the spreading of the human aggregates were also enhanced in this condition. From these observations, the author suggested that the formation and the spreading of human αSyn aggregates may require the absence of other homologous αSyn. However, another study disproved this hypothesis. In a mouse model expressing mouse synucleins, Desplats et al. found that human αSyn aggregates can be transmitted from one neuron to another (Desplats et al., 2009). The authors concluded that a cell-to-cell transmission of human αSyn aggregates is possible and could explain the progression of PD from the *substantia nigra* to peripheral regions in the brain. Therefore, the cause of αSyn aggregation and spreading *in vivo* are still unclear and further investigation is required to identify the factors of αSyn aggregation. A potential factor in the aggregation of αSyn could be the lipid composition of the plasma membrane. Indeed, by using NMR to study αSyn interactions with small unilamellar vesicles of different composition mimicking inner and outer leaflets of the plasma membrane, Man et al showed that αSyn preferentially binds to the inner membrane surface (Man et al., 2021). However, changes in lipid

composition with increased amounts of gangliosides have been related to neurodegeneration, with even ganglioside clustering observed at presynaptic termini of Alzheimer's brains (Yamamoto et al., 2008). Increasing ganglioside concentration in vesicle composition leads *in vitro* to a higher affinity of αSyn for both the inner and the outer membrane leaflets (Man et al., 2021). This lipid modification at the plasma membrane could be involved in αSyn propagation between neurons.

These observations concerning the transmission of αSyn from one neuron to another one suggest that αSyn presents a prion-like behaviour. Prion proteins are associated with neurodegenerative disorders called transmissible spongiform encephalopathies. In those disorders, the prion protein PrP^{C}, which physiologically adopts a soluble helical structure, rearranges to an isoform called PrP^{Sc} rich in β-strands. The PrP^{Sc} isoform becomes an infectious molecule which spreads to other neurons and triggers the conformational change from PrP^{C} to PrP^{Sc} of native prion proteins. A potential origin for this disorder would be the "infection" by misfolded PrP^{Sc} proteins (Iadanza et al., 2018). If αSyn follows a similar mechanism, what could be the origin of the infection?

A recent theory suggests that αSyn aggregation does not start in the brain but in the gut. Indeed, immunostaining of colon tissues of PD patients showed that αSyn is present in these tissues before the onset of motor symptoms (Shannon et al., 2012). Although this result may look surprising, recent studies support this model. In 2018, the vermiform appendix was shown to influence PD progression (Killinger et al., 2018). αSyn aggregates are abundant in the appendix of healthy people, including people younger than 20 years. The presence of αSyn aggregates in the appendix therefore seems common. However, undergoing an appendectomy before the onset of PD delays the progression of the disease. It was therefore suggested that the appendix may be a source of αSyn aggregates which are transported to the brain via the vagal nerve. αSyn

aggregates in the appendix would have a similar effect on native αSyn in the brain as infectious PrP^{Sc} with native PrP^{C}. This hypothesis is also supported by an αSyn KO mouse model mimicking one form of familial PD. It has been observed that an intestinal infection can trigger PD in this mouse model, highlighting the importance of the gut-brain axis in PD (Matheoud et al., 2019). More precisely, the intestinal infection of Pink1 KO mice with Gram negative bacteria induces an autoimmune response with the presence of mitochondria-specific $CD8^{+}$ T-cells within the brain. This autoimmune response is cytotoxic and leads to the impairment of synaptic terminals and the death of dopaminergic neurons via a mechanism which needs to be determined (Matheoud et al., 2019). Recently, it was shown that a vagotomy, a surgical procedure in which the vagal nerve is cut, prevents PD symptoms in mice, even after injection of αSyn fibrils in the guts (Kim et al., 2019). The transmission of αSyn aggregates from the gut to the brain could be due to a loss of some protective mechanism related to aging. But what is the mode of action of αSyn within a cell?

It is assumed that the physiological and pathological roles of αSyn are related to vesicle trafficking (Lautenschläger et al., 2017). Recently, LBs have been studied using correlative light and electron microscopy to uncover the origin of the toxicity. Surprisingly, LBs do not contain amyloid fibres. LBs are mainly composed of dysmorphic vesicles and aggregated organelles surrounded by distorted mitochondria (Shahmoradian et al., 2019). This suggests that αSyn toxicity does not require the formation of amyloid fibres. αSyn interactions with the lipid bilayer may be the key to understanding its toxicity. In yeast, αSyn aggregation leads to the accumulation of vesicles at the plasma membrane (Soper et al., 2008). In the αSyn KO mouse model, inhibiting αSyn leads to the depletion of distal vesicle pools (Murphy et al., 2000). These discoveries suggest that αSyn toxicity derives from a disruption of its

physiological function in vesicle trafficking. Therefore, understanding αSyn interactions *in vivo* is crucial to distinguish its physiological role from its pathological one. In 2019, Ramezani and co-workers studied αSyn interactions with vesicles in a mammalian cell model using wild-type (WT) αSyn, the A30P and V70P αSyn mutants in confocal experiments (Ramezani et al., 2019). The A30P mutant disrupts the first helix of the broken αSyn helical structure (green sphere in figure 1.2C), destabilizing its membrane binding. On the contrary, the V70P mutant destabilises the second helix, preventing the formation of the broken helical structure. By studying these mutants, it is therefore possible to relate αSyn conformation to a specific role within a cell. They showed that at low concentrations corresponding to the physiological level, the second helix (and thus the broken conformation) is required to reduce exocytosis. Conversely, at high concentration, corresponding to the potential αSyn pathological function, the helix of the N-domain is required for exocytosis. They also showed that a high concentration of WT αSyn causes a modest inhibition of endocytosis via the involvement of the C-terminal domain. Using these mutants and several truncations gave the first ideas about the αSyn conformation in different key cellular regions for different concentrations. But Ramezani et al. also studied αSyn colocalization with lipids. Thus, at high expression WT αSyn is colocalised with endosomes at the plasma membrane and with lipid droplets or mitochondria. The co-localisation with mitochondria is increased under stress conditions but inhibited with the A30P and V70P mutants, showing that both helices are required for mitochondrial binding. All these observations suggest that αSyn toxicity may arise from an upregulation of its physiological function and its interactions with lipids. But a recent structural study contradicts this model (Trinkaus et al., 2021). Using cryo-electron microscopy, Trinkaus et al. found that neuronal inclusions are mostly composed of filaments of αSyn and that small fibres mediate the seeding of the

aggregates. However, a few factors limit the interpretations of this study. The study was performed using the A53T mutant, because of its higher seeding abilities. Also, neurons were incubated with preformed fibres. Therefore, this study looked more at the propagation of αSyn aggregates than its aggregation process.

Thus, information on the causes of αSyn toxicity remains contradictory and the ambiguous relationship between αSyn and lipids prevents a clear determination of the physiological and pathological functions of αSyn. *In vitro*, the first studies suggested that amyloid fibres caused αSyn toxicity. However, recent results suggest that small oligomers are responsible. *In vivo* studies using cell lines or animal models contradict the *in vitro* experiments and suggest that αSyn overactivity is sufficient for neuronal death. Considering this unsolved problem, targeting a specific conformation for a treatment may be risky since currently, there is no clear evidence of a well-identified structure causing PD. Targeting the wrong assembly could i) trigger the formation of the pathological assembly by shifting the equilibria between the different species at a high concentration and ii) prevent the potential physiological role of this conformation. Consequently, a versatile approach is necessary to target αSyn toxicity.

1.2 Alpha-synuclein disaggregation by chaperones

In response to protein misfolding and aggregation, all organisms have developed a protein quality control system, known as proteostasis. Proteostasis modulates protein synthesis, folding, unfolding, degradation and disaggregation within a cell. Crucial proteins involved in proteostasis are the chaperone proteins in association with other systems such as lysosomes and proteases (Saibil, 2013). Upon stress, proteins tend to be misfolded and aggregated, losing their biological function and leading to cell death. Heat shock proteins (HSPs), whose expression is highly increased by stress conditions

such as heat, are essential for cell survival and oversee the disaggregation, unfolding, refolding and degradation of denaturated proteins within a cell (Rosenzweig et al., 2019). Chaperones can protect cells from protein aggregation via three main functions: i) refolding of misfolded proteins, ii) trapping aggregates to reduce their toxicity and iii) disassembling aggregates (Wentink et al., 2019). Initially, chaperones protect cells by preventing protein aggregation. The general mechanism is that they recognise exposed hydrophobic surfaces of misfolded proteins and promote their refolding or their degradation. For instance, BiP, which is the human Hsp70 associated to ER, can recognise a mutant prion protein, trap it in the ER and mediate its degradation via the proteasome (Jin et al., 2000). DNAJA2, one of the human J-domain proteins (see section 1.2.2), inhibits tau aggregation *in vitro* and reduce the spreading of tau aggregates *in vivo* (Mok et al., 2018). Chaperones can also reduce aggregate toxicity when aggregation cannot be blocked. For example, the small HSPB1 can reduce the toxicity of beta-amyloid (Aβ) aggregates in mouse cells by sequestering them to form larger non-toxic aggregates composed of Aβ and HspB1 (Ojha et al., 2011). Lastly, chaperones can disassemble protein aggregates. In bacteria, yeast and plants, disaggregation is mediated by the hexameric Hsp100 AAA+ ATPase chaperones: ClpB in *E. coli*, Hsp104 in yeast and Hsp101 in plants, in cooperation with the Hsp70 system (Doyle and Wickner, 2009; Queitsch et al., 2000). The Hsp100 chaperones share a common mechanism: the substrate is bound in the central pore of the hexamer via interactions with flexible tyrosine residues and then pulling forces are applied to it through ATP-coordinated movements of each subunit of the hexamer (Deville et al., 2017; Deville et al., 2019). The Hsp70 system, composed of Hsp70, J-domain protein and nucleotide exchange factor, then intervenes to disassemble aggregates (Glover and Lindquist, 1998; Goloubinoff et al., 1999). However, the mechanism underlying protein

disaggregation in metazoa is still poorly understood. Unlike bacteria, yeast and plants, Hsp100 does not exist in humans (Saibil, 2013).

A few mammalian systems can resolubilise aggregates. For instance, the chaperone-protease HTRA1 can disaggregate tau amyloid fibres both *in vitro* and *in vivo* (Tennstaedt et al., 2012). This mechanism is ATP-independent and depends largely on the PDZ domain of HTRA1 (Poepsel et al., 2015). Recently, the Fas Apoptosis Inhibitory Molecule (FAIM) protein has been shown to disassemble and solubilise *in vitro* mutant SOD1 aggregates, similar to those found in amyotrophic lateral sclerosis. FAIM can also counteract intracellular accumulation and aggregation of SOD1 mutant (Kaku et al., 2020). Lastly, an ATP-dependent system involving specific J-domain proteins, Hsp70 and Hsp110 chaperones has been found (Gao et al., 2015; Nillegoda and Bukau, 2015). The J-domain proteins specify the affinity of Hsp70 for the substrate and Hsp110 accelerates the disaggregation activity (Nillegoda et al., 2015; Rampelt et al., 2012). This model system is more broadly applicable because it operates on αSyn, tau and exon1 huntingtin amyloid fibres (Gao et al., 2015; Nachman et al., 2020; Scior et al., 2021). This chaperone trio is also able to disassemble αSyn oligomers (Franco et al., 2021). Understanding this mechanism is essential for understanding the disaggregation process in humans. The following sections will describe the biochemical and structural details of Hsp70, the J-domain proteins and Hsp110.

1.2.1 The crucial Hsp70 proteins in protein refolding

Hsp70 proteins are the most abundant chaperones and are very well conserved across species (Mogk et al., 2018). They take on diverse housekeeping activities (e.g. protein folding, complex assembly and disassembly, protection from proteolysis) as well as stress-induced roles (e.g. protein aggregation prevention, protein disaggregation and

degradation) (Rosenzweig et al., 2019). The importance of Hsp70 in proteostasis is highlighted by its conservation between species. Hsc70, the constitutively expressed cytosolic Hsp70 in human, and DnaK, the bacterial Hsp70, share 53% sequence identity (Zuiderweg et al., 2013). The variety of Hsp70 substrates arises from its substrate recognition: only a 5-to-7-residue sequence composed of a central hydrophobic region surrounded by basic residues is sufficient for targeting to Hsp70 (Rüdiger et al., 1997). It was estimated that such a sequence occurs every 36 residues on average in proteins (Rüdiger et al., 1997).

All Hsp70 family members share the features observed in DnaK: an ATPase domain, or nucleotide-binding domain (NBD), a substrate-binding domain (SBD) and an unstructured C-terminus. The SBD is frequently divided into a substrate-binding domain rich in β-strands (SBDβ) and a lid domain rich in α-helices (SBDα) (figure 1.5A, Rosenzweig et al., 2019; Saibil, 2013). The NBD is composed of two lobes surrounding the ATP-binding cleft. Bound ATP can mediate inter-domain movements (Flaherty et al., 1990). Lastly, the NBD and SBD regions are connected by a flexible linker which plays a crucial role in allosteric regulation (figure 1.5A).

Hsp70 activity is ATP-dependent and its affinity for substrate is controlled by its ATPase cycle (Rosenzweig et al., 2019). When ATP binds to the catalytic centre, it causes the rotation of the NBD lobes to close the cleft. This triggers the insertion of the linker into the NBD domain which leads to the docking of SBDα and SBDβ to the NBD as well as the detachment of SBDα from SBDβ (figure 1.5B, Kityk et al., 2018, 2012) In this conformation, called the ATP-bound state or open conformation, the SBD is open and can interact with a substrate. Hsp70 proteins preferentially bind substrates with hydrophobic residues, especially aliphatic residues, surrounded by positively charged amino acids (Rüdiger et al., 1997). Although this predilection for hydrophobic

residues looks non-selective as mentioned above, these are generally localised in the core of the protein. Thus, unfolded proteins tend to bind to Hsp70s. The docking of SBDβ to NBD disfavours ATP hydrolysis (Kityk et al., 2015). Then, when the substrate binds to the hydrophobic surface of SBDβ, it induces the release of SBDβ and SBDα from NBD. The SBDα lid can then interact with SBDβ, trapping the substrate between the two domains (figure 1.5C). In parallel, the dissociation of the SBD regions causes a rearrangement of the lobes of NBD which can hydrolyse ATP (Flaherty et al., 1990; Zhu et al., 1996). In this new conformation called the ADP-bound state or closed conformation, Hsp70 has a high affinity for substrate (Rosenzweig et al., 2019). When ADP is replaced by a new ATP molecule, the lid opens, leading to the release of the substrate. It is postulated that consecutive trapping and release of extended substrate will unfold non-native assemblies and correct them by disrupting long range interactions in the unfolded substrate (Sekhar et al., 2015, 2016).

Nevertheless, in the closed conformation, after substrate binding and before ATP hydrolysis, the linker is also released in an extended configuration which cannot keep the optimal NBD conformation for ATP hydrolysis. Consequently, although ATPase activity is achievable in the presence of the substrate, it is not highly stimulated (Rosenzweig et al., 2019). For instance, Hsc70 requires around 10 minutes to hydrolyse a single ATP (Tzankov et al., 2008). Therefore, Hsp70 proteins need the assistance of co-chaperones to trigger ATP hydrolysis, in particular J-domain proteins.

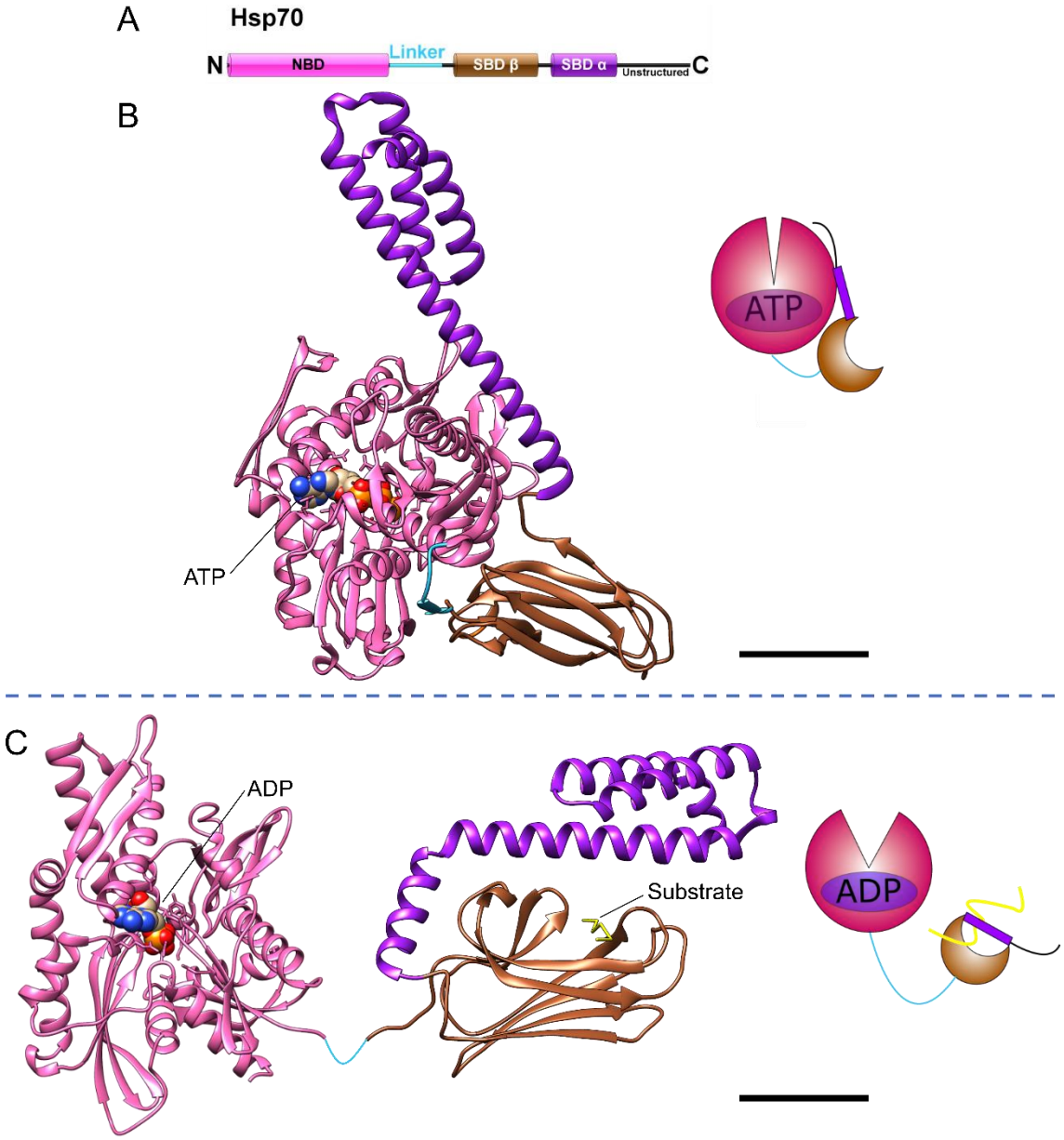

Figure 1.5: The Hsp70 proteins.

(A) Schematic representation of the different domains of Hsp70 proteins. (B) Ribbon representation of the ATP-bound state of the *E. coli* Hsp70 (DnaK, PDB: 4B9Q, Kityk et al., 2012). (C) Ribbon representation of the ADP-bound conformation (PDB: 3HSC for the NBD region, Flaherty et al., 1990; 1DKZ for the SBD region, Zhu et al., 1996). Schematic cartoons on the right-hand side correspond to the conformations shown in (B) and (C). Scale bars, 20 Å.

1.2.2 DNAJ proteins recognise the substrate

The DNAJ proteins, called J-domain proteins, define the specificity of Hsp70 for substrate and can stimulate the ATP hydrolysis rate by up 1000-fold (Jordan and McMacken, 1995). 54 DNAJ proteins, whose size varies from 10 to 520 kDa, are expressed in humans, 22 in yeast and 6 in bacteria (Nillegoda and Bukau, 2015). Their variety attests to the diversity of their function and their substrate specificity (Kampinga et al., 2009). Although the wide size range of the J-domain proteins may prevent us from classifying them in a single family, all of them possess a J-domain.

DNAJ proteins have been classified into three categories according to their sequence and their similarity to *E. coli* DNAJ. Class A J-domain proteins encompass a N-terminal J-domain shared with the bacterial DnaJ, a glycine-phenylalanine-rich (G/F) linker, two C-terminal β-sandwich domains called CTD-I and CTD-II with a zinger-finger-like region (ZFLR) inserted into CTD-I and a C-terminal dimerization domain (figure 1.6A-B, Barends et al., 2013; Greene et al., 1998; Walsh et al., 2004). Class B J-domain proteins are similar to class A proteins except that they do not possess a ZFLR domain (figure 1.6A, Kampinga and Craig, 2010). Lastly, class C J-domain proteins are very diverse with very specific functions, some of them binding to only one substrate (figure 1.6A, Kampinga and Craig, 2010). Class A and B J-domain proteins, but not class C, can form homodimers in solution (Rosenzweig et al., 2019).

J-domain proteins can stimulate Hsp70 ATPase activity via the interaction between the J-domain and the ATPase domain. This binding relies on two helices (II and III) of the J-domain and a linking loop containing the highly conserved histidine-proline-aspartate (HPD) motif (Szyperski et al., 1994; Tsai and Douglas, 1996). Mutations in this highly conserved region affect the binding of DNAJ to Hsp70 (Kelley, 1998). Recently,

solving the X-ray structure of the J-domain of *E. coli* DnaJ bound to the open-conformation of DnaK helped explain the molecular mechanism of DnaJ-stimulated ATP hydrolysis by DnaK (figure 1.7A, Kityk at al., 2018). Via polar and electrostatic interactions, the J-domain binds to the interface between the NBD and SBDβ domains of Hsp70. The HPD motif restrains Hsp70 NBD to a conformation that favours ATP hydrolysis. This structure explains why these key residues can stimulate HSP70 ATPase activity and why they are highly conserved (Kelley 1998; Kityk et al., 2018). The role of J-domain proteins in Hsp70 ATPase activity is summarised in figure 1.7B. In the absence of substrate and J-domain protein (case ①), Hsp70 displays a very low ATPase activity because of the inhibitory effect of SBD on NBD. In the presence of substrate (case ②), the substrate triggers the dissociation of SBD from NBD. However, the affinity of Hsp70 for the substrate is low and the substrate dissociation can occur before ATP hydrolysis. The addition of J-domain proteins (case ③) helps to trap the substrate in Hsp70, increasing the ATPase activity (Kityk et al., 2018; Rosenzweig et al., 2019).

Another key function of J-domain proteins is their binding to substrate. The C-terminal domains of class A and B J-domain proteins have been found to bind to unfolded linear sequences rich in hydrophobic motifs, especially aromatic residues (Brehmer et al., 2001; Jiang et al., 2019; Lu and Cyr, 1998; Rüdiger et al., 2001). Because of low affinity between different substrates and J-domain proteins, it has been suggested that interactions occur through multiple weak binding sites (Feifel et al., 1998). Recently, interactions between an unfolded protein and different J-domain proteins have been studied by NMR (Jiang et al., 2019). Four binding sites have been discovered in the C-terminal domains of the dimeric DNAJs. Each subunit possesses a binding site at the CTD-I domain and another one at the CTD-II domain (figure 1.6B). All binding sites are composed of a couple of hydrophobic β-strands surrounded by polar residues.

Interestingly, the substrate is in competition with the Hsp70 C-terminus to interact with CTD-II binding sites. The EEVD motif at the end of Hsp70 C-terminus, which is very well conserved in eukaryotes, seems to play a crucial role: its deletion prevents Hsp70 refolding activity (Yu et al., 2015). Therefore it has been suggested that 1) the substrate binds to the J-domain protein via weak interactions with the four binding sites present in CTD-I and CTD-II domains; 2) Hsp70 strongly binds to the J-domain of J-domain proteins via its SBD and NBD domains; 3) Hsp70 C-terminal domain weakly interacts with CTD-II binding sites via its EEVD motif, decreasing the affinity of the substrate for the J-domain protein; and 4) the substrate is transferred from the J-domain protein to Hsp70.

In the case of DNAJB1 (a class B J-domain protein in humans), which is the J-domain protein involved in αSyn amyloid fibril disaggregation, the mechanism is slightly different. Instead of four binding sites, DNAJB1 homodimer only displays two binding sites in the CTD-I domain (Jiang et al., 2019). Nevertheless, the competition between the substrate and the Hsp70 C-terminal region still occurs.

Thus, J-domain protein diversity helps to explain Hsp70 functional specificity. However, once Hsp70 has hydrolysed ATP and trapped the substrate in its closed SBD, the complex formed of Hsp70 with substrate and ADP is very stable and the release of the substrate requires the involvement of a nucleotide exchange factor (NEF) to exchange ADP with ATP, which triggers the opening of the SBD (Brehmer et al., 2001; Mayer and Bukau, 2005).

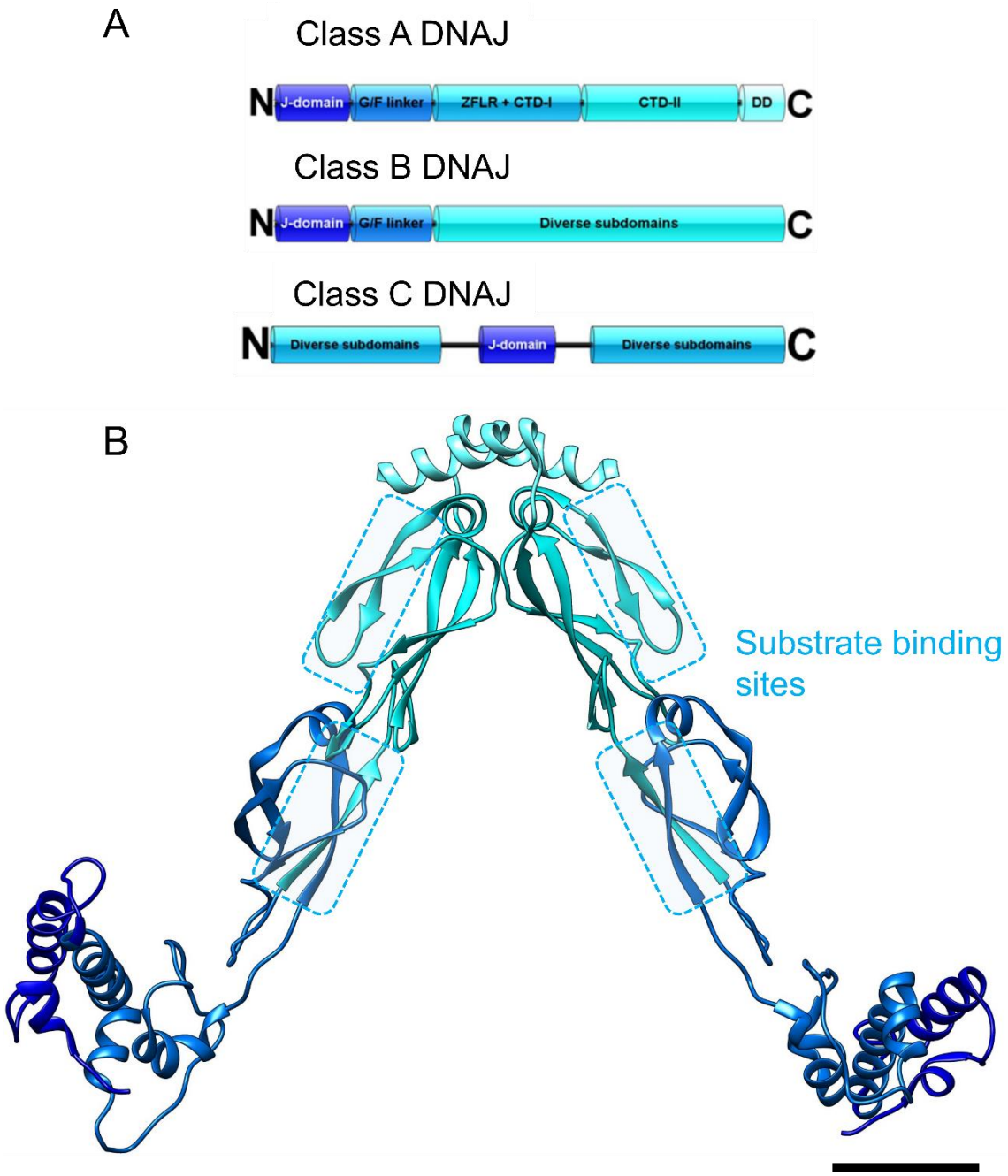

Figure 1.6: The J-domain proteins.

(A) Schematic representations of the different domains associated with the DNAJ classes A, B, and C. (B) Ribbon representation of the bacterial dimeric DnaJ (PDB: 4J80; Barends et al., 2013). Blue dashed boxes represent the substrate binding sites. Scale bar, 20 Å.

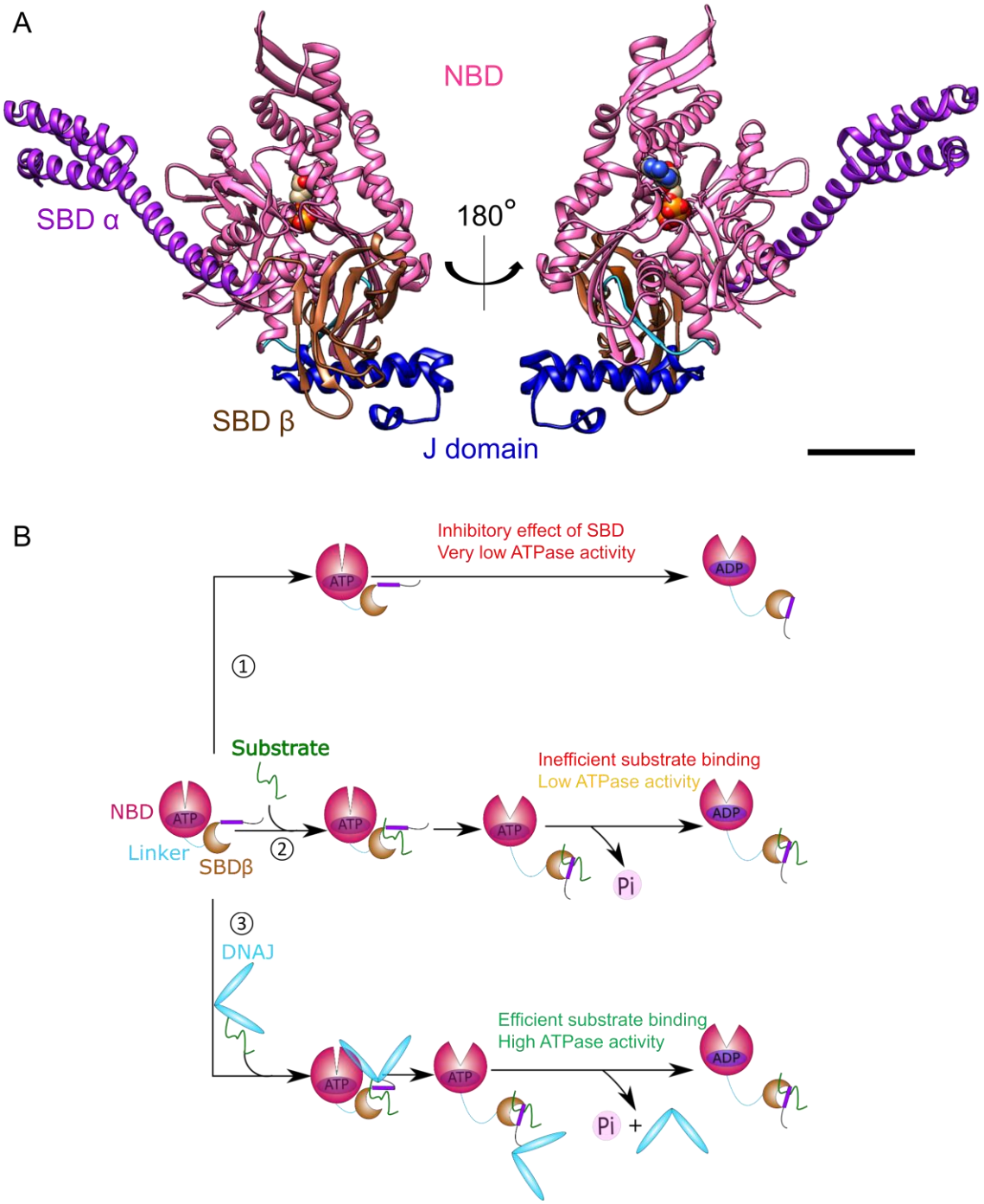

Figure 1.7: The activation of Hsp70 proteins by J-domain proteins.

(A) Ribbon representation of the *E. coli* J-domain in complex with DnaK protein (PDB: 5NRO, Kityk et al., 2018). The J-domain binds to the NBD region, the SBDβ and the linker. Scale bar, 20 Å. (B) The activation of Hsp70 without substrate (①), with substrate (②) and in the presence of J-domain proteins (③). The figure was adapted from Rosenzweig et al., 2019.

1.2.3 The Hsp110 proteins act as nucleotide exchange factors

In eukaryotic cells, Hsp70 nucleotide exchange function depends on NEFs. There are three different families of NEF in human: BAG proteins, HspBP1 proteins and Hsp110 proteins (Bracher and Verghese, 2015; Dragovic et al., 2006). Hsp110 proteins are members of the Hsp70 superfamily, with the same domain structure. Some additional residues differentiate Hsp70 from Hsp110 proteins (figure 1.8, Liu and Hendrickson, 2007; Rosenzweig et al., 2019). However, Hsp110 proteins do not present the same ATP activity, suggesting a different physiological function (Shaner et al., 2004).

The NEF activity is a conserved mechanism between the three NEF families in human (Bracher and Verghese, 2015). Hsp110 proteins can regulate the ADP-bound conformation of Hsp70s via a head-to-head interaction. Two X-ray structures of the yeast Hsp110 (Sse1) in complex with either the full-length bovine Hsp70 or the truncated yeast Hsp70 (Ssa1) containing only the NBD have been solved (Polier et al., 2008; Schuermann et al., 2008). Sse1 is very similar to the human Hsp110, called Apg2, which will be described in αSyn fibril disaggregation later in this chapter. In the X-ray structures, the NBD of Hsp110 binds to the NBD of Hsp70 via several electrostatic intermolecular interactions and hydrogen bonds. Interestingly, residues involved in Hsp70-Sse1 interactions are very well conserved between species for both Hsp70s and Hsp110s (Schuermann et al., 2008). The formation of the complex is mostly limited to Hsp110-NBD and Hsp70-NBD interactions, suggesting that the binding does not directly influence Hsp70 interactions with the substrate. This complex blocks Hsp70 NBD in its open conformation, triggering ADP release. Moreover, the complex forms a pore composed of subdomains of each NBD. The pore inner surface is positively charged while the outer face is negatively charged. This charge distribution may

facilitate ADP release from Hsp70 and ATP binding. ATP binding then triggers complex dissociation.

In addition to its NEF activity, because of its close homology with Hsp70, Hsp110 possesses an ATP-dependent holdase activity to stabilise unfolded proteins and interact with J-domain proteins (Mattoo et al., 2013).

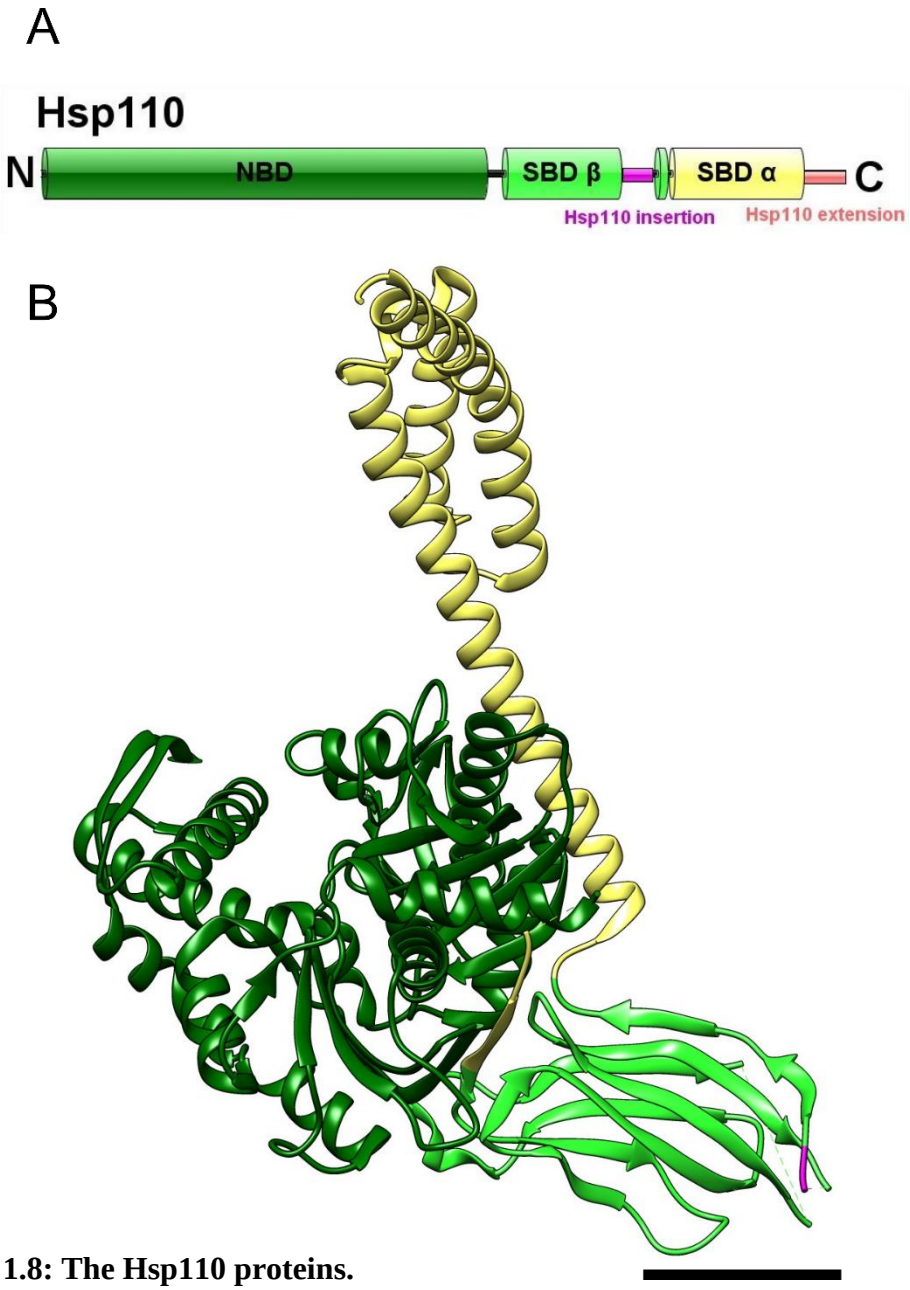

Figure 1.8: The Hsp110 proteins.

(A) Schematic representation of the different domains of Hsp110 proteins. (B) Ribbon representation of the yeast Hsp110, Sse1 (PDB: 2QXL, Liu et al., 2007). Scale bar, 20 Å.

1.2.4 The Hsp70 system disaggregates amyloid fibres *in vitro*

As described above, Hsp70 function in protein unfolding and disaggregation requires the involvement of two co-chaperones and is summarised in figure 1.9 (Rosenzweig et al., 2019). First, the J-domain protein recognises the substrate (step 1), thus increasing Hsp70 affinity for the substrate. Then, Hsp70 binds to the J-domain protein and competes with the substrate (step 2). Once the substrate binds to Hsp70, the J-domain protein stimulates ATP hydrolysis, causing a conformational change of Hsp70. In this new conformation, the substrate is trapped in an extended state. J-domain protein is then released (step 3). Hsp110 (NEF) binds to Hsp70 without affecting the substrate (step 4). The new complex, via the formation of an entry/exit pore between Hsp110 and Hsp70, releases ADP (step 5) and interacts with a new ATP (step 6). Once ATP binds to the Hsp70 NBD, Hsp110 and substrate are released (step 7). The substrate is either unfolded or still misfolded and a new Hsp70 cycle can start.

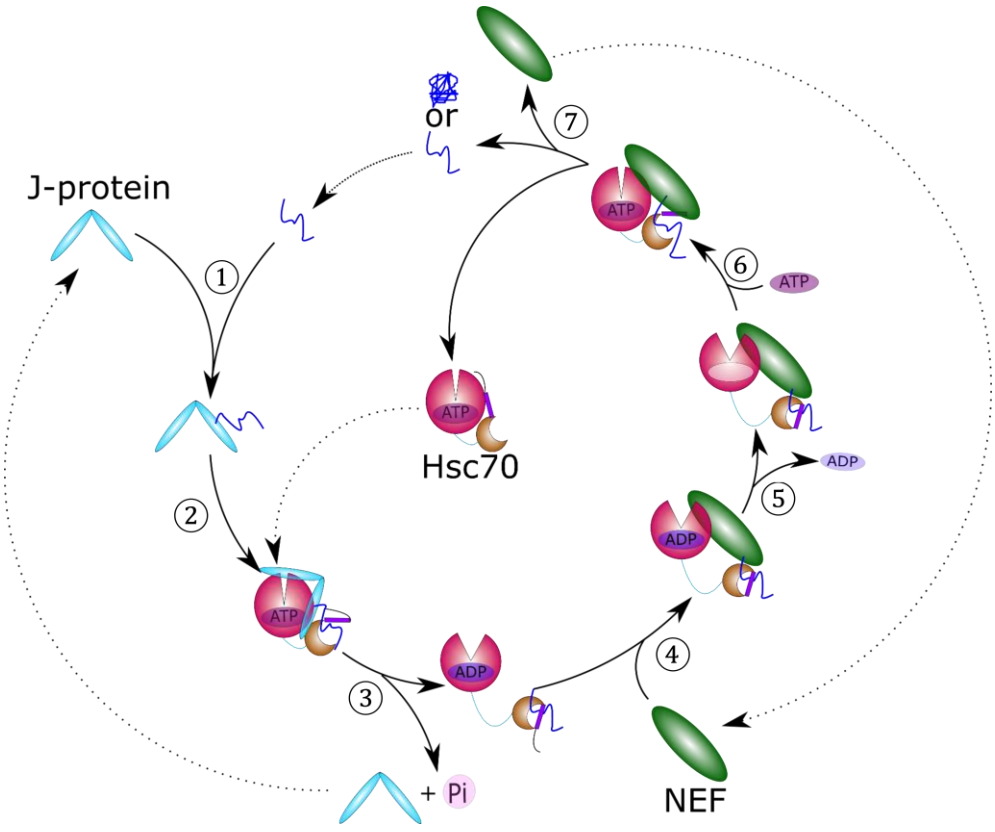

Figure 1.9: The ATPase cycle of Hsc70.

In humans, Hsp70 system can resolubilise protein aggregates involved in disorders. DNAJA2 and DNAJB1 (J-domain proteins) coupled with Hsc70 and Apg2 (Hsp110) can solubilise amorphous αSyn aggregates (Nillegoda et al., 2015). And, as mentioned above, DNAJB1, Hsc70 and Apg2, without DNAJA2 involvement, can disassemble αSyn, tau and huntingtin exon1 amyloid fibres *in vitro* in a chaperone-concentration-dependent manner by fragmentation and depolymerisation (figure 1.10, Gao et al., 2015; Nachman et al., 2020; Scior et al., 2021). Two models are debated for fibril disassembly: The Clamp and Walk model and the nucleation model (Mattoo et al., 2013; Nillegoda and Bukau, 2015). In the Clamp and Walk model, a heterodimer composed of Hsc70 and Apg2 is formed. This heterodimer "walks" on fibres through multiple ATPase cycles of low affinity (ATP-bound state) and high affinity (ADP-bound state) for substrate. These cycles generate pulling forces to extract peptide loops from aggregates. In the nucleation model, several Hsc70s are recruited by the DNAJB1 proteins. A large complex composed of Hsp110s and multiple DNAJB1s as well as Hsp70s is formed. Single subunits of fibres are released via an entropic pulling mechanism. However, a recent study, which analysed the function of each chaperone, supports the nucleation model (Wentink et al., 2020). By using various biophysical and biochemical techniques as well as NMR, Wentink et al. showed that in a first stage, dimeric DNAJB1, which has the highest affinity for the fibres among the three chaperones, binds to the flexible C-terminus of αSyn. This increases the binding affinity of Hsc70 for the fibres by 10- to 20-fold, which leads to Hsc70 recruitment to the flexible N-terminus of αSyn and Hsc70 clustering (Gao et al., 2015; Wentink et al., 2020). In a few studies, it was shown that only a class B DNAJ is able to promote fibre disaggregation (Gao et al., 2015; Scior et al., 2021). Recently, Faust et al. gave an explanation for this observation with NMR observations (Faust et al., 2020). Class B J-

domain proteins possess an additional helix 5 in the GF region which is docked to the J-domain, inhibiting the direct interaction between the J-domain of DNAJB1 and Hsc70. Instead, the interaction between Hsc70 and DNAJB1 is a 2-step mechanism. First, the EEVD motif at the C-terminus of Hsc70 interacts with the CTD-I of DNAJB1. This triggers the undocking of the helix 5 and frees the DNAJB1 J-domain to interact with Hsc70. This additional helix 5 is not present in class A DNAJ proteins, which cannot promote the disaggregation of amyloid fibres. This hypothesis was then confirmed by using a mutant of DNAJB1, ΔH5, which lacks helix 5. This mutant could not trigger the disaggregation of αSyn amyloid fibres (Faust et al., 2020). Although the reason is still unknown, this 2-step mechanism for the interaction between DNAJB1 and Hsc70 is necessary for the disaggregation of amyloid fibres. Then, Wentink et al showed indirectly by Fluorescence Resonance Energy Transfer (FRET) microscopy and fluorescence anisotropy that Apg2 acts as a nucleotide exchange factor and triggers the release of only non-clustered Hsc70 molecules, an action attributed to the large size of Apg2 (figure 1.10A, Wentink et al., 2020). The cooperation between Hsc70 and its cochaperones enables a dense organisation of Hsc70 on the fibre surface, creating an entropic drive for fibre disassembly by pulling forces (figure 1.10A).

This mechanism has also been studied by negative stain electron microscopy (figure 1.10B-D, Gao et al., 2015). In the presence of chaperones and ATP, amyloid fibres were much shorter after a 4h-incubation (figure 1.10B). Negative stain tomograms of the fibres decorated with the 3 chaperones and ATP displayed globular complexes bound to the fibres (figure 1.10C). Lastly, the binding of each individual chaperone on the fibres was also investigated (figure 1.10D). While Hsc70 and Apg2 decorations were irregular and sparse, DNAJB1 decoration was denser and regular with a 5nm-spacing along the fibre (figure 1.10D).

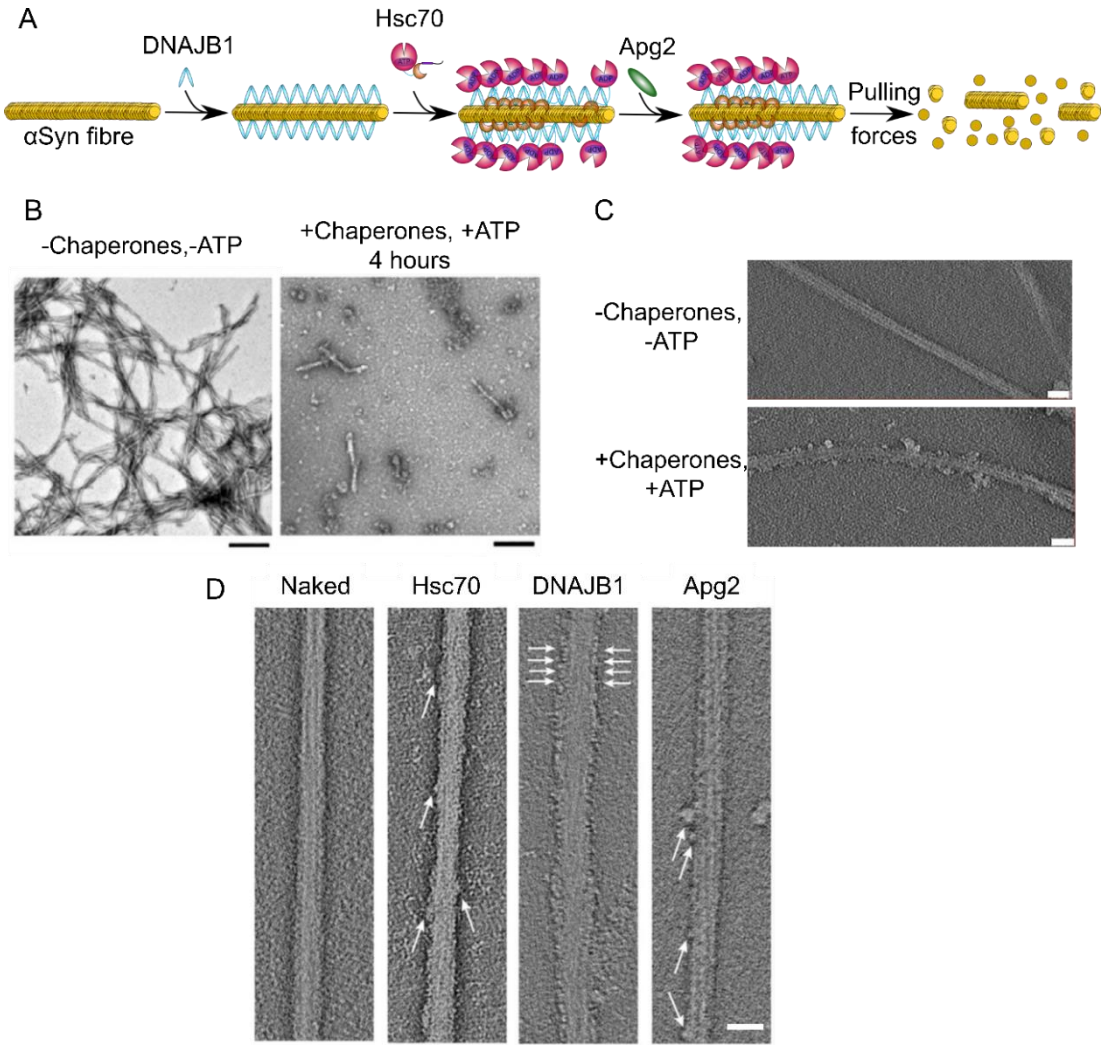

Figure 1.10: The tripartite Hsp70 chaperone system disaggregates αSyn amyloid fibres.

(A) Cartoon representation of the amyloid fibre disaggregation by the tripartite system. The figure was adapted from Wentink et al., 2020. (B) Negative stain TEM pictures of αSyn amyloid fibres in the absence (left picture) and in the presence of the chaperones and ATP (right picture) after 4 hours. The scale bars represent 250 nm. (C) Sections through a negative stain tomogram of αSyn fibres without the chaperones (upper panel) and with the chaperones and ATP (lower panel). (D) Sections through a negative stain tomogram of αSyn fibres without chaperones, with Hsc70, DNAJB1 or Apg2. The white arrows highlight chaperones bound to the fibres. The white scale bars in (C) and (D) represent 20 nm. Panels (B), (C) and (D) were adapted from Gao et al., 2015.

Recently, a few studies focused on the dynamics of the disaggregation by atomic force microscopy (AFM) or fluorescence microscopy. Using microfluidic diffusional sizing to determine the length of the fibres over time, Schneider et al. showed that monomers are directly extracted from αSyn amyloid fibre ends (Schneider et al., 2021). By time-course AFM, Beton et al. confirmed first that αSyn fibre disaggregation occurs by both depolymerisation and fragmentation (figure 1.11A, Beton et al., 2021). The depolymerisation is unidirectional, suggesting that the polarity of the fibres influences the disaggregation with one end more accessible for chaperone binding. The depolymerisation occurred in rapid bursts and a localised height increase was observed before the depolymerisation (figure 1.11B-D). After rejecting alternative hypotheses, it was shown that the height increase corresponds to a dense decoration of chaperones on the fibre surface. Franco et al. also studied the disaggregation of αSyn amyloid fibres by AFM and found that the two protofilaments are unzipped in a first step before αSyn monomers are released (Franco et al., 2021).

The consequences of the disaggregation of amyloid fibres and short oligomers by the Hsc70 disaggregase system for toxicity is still debated. αSyn monomers and small oligomers resulting from the disaggregation of amyloid fibres are less toxic for cells than the initial fibres (Gao et al., 2015). This suggests a protective role of the chaperones. However, tau monomers and oligomers resulting from the same process are seeding-competent species that can induce tau aggregation in cells (Nachman et al., 2020).

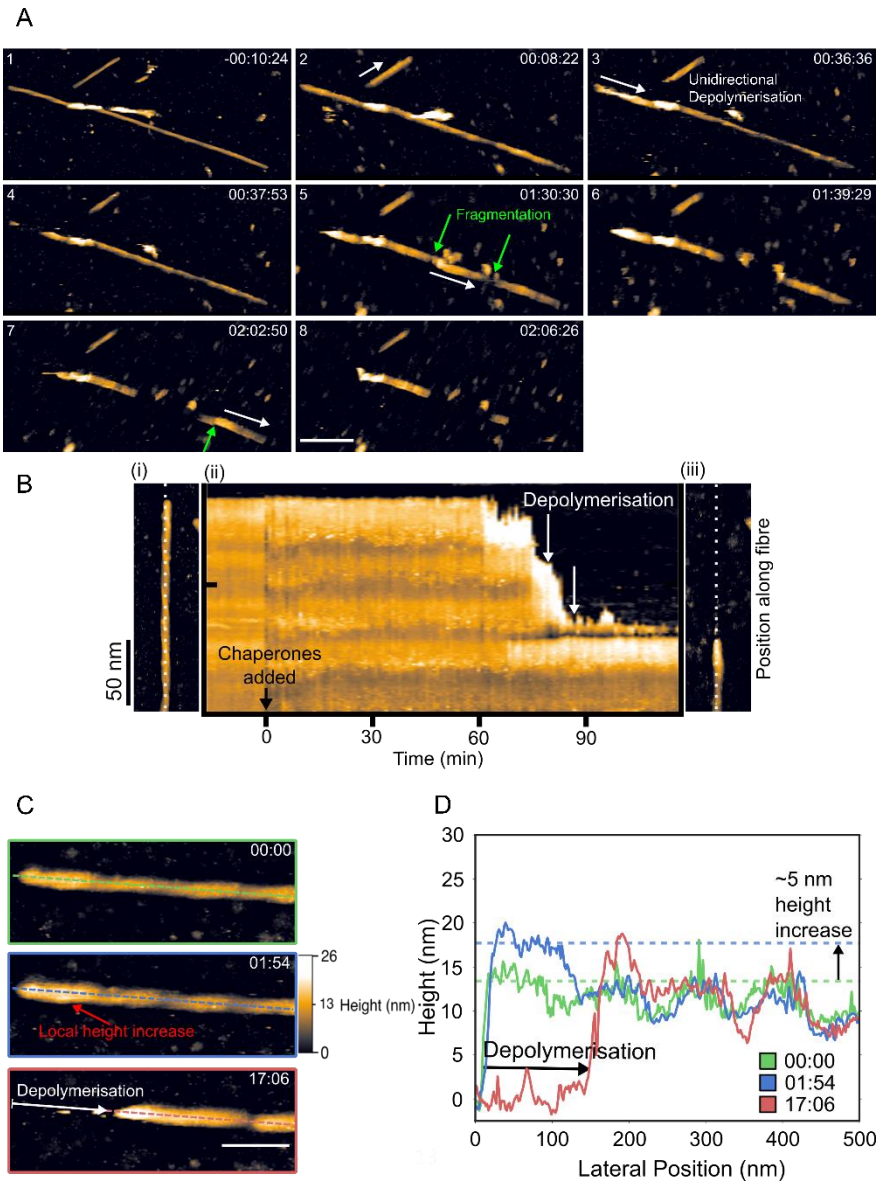

Figure 1.11: αSyn amyloid fibres are disassembled in rapid bursts of depolymerisation preceded by a local dense recruitment of chaperones.

(A) Frames at different timepoints showing the disaggregation of αSyn amyloid fibres. Fibres are disassembled by depolymerisation (white arrows) and fragmentation (green arrows). The time stamp is in hours:minutes:seconds, with the chaperones and ATP added at time 0:00:00. Scale bar, 250 nm. (B) Kymograph showing the disaggregation of a fibre: (i) the fibre before disaggregation, (ii) kymograph showing the fibre as a function of time with rapid depolymerisation events, (iii) the last frame showing the fibre being mostly disassembled. (C) A local height increase, characterised by a brighter segment of fibres, precedes fibre depolymerisation. (D) Height profiles of the fibre shown in the 3 panels in (C) showing a 5 nm height increase at fibre surface before depolymerisation. The images were adapted from Beton et al., 2021.

1.3 Aims of the project

1.3.1 The aggregation of alpha-synuclein

αSyn toxicity remains poorly understood. While the origins of αSyn toxicity and the mechanism underlying its aggregation have been well studied *in vitro, in vivo* observations are rare and often limited to fluorescence studies. Cell models are more accessible than *in vivo* models for the study of αSyn aggregation, although αSyn aggregates in cell models may be different from *in vivo* αSyn aggregates. However, since αSyn is toxic in cell models, it is interesting to obtain more information about αSyn aggregates in these models by electron microscopy. Correlative light and fluorescence microscopy constitutes a powerful technique to study αSyn aggregation in a yeast cell model. This way, *in vitro* experiments can confirm *in situ* observations. Consequently, in this project, I aim to answer the following questions:

- What is the morphology of αSyn aggregates *in situ* in a yeast cell model?
- What are the mechanisms of membrane disruption and membrane clustering *in vitro*? If relevant, what are the structural details of this clustering?

1.3.2 The disaggregation of alpha-synuclein amyloid fibres by the Hsc70 system

A chaperone model has been built to study αSyn disaggregation *in vitro* (figure 1.10A). However, there is a lack of structural information about this model and the currently suggested function of Apg2 which reorganises isolated Hsc70 molecules is based on indirect measurements. Therefore, I aim to answer the two following questions:

- How does Apg2 reorganise Hsc70 bound to the fibre?
- What is the structure of the initial complex formed of DNAJB1 bound to αSyn amyloid fibres?

2. Materials and methods

2.1 Protein expression

2.1.1 Materials

The plasmids for the expression of the WT proteins (αSyn, Hsc70, DNAJB1, Apg2) and their mutants were kindly provided by Professor Bernd Bukau's group. The plasmids used in this thesis were pT7-7 for αSyn and pCA528 with a His_6-Smt_3 tag at the N-terminus for the chaperones. The purified mutant of DNAJB1 lacking the J-domain and the G/F linker, called ΔJ-DNAJB1, was provided by Professor Rina Rosenzweig's group and stored in 25 mM HEPES, 200 mM KCl, 10 mM $MgCl_2$, 2 mM DTT, pH 7.5.

LB media powder (37g, Sigma Aldrich, USA) was dissolved in distilled water (1 L) to prepare LB medium. Media were autoclaved at 121°C, 15 psi for 15 minutes to sterilise them before use. Where necessary, antibiotics were added to media to reach the following final concentrations: 100 µg/mL for ampicillin (Sigma Aldrich, USA), 50 µg/mL for kanamycin (Melford Biolaboratories, UK), and 34 µg/mL for chloramphenicol (Duchefa Biochemie, Netherlands).

LB agar powder (37 g, Sigma Aldrich, USA) was dissolved in distilled water (1 L) and the solution was sterilised as described above. When the solution was hand hot, antibiotics were added to reach the final concentrations mentioned above. The solution (20 mL) was then poured into a sterile plastic petri dish and dried in a sterile environment to prepare the LB agar plates.

The plasmid for the expression of the GFP-tagged αSyn (pME3945) in *S. cerevisiae* yeast cells was kindly provided by Professor Tiago Outeiro. A KLID linker connected the GFP tag to the C-terminus of αSyn.

2.1.2 Transformation of competent cells by heat shock

Transformation competent cells (50 µL) were thawed on ice. Relevant plasmid DNA (0.5 µL, pT7-7 vector for αSyn and its mutant, pCA528 vector for the chaperones and their mutant) was transferred into a sterile 1.5 mL Eppendorf tube and competent cells (25 µL) were carefully pipetted onto the plasmid droplet. This solution was incubated for 30 minutes (min) on ice before being incubated at 42°C for 45 seconds (s) for the heat shock. Cells were then promptly returned to the ice for 5 additional min. Prewarmed LB medium (950 µL) was mixed to the cells and the cell suspension was then incubated at 37°C, 180 rpm for 1 hour. The cell suspension was then centrifuged for 5 min at 2,370 g, supernatant was discarded and cell pellet was resuspended in 200 µL LB medium before being spread on LB agar plates in sterile conditions and incubated at 37°C overnight.

2.1.3 αSyn expression

Human αSyn was expressed as a native untagged protein. Cells from transformed cell plates (*E. coli* BL 21 competent cells, ThermoFisher Scientific, USA) were inoculated with ampicillin (100 µg/mL) LB medium (100 mL) and cultured overnight at 37°C. The following day, the culture was diluted into ampicillin LB medium (8x0.5 L) in order to yield an initial optical density of 0.05 measured at a wavelength of 600 nm (OD_{600}). Cells grew at 37°C, 200 rpm until an OD_{600} reading of 0.6-0.8 was obtained. Protein expression was triggered by adding 0.5 mM IPTG. Cells were then shaken at 200 rpm for 4 hours at 37°C. Cells were centrifuged at 6,300 g for 10 min at 4°C using an Avanti J-20 I (Beckman Coulter) centrifuged equipped with a JLA 8.1 rotor (Beckman Coulter). The pellet was resuspended in Tris-buffered saline (50 mM Tris-HCl, 150 mM NaCl, pH 7.50) and centrifuged again at 4,200 g for 20 min at 4°C using a Rotina 420R

(Hettich, Germany). The pellet was then flash frozen in liquid nitrogen and stored at -20°C until cell lysis.

2.1.4 Chaperone expression

Human WT chaperones and their mutants were expressed as native sequences with a N-terminal His_6-Smt_3 tag to enable purification via ion metal affinity chromatography (His_6 tag) and site-specific cleavage (Smt_3 tag for SUMO protease Ulp1). Cells from transformed cell plates (Rosetta *E. coli* cells, Novagen, USA) were inoculated with kanamycin (50 µg/mL) and chloramphenicol (34 µg/mL) LB medium (100 mL) and cultured overnight at 37°C. The chaperone expression was performed as described above for αSyn expression, using kanamycin and chloramphenicol antibiotics instead of ampicillin.

2.2 Protein purification

2.2.1 Materials

The Ulp1 protease was kindly provided by Shomon Miah from Dr Cara Vaughan's group. I used the following buffers for the experiments:

	Buffer	Composition					
αSyn	αSyn Lysis buffer	100 mM Tris-HCl	10 mM EDTA	2mM DTT	pH 8.0		
	αSyn dialysis buffer	25 mM Tris-HCl	2mM DTT	pH 7.7			
	αSyn A buffer	25 mM Tris-HCl	2mM DTT	pH 7.7			
	αSyn B buffer	25 mM Tris-HCl	1 M NaCl	2mM DTT	pH 7.7		
	αSyn SEC buffer	50 mM $NaPO_4$	100 mM NaCl	pH 7.3			
	αSyn fibrillation buffer	50 mM $NaPO_4$	100 mM NaCl	0.05% w/v NaN_3	pH 7.3		
Hsc70 and Apg2	Hsp70/110 lysis buffer	50 mM HEPES	150 mM KCl	5 mM $MgCl_2$	2mM DTT	pH 7.50	
	Hsp70/110 wash 1 buffer	50 mM HEPES	150 mM KCl	5 mM $MgCl_2$	0.1 mM PMSF	2mM DTT	pH 7.50
	Hsp70/110 wash 2 buffer	50 mM HEPES	150 mM KCl	5 mM $MgCl_2$	40 mM imidazole	2mM DTT	pH 7.50
	ATP wash buffer	50 mM HEPES	150 mM KCl	5 mM $MgCl_2$	5 mM ATP	2mM DTT	pH 7.50
DNAJB1	DNAJ lysis buffer	50 mM HEPES	750 mM KCl	5 mM $MgCl_2$	10% glycerol	pH 7.50	
	DNAJ wash 1 buffer	50 mM HEPES	150 mM KCl	40 mM imidazole	10% glycerol	5 mM $MgCl_2$	pH 7.50
	DNAJ wash 2 buffer	50 mM HEPES	50 mM KCl	40 mM imidazole	10% glycerol	5 mM $MgCl_2$	pH 7.50
	DNAJ elution buffer	50 mM HEPES	750 mM KCl	500 mM imidazole	10% glycerol	5 mM $MgCl_2$	pH 7.50
	DNAJ SEC buffer	50 mM HEPES	750 mM KCl	5 mM $MgCl_2$	10% glycerol	pH 7.50	
	HKMD buffer	50 mM HEPES	50 mM KCl	5 mM $MgCl_2$	2mM DTT	pH 7.50	
	HKMT buffer	50 mM HEPES	50 mM KCl	5 mM $MgCl_2$	2mM TCEP	pH 7.50	
	HD buffer	50 mM HEPES	2mM DTT	pH 7.50			
	Disaggregation buffer	HKMD buffer	20 ng/µL pyruvate kinase	6 mM PEP	5 mM ATP		
	Liposome buffer	20 mM HEPES	150 mM NaCl	pH 7.5			

Table 2.1: List of buffers used in this study.

2.2.2 General protocols

2.2.2.1 Determination of the protein concentration by absorbance at 280 nm

Protein concentration was determined by absorbance at 280 nm using a DeNovix DS-11 spectrophotometer (DeNovix, USA). The spectrophotometer was first blanked with the appropriate sample buffer. Three readings were recorded for each sample, and the concentration was determined from the Beer-Lambert law:

$$A_{280} = \varepsilon lc \text{ (equation 1)}$$

where A_{280} is the absorbance at 280 nm measured by the spectrophotometer; ε is the molar extinction coefficient; l is the optical path length (expressed by DeNovix DS-11 as 1 cm equivalent values); and c is the molar concentration of the sample. The average of the three measures was calculated and considered as the concentration of the sample.

The molar extinction coefficients were determined using the Protparam programme of the ExPASy server (Gasteiger et al., 2005). The following coefficients were determined:

Protein	Molar extinction coefficient ($L.mol^{-1}.cm^{-1}$)
WT αSyn	5,960
DNAJB1	18,910
ΔJ-DNAJB1	8,605

Table 2.2: List of the molar extinction coefficients used in this study.

2.2.2.2 Determination of the protein concentration by Bradford Assay

Some proteins were purified in the presence of ATP (Hsc70, its mutant and Apg2) whose absorbance peak is at 260 nm. Therefore, the absorbance given by the DeNovix DS-11 spectrophotometer was biased. Instead, protein concentration was measured by the Bradford Assay.

First, a serial dilution of bovine serum albumin (BSA, Sigma Aldrich, USA) between 0.1 g/L and 14 g/L was prepared. Each BSA concentration (3 µL) was diluted into 1X Bradford reagent (3 mL, Sigma Aldrich, USA) and incubated for 2 min at room temperature before measuring the absorbance at 595 nm using a UV-Vis 1 mL cuvette (ThermoFisher Scientific, USA) and a BioPhotometer D30 spectrophotometer (Eppendorf, Germany). The points corresponding to the absorbance at 595 nm were plotted as a function of the mass concentration and fitted by linear regression using Excel software (Microsoft).

A similar protocol was followed for the sample of interest. However, three readings from three different diluted samples were taken in order to minimise variations. The mass concentration was calculated using the standard curve. The molar concentration was then determined from the mass concentration and the molecular weight.

2.2.2.3 Determination of the protein purity by Sodium Dodecyl Sulphate-Polyacrylamide Gel Electrophoresis (SDS-PAGE)

Solutions composed of sample (5 µL), 4X NuPAGE SLS sample buffer (7.5 µL, ThermoFisher Scientific, USA), and deionised water (17.5 µL) were incubated at 90°C for 5 minutes. Solutions (10-15 µL) were then centrifuged at 16,000g for 30 sec and loaded onto BOLT 4-12% Bis-Tris Plus, 15-well gels (ThermoFisher Scientific, USA). A Precision Plus Protein^{TM} 10-250 kDa ladder (Bio-Rad, USA) was added to at least one well in the gels. Gels were incubated in 1X Bolt^{TM} MES SDS running buffer (ThermoFisher Scientific, USA) in the chamber of a Mini Gel Tank (ThermoFisher Scientific, USA). Electrophoresis ran for 45 minutes at 180 V, and 400 mA. After electrophoresis, the gel was immersed in InstantBlue^{TM} Coomassie protein stain (Expedeon) for at least 20 minutes. It was then washed 3 times in distilled water before

being scanned. The image of the gel was analysed using Fiji ImageJ software (Schindelin et al., 2012). When necessary, the images were rotated to have all the bands horizontal. A rectangle was then drawn to select only the bands of interest and the intensity of the bands was plotted. Each peak was separated and its area measured.

2.2.3 αSyn purification

The αSyn purification and fibrillation steps were performed by following Dr Anne Wentink's protocol established in Professor Bernd Bukau's laboratory.

2.2.3.1 αSyn purification

The pellet was defrosted at 37°C in αSyn lysis buffer containing protease inhibitor cocktail tablets (Roche, table 2.1). The sample was then vortexed to resuspend the pellet. Cells were lysed by sonication (3 cycles of 2 minutes, 60% amplitude, 1 s on, 1 s off; Vibra-Cell™ Ultrasonic Liquid Processors, SONICS). The sample was centrifuged at 48,384 g for 1 hour at 4°C to pellet cell debris and insoluble proteins. The supernatant (soluble fraction) was then collected.

The soluble fraction was boiled for 20 minutes and then centrifuged at 48,384 g for 45 minutes at 4°C to pellet aggregated proteins. The supernatant was again collected, and 30 mg/mL streptomycin sulphate was added. The resulting solution was incubated for 30 minutes at 4°C, then centrifuged at 48,384 g for 30 minutes at 4°C. The pellet, containing aggregated cellular DNA, was discarded. The supernatant was collected and inoculated with 400 mg/mL ammonium sulphate to precipitate the protein. The resulting solution was incubated at 4°C for 30 minutes and was then centrifuged at 48,384 g for 30 minutes at 4°C. Finally, the pellet was resuspended in αSyn dialysis buffer (table 2.1) and dialysed overnight in deionised water using a pre-wetted RC dialysis tubing with a 3.5 kDa MWCO (Spectrum Labs, Greece).

The following day, the dialysed sample underwent ion exchange chromatography: the sample was loaded on to a HiTrap Q HP 1 mL Column (GE Healthcare, USA) by a single passage with a tabletop peristaltic pump. The column was attached to an ÄKTA purifier system. Purification was based on a linear 60 mL, 0-600 mM NaCl gradient using αSyn A and αSyn B buffers (table 2.1). 2-mL fractions were analysed by SDS-PAGE. Sufficiently pure αSyn fractions were pooled together, concentrated to 1-3 mM using AMICON 10 kDa centrifugal concentrators, aliquoted, flash-frozen in liquid nitrogen and stored at -80°C until use.

Aliquots were purified by size exclusion chromatography. A Superdex 200 Increase 10/300 gel filtration column (GE Healthcare, USA) pre-equilibrated in αSyn SEC buffer was used (table 2.1). The sample was purified at a 0.5 mL/min flow rate, at 4°C in αSyn SEC buffer on an ÄKTA purifier system. 0.5 mL fractions were analysed by SDS-PAGE to identify pure fractions corresponding to monomeric αSyn which were then combined and concentrated up to 2.5 mM.

S9C αSyn mutant was expressed and purified as described above. TCEP was added to a final concentration of 2 mM in the purification buffers.

2.2.3.2 αSyn fibrillation reaction

The αSyn sample was filtered and diluted to 200 μM with αSyn fibrillation buffer (table 2.1) in a 1.5 mL Protein LoBind Eppendorf tube (Eppendorf, Germany). Sodium azide (0.05%, w/v) and preformed αSyn amyloid fibres (1%, v/v) were added in sterile conditions. The solution was then shaken at 1,000 rpm, 37°C for a week using an orbital shaker (PCMT Thermoshaker, Grant-bio, UK). Amyloid fibres were stored at room temperature.

S9C:WT (1:2) amyloid fibres were prepared following the same protocol, with the addition of 2 mM TCEP in the fibrillation buffer.

2.2.4 Chaperone purification

The chaperone purification was performed following a protocol optimised by Ennio D'Amico and Dr Nadinath Nillegoda in Professor Bernd Bukau's laboratory (Nillegoda et al., 2015).

2.2.4.1 DNAJB1 purification

The pellet was defrosted at 37°C in DNAJ lysis buffer containing protease inhibitor cocktail tablets (Roche, table 2.1). The sample was vortexed to resuspend the pellet. Cells were lysed by sonication (3 cycles of 2 minutes, 60% amplitude, 1 s on, 1 s off; Vibra-Cell™ Ultrasonic Liquid Processors, SONICS). The sample was centrifuged at 48,384 g for 1 hour at 4°C to pellet cell debris and insoluble proteins. The supernatant was then collected.

2g of Ni-IDA beads (Macherey-Nagel) were added to the supernatant, which was incubated for at least 2 hours at 4°C. The solution was kept on ice for at least 5 minutes to settle the bead pellet by gravity. The unbound fraction was collected and analysed by SDS-PAGE. Beads were washed three times by adding 1 column volume (CV=5mL) DNAJ wash 1 buffer (table 2.1), resuspending the beads, waiting for settling, and discarding the supernatant. The same process was repeated three times with 1 CV DNAJ wash 2 buffer (table 2.1). Protein was eluted by adding 1 CV DNAJ elution buffer (table 2.1) and collecting the supernatant until absorbance reading at 280 nm for the collected fractions was less than 0.1 AU. Fractions were analysed by SDS-PAGE. Fractions containing relatively pure DNAJB1 were pooled and concentrated using a 15 mL 10 kDa centrifugal concentrator (AMICON) to a volume smaller than 3 mL. The

concentrated sample was loaded onto a 3 mL GeBAflex-Maxi dialysis tube (Generon, UK) with 100 µL of Ulp1 protease to cleave the tag. The concentrated sample was dialysed overnight into DNAJ lysis buffer at 4°C (table 2.1).

The following day, 2g of Ni-IDA beads were added to the cleaved product. The sample was diluted in DNAJ lysis buffer (table 2.1) to a final volume of 10 mL. The mixture was incubated at 4°C for at least 1 hour, and then kept on ice for at least 5 minutes to settle the bead pellet by gravity. The unbound fraction, which contained cleaved DNAJB1, was collected. The beads were washed by repeatedly adding 1 CV of DNAJ lysis buffer (table 2.1) until reaching an absorbance at 280 nm lower than 0.01 AU. The beads were washed with 3 CVs of DNAJ elution buffer (table 2.1). All the fractions were analysed by SDS-PAGE. Fractions containing sufficiently pure DNAJB1 were collected, pooled and concentrated with a 15 mL 10 kDa centrifugal concentrator until reaching 250 µM. The concentrated sample was then aliquoted (V=500 µL) and flash-frozen in liquid nitrogen before being stored at -80°C.

Aliquots were purified by size exclusion chromatography. A Superdex 200 Increase 10/300 gel filtration column (GE Healthcare, USA) pre-equilibrated in DNAJ SEC buffer was used (table 2.1). The sample was purified at a 0.5 mL/min flow rate, at 4°C in DNAJ SEC buffer (table 2.1) on an ÄKTA purifier system. 0.5 mL fractions were analysed by SDS-PAGE to identify pure fractions corresponding to dimeric DNAJ. Pure fractions were then pooled and concentrated up to 300 µM.

2.2.4.2 Hsc70 and Apg2 purification

Hsc70 and Apg2 were purified in parallel following the same protocol. The cell pellets for Hsc70 and Apg2 were defrosted at 37°C in Hsp70/110 lysis buffer (table 2.1) containing protease inhibitor cocktail tablets (Roche). The sample was vortexed to

resuspend the pellet. Cells were lysed by sonication (3 cycles of 2 minutes, 60% amplitude, 1 s on, 1 s off; Vibra-Cell™ Ultrasonic Liquid Processors, SONICS). The sample was centrifuged at 48,384 g for 1 hour at 4°C to pellet cell debris and insoluble proteins. The supernatant was then collected.

2g Ni-IDA beads (Macherey-Nagel) were added to the solution, which was incubated for at least 2 hours at 4°C. The solution was kept on ice for at least 5 minutes to settle the bead pellet by gravity. The unbound fraction was collected and analysed by SDS-PAGE. Beads were washed three times by adding 1 CV (CV=5mL) Hsp70/110 wash 1 buffer (table 2.1), resuspending the beads, waiting for settling, and discarding the supernatant. The beads were incubated in ATP wash buffer (table 2.1) for 15 minutes at 4°C before removing the supernatant. A second wash with ATP wash buffer (table 2.1) was performed. Beads were then repeatedly washed with 1 CV Hsp70/110 wash 2 buffer (table 2.1) until the absorbance at 280 nm for collected fractions was lower than 0.01 AU. The resin containing the bound chaperones was incubated overnight at 4°C with 100 µL SUMO protease in Hsp70/110 lysis buffer (table 2.1) to cleave the His_6-Smt_3 tag from the chaperones.

The following day, the resin was put on ice to settle the bead pellet. The supernatant containing the cleaved chaperone was collected. Beads were washed with 1 CV Hsp70/110 lysis buffer (table 2.1) until reading absorbance at 280 nm lower than 0.01 AU. The unbound and collected fractions were analysed by SDS-PAGE. Pure fractions were pooled, concentrated using a 15 mL 10 kDa centrifugal concentrator (AMICON). Hsc70 and Hsp110 were concentrated up to 100 µM and 25 µM, respectively. Samples were then aliquoted, flash-frozen and stored at -80°C.

The T111C Hsc70 (T111C, C267A, C574A, C603A) mutant was expressed and purified as described above. DTT was replaced by TCEP in all the buffers.

2.3 Yeast cell transfection and growth

Dr Natasha Burgess performed the yeast cell transfection and growth. Yeast cells were grown using standard culturing techniques in synthetic dropout (SD) medium (7 g/L yeast nitrogen base, 1.9 g/L synthetic dropout without uracil, 100 mg/L adenine). Cells were grown in medium containing 2% glucose or 2% raffinose as the sole source of carbon until reaching an OD_{600} of 0.6. Yeast cells were then washed and diluted in medium containing 2% galactose as the only source of carbon for the induction of αSyn expression. Cells were incubated at 30°C with shaking at 220 rpm for 6 hours.

2.4 Liposome preparation

All lipids were purchased from Avanti Lipids, US. Liposome samples of DOPE:DOPS:DOPC (5:3:2 molar ratio) were prepared from stock solutions of lipids at 10 mg/mL in chloroform (96.4 µL DOPE; 63 µL DOPS; 40.6 µL DOPC). The lipid mix was dried under a stream of nitrogen gas for at least 5 min before being resuspended in liposome buffer (table 2.1) to get a final concentration of 20 mg/mL. Lipids were then vortexed (30 s), sonicated (10 min, 42 kHz, Branson 1510 Cleanosonic sonicator), flash-frozen in liquid nitrogen and thawed. The four-step process (vortex, sonication, flash-freezing and thawing) was repeated 5 times. The solution was then extruded using an Avanti Lipids Mini-Extruder (Avanti Lipids, USA) 21 times through a membrane with a 80-nm-diameter pore to form a homogeneous solution of liposomes. Liposomes were stored at 4°C and used within 48 hours.

2.5 In vitro disaggregation and binding assays

2.5.1 Thioflavin-T spectroscopic assay

10 mM thioflavin-T (ThT, Sigma Aldrich, USA) aliquots were prepared in ethanol and stored in the -80°C freezer. Amyloid fibres were sonicated using a Branson 1800 cleaner (Branson, USA) for 1 hour at 42 kHz to disperse them. Amyloid fibres (10 µM) were incubated with ThT (75 µM) for 30 minutes at 30°C. Meanwhile, a solution of the chaperones was prepared in the disaggregation buffer (table 2.1). This solution contained dimeric DNAJB1 at 2.5 µM (monomer concentration), Hsc70 at 5 µM, Apg2 at 0.5 µM, ATP at 6.25 mM (Sigma Aldrich, USA), phospho-enol pyruvic acid (PEP) at 7 mM (Sigma Aldrich, USA) and pyruvate kinase at 25 ng/µL (Sigma Aldrich, USA). Fibres and the mix of the chaperones were added onto a black, flat non-binding bottom surface, 96-well plate (Corning, USA). The final concentrations of amyloid fibres (monomer concentration), DNAJB1, Hsc70, and Apg2 were 2µM, 2µM, 4 µM, and 0.4 µM, respectively. Plates were sealed with transparent tape (Bio-Rad, USA) to prevent evaporation. The ThT signal was measured every 5 min for 16 hours using a FLUOstar Omega plate reader (BMG Labtech, UK). The excitation and emission wavelengths were 448 nm and 482 nm, respectively. The plate was shaken at 200 rpm for 5 s every 30 s and before each measurement. Background ThT fluorescence of chaperones and buffer was subtracted and ThT fluorescence was normalised to the fluorescence intensity of the first time point (t = 0 min). At least 3 independent experiments were performed for each condition. A single experiment was performed to assess the activity of a new chaperone batch or the disassembly of a new fibre batch. When indicated (figure 4.8E-F), the disaggregation efficiency was calculated by averaging the values during the final hour for each experiment. The plots of normalised intensity over time as

well as the linear regression showing the disaggregation efficiency as a function of Hsc70 bound fraction were calculated and plotted in Microsoft Excel (for Windows 365, version 16.0.13127.21624).

2.5.2 Binding assay

For all the different binding assays, aliquots of chaperones were first defrosted and centrifuged at 4°C for 30 min in order to remove any aggregates and αSyn amyloid fibres were sonicated for 15 min at high frequency using a CPX 2800 Bransonic Ultrasonic bath (Branson, USA).

Regarding the binding of WT DNAJB1 or ΔJ-DNAJB1 to αSyn amyloid fibres, fibres (20 μM, monomer concentration) were mixed with DNAJB1 (4-12 μM) in HKMD or HD buffer (table 2.1) and incubated at 30°C for 30 min in 1.5 mL Protein LoBind tubes (Eppendorf, Germany). Soluble and fibrillar materials were then separated by centrifugation at 16,000g for 30 min in a tabletop centrifuge. The supernatant was then carefully collected, and both supernatant and pellet were mixed with 4X NuPAGE SLS running buffer and deionised water. Samples were then incubated at 90°C for at least 30 minutes to break up the fibres. Samples were then analysed by SDS-PAGE as previously described. At least 3 independent experiments were performed for each condition. When indicated, the statistical analyses were performed in Prism 8 (GraphPad). Data were analysed using a one-way ANOVA test with Tukey's multiple comparisons test.

Regarding the binding of DNAJB1, Hsc70 and Apg2 to αSyn amyloid fibres, fibres (40 μM, monomer concentration) were incubated with Hsc70 (8 μM), DNAJB1 or ΔJ-DNAJB1 (4 μM), and Apg2 (different concentrations as indicated in chapter 4) in the disaggregation buffer for 1 hour at 30°C. The protocol was then identical to the previous

protocol. At least 3 independent experiments were performed for each condition. When indicated, the statistical analyses were performed in Prism 8 (GraphPad). Data were analysed using a two-way ANOVA test with Tukey's multiple comparisons test.

2.6 Transmission Electron Microscopy

2.6.1 Electron microscope

2.6.1.1 Overview

A comprehensive understanding of biological processes requires determination of the three-dimensional (3D) structure of macromolecular assemblies, both *in vitro* and in cells. The electron microscope (EM), whose imaging is done with an electron beam, has become a powerful tool over the last decade to determine the structures of various biological samples and their dynamics at the angstrom scale (Kühlbrandt, 2014). There are different electron microscopes such as the transmission EM (TEM), in which the electrons pass through the sample, and the scanning EM (SEM), in which secondary electrons emitted by the sample are detected. The following sections will focus on the TEM only.

The principle of a TEM is similar to a light microscope (figure 2.1): 1) a point source emits a beam (light or electrons), 2) a first lens system renders the beam parallel to the optical axis before passing through the sample, 3) a second lens system magnifies the produced image and 4) a detector reads out the incoming signal. However, unlike light microscopes which are limited by the wavelength of visible light, which is several hundred nanometres (nm), the wavelength (λ) of an electron in a TEM depends on its energy following this equation:

$$\lambda = \frac{h}{(2meV)^{1/2}} \ (equation\ 2)$$

where h is Planck's constant (6.63×10^{-34} kg.m².s^{-1}), m is the mass of an electron (9.1×10^{-31} kg), e is the absolute charge of an electron (1.60×10^{-19} C) and V is the accelerating voltage of the microscope. For instance, with an accelerating voltage of 300 kV, the wavelength is around 2 pm. This very small wavelength enables the resolution of structures at the atomic scale (Kühlbrandt, 2014). However, this technique also presents drawbacks. Using a high voltage gives a high energy to the electrons which can transfer it to the sample, causing sample damage with atom ionization, X-ray emission and free-radical formation (Orlova and Saibil, 2011). Also, since the electron wavelength is so tiny, the electron beam can be scattered by any molecules present in the microscope, bringing noise and artefacts to the final image. Therefore, the microscope column must always be under high vacuum. The following sections will describe more in detail each stage of the electron microscope imaging system from the electron source to the detectors.

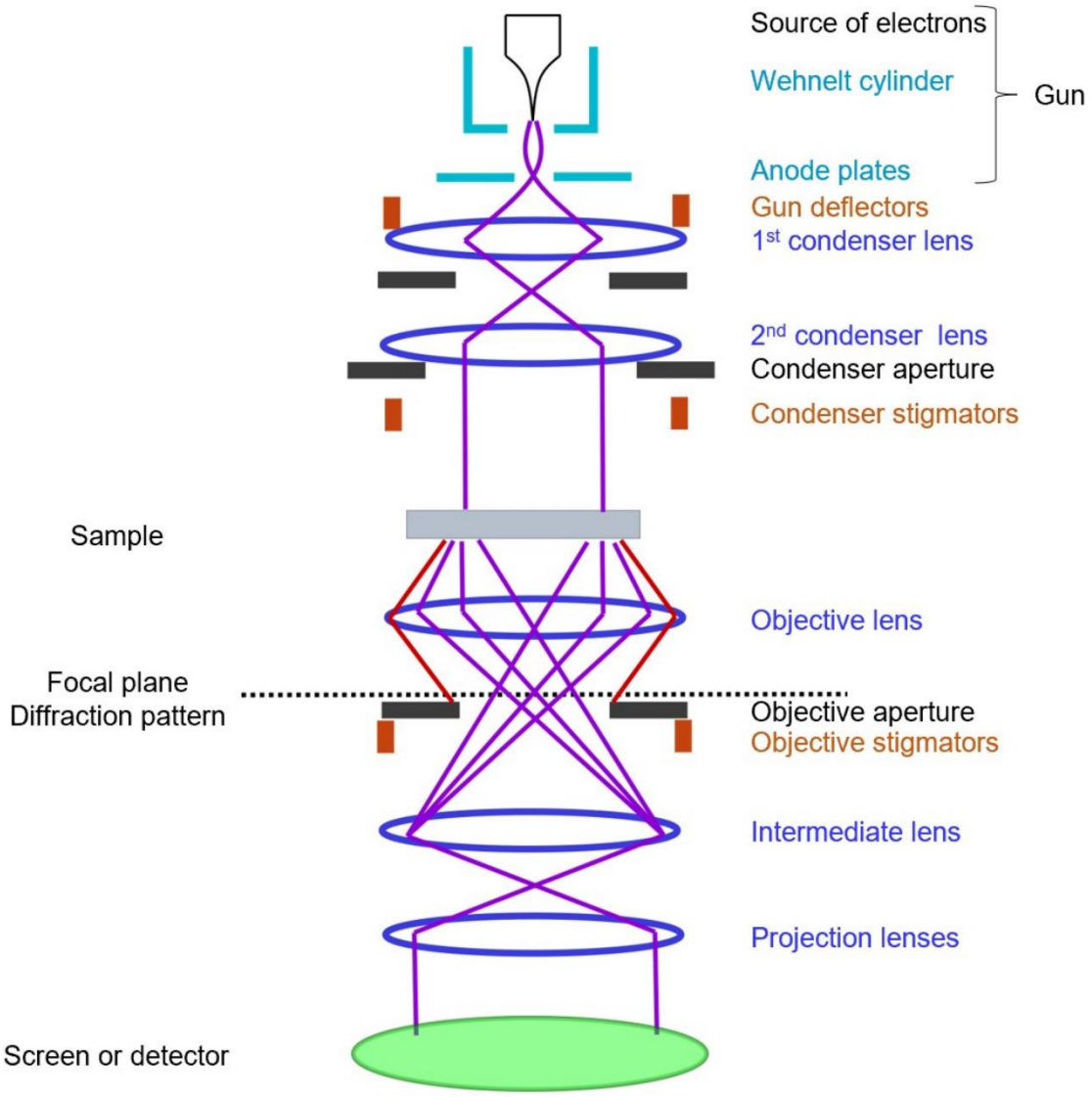

Figure 2.1: Overview of a transmission electron microscope optical system. The figure was adapted from Orlova and Saibil, 2011.

2.6.1.2 Guns and column

The beam of electrons is emitted by the electron gun. The principle consists of extracting and accelerating electrons from a source. There are two main sources: a thermal emission source or a field emission gun (FEG). In a thermal emission source, such as a bent tungsten or lanthanum hexaboride LaB_6 filament, the filament is heated to extreme temperatures (2000-3000°C for a tungsten filament for instance) so that the filament can emit electrons (Orlova and Saibil, 2011). In the case of a FEG, the electron

beam is smaller, brighter and more coherent because of the extremely sharp tip (10-25 nm radius) coated with ZrO_2 (Orlova and Saibil, 2011). After emission, the electrons focus because of the global negative charge of the Wehnelt cylinder before being accelerated by consecutive anodes with increasing voltages (up to 100-300 kV depending on the microscope).

Once accelerated, the diverging electron beam is controlled by the gun deflectors that align the rays of electrons to the optical centre of the condenser lenses (figure 2.1). The condenser lens system determines the intensity and the diameter of the electron beam and ensures that the beam is parallel to the optical axis before illuminating the sample. An electron lens is composed of a circular coil of wires, creating an electromagnetic field in the central hole. This field is then used to determine the trajectory of the electrons because of their charge. The condenser lens system is followed by the condenser aperture which blocks rays diverging from the optical axis. Lastly, the condenser stigmators locally compensate artefacts coming from the condenser lenses to get a parallel beam. The beam is now parallel and suitable for imaging the sample.

2.6.1.3 Sample preparation

Since the column must be maintained under high vacuum, the sample must be fixed to prevent its evaporation. Two main approaches exist: negative staining (dehydrated) or cryogenic conditions. These methods enable the imaging of a wide variety of samples, from *in vitro* formed complexes to cells and tissues.

In negative staining, the sample is applied to a grid, embedded in a solution containing heavy metal salt such as uranyl acetate, blotted to remove the excess of solvent and dried. This produces a thin layer of stain surrounding the biological specimen. This technique is simple, fast and displays samples with a high contrast. However, the

sample is not kept in a physiological environment because of the acidity of the staining solution and the drying step. This can lead to sample deformation or disassembly. Adding a layer of staining also limits the resolution of the structure because of the grain size of the stain. Therefore, this technique is generally used to quickly check sample homogeneity.

Cryogenically frozen samples are maintained in a near-native, hydrated, physiological environment. Samples are added to a grid, blotted and plunged into liquid ethane or propane. Using liquid ethane or propane rather than liquid nitrogen enables sample cooling at a vitrification rate of 10^6 °C/s to produce vitreous rather than crystalline ice (Dubochet et al., 1988). The sample is then maintained at a temperature below 170°C and imaged by cryo-EM. This approach enables the resolution of structures at atomic resolution in a native-like environment.

2.6.1.4 Image formation

2.6.1.4.1 Interactions between the electrons and the sample

TEM images are formed by variations in the intensity of the electron beam due to its interaction with the sample. When the electron interacts with the atoms of the sample, it can be scattered. Image formation depends on interference between scattered and unscattered electrons. There are three main types of interactions between the electron and the sample:

- The electron does not interact with the atoms of the sample. Therefore, the electron is not scattered and its energy is not modified (case 1 in figure 2.2)
- The electron interacts with the sample, resulting in the scattering of the electron but without transferring energy (case 2 in figure 2.2). This is called elastic scattering. As the electron has not lost energy, its wavelength is unchanged.

However, the electron undergoes a phase shift. Both the scattering angle and the phase shift depends on the sample with greater deflections and phase shifts produced from molecules with higher atomic numbers.

- The electron interacts with the sample and transfers energy to it (cases 3 and 4 in figure 2.2). This is called inelastic scattering. The incident electron interacts with an atomic electron and transfers energy to it. The atomic electron then loses energy either by emitting X-rays or by being ejected from the electronic cloud if the energy transfer is sufficiently high (cases 3 and 4 in figure 2.2, respectively). Because of this energy loss, the scattered electron has a longer wavelength and focuses in different planes than the elastically scattered or unscattered electrons, leading to chromatic aberration and additional noise in the image (Orlova and Saibil, 2011).

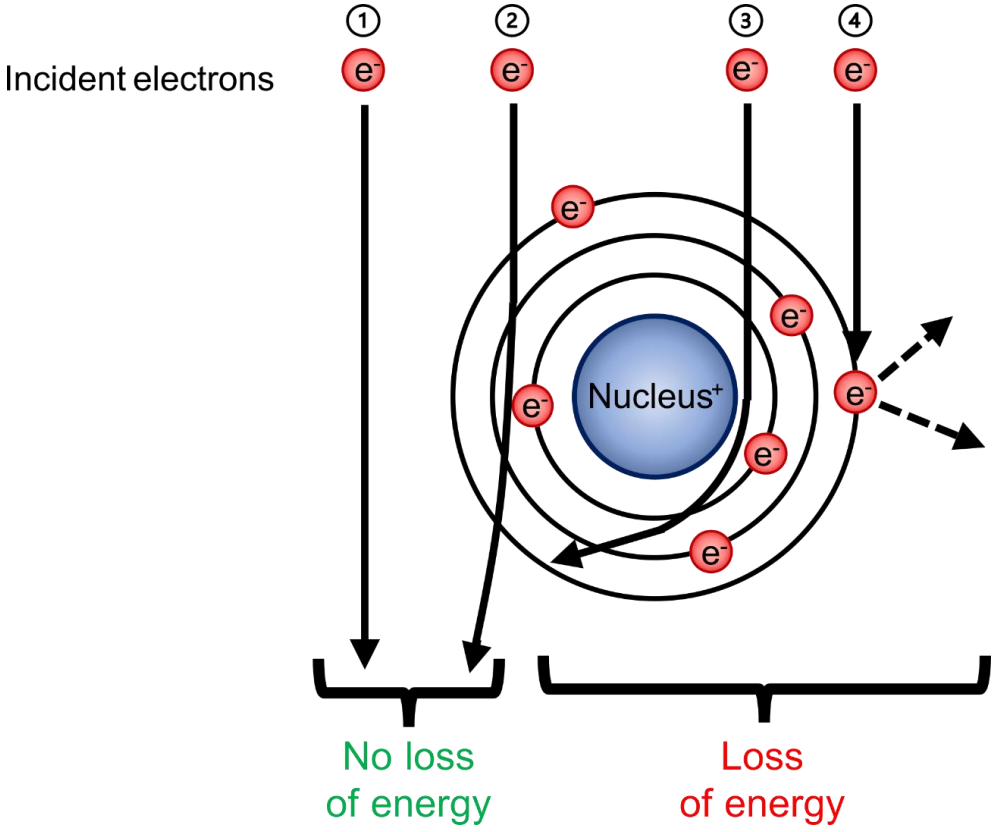

Figure 2.2: Interactions between the electron and the sample.
The figure was adapted from Orlova and Saibil, 2011.

The image contrast results from two different components: amplitude contrast and phase contrast.

Amplitude contrast is generated by the absorption of electrons by the sample (figure 2.3A) and can be enhanced by inserting an objective aperture in the back focal plane, where the diffraction pattern is formed (figure 2.1). The aperture blocks the electrons scattered at high angles, thus reducing the noise (red rays in figure 2.1).

Phase contrast is generated by the interference between the unscattered electrons and the elastically scattered ones. Indeed, the phase shift caused by the scattering electrons also bears information about the sample (figure 2.3B). Thanks to the spherical aberrations of the lenses, whose strength decreases gradually from the optical axis, this difference in path length between the unscattered and elastically scattered electrons can be detected and produces the phase contrast.

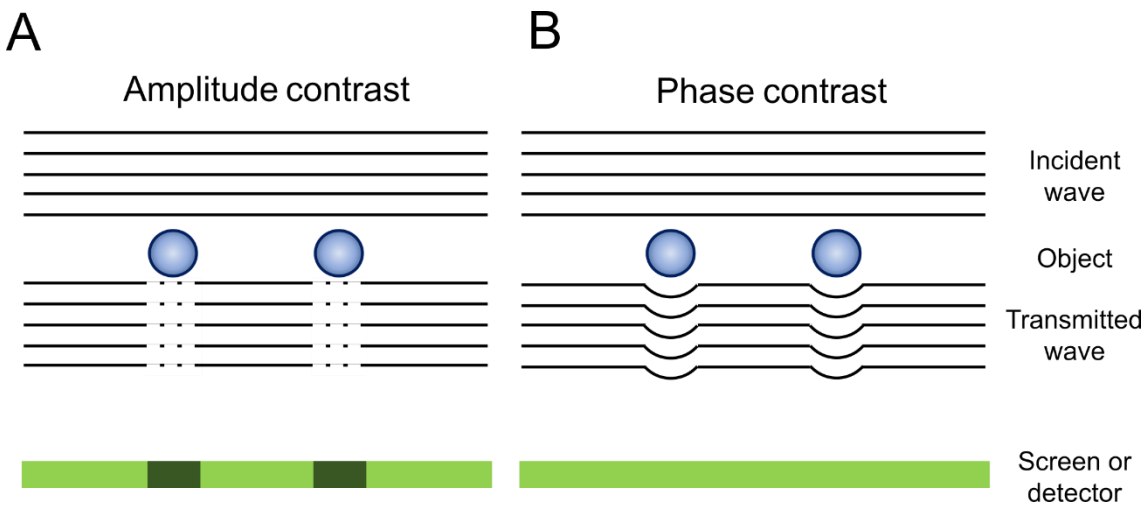

Figure 2.3: Amplitude (A) and phase (B) contrast.
The figure was adapted from Orlova and Saibil, 2011.

An image is formed by both amplitude and phase contrast. Negative stain samples display a high contrast, due to the heavy metals present in the dried stain that generate a high amplitude contrast. Frozen biological samples are mainly composed of atoms whose atomic number is relatively small (O, N, C, H), leading to a very weak amplitude

contrast and a final image which is mostly defined by the phase contrast. Moreover, the inelastically scattered electrons damage the sample, requiring the experimenter to use a low electron dose, which causes a low signal to noise ratio (Orlova and Saibil, 2011).

2.6.1.4.2 Contrast transfer function

An efficient approach to enhance the image contrast is the defocusing of the microscope. Indeed, increasing the defocus increases the pathlength of the scattered electrons because of the spherical aberrations of the lenses. This converts the phase contrast into visible amplitude contrast. This phenomenon is described by the contrast transfer function (CTF). The CTF is a sinusoidal function of the spatial frequency that depends on the defocus. Therefore, the CTF is plotted in Fourier space, varies between -1 and 1 and indicates the transfer of contrast to the image at each spatial frequency.

2.6.1.5 Detectors

Lastly, the image must be detected. The intermediate lens focuses the electrons coming from the objective aperture and the projector lens system then determines the desired final magnification of the image (figure 2.1).

Because of the poor contrast in biological cryo-EM images, an important factor that limited the impact of cryo-EM was the detection of the signal. Originally, photographic films were used to record images. Films are cheap and had sufficient spatial resolution. However, their handling was not convenient because of their loading into the microscope, the chemical processing, the drying and the digitisation which could bring additional artefacts.

Films were then replaced by charge-coupled device (CCD) cameras which are less laborious to use (figure 2.4). However, the electrons must be converted into photons, causing signal loss and degradation. The photons pass through the fibre optic coupling

before being recorded on the sensor. During the conversion, the photons can be scattered far away from the incident electron, adding noise and artefacts to the final image.

More recently, direct electron detectors (DEDs) were invented. Unlike CCD detectors, DEDs directly read electrons by a CMOS (complementary metal-oxide-semiconductor) electron sensor (figure 2.4). These new detectors have high sensitivity and significantly improve the signal-to-noise ratio because of direct readout of the electrons. The high sensitivity also allows the use of a lower dose rate. In addition, counting mode can be used. In this mode, each detected electron is normalised and has the same weight. The lower dose rate and the high frame rate of the DEDs prevent the hitting of more than one electron in the same area of the detector and the subsequent loss of quality in the image, called coincidence loss. Also, the high frame rate allows the correction of beam-induced lateral-drift and stage movement during image recording (Zheng et al., 2017).

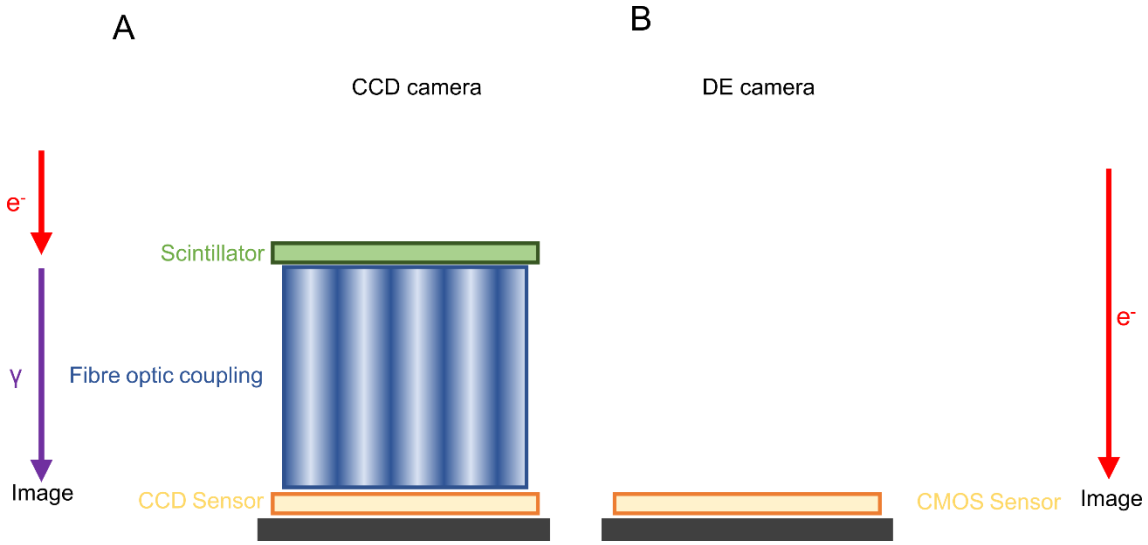

Figure 2.4: Diagrams of a CCD (A) and a DED (B).
The figure was adapted from Orlova and Saibil, 2011.

This improvement with DEDs was quantified by determining the Detective Quantum Efficiency (DQE) of both CCD and DEDs (Ruskin, et al., 2013). The DQE measures the signal to noise output/input as a function of spatial frequency (McMullan et al.,

2009). DQE values vary between 0 and 1, corresponding to full noise or signal respectively. CCD cameras can have a DQE up to 0.4 whereas DEDs can reach a DQE of 0.8 or more.

2.6.1.6 Processing

The final aim of cryo-EM processing is the reconstruction of the 3D structure of the sample. There are two main approaches to reach this goal: single particle analysis and tomography.

2.6.1.6.1 Single particle analysis

The reconstruction of 3D structures from cryo-EM images relies on the central section theorem (Orlova and Saibil, 2011). Cryo-EM images are two-dimensional (2D) projections of the object and their Fourier Transform (FT) represents the central section of the 3D FT of the object. Thus, if 2D projections coming from different orientations of a same object can be obtained, it is possible to produce a 3D reconstruction of the object. This requirement can be challenging. When the distribution of the sample is not even within the vitreous ice, laborious approaches must be attempted such as coating the grid with a specific solution to make it more hydrophilic or hydrophobic or tilting the stage at different angles for the data collection.

In the work described below, the structures of WT αSyn amyloid fibres alone and WT αSyn amyloid fibres decorated with ΔJ-DNAJB1 were determined using the single-particle analysis approach in Regularised Likelihood Optimisation (RELION) 3.1 programme (Scheres, 2012a; Zivanov et al., 2018a).

RELION is a programme that uses a Bayesian statistical approach to determine the most likely orientation of each particle, considering the flexibility of the sample and the

signal to noise ratio (Scheres, 2012a). Several steps are required to produce the 3D structure of a sample:

- Preprocessing: the frames within a stack are aligned to correct for beam-induced shifts as well as stage drifts and specimen movements. Aligned micrographs are then CTF-estimated to estimate the defocus. The micrographs showing ice contamination, ice crystallisation or other artefacts can also be manually discarded during that step.
- Particle picking and extraction: particles of interest are first detected before subregions are extracted at the detected positions from the micrographs. Particle picking was initially performed manually but the large number of particles needed made this task laborious. Detecting all the different particle views required for a 3D reconstruction was also sometimes challenging. Programmes based on deep-learning such as SPHIRE-crYOLO and Topaz-picking were designed to solve these problems (Bepler et al., 2019; Wagner et al., 2019).
- 2D classification: 2D classification sorts a data set of images into subsets with similar features. This step enables abnormal particles displaying contaminants or other artefacts to be excluded via an iterative process. The particles are sorted out by cross-correlation in different 2D class averages whose number is set by the user. The particles are assigned to a specific class average according to their highest probability to belong to this class, i.e. their similarity to others in the same class and their dissimilarity to images in other classes. The best 2D class averages that display diverse orientations of the sample with well resolved features are selected for the following steps.
- Initial model: an initial low-resolution model is produced. This step makes it possible to determine if the particle orientations are sufficiently well distributed

of if further data must be recorded following one of the protocols mentioned above.

- 3D classification: 3D classification sorts a heterogeneous data set into a set of distinct structural classes. The goal is to get the most homogeneous and stable 3D reconstruction from the particles. The initial model, which is strongly low pass filtered, is used to sort out the particles and generate different 3D reconstructions whose number is set by the user. Like the 2D classification, this step is iterative. Although the 2D class averages are carefully selected, the sample may still be heterogeneous and this step sorts out the main orientations of the reconstructed sample.
- 3D refinement: once a homogeneous reconstruction has been selected, the selected data set is refined to high-resolution, assessed by the "gold-standard" approach to generate the Fourier Shell Correlation (FSC). During the refinement step, the iterative process may cause a gradual increase in noise at the high frequencies, known as overfitting, which can be included in the reconstruction and lead to an erroneous structure by adding spurious high-resolution details. The gold-standard approach identifies this risk by splitting the data into two halves that are independently reconstructed and their FSC is calculated to estimate the resolution (Scheres and Chen, 2012).
- Mask creation and postprocessing: the map obtained from the 3D refinement step contains information from the sample and noise from the solvent, meaning that the resolution is under-estimated as the correlation is lower because of noise. Therefore, a mask is required to exclude the solvent from the FSC calculation. The map can also be sharpened via the B-factor (Rosenthal and Henderson, 2003).

- CTF refinement: this step estimates the defocus for each particle. Local refinement of the CTF correction can improve the final resolution of the map.
- Model fitting and validation: Once a high-resolution map is determined, the atomic model of the protein is determined by fitting the map with a pre-existing model or by *de novo* model building. Pre-existing models are generally adjusted to the solved map as differences can arise from the flexibility of the sample.

The programmes and parameters used for each step in this study are described in more detail in section 2.6.5.

A helical reconstruction requires additional parameters to be determined: the pitch of the filament, its helical rise and its helical twist. The pitch is the distance corresponding to a 180° rotation of the filament. The helical rise and the helical twist are the distance or the rotation separating two adjacent subunits within a filament, respectively. By knowing two of these parameters, the third one can be determined. A common feature of amyloid fibres is the 4.75-Å distance between two adjacent cross-β repeats (Scheres, 2020). Therefore, only the pitch or the helical twist must be found to determine the structure. From RELION 3.1, the initial model step can be replaced by an initial reprojection for the determination of the pitch in the case of a helical reconstruction (Scheres, 2020). The 2D class averages, which display fragments with different orientations of a same amyloid fibre, are aligned by projection matching. An initial cross-section, which is the plane perpendicular to the fibre axis, is also generated at this step to get an initial view of the fibre secondary structure. The initial reprojection can then be used for the 3D classification or the 3D refinement step.

2.6.1.6.2 Tomography

Tomography is another approach for 3D structure determination. Unlike single-particle analysis, tomographic reconstruction is usually done in real space (Orlova and Saibil, 2011). The region of interest is imaged at different tilt angles. Usually, images are recorded between -60° and +60° with an increment of 2-3°.

A first essential factor in the acquisition of tilt series is the electron dose. The sample accumulates electron dose during the acquisition. Because of radiation damage, the last collected images contain less information. Therefore, the information in the first acquired images is crucial. Moreover, the ice is thicker at high tilt angles, leading to a loss of information. Different tilt schemes have been implemented for the acquisition of cryo-tomograms to consider the influence of the electron dose. The optimal tilt-scheme is now the dose symmetric one: the first image is acquired at zero degree and the following images are collected at increasing tilt angles while the tilt direction oscillates (for instance: 0°, -3°, +3°, +6°, -6°, etc.). It is considered optimal because the first images, which lose less information due to the radiation damage compared to the last ones, are acquired at tilt angles where the ice is thinner (Wan and Briggs 2016).

A second crucial parameter is the precise alignment of the tilted images. This precision is achieved by the addition of 5-to-20-nm-diameter gold beads to the sample before freezing it. The high atomic number of gold enables a high contrast for the beads and their small size ensures a very precise alignment between the different images.

The reconstruction of a tomogram from a tilt series relies on the back projection algorithm. For each tilt, an image has been recorded and the interactions between the electron beam and the specimen have determined the contrast of each molecule. Back projection produces rays of pixels whose intensity is determined from the projections

(figure 2.5). This method is relatively simple and produces a 3D volume of the sample quickly.

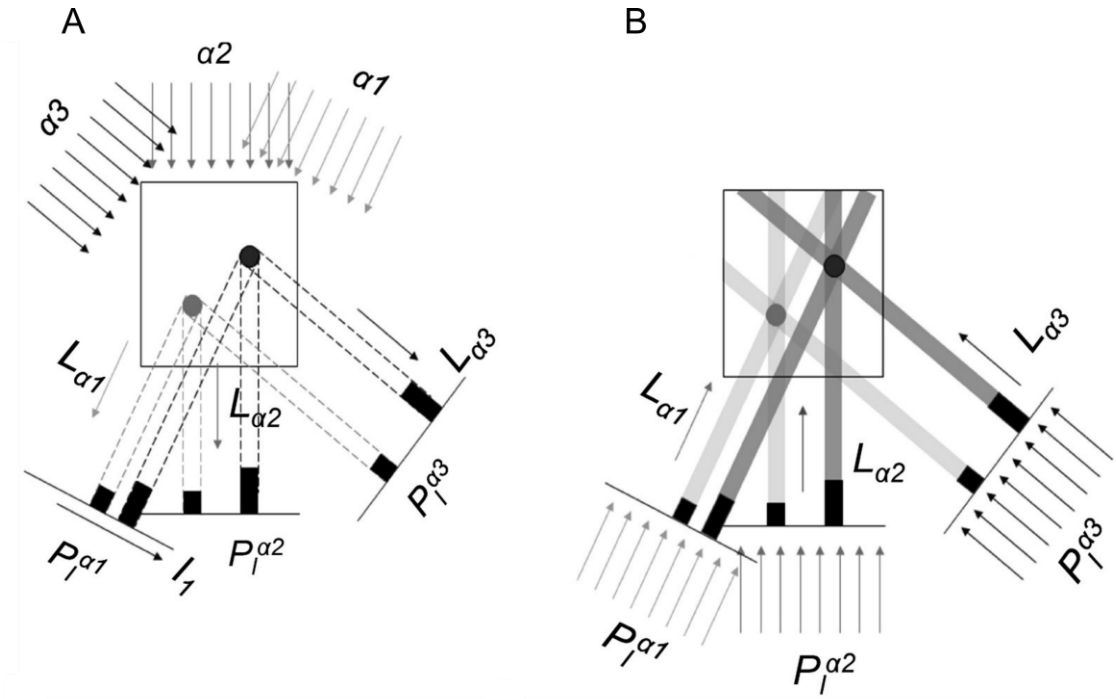

Figure 2.5: The principle of back projection.
(A) The electron beam produces the projections $P_l^{α1}$, $P_l^{α2}$ and $P_l^{α3}$ acquired at the angles α1, α2 and α3, respectively. (B) Back projections are generated by reversing the directions $L_{α1}$, $L_{α2}$ and $L_{α3}$ and by creating rays of pixels whose density is determined by the original projections $P_l^{α1-3}$. The figure was adapted from Orlova and Saibil, 2011.

2.6.2 Sample preparation

2.6.2.1 Negative stain grid preparation

For all the negative stain experiments, CF300-Cu carbon film grids (Electron Microscopy Sciences, UK) were negatively glow discharged for 60 s at 30 mA using a PELCO easiGlow Glow Discharge Cleaning System (Pelco, USA).

To check the formation of αSyn fibres, 4 µL of solution containing fibres (10 µM, monomer concentration) were applied for 1 min at room temperature to the glow-discharged grids and being blotted. The grid was then stained with 2% (w/v) uranyl

formate and immediately blotted. The staining and blotting steps were performed 3 times.

To visualise the complexes formed of chaperones bound to fibres, αSyn fibres (10 μM monomer) were mixed, when indicated, with Hsc70 (10 μM), Apg2 (1 μM), and WT or ΔJ-DNAJB1(5 μM monomer) for 1 hour at 30°C in the disaggregation buffer (or HKMD buffer for the control without chaperones). The sample application to a grid and staining steps were performed as described above.

2.6.2.2 Cryo-EM grid preparation for screening and single particle analysis

For the *in vitro* experiments on soluble αSyn mixed with DOPE:DOPS:DOPC liposomes, the final concentrations of liposomes and αSyn were 5.3 mg/mL and 1.7 mM to get a final protein to lipid molar ratio of 1:4. The solution was incubated for 1h at 37°C. 300-mesh lacey carbon film copper grids (Agar Scientific, UK) were negatively glow-discharged using the same protocol as described in section 2.6.2.1. After incubation, 4 μL of solution was loaded onto the glow-discharged grids. The cryo-EM samples were prepared using a FEI Vitrobot system (ThermoFisher Scientific, USA) operating at 4°C, 100% humidity. Grids were stored in liquid nitrogen.

For the experiments on αSyn fibres incubated with different chaperones, aliquots of chaperones were first defrosted and centrifuged at 4°C for 30 min to remove any aggregates. Fibres were sonicated for 30 minutes using a Branson 1800 ultrasonic cleaner (Branson, USA) to produce dispersed fragments of αSyn fibres. The dispersed fibres were mixed either with i) chaperones (DNAJB1:Hsc70 or DNAJB1:Hsc70:Apg2) as indicated in table 2.3 for 1h at 30°C in disaggregation buffer (table 2.1) or with ii) ΔJ-DNAJB1 as indicated in table 2.3 for 10 min at 30°C in HD buffer (table 2.1). C-flat

grids (Protochips, USA) were used for grid preparation. They were glow-discharged as described in section 2.6.2.1. 4 µL of solution was applied onto them and they were blotted and plunged into liquid ethane using an automated Leica EM GP2 (Leica Microsystems, Germany) using the settings indicated in table 2.3.

Sample	αSyn:ΔJ-DNAJB1	αSyn:DNAJB1:Hsc70	αSyn:DNAJB1:Hsc70:Apg2
αSyn fibres (monomer concentration, µM)	6	6	6
DNAJB1 concentration (µM)	2.4	3	3
Hsc70 concentration (µM)	0	6	6
Apg2 concentration (µM)	0	0	0.6
Grid type (hole size/spacing in µm), mesh	C-flat 2/2, 400	C-flat 1.2/1.3, 400	C-flat 1.2/1.3, 400
Leica blotting time (s)	5	5	5
Leica additional move (mm)	0.2	0.2	0.2
Leica chamber temperature (°C)	15	15	15
Leica chamber humidity (%)	75	75	75

Table 2.3: The protein concentrations, grids, and vitrification parameters used for sample preparation for reconstruction or fibre scoring.

For the experiments on αSyn fibres incubated with WT DNAJB1 in HKMD or HD buffer (table 2.1), the samples were prepared by Dr Joe Beton using conditions similar to the ones described for the αSyn:ΔJ-DNAJB1 sample in table 2.3.

2.6.2.3 Cryo-EM grid preparation for cryo-tomography

Cryo-EM grids of sonicated αSyn fibres incubated with chaperones were prepared as described in section 2.6.2.2. However, before plunge freezing in ethane, 3 µL of 10 nm Protein-A-coated gold fiducial (Electron Microscopy Sciences, UK) were applied onto

the grid and immediately blotted for 5 s using an additional move of 0.2 mm. The grids were then plunge-frozen in liquid ethane.

Cryo-grids of yeast cells transfected with αSyn were prepared by Dr Natasha Burgess and are listed in table 2.4. For cryo-EM of vitreous sections (CEMOVIS), transfected yeast cells were concentrated by centrifugation (10 min, 3,000g) and resuspended in SD medium containing 20% dextran. The cell suspension was quickly transferred into a Leica type A aluminium specimen carrier (200 µm indentation, Leica Microsystems, Germany) and covered with the flat side of a type B specimen carrier and high-pressure frozen using an EM HPM100 system (Leica Microsystems, Germany). Cryo-sections of 70 nm thickness were cut using an EM UC7 Ultramicrotome equipped with an EM FC7 cryo-chamber (Leica Microsystems, Germany) and applied onto glow-discharged grids (Electron Microscopy Sciences, UK) coated with 10 nm Protein-A-coated gold fiducial (Electron Microscopy Sciences, UK). Vitreous cryo-sections mounted on EM grids were imaged by light microscopy using DIC and GFP fluorescence (excitation filter 440-470 nm, emission filter 525-550 nm) channels of an Axio Scope.A1 microscope (Zeiss, Germany) equipped with an Orca R2 CCD camera and a cryo-stage (Linkam Scientific Instruments, UK).

Regarding the focused ion beam (FIB) milling experiments, transfected yeast cells were pelleted by centrifugation (10 min, 3,000g) and resuspended in SD medium. Cells were applied onto glow-discharged grids coated with 10 nm Protein-A-coated gold fiducial (Electron Microscopy Sciences, UK) and plunge-frozen using a Vitrobot system (ThermoFisher, USA).

For *in vitro* experiments of soluble αSyn incubated with DOPE:DOPS:DOPC liposomes, liposomes and recombinant αSyn were mixed to yield a protein to lipid

molar ratio of 1:15 and incubated for 1h at 37°C. 15 µL of 10-nm-diameter uncoated gold fiducials (BBI solutions, UK) were then added to 30 µL of the sample solution just before grid preparation. Cryo-grids were prepared as described in table 2.4.

Sample	αSyn transfected in yeast	αSyn transfected in yeast	αSyn:liposomes
Technique	CEMOVIS	FIB-milling	*in vitro*
Sample prepared by	Dr Natasha Burgess	Dr Natasha Burgess	Me
αSyn concentration (mM)	-	-	1
DOPE:DOPS:DOPC concentration (mM)	-	-	15
Grid type (hole size/spacing in µm), mesh	Gilder Finder CF200F1-Cu grids	Quantifoil R 2/4 (or R 3.5/1), 200 mesh finder grids	Lacey carbon film grids, 300 mesh
Vitrobot blotting time (s)	Unknown	Unknown	4
Vitrobot blot force	Unknown	Unknown	-10
Vitrobot chamber temperature (°C)	Unknown	Unknown	4
Vitrobot chamber humidity (%)	Unknown	Unknown	100

Table 2.4: The protein concentrations, grids, and vitrification parameters used for sample preparation for tomogram reconstructions shown in chapter 3.

2.6.3 Data collection

2.6.3.1 Negative stain grid acquisition

Negative stain images were acquired on a Tecnai TF20 electron microscope (ThermoFisher, USA) equipped with FEG source operating at 200 keV. Images were recorded with a DE-20 direct electron detector (Direct Electron, USA) at a magnification corresponding to 1.83 Å/pixel using a total dose of ~30 $e^-/Å^2$.

2.6.3.2 Cryo-EM grid screening and analysis

Images of DOPE:DOPS:DOPC liposomes incubated without or with soluble αSyn (figure 3.8A-B) were acquired on the same microscope using the same detector at a magnification corresponding to 3.6 nm/pixel and a total dose of ~30 $e^-/Å^2$. At least 2 independent experiments were performed for each condition. When indicated, the statistical analyses were performed in Prism 8 (GraphPad). Data were tested for normality using a Shapiro-Wilk test. Since the distribution was not normal, the data were analysed using a two-tailed Mann-Whitney test to investigate the influence of αSyn on the fusion of liposomes. A two-sided Chi-squared test was performed to study the influence of αSyn on the tubulation of liposomes.

Images of αSyn amyloid fibres incubated with different chaperone mixtures (figure 4.11) were acquired using the same settings as described in section 2.6.3.1.

2.6.3.3 Tilt series acquisition

All the tilt series that were used to reconstruct the tomograms displayed in chapter 3 were acquired at the Electron Bio-Imaging Centre (eBIC) at Diamond. Data collection of the *in situ* and *in vitro* experiments was done by Dr Natasha Burgess and Dr Daniel Clare, respectively. The imaging parameters for the data collections are listed in table 2.5.

Sample	αSyn transfected in yeast - CEMOVIS	αSyn transfected in yeast – FIB-milling	αSyn:liposomes
Microscope	FEI Polara	FEI Titan Krios	FEI Titan Krios
Acceleration voltage (kV)	300	300	300
Camera	K2 Summit detector with BioQuantum energy filter	K2 Summit detector with BioQuantum energy filter	K3 detector with BioQuantum energy filter
Phase Plate	No	No	Volta
Energy filter slit width (eV)	-	-	20
Pixel size (Å)	5.405	7.425	1.63
Tilt range (°)	±57	±54	±60
Increment (°)	3	3	3
Tilt-scheme	Dose symmetric	Dose symmetric	Dose symmetric
Total dose (e^-/ Å^2)	-	-	82
Defocus range (µm)	5	5 - 7	0.2
Number of acquired tilt series	~30	32	77
Number of reconstructed tomograms	17	28	17

Table 2.5: Microscope and parameters used for the acquisition of the tilt series whose tomograms are shown in chapter 3.

All the tilt series that were used to reconstruct the tomograms displayed in chapter 4 (figure 4.13) were collected at Birkbeck College, Institute of Structural and Molecular Biology by Dr Natalya Lukoyanova. The imaging parameters used for the collection of the tilt series are found in table 2.6.

Sample	αSyn:DNAJB1:Hsc70	αSyn:DNAJB1:Hsc70:Apg2
Microscope	FEI Titan Krios	FEI Titan Krios
Acceleration voltage (kV)	300	300
Camera	K3 detector with BioQuantum energy filter	K3 detector with BioQuantum energy filter
Energy filter slid width (eV)	20	20
Pixel size (Å)	2.13	2.13
Frames/tilt	20	10
Tilt range (°)	±60	±60
Increment (°)	3	3
Tilt-scheme	Dose symmetric	Dose symmetric
Total dose (e^-/ Å^2)	150	150
Defocus range (µm)	2 - 5	2 - 5
Number of acquired tilt series	30	23
Number of reconstructed tomograms	10	23

Table 2.6: Microscope and parameters used for the acquisition of the tilt series whose tomograms are shown in chapter 4.

2.6.3.4 Single particle data collection

Movies of αSyn amyloid fibres incubated with either ΔJ-DNAJB1 or DNAJB1:Hsc70:Apg2 were collected Birkbeck College, Institute of Structural and Molecular Biology by Dr Natalya Lukoyanova. Movies of αSyn amyloid fibres incubated with DNAJB1:Hsc70 were collected at the Electron Bio-Imaging Centre (eBIC) at Diamond. The imaging parameters used for the movie collections are found in table 2.7.

Sample	αSyn:ΔJ-DNAJB1	αSyn:DNAJB1:Hsc70	αSyn:DNAJB1:Hsc70:Apg2
Microscope	FEI Titan Krios	FEI Titan Krios	FEI Titan Krios
Acceleration voltage (kV)	300	300	300
Camera	K3 detector with BioQuantum energy filter	K3 detector with BioQuantum energy filter	K3 detector with BioQuantum energy filter
Energy filter slit width (eV)	20	20	20
Pixel size (Å)	0.5335 using super resolution mode	0.53 using super resolution mode	0.53 using super resolution mode
Frames/movie	50	50	50
Total dose (e^-/Å^2)	49	54	51
Defocus range (μm)	1.5 – 3.0	1.5 – 3.3	1.5 – 3.3
Number of movies	9,943	2,424	4,039

Table 2.7: Microscope and parameters used for the acquisition of the datasets for fibre scoring in chapter 4 (figure 4.12) and cryo-EM reconstruction in chapter 5.

For fibre scoring in chapter 4 (figure 4.12), the statistical analyses were performed in Prism 8 (GraphPad). Data were analysed using a two-sided Chi-squared test to study the influence of Apg2 on the proportion of decorated fibres. The results were confirmed by Erin Johnston, a research assistant in the group, who performed a blinded analysis.

For the experiments on αSyn fibres incubated with WT DNAJB1 in HKMD or HD buffer (table 2.1), the datasets were collected by Dr Joe Beton using settings similar to the ones described for the αSyn:ΔJ-DNAJB1 sample in table 2.7.

2.6.4 Tomogram reconstruction and analysis

Tilt series of the *in vitro* samples underwent whole-frame alignment in MotionCor2 version (Zheng et al., 2017) and were dose weighted using custom scripts provided by Professor Carolyn Moores' group before reconstructing the tomograms using IMOD version 4.9.0 (Kremer et al., 1996). Tomograms of αSyn amyloid fibres incubated with chaperones were binned by 4 in X and Y whereas tomograms of αSyn incubated with liposomes were binned by 2. The tomogram of αSyn amyloid fibres incubated with DNAJB1:Hsc70:Apg2 displayed in figure 4.13B-C was CTF-corrected in IMOD.

Dr Natasha Burgess reconstructed the *in situ* tomograms and applied a SIRT-like filter to them using IMOD. The tomograms were binned by 3 in X and Y and averaged over 10 z-slices. The correlations between the fluorescence and low-magnification EM images were performed using the TurboReg plugin to FIJI software (Thevenaz et al., 1998). The same process was repeated between the low-magnification EM images and the high-magnification tomograms. FIB milling gave higher quality tomograms, but the correlation was less certain because the fluorescence had to be recorded before milling. An additional intermediate magnification EM image was necessary for the correlation.

2.6.5 Image processing for single-particle analysis

2.6.5.1 Motion correction and CTF estimation

The collected movies were gain corrected, binned by a factor of 2, and motion corrected with the CPU implementation of MotionCor2 in RELION 3.1 using patch tracking and dose-weighting (Zheng et al., 2017; Zivanov et al., 2018b). Aligned non-dose weighted micrographs were CTF estimated using CTFFIND-4.1 (Rohou and Grigorieff, 2015). Micrographs whose maximum resolution estimated by RELION was worse than 7 Å were discarded. Then, the power spectra of the micrographs were individually verified

and the micrographs showing crystalline ice were discarded. Micrographs of WT αSyn fibres incubated with DNAJB1:Hsc70 or DNAJB1:Hsc70:Apg2 (the last two columns in table 2.7) were denoised using the U-net (small) model in TOPAZ-Denoise (Bepler et al., 2020).

2.6.5.2 Image processing – WT αSyn amyloid fibres

The reconstruction of WT αSyn amyloid fibres presented in chapter 5 was done using the dataset of WT αSyn amyloid fibres incubated with ΔJ-DNAJB1 (table 2.7). The workflow followed for the reconstruction is summarised in figure 2.6. The reconstruction of the fibre was done using RELION 3.1 (Zivanov et al., 2018a).

The coordinates of the decorated fibres were determined by training a model in SPHIRE-crYOLO using 100 micrographs randomly selected from 9,005 micrographs using the helical picking option (Wagner et al., 2019).

911,478 particles were extracted in boxes of 420 pixels (44.5 nm) with an inter-box distance of 42 pixels (4.45 nm) along the fibre axis and were binned by a factor 3.3 to yield 128-pixel boxes. The extracted particles were sorted out by performing 3 consecutive reference-free 2D classifications using 200 classes, a cylindrical mask of 340 Å, a soft-edge circular mask of 400 Å and a regularisation parameter of 1. Only the 2D class averages displaying fragments of fibres decorated with ΔJ-DNAJB1 were selected. The corresponding particles were re-extracted without binning. Particles underwent two additional reference-free 2D classifications using 100 classes, a cylindrical mask of 140 Å to ignore the density of ΔJ-DNAJB1 in the alignment, a soft-edge circular mask of 400 Å and a regularisation parameter of 1 and then 8. Only 2D class averages (93,493 particles) displaying the 4.8 Å cross-β repeat were selected to produce an initial reprojection and cross-section of the fibre, using a maximum

resolution of 5 Å, a pitch of 620 Å and a cylindrical mask of 200 Å. High resolution refinements from the initial reprojection were performed using a pitch of 620 Å, a helical twist of -1.38° and a helical rise of 4.75 Å. The search ranges for alignment were limited to 3 pixels in order to restrain the misalignment of the particles in the first iterations. The resulting unfiltered map was subject to postprocessing to estimate the resolution using a lowpass filter of 7 Å for the mask. The masked postprocessed map was subject to CTF refinement to correct the defocus of each particle. The 3D refinement and postprocessing steps were repeated using the CTF-refined particles and a 4.5 Å lowpass filtered mask to see individual 4.8 Å cross-β repeats within the fibre . The resolution of the final map was estimated at 3.2 Å for a value of 0.143 for the FSC of the corrected map. The B-factor used for the postprocessing step was estimated by RELION (-84 $Å^2$).

An initial structure was built by fitting the structure of the N-terminally acetylated WT αSyn fibre (PDB: 6OSJ) into the postprocessed map using COOT (Emsley and Cowtan, 2004).

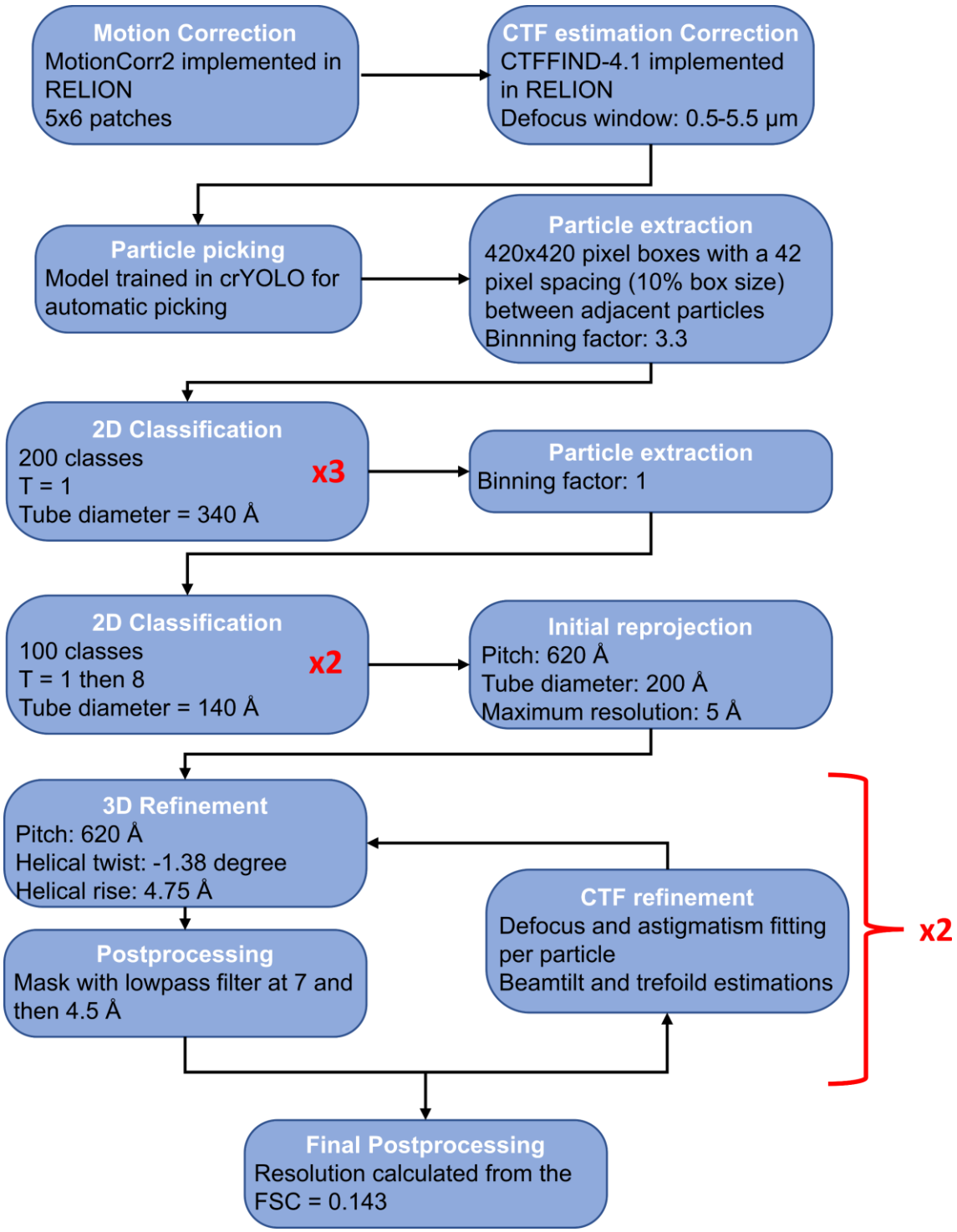

Figure 2.6: Diagram of the image processing workflow for the reconstruction of the fibres alone.

2.6.5.3 Image processing – Complex formed of WT αSyn amyloid fibres and ΔJ-DNAJB1

The reconstruction of WT αSyn amyloid fibres decorated by ΔJ-DNAJB1 presented in chapter 5 was done using the dataset of WT αSyn amyloid fibres incubated with ΔJ-DNAJB1 (table 2.7). The workflow followed for the reconstruction is summarised in figure 2.7. The reconstruction of the fibre was done with RELION 3.1 (Zivanov et al., 2018a).

The particles used for the processing came from the initial steps that were described in the previous section (particle picking, particle extraction and three reference free 2D classifications). The particles were binned by a factor of 3.3 during the extraction in order to 1) get a 128x128-pixel particle box size and 2) get a coarse alignment of the decorated fibres because of the flexibility of the complex. The 3.3x-binned 2D classes displaying a regular decoration of ΔJ-DNAJB1 on the fibre and a correct horizontal alignment of the fibre were selected to produce an initial reprojection and cross-section of the decorated fibre, using a maximum resolution of 8 Å, a pitch of 620 Å and a cylindrical mask of 340 Å. A round of 3D classification was performed to sort out different conformations of the complex, using 4 classes, a C2 symmetry, a pitch of 620 Å, a helical rise of 40 Å, a helical twist of -11.6° and a regularisation parameter of 4. One of the 3D classes displayed a horseshoe-like shape density for ΔJ-DNAJB1 and was submitted to 3D-auto refinement without applying symmetry and using the helical option (pitch of 620 Å, helical twist of -11.6 degrees, helical rise of 40 Å) and a low-pass filter of 30 Å.

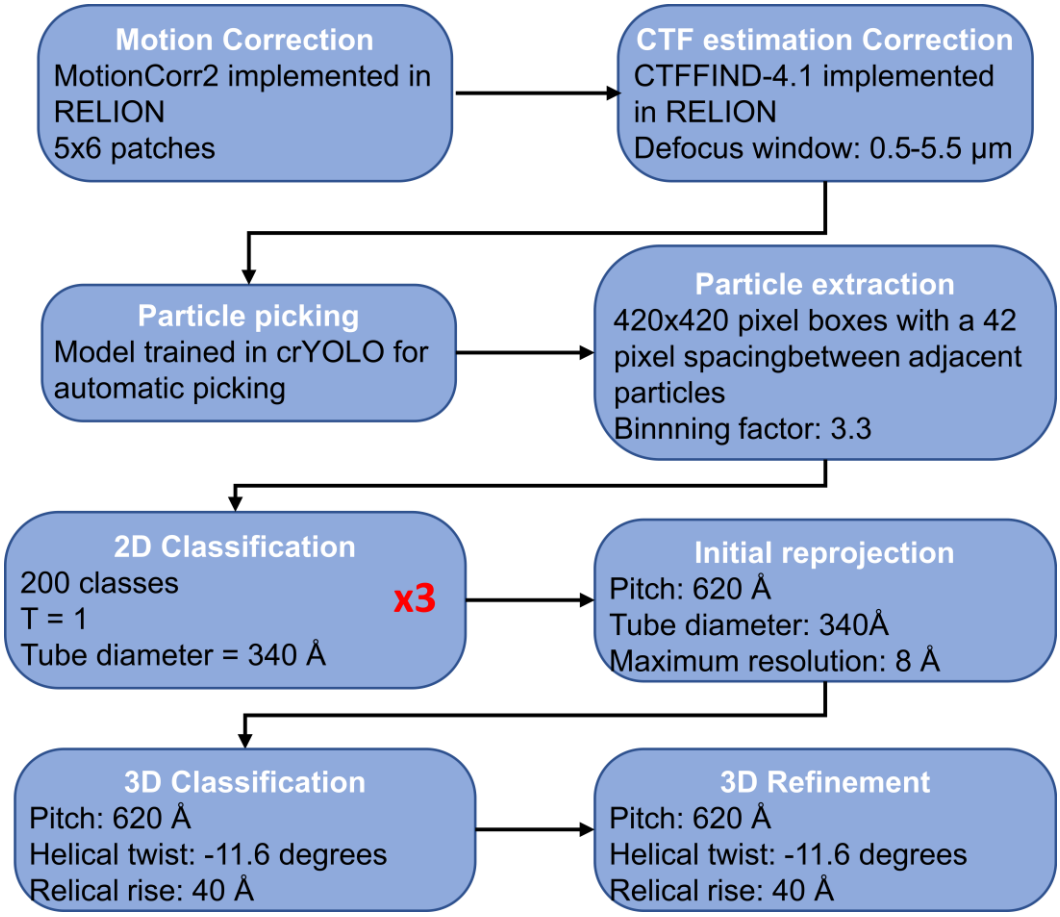

Figure 2.7: Diagram of the image processing workflow for the reconstruction of the fibres decorated by ΔJ-DNAJB1.

2.7 Total internal reflection fluorescence microscopy

2.7.1 Principle of total internal reflection fluorescence microscopy

Total internal reflection fluorescence (TIRF) microscopy uses reflection from an interface with a change in refractive index (n) to illuminate only fluorophores close to the glass surface (Fish, 2009). When light encounters the interface, it is either refracted as it goes through the second medium or reflected at the interface. This phenomenon is governed by Snell's law (equation 3):

$$n_A \times \sin(\theta_A) = n_B \times \sin(\theta_B) \ \ (equation\ 3)$$

where n_A and n_B are the refractive indices of medium A and B and θ_A and θ_B are the incident and refracted beam angles, respectively.

From a critical angle, called θ_C, the laser is totally reflected. Therefore $\sin(\theta_B) = 1$ and equation 3 becomes:

$$n_A \times \sin(\theta_C) = n_B \ (equation\ 4)$$

From the previous equation, the critical angle can then be determined:

$$\theta_C = \sin^{-1}\left(\frac{n_B}{n_A}\right) \ (equation\ 5)$$

Therefore, the critical angle can be determined from the refractive indices of media A and B. For *in vitro* biochemical experiments, medium A is usually glass ($n_A \approx 1.52$) and medium B is the aqueous physiological buffer ($n_A \approx 1.33$). Consequently, for an incident angle higher than 61°, the incident beam is fully reflected back into medium A at the interface. Although the beam does not pass through medium B, the reflected beam generates a limited electromagnetic field adjacent to the medium interface, whose spatial frequency is identical to the spatial frequency of the incident beam (figure 2.8, Fish 2009). The evanescent field decays exponentially from the medium interface following this equation:

$$E(z) = E_0 e^{-z/d} \ (equation\ 6)$$

where E(z) is the energy at a distance z from the medium interface (figure 2.8), E_0 is the energy at the medium interface and d is the penetration depth, which is proportional to the incident wavelength.

As the energy of the evanescent field decays rapidly with distance from the medium interface, only fluorophores which are close to the glass surface (up to 200 nm) are

excited (figure 2.8). This approach enables a higher signal-to-noise ratio since the background is less noisy.

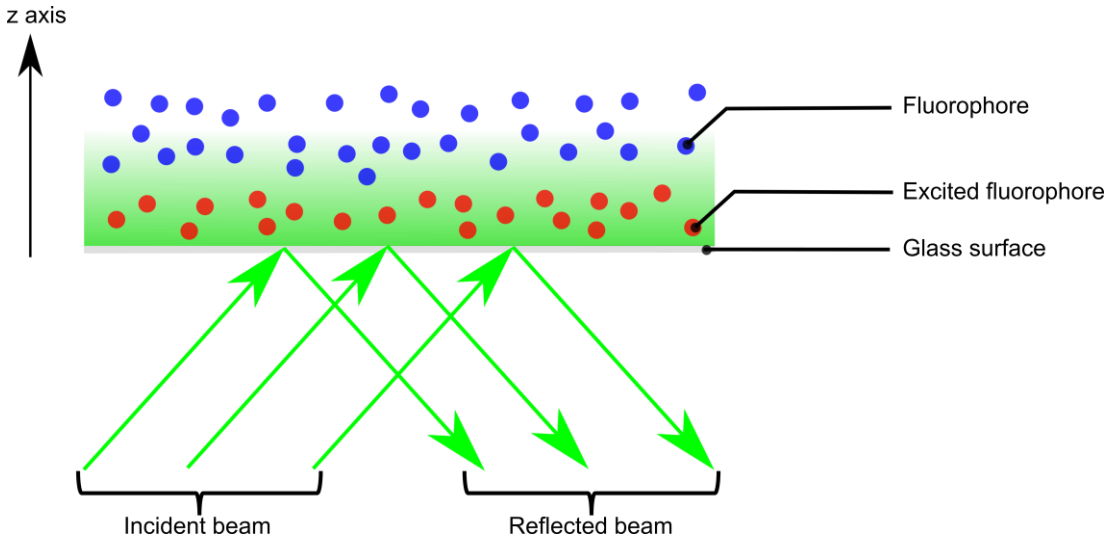

Figure 2.8: The principle of evanescence field in TIRF microscopy. The figure was adapted from Fish, 2009.

2.7.2 Sample preparation

S9C:WT (1:2) αSyn amyloid fibres (10 µM, monomer concentration) were incubated with Alexa Fluor 647 maleimide dye (10-fold molar excess, 100 µM, ThermoFisher Scientific, USA) and Biotin-X, SE dye (2.5-fold molar excess, 25 µM, ThermoFisher Scientific, USA) for at least 2 hours at room temperature in the dark in HKMT buffer. T111C Hsc70 (20 µM) was incubated with Alexa Fluor 488 maleimide dye (10-fold molar excess, 200 µM, ThermoFisher Scientific, USA) for at least 2 hours at room temperature in the dark in HKMT buffer. Labelled Hsc70 was then buffer exchanged using PD SpinTrap G-25 column (Cytiva, USA) pre-equilibrated in HKMD buffer. For the experiments with labelled Hsc70, labelled amyloid fibres (1 µM) were incubated with labelled T111C Hsc70 (2 µM), DNAJB1 (1 µM) and Apg2 (0.2 µM, if indicated) in disaggregation buffer for 1 hour at 30°C in the dark.

2.7.3 Data acquisition

Chambers were prepared using glass slides, biotin-PEG coverslips, and double-sided tape. Chambers were passivated with 0.5% BSA for at least 10 min, washed twice in HKMD buffer, incubated twice in 0.5 mg/mL neutravidin for 2 min, washed three times in HKMD buffer, incubated with the sample for 10 min, and washed three times in HKMD buffer. Samples were imaged on an Eclipse Ti-E inverted microscope with a CFI Apo TIRF 1.49 N.A. oil objective, Perfect Focus System, H-TIRF module, LU-N4 laser unit (Nikon) and a quad band filter set (Chroma). Frames were recorded on an iXon DU888 Ultra EMCCD camera (Andor), controlled with NIS-Elements AR Software (Nikon) with an exposure time of 100 ms. The images were acquired at a pixel size of 90 nm.

2.7.4 Data analysis

To determine the overall fluorescence of the fibres, Hsc70 and αSyn fluorescence intensities were measured with ImageJ FIJI software (Schindelin et al., 2012) by determining the plot profile of 65 fibres from 3 independent experiments for each condition. The minimum value for each plot profile was considered as background and subtracted. The statistical analysis were performed in Prism 8 (GraphPad). Data were first analysed by running a Shapiro-Wilk test to check their normality. A two-tailed Mann Whitney test was then performed as the data did not have a normal distribution.

To evaluate the distribution of bound Hsc70, Hsc70 and αSyn fluorescence intensities were measured along the fibres. The intensities in the first and last 3 pixels of each fibre were compared: the ratio of Hsc70 intensity divided by αSyn intensity was calculated at each end and the lower ratio was then subtracted from the higher one. The division by αSyn intensities served to minimise the influence of variations in fibre distance from the

glass surface. 54 fibres from 3 independent experiments were measured. Statistical analyses were performed as described above using Prism 8 (Shapiro-Wilk test followed by a two-tailed Mann Whitney test as the data did not have a normal distribution).

3. Results: αSyn aggregation in *S. cerevisiae* and *in vitro*

3.1 Introduction

In this chapter, I explain first the strategy employed for the study of αSyn aggregation in *S. cerevisiae* cells. I then characterise the aggregation of αSyn in yeast cells observed by CEMOVIS and FIB-milling techniques using a correlative light and electron microscopy (CLEM) approach. I continue by explaining the purification of αSyn and the preparation of liposomes for *in vitro* experiments. Finally, I describe the cryo-EM and cryo-electron tomography (cryo-ET) *in vitro* assays to study the interactions between αSyn and liposomes.

3.2 Strategy of the in situ experiments

Dr Natasha Burgess, a former postdoc in the group, prepared yeast samples, made cryo grids, collected fluorescence images and tilt series, and reconstructed the tomograms. I performed the CLEM correlation and analysed the results. The plasmid for αSyn transfection in yeast cells was kindly provided by Professor Tiago Outeiro's group.

Yeast cells were transfected with an αSyn construct (pME3945) with a GFP tag at the C-terminus. First, αSyn aggregation was monitored by fluorescence microscopy (figure 3.1). αSyn aggregation followed a time course similar to that observed in a previous study using this plasmid (Petroi et al., 2012): 4 hours after induction, GFP-tagged αSyn displayed a ring of fluorescence at the plasma membrane (figure 3.1B). After 7h, bright fluorescent spots appeared in the cytoplasm or close to the plasma membrane (figure 3.1C), suggesting the formation of cytosolic inclusions. After 16 hours, several

fluorescent spots were present within the cells (figure 3.1D), leading to cell death. The cytosolic inclusions could be due to the GFP tag. However, a previous study showed that transfecting yeast cells with the same plasmid expressing only the GFP tag did not produce inclusions (Petroi et al., 2012).

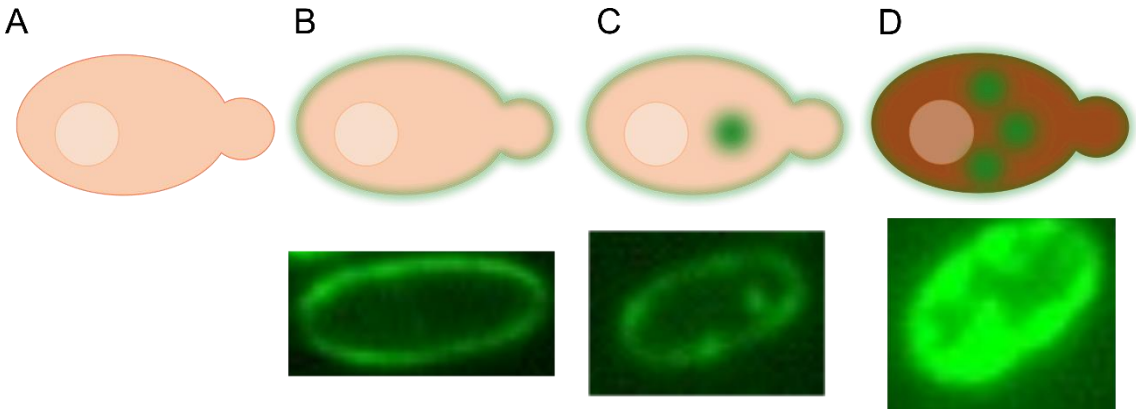

Figure 3.1: Time course of αSyn aggregation in yeast cells.
The upper panels display cartoons of a yeast cell at the different stages of αSyn aggregation while the lower panels display fluorescence pictures at the corresponding time points. (A) Before the induction of αSyn expression, the yeast cell is healthy. (B) Initially, GFP-tagged αSyn is localised at the plasma membrane, displaying a ring of fluorescence. (C) At a later stage, some cytosolic inclusions are formed, seen as fluorescent spots. (D) Finally, large cytosolic aggregates are formed within the cell, leading to cell death.

To determine αSyn structure in the inclusions and at the plasma membrane, Dr Natasha Burgess used a CLEM approach based on two complementary techniques (figure 3.2). She prepared thin cryo sections using the CEMOVIS and FIB-milling methods. The CEMOVIS technique guaranteed the correlation between the fluorescence and EM data since the cells were cryo-sectioned before recording fluorescence images (figure 3.2A). On the other hand, mechanical artefacts, such as damage by the diamond knife and compression of the sample, were introduced and prevented us from obtaining fine structural details. Therefore αSyn aggregation was also studied using FIB-milling, which reveals fine structural details owing to better sample preservation. However,

fluorescence images were recorded before producing the 200-nm-thick lamellae (figure 3.2B). This led to uncertainty about the correlation between fluorescence and EM data since the presence of the fluorescent regions in the lamellae was not guaranteed. Because of this ambiguity, CEMOVIS data were analysed first to identify the main features of αSyn aggregation. Then, the FIB tomograms showing similar characteristics were analysed.

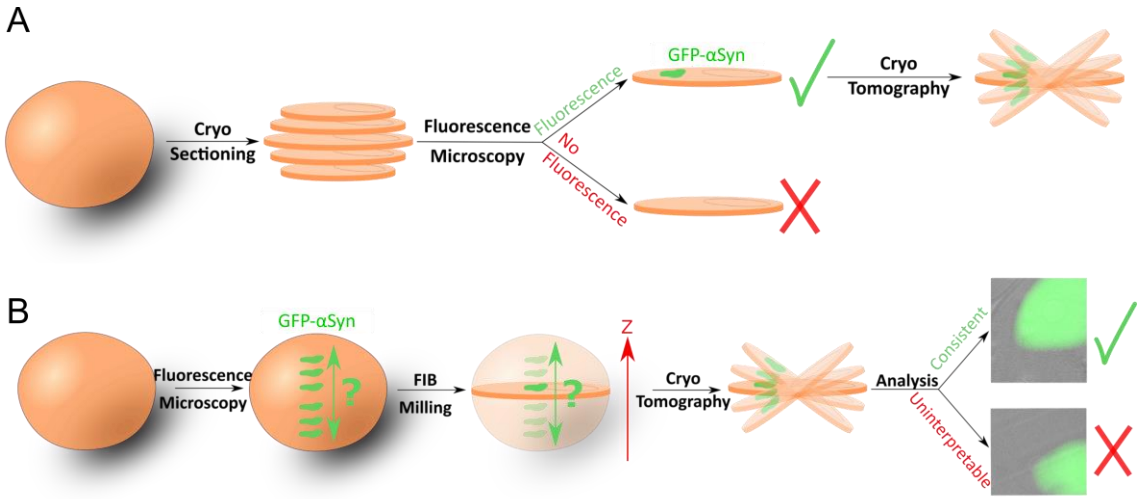

Figure 3.2: Strategy of the *in situ* experiments.
(A) Cartoon of the CEMOVIS experiment workflow. CEMOVIS experiments gave a reliable correlation between the fluorescence and the tomograms since the cryo-sections themselves were imaged by fluorescence microscopy. But the CEMOVIS tomograms gave poor structural information. (B) Cartoon of the FIB-milling workflow. Tomograms of FIB-milled lamellae gave structural details of αSyn aggregation. However, the yeast cells were imaged by 2D fluorescence microscopy before making the lamellae, so that the height of the fluorescence on the z axis was unknown. Therefore, only the FIB tomograms showing features similar to those seen by CEMOVIS were analysed.

3.3 αSyn aggregation leads to the formation of amorphous aggregates that are associated with membranes in situ

First, fluorescence images were correlated with the CEMOVIS tomogram sections using an intermediate medium-magnification EM image (figure 3.3). After correlating all the tomograms, the main features of αSyn aggregation were listed (figure 3.4). In the first

stage of αSyn aggregation, αSyn accumulated at the plasma membrane (figure 3.1) and colocalised with tubulated ER and vesicles (figure 3.4A). In the subsequently formed cytosolic inclusions, αSyn was colocalised with lipid droplets or associated with the clustering of vesicles (figure 3.4B-C).

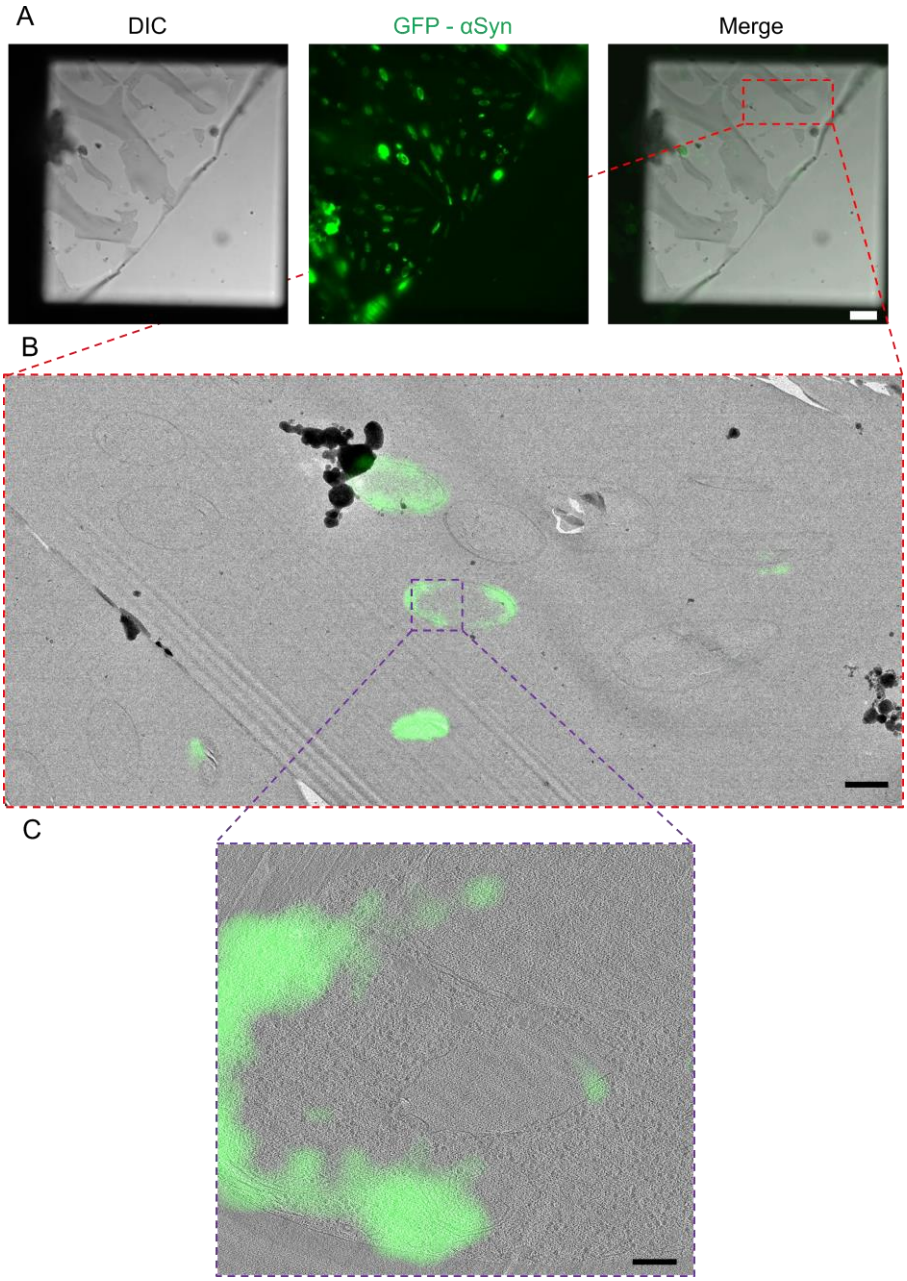

Figure 3.3: An example of a CEMOVIS correlation from the picture taken from an optical microscope (A) to the tomogram section (C) via an intermediate picture at a medium magnification (B).

DIC: Differential interference contrast. GFP: Green fluorescent protein. Scale bars, 10 µm in (A), 1 µm in (B) and 100 nm in (C).

Both features were often observed in the same inclusion, with the fluorescence centred on the clustered vesicles, suggesting a higher local concentration of αSyn with the vesicles rather than with the lipid droplets. The concentration of ribosomes was lower in these inclusions, suggesting the presence of amorphous αSyn aggregates in the cytoplasm. In a few cases, the bright fluorescent spots corresponded to vacuoles internalising αSyn, showing a cellular response to the cytosolic inclusions (figure 3.4D). No amyloid fibres were observed in the tomograms, indicating that their presence is not required for αSyn toxicity, at least in yeast cells. This first analysis enabled us to identify the main features of αSyn aggregation in yeast. They were then further studied by FIB-milling.

After correlating the fluorescence images and FIB-milled tomogram sections, only the tomograms displaying features resembling those in the CEMOVIS data were analysed. At the plasma membrane, αSyn was associated with tubulation of the ER (figure 3.5A). The cytosolic inclusions were composed of clusters of vesicles and lipid droplets (figure 3.5B). The vesicles often displayed a distorted or tubular shape and some of them presented angular, polygonal shapes. Again, ribosomes were excluded from the fluorescent regions, which displayed a darker background, indicating the presence of amorphous aggregates (figure 3.5B). The fluorescence covered areas bigger than the vesicular clusters but none of them showed fibrillar aggregates (figure 3.5B). Mitochondria often surrounded the fluorescent inclusions (figure 3.5C). This would suggest an association between αSyn aggregation and mitochondria as previously reported (Ramezani et al., 2019). However, mitochondria were not associated with αSyn inclusions in the CEMOVIS data. Therefore, this observation is less certain. Vacuoles were also highlighted by the bright fluorescent spots (figure 3.5C). Based on their clear

morphology, the vacuoles were internalising αSyn aggregates, suggesting a cell response to αSyn toxicity.

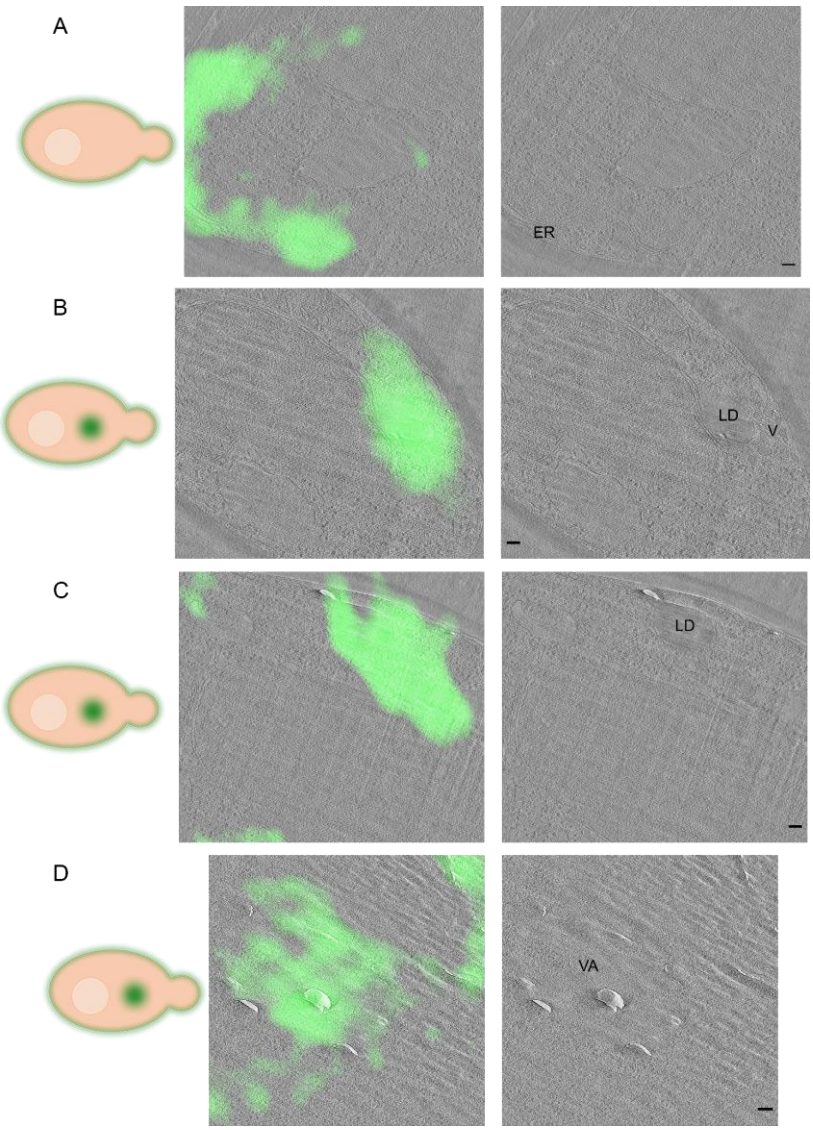

Figure 3.4: Representative CEMOVIS tomographic slices of abnormal membranous, vesicular, and organelle structures.

(A) In the first stages of αSyn aggregation, αSyn was colocalised at the plasma membrane with tubulated endoplasmic reticulum. (B-D) When the fluorescence corresponded to cytosolic bright spots, different phenomena were observed. αSyn was sometimes colocalised with lipid droplets as shown in (B). αSyn also triggered the clustering of vesicles as shown in (C). Last, the bright fluorescence spots sometimes displayed vacuoles internalising αSyn as shown in (D). ER, Endoplasmic reticulum; V, vesicle; LD, lipid droplet; VA, vacuole. The tomograms were binned by 3 in X and Y and averaged over 10 slices in Z. The cartoons on the left-hand side indicate the localisation of αSyn fluorescence within a yeast cell (plasma membrane in A or plasma membrane and cytosolic bright spot in B-D). Scale bars, 50 nm.

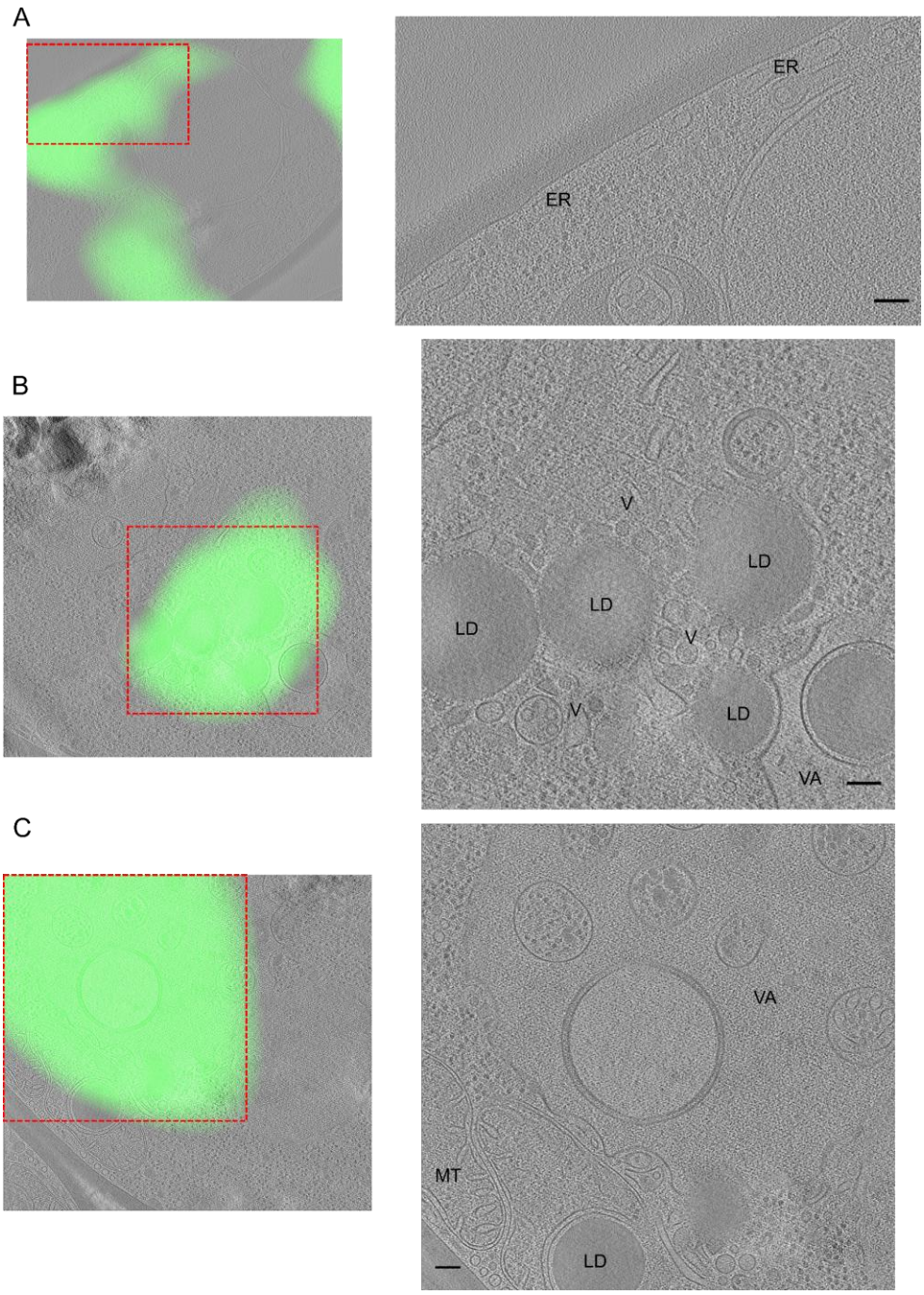

Figure 3.5: Representative FIB tomographic slices of abnormal membranous, vesicular, and organelle structures.

The pictures on the left-hand side show overviews of the yeast lamellae while the right-hand side pictures display high-magnification tomographic slices. (A) αSyn initially colocalised at the plasma membrane with tubulated endoplasmic reticulum. (B) Later, αSyn triggered the clustering of vesicles and lipid droplets in the cytoplasm. (C) At the same stage, a cell response occurred with the internalisation of αSyn by vacuoles. ER, Endoplasmic reticulum; V, vesicle; LD, lipid droplet; VA, vacuole; MT, Mitochondria. The tomograms were binned by 3 in X and Y and averaged over 10 slices in Z. Scale bars, 100 nm.

Overall, αSyn aggregation is associated with the formation of amorphous aggregates rather than fibrillar aggregates in yeast cells, and the aggregates appear to cause the distortion of membranes and clustering with lipid droplets. These observations suggested that an *in vitro* study of the effects of αSyn on liposomes might provide insight into the mechanisms underlying the toxicity of αSyn.

3.4 The purification of recombinant αSyn

A plasmid for the expression of WT recombinant αSyn (pT7-7) was kindly provided by Professor Bernd Bukau's lab. αSyn was expressed in BL21 (DE3) bacteria cells. The bacterial cell suspension was sonicated ("sonicated" fraction in figure 3.6A) and centrifuged to pellet cell debris. The supernatant was collected ("supernatant" fraction in figure 3.6A) and boiled to precipitate most of the contaminants before being centrifuged ("boiled" fraction in figure 3.6A). Streptomycin sulphate was added to the supernatant to precipitate DNA. The solution was then centrifuged and supernatant was collected ("streptomycin sulphate" fraction in figure 3.6A). Ammonium sulphate was incorporated into the supernatant which was then centrifuged. The supernatant ("ammonium sulphate – supernatant" fraction in figure 3.6A) was discarded and the pellet ("ammonium sulphate – pellet" fraction in figure 3.6A) was resuspended in TBS and dialysed overnight in deionised water to reduce the salt concentration ("dialysed" fraction in figure 3.6A). All the fractions were analysed by SDS-PAGE the following day (figure 3.6A). Several bands were still visible on the gel after the dialysis, indicating that the sample was not pure. Since the αSyn isoelectric point is 4.67, αSyn can be purified by anion exchange chromatography. Therefore, dialysed αSyn was loaded onto an anion exchange column and eluted with a linear gradient from 0 to 600 mM sodium chloride (figure 3.6B). A large peak was observed between 5 and 30 mL. The peak was asymmetric with small intermediate peaks that could correspond to

impurities. Fractions of interest were analysed by SDS-PAGE (figure 3.6C). Fractions showing a massive band at 15 kDa corresponding to αSyn were pooled, concentrated, aliquoted and flash-frozen in liquid nitrogen. Faint bands at higher molecular weights were visible, confirming that the fractions were not completely pure. A size exclusion chromatography step was therefore necessary. The following day, aliquots were defrosted, centrifuged at high speed to pellet aggregates and loaded onto a Superdex S200 column (figure 3.6D). A peak at 14 mL was visible. Again, the peak was asymmetric. The fractions of interest were analysed by SDS-PAGE (figure 3.6E). All the fractions contained pure αSyn. The asymmetry of the peak was attributed to the presence of different αSyn conformations. Fractions that were sufficiently pure were pooled, concentrated up to 2.5 mM, aliquoted, flash-frozen in liquid nitrogen and stored in the -80°C freezer.

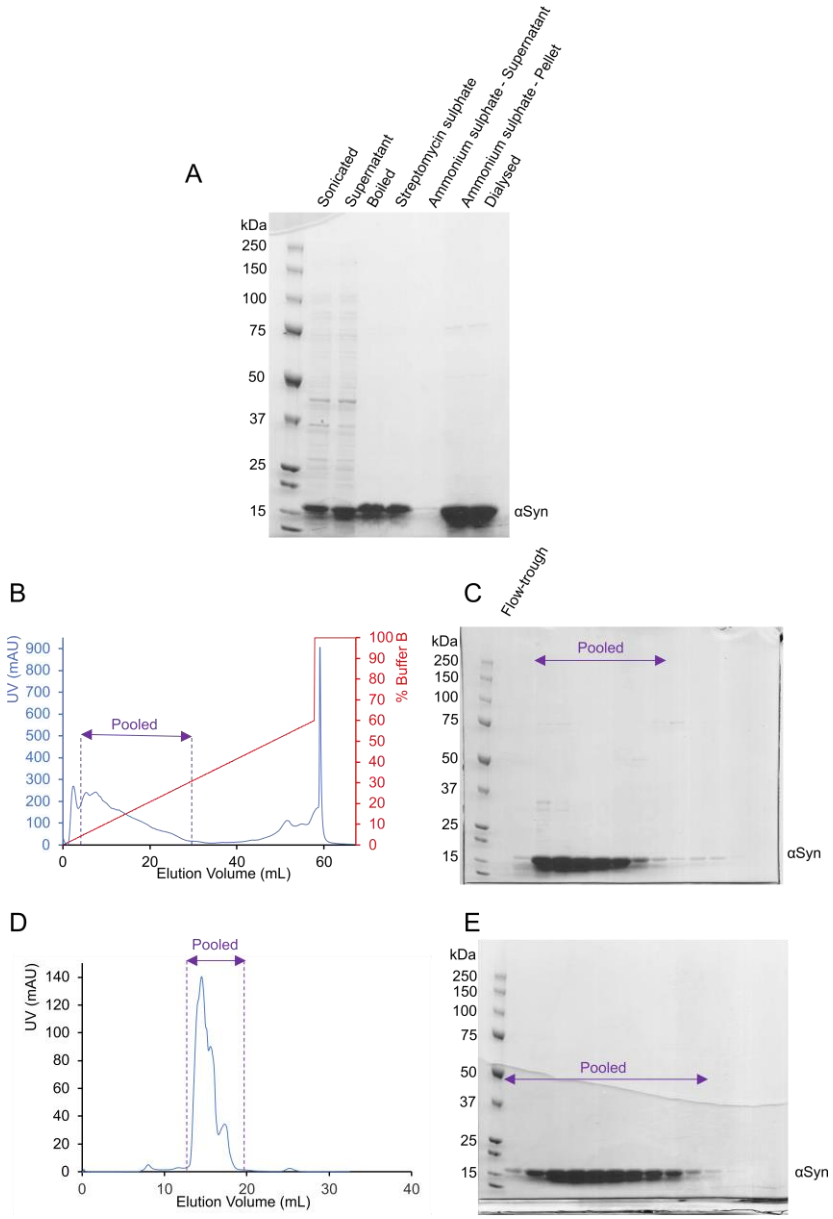

Figure 3.6: The purification of αSyn.

(A) SDS-PAGE of the stages of αSyn purification performed on the first day. The fractions were analysed after sonication, centrifugation, boiling for 20 minutes, streptomycin sulphate treatment (30 mg/mL) for 30 minutes, ammonium sulphate treatment (400 mg/mL) for 30 minutes and overnight dialysis. (B-C) The anion exchange chromatogram and its associated SDS-PAGE. αSyn was purified by ion exchange chromatography using a HiTrap Q HP 1 mL column. αSyn was eluted with a linear gradient from 0 to 600 mM sodium chloride. (D-E) The size exclusion chromatogram and its associated SDS-PAGE. αSyn was purified by size exclusion chromatography using a Superdex S200 column. The markers are noted as kDa in size in all the gels. A double band is visible for αSyn in all the gels because of an artefact due to the gel scanner.

3.5 αSyn triggers liposome fusion and tubulation in vitro

The affinity of αSyn for vesicles has been well studied and different parameters such as the size and charge of the vesicles influence αSyn interactions with lipids (Galvagnion et al., 2016; Kjaer et al., 2009). Thus, αSyn has higher affinity for negatively charged vesicles with a 50 nm diameter. Different lipid compositions have been reported in studies of αSyn interactions with lipids. Most of them used phosphatidylglycerol (PG), or its derivatives (Xue et al., 2009). However, PG is not endogenously expressed in the brain and other lipids were assessed. In this chapter, liposomes composed of DOPE:DOPS:DOPC (5:3:2, molar ratio) were used for several reasons. First, they are physiologically relevant to the composition of synaptic vesicles. Beside proteins and cholesterol, synaptic vesicles are mostly composed of phosphatidylcholine (36%, molar percentage), phosphatidylethanolamine (23%), phosphatidylinositol (19%), and phosphatidylserine (12%) (Takamori et al., 2006). The DOPE:DOPS:DOPC liposomes display a global negative charge (figure 3.7A), encouraging αSyn interactions with lipids. The lipids are also unsaturated, increasing their αSyn affinity (Middleton and Rhoades, 2010). Lastly, this composition has often been used in recent years and using this composition facilitates comparisons (Fusco et al., 2016, 2014; Man et al., 2021).

DOPE:DOPS:DOPC liposomes were formed by repeated cycles of sonication and flash-freezing in liquid nitrogen followed by one step of extrusion to homogenise their size. Liposome formation was checked by negative staining (figure 3.7B). Some liposomes displayed a distorted shape because of the drying step in negative stain.

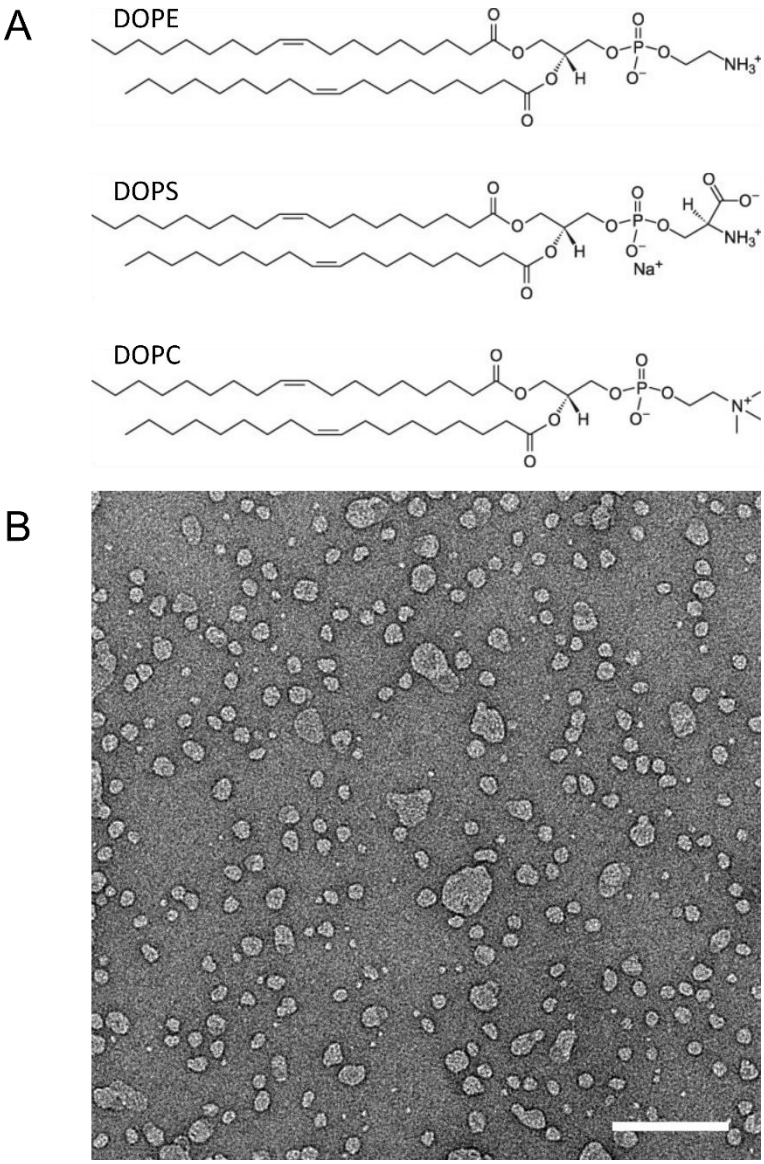

Figure 3.7: The formation of DOPE:DOPS:DOPC (5:3:2 molar ratio) liposomes. (A) Molecules of DOPE, DOPS, and DOPC. DOPE and DOPC are neutral whereas DOPS has a global negative charge. (B) Negative stain TEM image of 1 mg/mL DOPE:DOPS:DOPC (5:3:2 molar ratio) liposomes. Scale bar, 100 nm.

Two conditions were assessed by cryo-EM: liposomes alone and liposomes incubated with soluble αSyn at a 1:4 protein to lipid molar ratio (figure 3.8). Without αSyn, liposomes were mostly circular and isolated (figure 3.8A). Only 2.2% of the liposomes were tubular, by the rarely observed fusion of two liposomes (figure 3.8C). Their average diameter was 41 ± 18 nm (figure 3.8E). On the contrary, when soluble αSyn was added, αSyn formed larger and tubulated liposomes (figure 3.8B): 30.3% of the

liposomes were tubular and half of them had an elongation ratio higher than 6 (figure 3.8C-D). These observations confirmed that tubulation was not random. The distribution of round liposomes was also different in the presence of αSyn: their average diameter was significantly higher at 64 ± 69 nm (figure 3.8E), with two additional peaks around 90 and 120 nm visible in the diameter distribution plot of round liposomes (figure 3.8F). Taken together, those observations confirm that αSyn can trigger liposome fusion and tubulation *in vitro*.

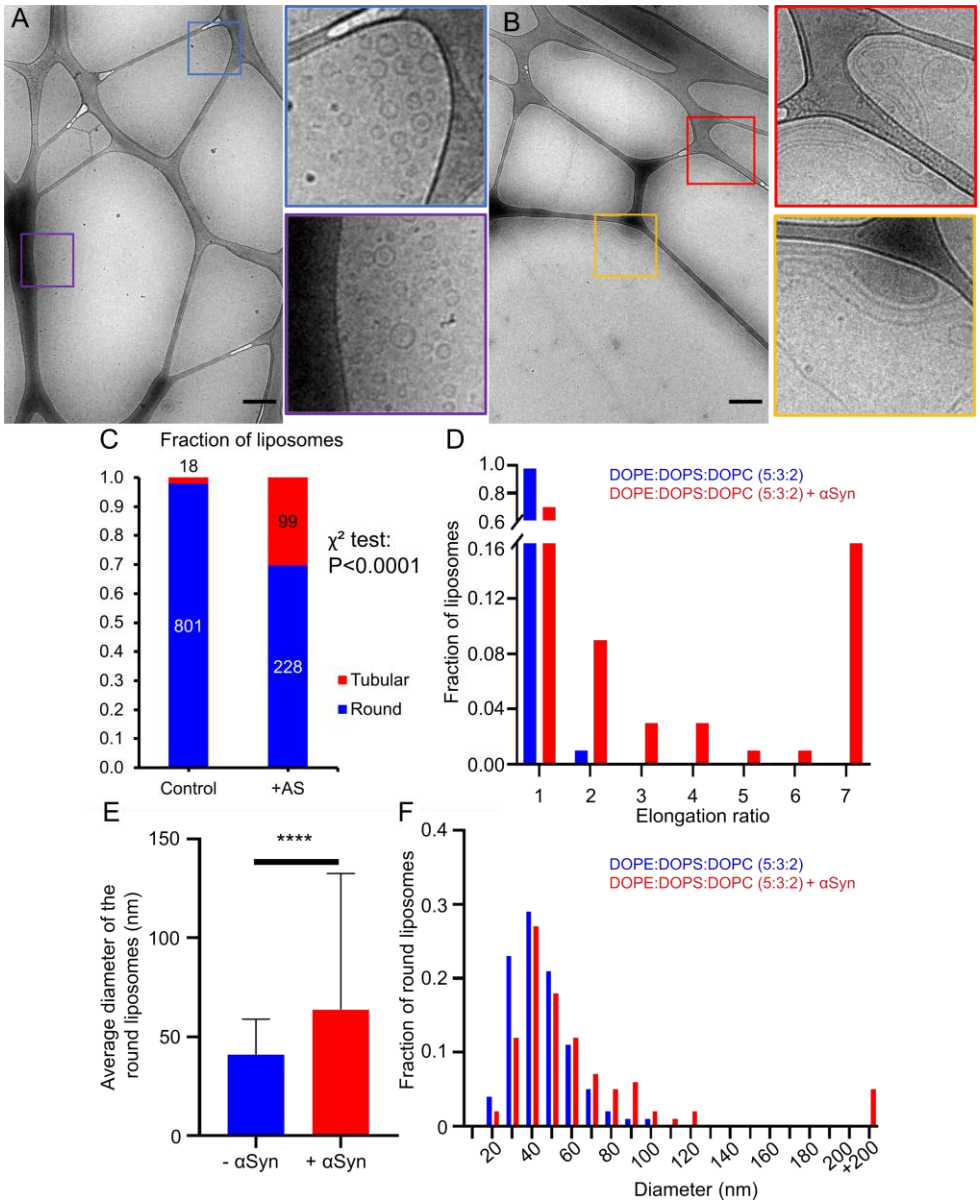

Figure 3.8: αSyn triggers fusion and tubulation of liposomes *in vitro*.

Cryo-EM overview and magnified pictures of liposomes without (A) or with (B) soluble αSyn (1:4 protein to lipid molar ratio, 1.7 mM αSyn, 6.8 mM liposomes). Giant liposomes and tubules are observed in the presence of αSyn. Scale bars, 500 nm. (C) The histogram showing the fractions of liposomes that were circular or tubular in the control condition and αSyn condition. A two-sided Chi-squared test was performed. (D) The distribution of circular and tubular liposomes without (blue) and with (red) αSyn. The elongation ratio corresponds to the ratio of liposome length to width. (E) Histogram of circular liposome diameters in both conditions. Data were tested for normality by performing a Shapiro-Wilk test. As the data did not display a normal distribution, they were analysed using a two-tailed Mann-Whitney test (P<0.0001). F) Diameter distribution of the circular liposomes in both conditions.

To examine the interactions of αSyn with liposomes, cryo-tomograms of tubular liposomes were collected on a Titan Krios microscope equipped with a K3 detector and a Volta phase plate (Danev et al., 2014, figure 3.9). Tomograms were reconstructed and a nonlinear anisotropic diffusion filter was applied (Frangakis and Hegerl, 2001). No density features, such as a continuous dark layer or randomly interspaced black dots, were observed at the tube surface. This absence of visible decoration suggests that either i) αSyn was mostly unfolded at the tube surface or ii) αSyn was present in a form that was not detectable by cryo tomography, such as monomers or small oligomers.

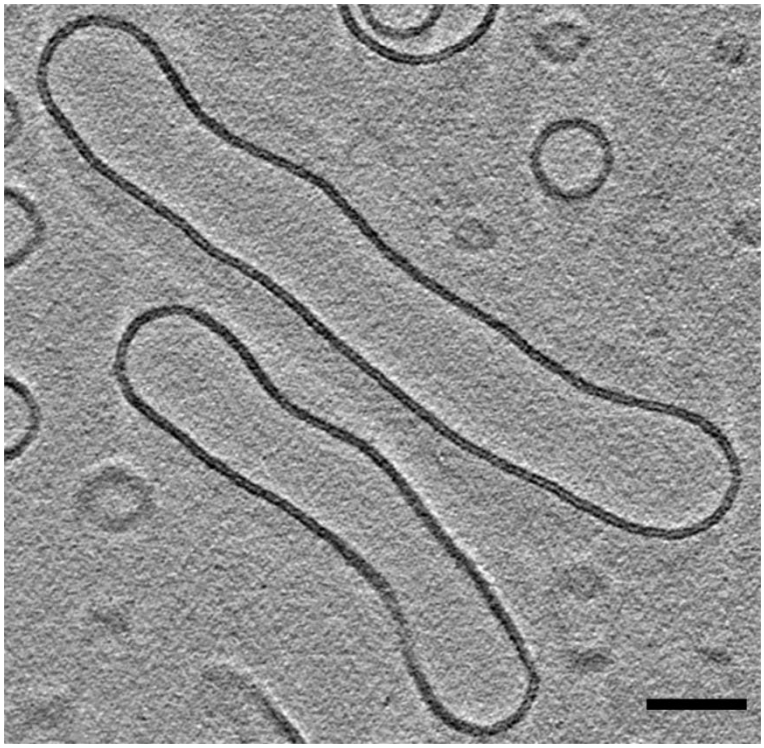

Figure 3.9: Section of a cryo-tomogram showing tubes of liposomes.
The tomogram was binned by 2 in X and Y and averaged over 10 slices in Z. The protein to lipid molar ratio was 1:15 (1 mM αSyn , 15 mM liposomes). The contrast was improved using a nonlinear anisotropic diffusion filter as implemented in IMOD. Scale bar, 50 nm.

3.6 Conclusion

Two complementary techniques were used to study αSyn aggregation in a yeast model. αSyn aggregation is characterised by its presence at the plasma membrane, colocalised with tubular ER. αSyn also formed cytosolic inclusions composed mainly of clustered vesicles and lipid droplets and amorphous aggregates. Surprisingly, no fibrillar aggregates were observed. αSyn aggregates were also internalised by vacuoles. *In vitro* experiments on soluble αSyn with liposomes confirmed the *in situ* observations since αSyn triggered liposome fusion and tubulation. Cryo tomograms of tubulated liposomes showed that those mechanisms appear to involve monomeric or small oligomeric forms of αSyn.

4. Results: αSyn disaggregation by the Hsp70 system *in vitro*

4.1 Introduction

In this chapter, I describe the expression and purification of Hsc70, DNAJB1, Apg2 and their mutants as well as αSyn fibrillation reaction. I then describe the assay that was used to validate the activity of the chaperones. I continue by describing the biochemical and biophysical assays that I used to investigate the function of Apg2. Then, I describe the TIRF optimisation and assay to confirm the biochemical results. Finally, I characterise the cryo-EM and cryo-ET results to get structural details on fibre decoration.

4.2 αSyn fibrillation

αSyn was purified as described in chapter 3 (figure 3.6). Amyloid fibres were prepared by incubating soluble αSyn (200 μM, monomer concentration) with preformed sonicated αSyn amyloid fibres (1%, v/v) at 37°C in an orbital shaker for a week at least. The formation of αSyn amyloid fibres was assessed by negative stain EM (figure 4.1).

Their width was ~10 nm, consistent with published literature (Guerrero-Ferreira et al., 2019, 2018; B. Li et al., 2018; Y. Li et al., 2018).

αSyn amyloid fibres were fluorescently labelled for the TIRF microscopy experiments. As the αSyn sequence does not contain any cysteines, a cysteine mutant was necessary. The mutation at residue 9 was chosen because it was already proven that this mutation does not interfere with αSyn fibrillation (Gao et al., 2015). S9C mutant was expressed using the same protocol as the one used for WT αSyn, with the addition of 2 mM TCEP

at each stage to break disulphide bonds. The chromatogram and the gel of the SEC show that purification was successful (figure 4.2).

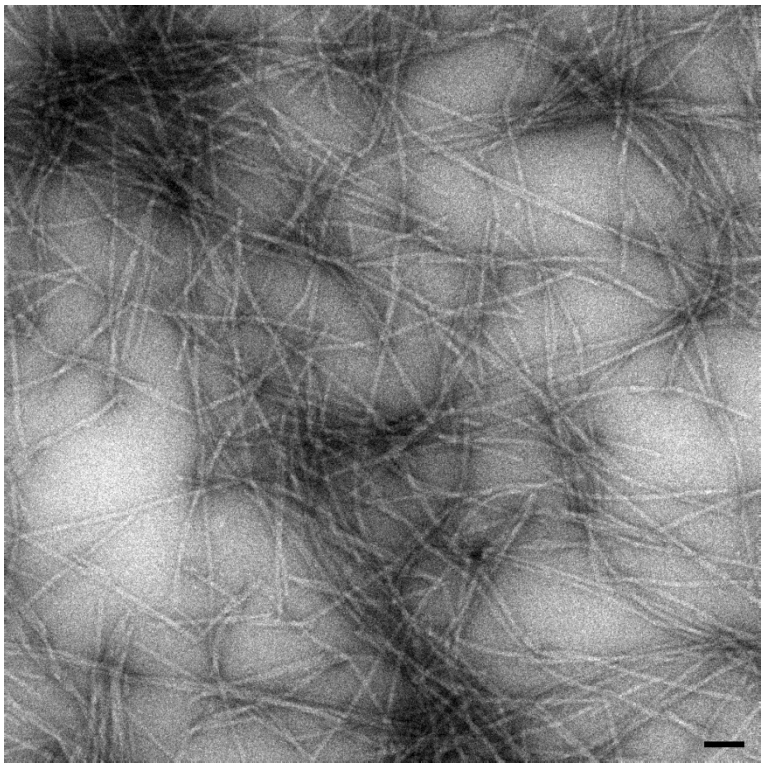

Figure 4.1: αSyn fibrillation.

Negative stain TEM image displaying αSyn amyloid fibres (10 µM, monomer concentration). Scale bar, 100 nm.

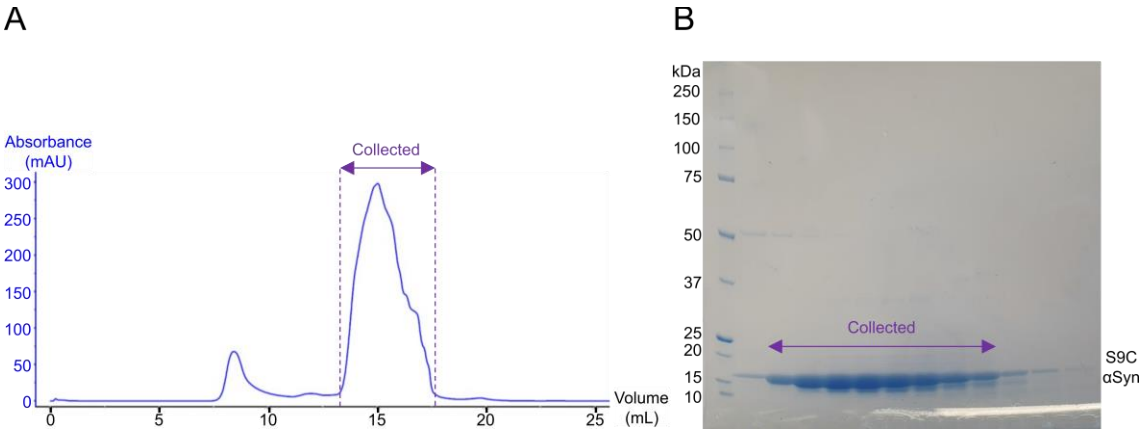

Figure 4.2: The purification of S9C αSyn mutant.

(A) Chromatogram of the size exclusion. αSyn was purified by size exclusion chromatography using a Superdex S200 column. (B) SDS-PAGE of the size exclusion chromatography. The markers are noted as kDa in size. A double band is visible for αSyn because of an artefact due to the gel scanner.

S9C:WT (1:2) fibres were prepared following the same protocol as the one used to make WT αSyn amyloid fibres, with the presence of 2 mM TCEP. Fibre formation was assessed by negative staining (figure 4.3A) before visualisation by TIRF microscopy (figure 4.3B). The protocol for visualisation by TIRF microscopy consisted in labelling the S9C:WT (1:2) fibres (10 µM, monomer concentration) with Alexa Fluor 647 maleimide dye (100 µM, 10-fold molar excess) for at least 2 hours at room temperature in the dark in HKMT buffer.

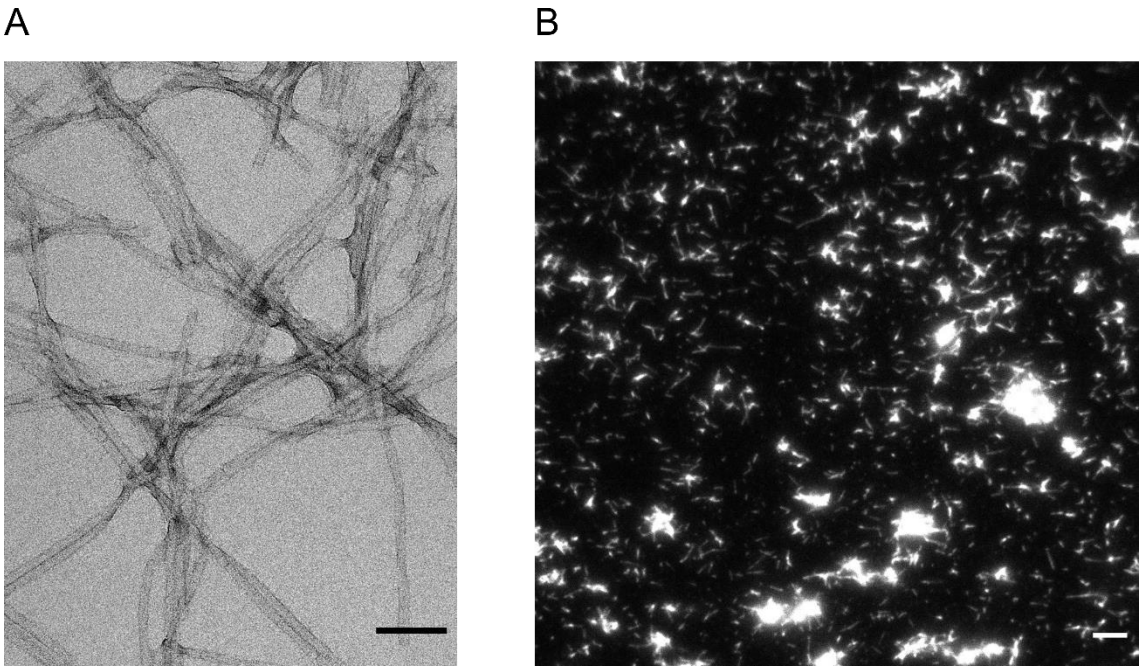

Figure 4.3: The fibrillation of S9C:WT (1:2) amyloid.
(A) Negative stain TEM image of S9C:WT (1:2 molar ratio) amyloid fibres (10 µM, monomer concentration). Scale bar, 100 nm. (B) TIRF image of S9C:WT (1:2) amyloid fibres (1 µM, monomer concentration) coupled to the Alexa Fluor 647 maleimide dye. Scale bar, 5 µm.

4.3 Chaperone expression and purification

Methods for purifying DNAJB1, Hsc70, Apg2 and their mutants have already been described (Gao et al., 2015). Plasmids (pCA528 with a His_6-Smt_3 tag at the N-terminus) and protocols were kindly provided by Professor Bernd Bukau's lab. The purified

truncated DNAJB1 mutant lacking the J-domain and the G/F linker, ΔJ-DNAJB1, was provided by Dr Rina Rosenzweig's group.

4.3.1 Chaperone expression

All the chaperones were expressed as fusion proteins with a His_6-Smt_3 tag in *Rosetta E. coli* bacteria cells.

4.3.2 DNAJB1 purification

DNAJB1 purification comprises three stages: immobilised metal affinity chromatography (IMAC), reverse IMAC, and size exclusion chromatography (SEC).

The soluble fraction (soluble fraction in figure 4.4A) was incubated with nickel beads to enable the binding of the His_6Smt_3 tag to the beads. Low-affinity impurities were separated from the beads by washing with 40 mM imidazole buffer (wash fractions in figure 4.4A). Finally, His_6-Smt_3 tagged DNAJB1 proteins were eluted (elution fractions in figure 4.4A). Several impurities were present in the eluted fractions. Only the first eluted fractions, that showed a sufficient amount of DNAJB1, were pooled and concentrated.

The sample was incubated overnight with Ulp1 enzyme to cleave the His_6-Smt_3 tag from DNAJB1. A reverse IMAC was then performed to separate cleaved DNAJB1 from the tag. Cleaved DNAJB1 was collected using wash buffer (wash fractions in figure 4.4B). A few impurities were also collected with the cleaved DNAJB1, including the Ulp1 enzyme displaying a band at 75 kDa. Beads were then washed using 500 mM elution buffer (elution fractions in figure 4.4B). His_6Smt_3 tag and trapped cleaved DNAJB1 were eluted. Wash fractions were pooled, concentrated and flash frozen.

Native DNAJB1 was then separated from the remaining contaminants by SEC. Three peaks were observed in the size-exclusion chromatogram (figure 4.4C). SDS-PAGE showed that DNAJB1 was present in peaks ① and ② while an impurity was eluted in peak ③ (figure 4.4D). Peak ① was at the column void volume and was therefore likely composed of DNAJB1 aggregates. Peak ② contained native DNAJB1 with a faint high molecular weight contaminant corresponding to Ulp1 enzyme (75kDa) and a low molecular weight contaminant that was likely degraded DNAJB1. Fractions of peak ② were collected and concentrated to 100-150 µM.

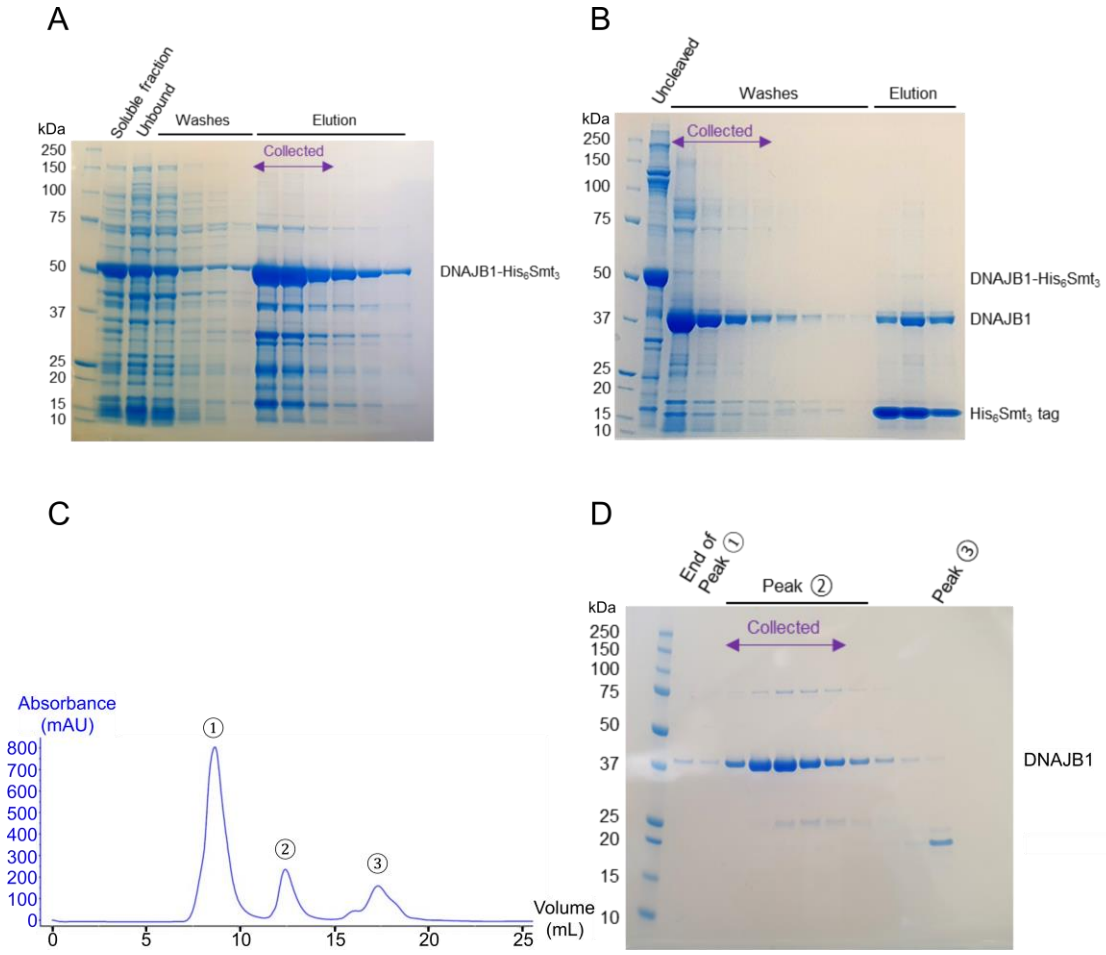

Figure 4.4: DNAJB1 purification.

(A) SDS-PAGE of the IMAC stage. The soluble fraction was incubated with nickel beads to enable the binding of the His_6Smt_3 tag to the beads. Low-affinity impurities were separated from the beads using 40 mM imidazole buffer (wash fractions). Finally, His_6-Smt_3 tagged DNAJB1 proteins were eluted (elution fractions) with 500 mM

imidazole buffer. Several impurities were present in the eluted fractions. (B) SDS-PAGE of the reverse IMAC stage. After overnight incubation with Ulp1 enzyme to cleave the His6-Smt3 tag from DNAJB1, a reverse IMAC was performed to separate cleaved DNAJB1 from the tag. Cleaved DNAJB1 was collected using the wash buffer (washes fractions). (C) Chromatogram of the size exclusion. DNAJB1 was purified by size exclusion chromatography using a Superdex S200 column. (D) SDS-PAGE of the size exclusion chromatography. The large band at 40 kDa corresponds to DNAJB1 whereas the faint band at 75 kDa corresponds to Ulp1 enzyme. The markers are noted as kDa in size in all the gels.

4.3.3 Hsc70 and Apg2 purification

Hsc70 and Apg2 WT proteins and their mutants were purified by column cleavage with IMAC. After binding, the column was washed with different buffers to discard low-affinity contaminants (wash fractions in figure 4.5A-B). One of the buffers contained 5 mM ATP to bind to Hsc70 and promote its open conformation. The His_6Smt_3 tag was then removed using the Ulp1 protease and the cleaved chaperones were then eluted (elution fractions in figure 4.5A-B). The first three elution fractions of each chaperone were pooled and Hsc70 was concentrated to 100 µM and Apg2 to 30 µM.

T111C Hsc70 mutant was purified following the same protocol, with 2 mM TCEP instead of 2 mM DTT (figure 4.5C).

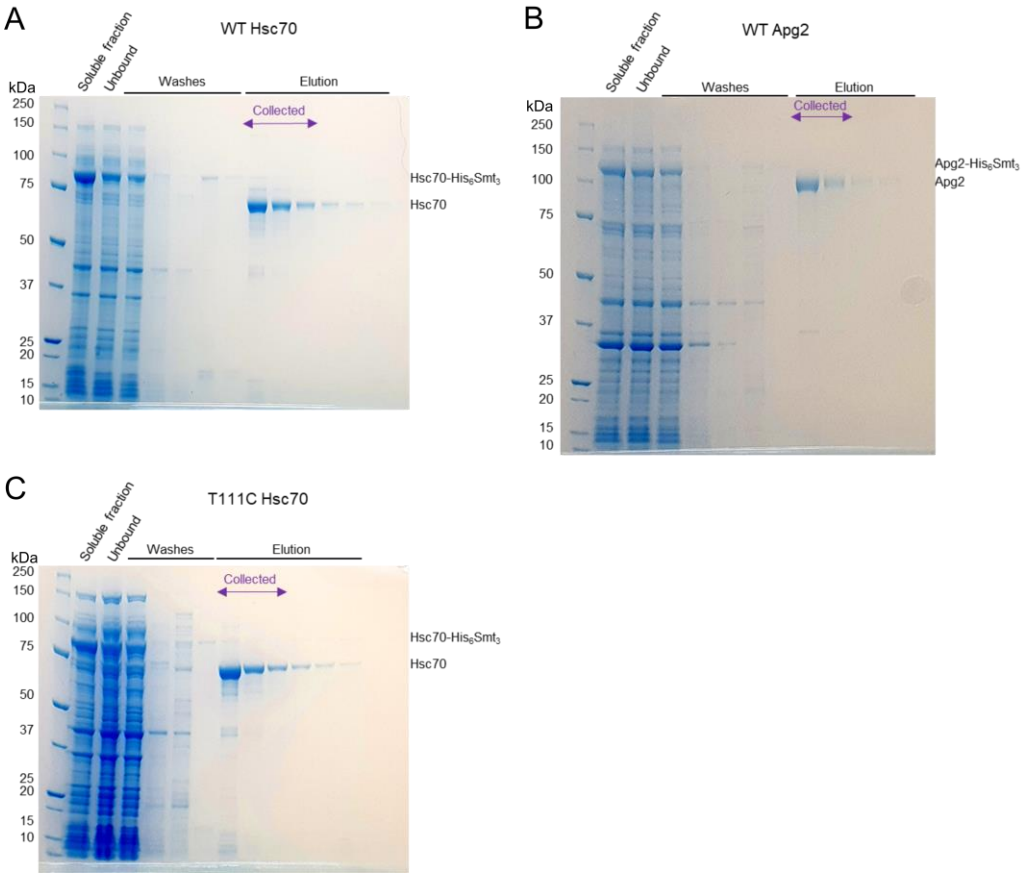

Figure 4.5: WT Hsc70, WT Apg2 and T111C Hsc70 mutant purification.
SDS-PAGE of the IMAC and reverse IMAC stages of WT Hsc70 (A), WT Apg2 (B), and T111C Hsc70 mutant (C). For the three proteins, low-affinity impurities were separated from the beads using 40 mM imidazole buffer and after an overnight incubation with Ulp1 enzyme, a reverse IMAC was performed to separate the cleaved chaperones (WT or T111C Hsc70, WT Apg2) from the tag. Cleaved chaperones were eluted using the wash buffer (elution fractions). The markers are noted as kDa in size in all the gels.

4.4 Assessment of αSyn fibre disaggregation in vitro

Each new batch of formed αSyn fibres and purified chaperones was first assessed by running a ThT fluorescence-based assay to confirm that i) the fibres can be disassembled or ii) the chaperones are active. ThT is a dye that emit fluorescence when bound to amyloid fibres and is commonly used to monitor amyloid fibre formation and disassembly *in vitro* (Biancalana and Koide, 2010; Gao et al., 2015; Naiki et al., 1989).

The linear correlation between ThT fluorescence and αSyn fibre concentration (monomer concentration) was first verified (figure 4.6A). As a strong correlation was observed, the ThT fluorescence-based assay could be used to monitor αSyn fibre disaggregation. This biochemical reaction is ATP-dependent and requires DNAJB1, Hsc70, and Apg2. The disaggregation of ThT-labelled αSyn amyloid fibres was monitored over time (figure 4.6B, blue curve). Disaggregation efficiency varied from batch to batch but, in the current example, around 80% of the fibres were disassembled after 16 hours when mixed with chaperones and ATP. On the contrary, in the condition lacking ATP (figure 4.6B, purple curve), no disaggregation was observed, confirming the ATP-dependence of the reaction. T111C Hsc70 mutant and S9C:WT (1:2) αSyn fibres were also assessed by comparing with a batch containing WT Hsc70 or WT αSyn fibres, respectively (figure 4.6C-D). As there was no significant difference between the cysteine mutants and the WT proteins, T111C Hsc70 and S9C:WT (1:2) fibres were used for the TIRF experiments.

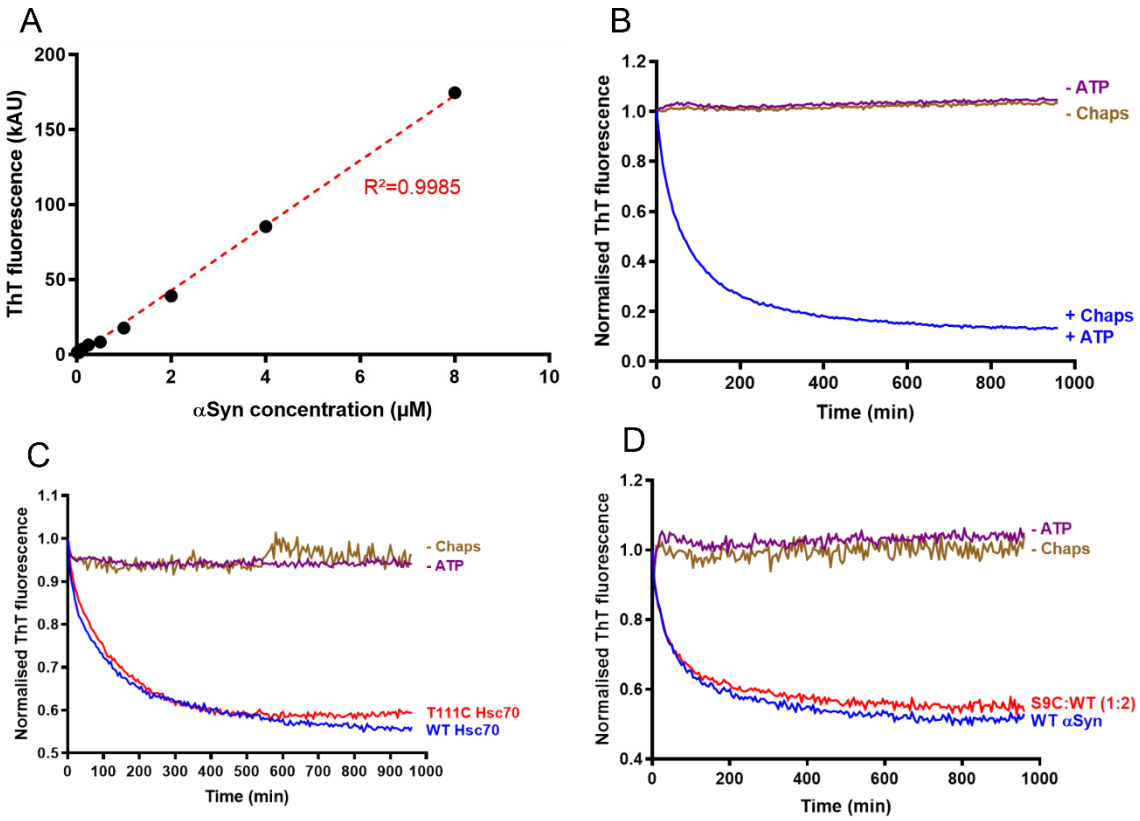

Figure 4.6: Disaggregation activity.

(A) Standard curve showing the correlation between the ThT fluorescence signal and the concentration of amyloid fibres (αSyn monomer concentration). (B) Disaggregation curves in the presence of chaperones and ATP (+ Chaps + ATP, blue curve), in the presence of chaperones without ATP (- ATP, purple curve) or in the presence of ATP without chaperones (- Chaps, brown curve). (C) An example of a ThT assay comparing the activity of T111C Hsc70 mutant (red curve) and the activity of WT Hsc70 (blue curve). (D) Disaggregation curves of the WT αSyn fibres (blue curve) and S9C:WT (1:2) αSyn fibres (red curve) in the presence of chaperones and ATP. For all the disaggregation assays (B-D), the concentrations were 2 μM αSyn amyloid fibres (monomer concentration), 4 μM Hsc70, 2 μM DNAJB1, 0.4 μM Apg2.

4.5 Apg2 recruits Hsc70 in a concentration-dependent manner

In the group, AFM experiments performed by Dr Joe Beton showed that fibres are decorated by large and extended clusters of chaperones before disaggregation (Beton et al., 2021). Biochemical and biophysical experiments performed by the collaborators proved that Hsc70 clustering is required for disaggregation (Wentink et al., 2020).

However, the exact molecular composition of the decoration has never been determined and the precise role of Apg2 in this process is unclear: Apg2 influences the disaggregation efficiency in a concentration-dependent manner but Apg2 also selectively recycles Hsc70 molecule not included into clusters because of its size (Wentink et al., 2020). Therefore, determining Apg2 function in the disaggregation would be of great value.

To determine the molecular composition of the fibre decoration observed in AFM experiments, a binding assay was performed (figure 4.7A). Two conditions were evaluated to understand Apg2 function: fibres were incubated with chaperones (+/- Apg2) and ATP and then centrifuged (40 µM αSyn monomer concentration, 8 µM Hsc70, 4 µM DNAJB1, 0.8 µM Apg2). After centrifugation, the pellet contained the fibres and the bound chaperones while the supernatant contained the unbound chaperones. Controls without the fibres were also performed to verify that Apg2 did not trigger the aggregation of the other chaperones. The controls did not display differences (figure 4.7A). However, in the presence of Apg2, a bigger band for Hsc70 was observed in the pellet, showing that Apg2 can trigger the recruitment of Hsc70 to the fibres (figure 4.7A,C). I then assessed if this additional recruitment would also require DNAJB1 by using a truncated mutant (ΔJ-DNAJB1) lacking the G/F linker and the J domain, which is the primary binding site of Hsc70 (40 µM αSyn monomer concentration, 8 µM Hsc70, 4 µM ΔJ-DNAJB1, 0.8 µM Apg2) (Greene et al., 1998). Without the J domain, Hsc70 was not recruited, even in the presence of Apg2 (figure 4.7B, C). Those observations were confirmed by negative stain EM of fibres alone (figure 4.7D), fibres incubated with WT DNAJB1, Hsc70, Apg2 and ATP (figure 4.7E), and fibres incubated with ΔJ-DNAJB1, Hsc70, Apg2 and ATP (figure 4.7F). In the presence of WT DNAJB1, fibres were thicker than the fibres alone and displayed a

fuzzy decoration. On the contrary, fibres incubated with ΔJ-DNAJB1 were as thin as the fibres alone and did not display a decoration. Therefore, initial recruitment of Hsc70 requires the J domain of DNAJB1, in agreement with previous literature (Wentink et al., 2020), and, unexpectedly, Apg2 can further stimulate Hsc70 binding to the fibres.

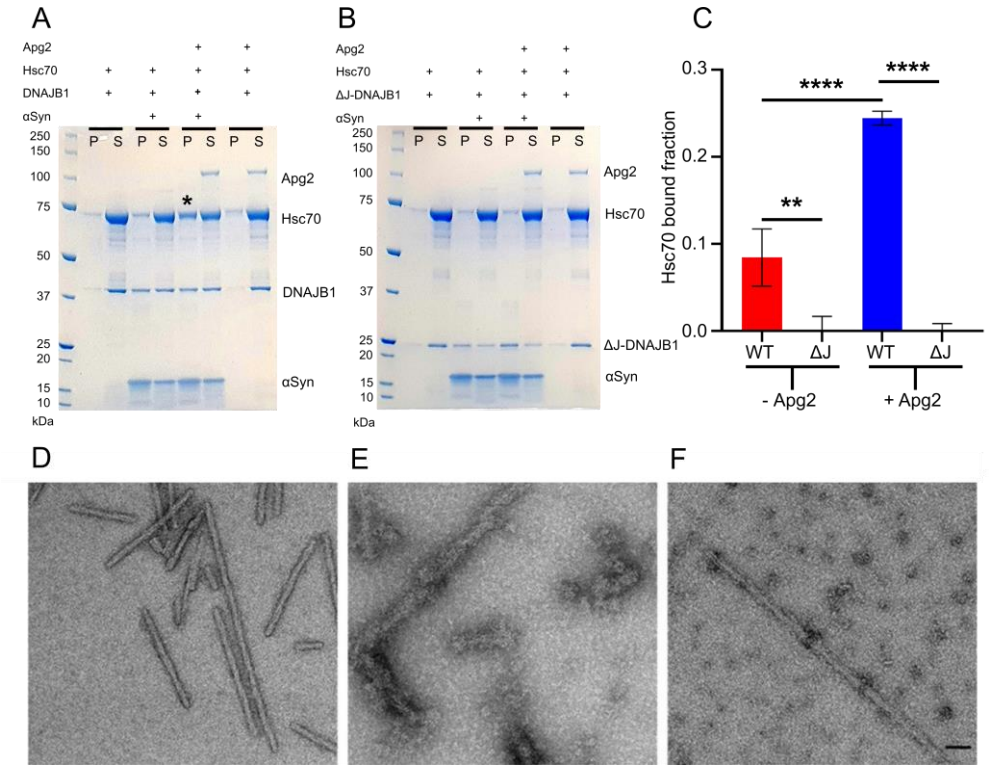

Figure 4.7: Apg2 greatly stimulates Hsc70 recruitment to the fibres.

(A) Binding assay for Hsc70 binding in the presence of WT DNAJB1: control of DNAJB1/Hsc70, αSyn fibres + DNAJB1/Hsc70, αSyn fibres + DNAJB1/Hsc70/Apg2, control of DNAJB1/Hsc70/Apg2. The concentrations are 40 μM αSyn (monomer concentration), 8 μM Hsc70, 4 μM DNAJB1, 0.8 μM Apg2. A larger band for Hsc70 is observed in the pellet for the condition where fibres are incubated with DNAJB1, Hsc70 and Apg2. This larger band is not observed in the control without fibres. The '*' highlights the condition where an increase of Hsc70 in the bound fraction is observed. P: pellet; S: supernatant. The amount of Hsc70 recruited to the fibres is shown in the pellet fractions. (B) Binding assay for Hsc70 binding in the presence of the truncated ΔJ-DNAJB1, lacking the J domain. The gel layout is similar to the previous one with ΔJ-DNAJB1 replacing WT DNAJB1. The concentrations are 40 μM αSyn (monomer concentration), 8 μM Hsc70, 4 μM ΔJ-DNAJB1, 0.8 μM Apg2. The band for Hsc70 in the pellet has a similar size for all the different conditions, including the controls

without fibres. Both Apg2 and J domain are required for enhancement of Hsc70 binding. ATP was present in both (A) and (B). The markers are noted as kDa in size in all the gels. (C) Histogram of Hsc70 bound fraction in each sample (N = 3 independent experiments, WT: WT DNAJB1, ΔJ: ΔJ-DNAJB1 mutant, -Apg2: condition with fibres + DNAJB1/Hsc70, +Apg2: condition with fibres + DNAJB1/Hsc70/Apg2). A 2-way ANOVA was performed with Tukey's multiple comparisons test (**: P=0.003; ****: P<0.0001). (D, E, F) Negative stain images displaying WT fibres alone (D), WT fibres with WT DNAJB1, Hsc70, Apg2 and ATP (E), or WT fibres with ΔJ-DNAJB1, Hsc70, Apg2 and ATP (F). In (D, E, F), the concentrations are 10 µM αSyn fibres and, when indicated, 10 µM Hsc70, 5 µM WT DNAJB1 or ΔJ-DNAJB1 mutant, 1 µM Apg2. Scale bar, 50 nm.

I then checked the dependence of Hsc70 recruitment on Apg2 concentration by doing a binding assay with different dilutions of Apg2 (figure 4.8A, 40 µM αSyn monomer concentration, 8 µM Hsc70, 4 µM DNAJB1, 8-4,000 nM Apg2). Controls of all the dilutions in the absence of fibres were also carried out (figure 4.8B, 8 µM Hsc70, 4 µM DNAJB1, 8-4,000 nM Apg2). When Apg2 concentration was increased, Hsc70 recruitment increased up to a saturating 1:10 Apg2:Hsc70 molar ratio (figure 4.8C). At a higher ratio, Hsc70 recruitment was less efficient. I then checked for a correlation between Apg2-stimulated Hsc70 recruitment and disaggregation activity, since it was already known that Apg2 concentration affects disaggregation efficiency (Wentink et al., 2020). I therefore performed a ThT assay with the same Hsc70:Apg2 ratios (figure 4.8D). Disaggregation efficiency was improved by increasing Apg2 concentration until reaching a maximum at a 1:10 Apg2:Hsc70 molar ratio (figure 4.8E). I then plotted the disaggregation efficiency obtained from the ThT assay as a function of Hsc70 recruitment obtained from the binding assay (figure 4.8F). A strong correlation was observed between those two factors (blue dots in figure 4.8F, R^2=0.900). Activity in the absence of Apg2 also fitted with the linear correlation (red dot, R^2=0.904). Those

biochemical and biophysical results show that a key function of Apg2 is to regulate the disaggregation by mediating Hsc70 recruitment.

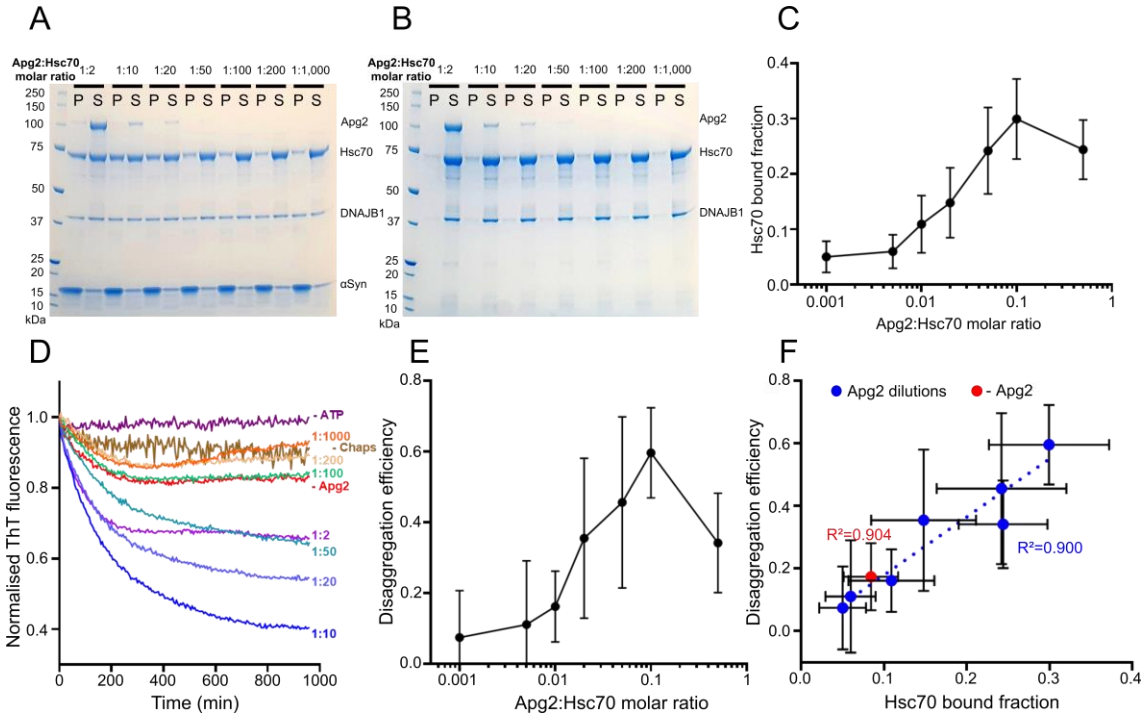

Figure 4.8: Dependence of Hsc70 recruitment and disaggregation activity on Apg2 concentration.

(A) Binding assay showing the dependence of Hsc70 recruitment on Apg2. The concentrations are 40 µM αSyn (monomer concentration), 8 µM Hsc70, 4 µM DNAJB1, 8-4,000 nM Apg2. The band of Hsc70 in the pellet is larger when Apg2 concentration increases until reaching a maximum for a 1:10 Apg2:Hsc70 molar ratio. (B) Control binding assay in the absence of fibres. The concentrations are 8 µM Hsc70, 4 µM DNAJB1, 8-4,000 nM Apg2. The size of Hsc70 band in the pellet does not vary when Apg2 concentration increases. ATP (5 mM) was present in both A and B. The markers are noted as kDa in size in all the gels. (C) Plot showing Hsc70 binding as a function of Apg2:Hsc70 molar ratio (N = 3 independent experiments). The action of Apg2 in recruiting Hsc70 to the fibres saturates at a molar ratio of Apg2:Hsc70 of 1:10. (D) Disaggregation activity measured by Thioflavin T fluorescence shows the same dependence on Apg2 as binding assays. High Apg2 (1:2 molar ratio) makes disaggregation less efficient. The concentrations are 2 µM αSyn (monomer concentration), 4 µM Hsc70, 2 µM DNAJB1, 4-2,000 nM Apg2. . (E) Quantification of the disaggregation efficiency as a function of Apg2:Hsc70 molar ratio (N = 3 independent experiments). The disaggregation efficiency was determined by taking the

values from the final hour of the assay curves in (D). (F) Plot showing the linear correlation between disaggregation activity and Hsc70 binding (R^2=0.900). Including the data point without Apg2 did not change the correlation coefficient, which was 0.904.

4.6 Apg2 recruits Hsc70 preferentially at one end of the fibre

To understand more about Hsc70 recruitment, I carried out TIRF microscopy. However, a few controls were needed. First, it had to be established that labelling the fibres with a fluorophore would not prevent their disassembly. Labelled fibres were already used for biophysical experiments (Wentink et al., 2020). However, they were centrifuged and washed several times to deplete any excess of the fluorophores. I could not follow this protocol as isolated, long fibres were necessary for the TIRF microscopy. I therefore labelled the fibres (10 µM, monomer concentration) with either the Alexa Fluor 488 or 647 maleimide dye using a 10-fold molar excess of dye (100 µM) for 2 hours at room temperature in the dark and carried out a ThT assay without depleting the excess of dye (figure 4.9A). I also added a control with unlabelled fibres. Unlabelled and Alexa Fluor 647-labelled fibre were disaggregated at the same efficiency (around 70% were disassembled) while disaggregation was slowed down when the fibres were labelled with Alexa Fluor 488 maleimide dye (only 40% were disassembled). Therefore, fibres labelled with Alexa Fluor 647 maleimide dye were used in the TIRF microscopy experiments. The second control was to assess the influence of the biotinylated linker. Again, fibres were labelled with different linkers (XSE NHS linker, and PEG2 or PEG11 maleimide linker) and a control without linker was added (figure 4.9B). None of the biotinylated linkers slowed down or prevented the disaggregation. I therefore chose the X-SE linker which binds to the first methionine of the sequence and lysines to avoid competition between the fluorophore and the linker. I then assessed if the concentration

of the X-SE linker would affect the disaggregation (figure 4.9C). Up to a 1.3 linker:αSyn molar ratio, the disaggregation was not affected. At a higher ratio, disaggregation was less efficient and depended on linker concentration. Using a ratio between 0.2 and 1.3X would seem a good choice. However, at those ratios, fibres were not efficiently attached to the glass coverslip. I therefore had to use a 2.5 ratio for the TIRF microscopy experiments.

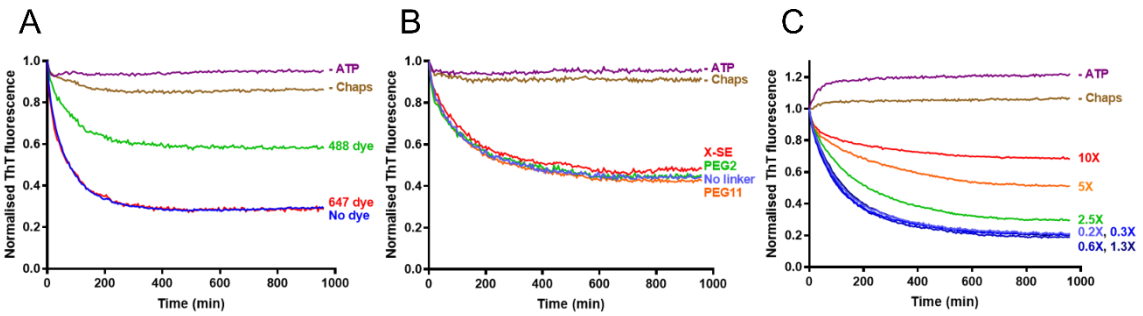

Figure 4.9: Dye and linker selection for TIRF assay.

(A) Disaggregation curves comparing unlabelled S9C:WT (1:2) fibres (blue curve), the same fibres labelled with Alexa Fluor 647 maleimide dye (red curve) or with Alexa Fluor 488 maleimide dye (green curve). (B) Disaggregation curves comparing unlabelled S9C:WT (1:2) fibres (blue curve), the same fibres labelled with the X-SE linker (red curve), the PEG2 linker (green curve), or the PEG 11 linker (orange curve). (C) Disaggregation curves displaying different dilutions of XSE linker (from 0.2 to 10X molar ratios between the linker and the amines of αSyn). In the three panels, controls in the presence of chaperones without ATP (- ATP, purple curve) or in the presence of ATP without chaperones (- Chaps, brown curve) were also performed. The concentrations are 2 µM αSyn (monomer concentration), 4 µM Hsc70, 2 µM DNAJB1, 0.4 µM Apg2.

In the TIRF microscopy experiments, fibres were labelled with the Alexa Fluor 647 maleimide dye and X-SE linker at a 2.5 molar ratio. Hsc70 T111C mutant was also labelled with Alexa Fluor 488 maleimide dye. I did not perform a ThT assay to check the activity of the labelled Hsc70 mutant since this mutant labelled with the same dye was previously used to study αSyn amyloid fibre disaggregation (Wentink et al., 2020).

I checked two conditions by TIRF microscopy: Alexa Fluor 647-labelled fibres incubated with WT DNAJB1 and Alexa Fluor 488-labelled T111C mutant, in the absence or presence of Apg2 (figure 4.10A). In agreement with the binding assays, Apg2 significantly stimulated Hsc70 recruitment (figure 4.10A, B) since Hsc70 fluorescence intensity was higher in the presence of Apg2. As fluorescence intensity depends on the distance of the sample from the glass surface in TIRF microscopy, I also recorded αSyn fluorescence in both conditions (figure 4.10C). No significant difference in αSyn fluorescence was observed between them. I also compared Hsc70 fluorescence intensity, relative to αSyn intensity, at the two ends of each fibre (figure 4.10D). Hsc70 fluorescence at each fibre end was divided by αSyn fluorescence at the same location to minimise the effect of fibre tilting. The difference of Hsc70 fluorescence intensities at the two ends was higher in the presence of Apg2, showing that Apg2 recruits Hsc70 preferentially to one end of the fibres (figure 4.10A, D).

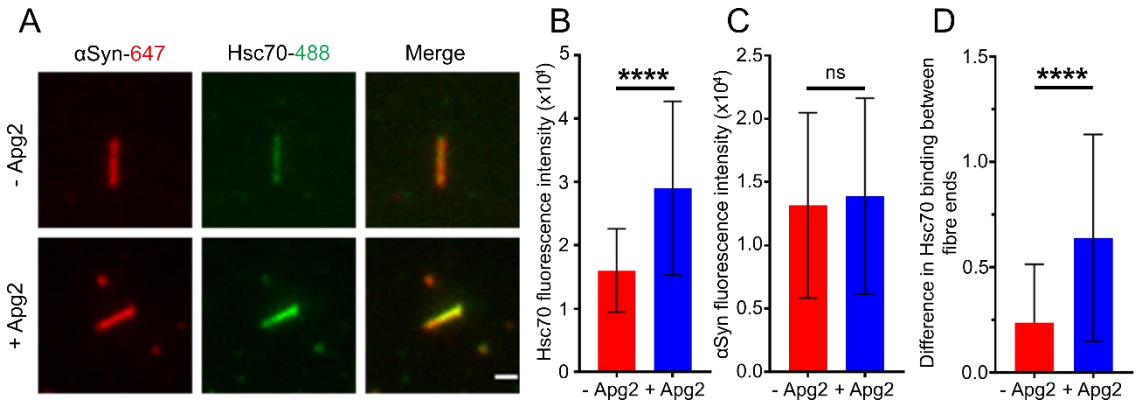

Figure 4.10: Apg2 recruits Hsc70, preferentially at one end of the fibre.

(A) TIRF microscopy images of the labelled αSyn fibres and Hsc70 in the absence or in the presence of Apg2 (upper and lower panels, respectively). Scale bar, 1 µm. The concentrations are 1 µM αSyn (monomer concentration), 2 µM Hsc70, 1 µM DNAJB1, 200 nM Apg2. (B, C) Quantitation of fluorescence intensity of Hsc70 (B) and αSyn (C) in the two conditions (+/- Apg2, N = 3 independent experiments, n = 65 fibres). (D) Quantitation of differences in Hsc70 binding between the two ends of the fibres, in the absence and presence of Apg2 (N = 3 independent experiments, n = 54 fibres). An end was defined as the first or last 3 pixels of a fibre. For each plot, data were tested for normality by performing a Shapiro-Wilk test. As the data did not display a normal distribution, they were analysed using a two-tailed Mann-Whitney test (****: P<0.0001, ns: not significant).

4.7 αSyn fibres display flexible dense clusters of chaperones in the presence of DNAJB1, Hsc70 and Apg2

αSyn fibres decorated with DNAJB1 alone, DNAJB1/Hsc70 or DNAJB1/Hsc70/Apg2 in the presence of ATP have already been studied by negative stain tomography (Gao et al., 2015). But the complexes have never been imaged by cryo-EM. The complex formed of αSyn fibres and DNAJB1 will be described in detail in chapter 5. This section focuses on the comparison between αSyn fibres decorated with DNAJB1/Hsc70 and αSyn fibres decorated with DNAJB1/Hsc70/Apg2.

The 2 assemblies were studied by cryo-EM using a Tecnai TF20 microscope with αSyn fibres alone as a control. In the control, fibres are ~10 nm thick (figure 4.11A). In the presence of DNAJB1, Hsc70 and ATP, chaperone decoration is scattered along the fibre (figure 4.11B). When Apg2 is added, dense elongated clusters of chaperones are observed (figure 4.11C).

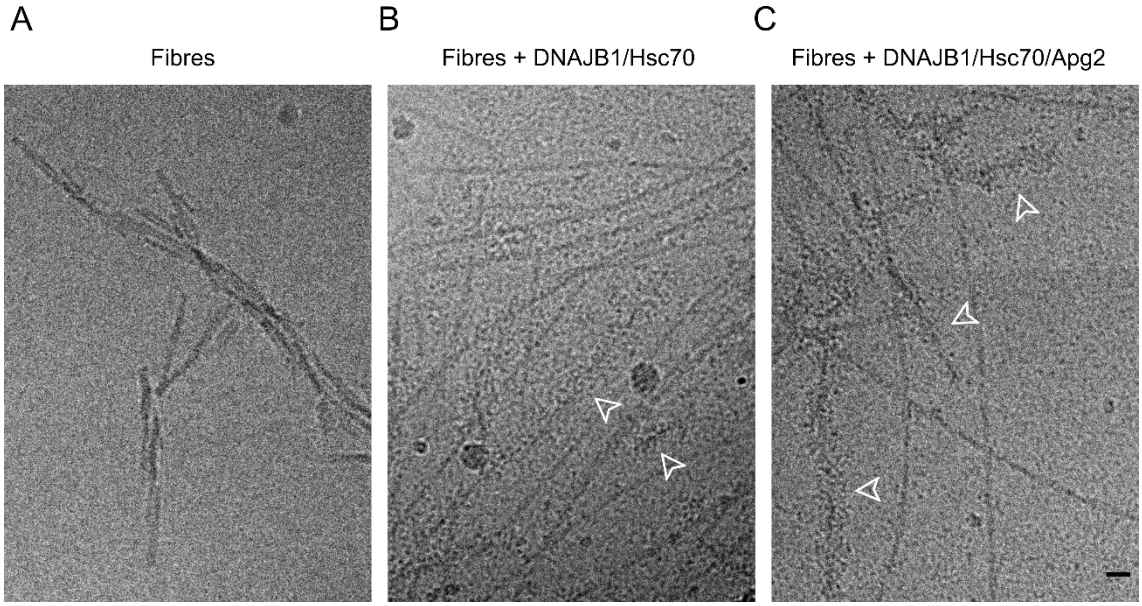

Figure 4.11: Cryo-EM images of decorated fibres.
Cryo-EM images showing αSyn fibres alone (A), αSyn fibres incubated with Hsc70/DNAJB1 and ATP (B) and fibres incubated with Hsc70/DNAJB1/Apg2 and ATP (C). Fibre decoration is highlighted with white arrows. The concentrations are 6 µM αSyn fibres (monomer concentration) and when indicated, 6 µM Hsc70, 3 µM DNAJB1, 0.6 µM Apg2 and 5 mM ATP. Scale bar, 30 nm

To quantify whether Apg2 promotes the decoration of fibres, two small datasets were collected on a Titan Krios and around 400 - 500 fibres were scored for each condition (figure 4.12A). Around two third of the fibres were decorated in both conditions (without or with Apg2, figure 4.12B). There were no statistically significant differences between the two conditions, showing that Apg2 does not nucleate the decoration of a fibre.

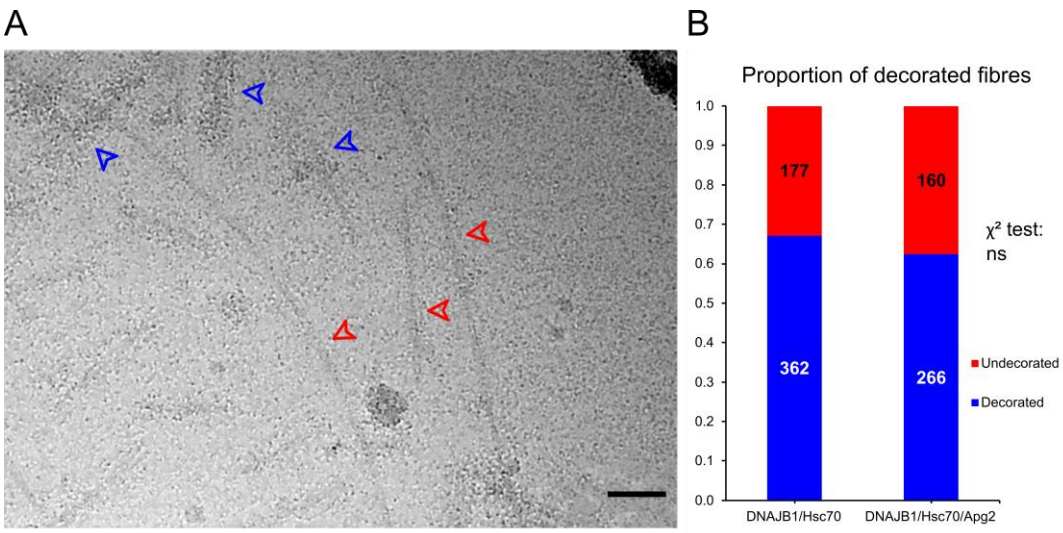

Figure 4.12: Apg2 does not nucleate the decoration of fibres.

(A) Cryo-EM images of αSyn fibres with DNAJB1, Hsc70, Apg2 and ATP showing undecorated (red arrows) and decorated (blue arrows) fibres. The images were denoised using Topaz denoise to facilitate fibre counting on a large data set of images from fibres incubated either with the full system or with the system lacking Apg2. Scale bar, 50 nm. The concentrations are 6 µM αSyn fibres (monomer concentration), 6 µM Hsc70, 3 µM DNAJB1, 5 mM ATP and when indicated 0.6 µM Apg2. (B) Stacked bar chart showing the number of decorate fibres. The numbers written inside the bars indicate the number of counted fibres for each category. Apg2 does not influence the proportion of decorated fibres. A two-sided Chi-squared test was performed. ns: Not significant. The results were confirmed by Erin Johnston, a research assistant in the group, who performed a blinded analysis.

The background was high in the cryo-EM images because of the large excess of unbound chaperones. In order to better resolve the complexes, cryo tomograms of both assemblies were collected (figure 4.13). Without Apg2, chaperones form short and sparse clusters along the fibres (figure 4.13A). With Apg2, chaperones form extended dense and flexible clusters roughly following the helical twist of the fibres (figure 4.13B). Chaperone assemblies were also observed in the background or bound to the fibres in the presence of Apg2 (white arrows in figure 4.13C). It was however not possible to determine the composition of the assemblies as dimeric DNAJB1, Hsc70 and Apg2 have similar molecular weights (80kDa, 70kDa, and 95 kDa, respectively). It

is possible that these assemblies are chaperone oligomers formed before binding to the fibres, explaining potentially why Apg2 recruits more Hsc70. However, another possibility is that they are a transient product of the disaggregation when the fibres are disassembled but αSyn flexible polymers are not depolymerised yet.

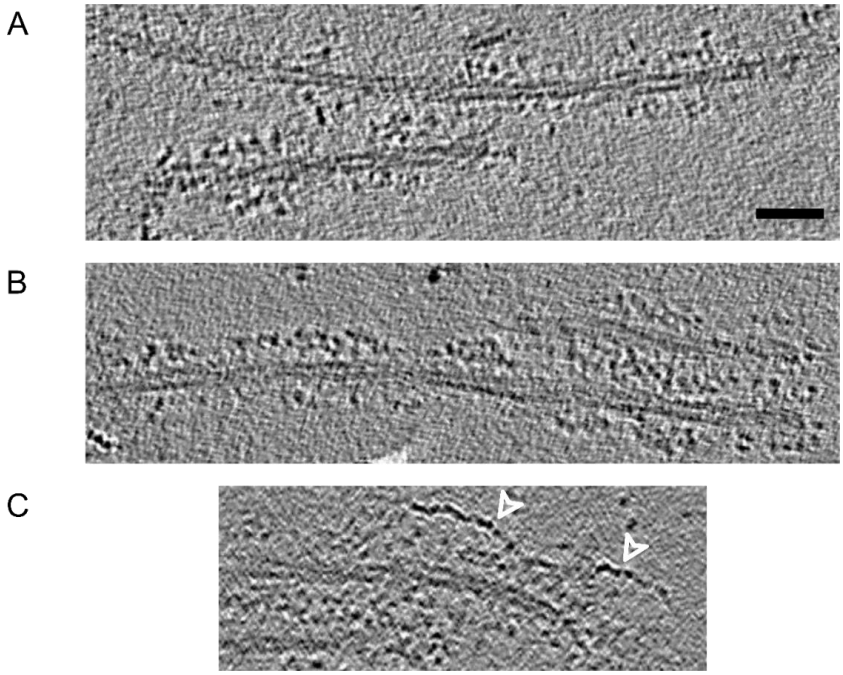

Figure 4.13: Cryo-electron tomography of fibre-chaperone complexes.
(A) Tomogram section of fibres incubated with Hsc70, DNAJB1 and ATP. (B) Equivalent view of fibres incubated with Hsc70, DNAJB1, Apg2 and ATP, showing extended stretches of densely clustered chaperones. (C) Chaperone polymers were observed in the sample with Apg2. The concentrations are 6 µM αSyn fibres (monomer concentration), 6 µM Hsc70, 3 µM DNAJB1, 5 mM ATP and when indicated 0.6 µM Apg2. The tomograms were binned by 4 in X and Y and averaged over 5 slices in Z. Scale bar, 30 nm.

4.8 Conclusion

Biochemical assays showed that the J domain of DNAJB1 is required for initial recruitment of Hsc70. Apg2 then triggers additional Hsc70 recruitment to the fibres and this improved recruitment is correlated to a more efficient disaggregation. This observed Hsc70 recruitment was also confirmed by TIRF microscopy. Cryo-EM and cryo-ET revealed that Apg2 leads to the formation of dense flexible clusters of chaperones, which are the active zones of disaggregation. TIRF microscopy showed that Hsc70 preferentially binds to one end of the fibre when Apg2 is present, in agreement with published time course AFM videos of the disaggregation showing that the disaggregation of the fibres by depolymerisation is polar (Beton et al., 2021).

5. Results: Cryo-EM of αSyn:DNAJB1 complexes

5.1 Introduction

The first stage of the disaggregation of αSyn amyloid fibres by the Hsc70 system is the binding of DNAJB1 to the fibres. DNAJB1 is essential for the disaggregation and cannot be substituted by other DNAJ proteins such as DNAJA1 (Gao et al., 2015). This is due to the presence of an additional helix 5 in the J-domain of DNAJB1 which inhibits the direct interaction between DNAJB1 J-domain and Hsc70 (Faust et al., 2020). Instead, a two-step mechanism is required for the DNAJB1-Hsc70 interaction as explained more in detail in chapter 1. However, the reason why this 2-step mechanism is required for the disaggregation of αSyn amyloid fibres is still unclear. Moreover, structural details of the binding of DNAJB1 to αSyn amyloid fibres are unknown. Therefore, EM of the complex of DNAJB1 bound to αSyn fibres could help explain the mechanism of disaggregation. Furthermore, comparing the complexes of αSyn amyloid fibres with either WT DNAJB1 or ΔJ-DNAJB1, a mutant lacking the J-domain and the G/F flexible linker, could clarify the specific function of DNAJB1 in the mechanism. In this chapter, I first explain the optimisation of DNAJB1 binding to αSyn amyloid fibres which was necessary to get a stable complex. Then, I briefly describe the low-resolution structure of αSyn amyloid fibres decorated by WT DNAJB1 which was found by Dr Joe Beton, a former PhD student and postdoc in the group. Lastly, I detail the sample preparation and the single particle analysis that I performed to study the complex formed of αSyn amyloid fibres with ΔJ-DNAJB1.

5.2 Optimising DNAJB1 binding

It has already been shown that a small fraction of DNJB1 binds to αSyn amyloid fibres at a 1:0.5 molar ratio in HKMD buffer (table 2.1, Gao et al., 2015). This observation was confirmed by cryo-EM (figure 5.1). DNAJB1 dimers, which appear as black dots in the cryo micrograph, weakly interact with the fibres and also produce a high background, impeding image processing. A first aim was therefore to optimise DNAJB1 binding to αSyn amyloid fibres.

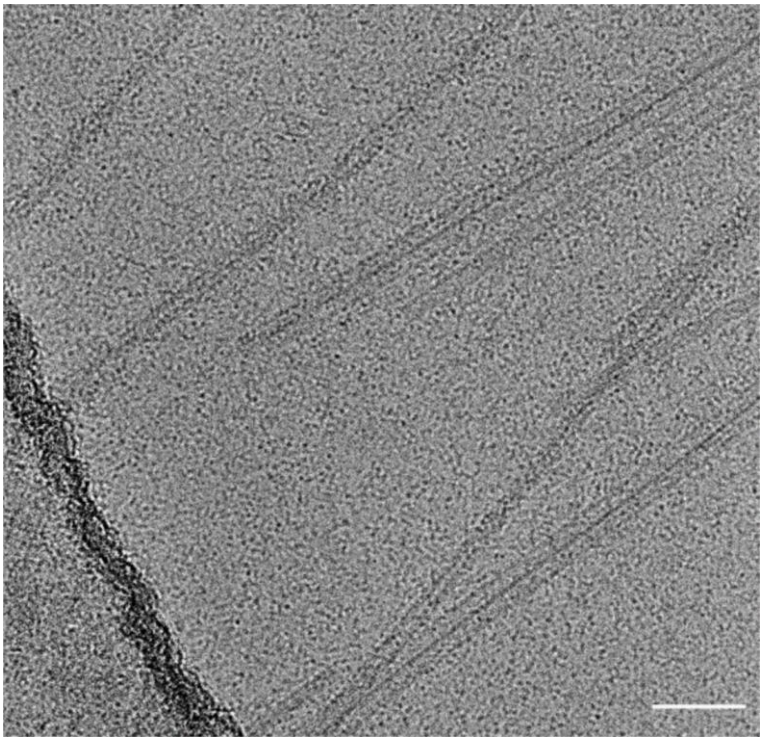

Figure 5.1: Cryo micrograph of αSyn amyloid fibres incubated with WT DNAJB1 in HKMD buffer.
The concentrations of αSyn fibres (monomer concentration) and DNAJB1 were 6 µM and 2.4 µM, respectively. The micrograph was collected by Dr Joe Beton on the in-house Titan Krios microscope operating at 300 kV. Scale bar, 50 nm.

By NMR, it has been reported that DNAJB1 binds to the C-terminal region of αSyn monomers, which is a domain rich in acidic and aromatic residues (residues 123-129, Wentink et al., 2020). Truncating this region prevents DNAJB1 binding to αSyn monomers and amyloid fibres (Wentink et al., 2020). Another NMR study has reported

that DNAJB1 binding sites are composed of hydrophobic β-strands surrounded by polar residues and DNAJB1 interactions are mostly electrostatic (Jiang et al., 2019). Therefore, optimising the buffer by changing the salt concentrations and pH could promote DNAJB1 binding to αSyn amyloid fibres.

A binding assay was used to find buffer conditions that maximise the amount of DNAJB1 bound to the fibres while minimising the unbound fraction. αSyn amyloid fibres were incubated with various concentrations of DNAJB1 in HKMD buffer or in deionised water, followed by centrifugation to separate the pellet from the supernatant (figure 5.2A-B, 20 μM αSyn monomer concentration and 4-12 μM DNAJB1). The pellet contained the insoluble αSyn fibres and bound DNAJB1 as well as aggregated DNAJB1 while the supernatant contained soluble, unbound DNAJB1. A control without fibres was added in each condition to check whether DNAJB1 aggregates in HKMD buffer or deionised water (first condition in each gel of figure 5.2A-B). A faint band was observed in the pellet of each control, confirming the presence of aggregates (figure 5.2A-B). Since the aliquots of DNAJB1 were centrifuged to remove the aggregates before starting the binding assay, the aggregates were formed during the incubation in HKMD buffer or deionised water. Around 15% of DNAJB1 aggregated in the two conditions, showing that water does not promote more DNAJB1 aggregation than the HKMD buffer. When DNAJB1 concentration increases, the total amount of DNAJB1 bound to the fibres also increases, with a larger amount for the different ratios in water (figure 5.2C). This first result would suggest that a molar ratio of 1:0.6 (αSyn:DNAJB1, monomer concentrations) is appropriate. However, the bound fraction of DNAJB1 decreases when DNAJB1 concentration increases (figure 5.2D). This is due to a gradual increase of unbound DNAJB1 that would give a gradually increasing background in cryo micrographs. Therefore, a molar ratio of 1:0.4 (20 μM αSyn monomer

concentration and 8 µM DNAJB1) seems to be a good compromise between efficient binding and a low background. Also, the unbound fraction of DNAJB1 was greatly reduced at all molar ratios in water, confirming improved DNAJB1 binding in this condition.

The differences observed between HKMD buffer and deionised wated could be explained by the ionic strength and pH. Indeed, although the pH of deionised water is supposed to be 7, deionised water can absorb carbon dioxide and form carbonic acid, reducing the pH of deionised water to 5.5. The influence of salt was examined first. DNAJB1 was mixed with αSyn fibres in HKMD buffer lacking potassium chloride, magnesium chloride or both salts (cases 2, 3 and 4 in figure 5.2E-F, 20 µM αSyn monomer concentration and 8 µM DNAJB1). The binding was improved in the buffers without potassium chloride, compared to the HKMD buffer (case 5 in figure 5.2E-F) even reaching the binding observed in deionised water (case 1 in figure 5.2E-F). Based on the standard deviations, the binding was slightly more stable in the condition without salts (case 4 in figure 5.2F). This condition was therefore used to check the effect of the pH between 5.5 and 7.5 with a 0.5 increment (figure 5.2G). The bound fraction of DNAJB1 was almost constant at 50% between pH 5.5 and 7.0 (figure 5.2H), but at pH 7.5 the bound fraction decreased to 32% (figure 5.2H). Since the pH range of HEPES is 6.8 - 8.2, the buffer without salts at pH 7.0 was chosen for the following experiments and called HD buffer.

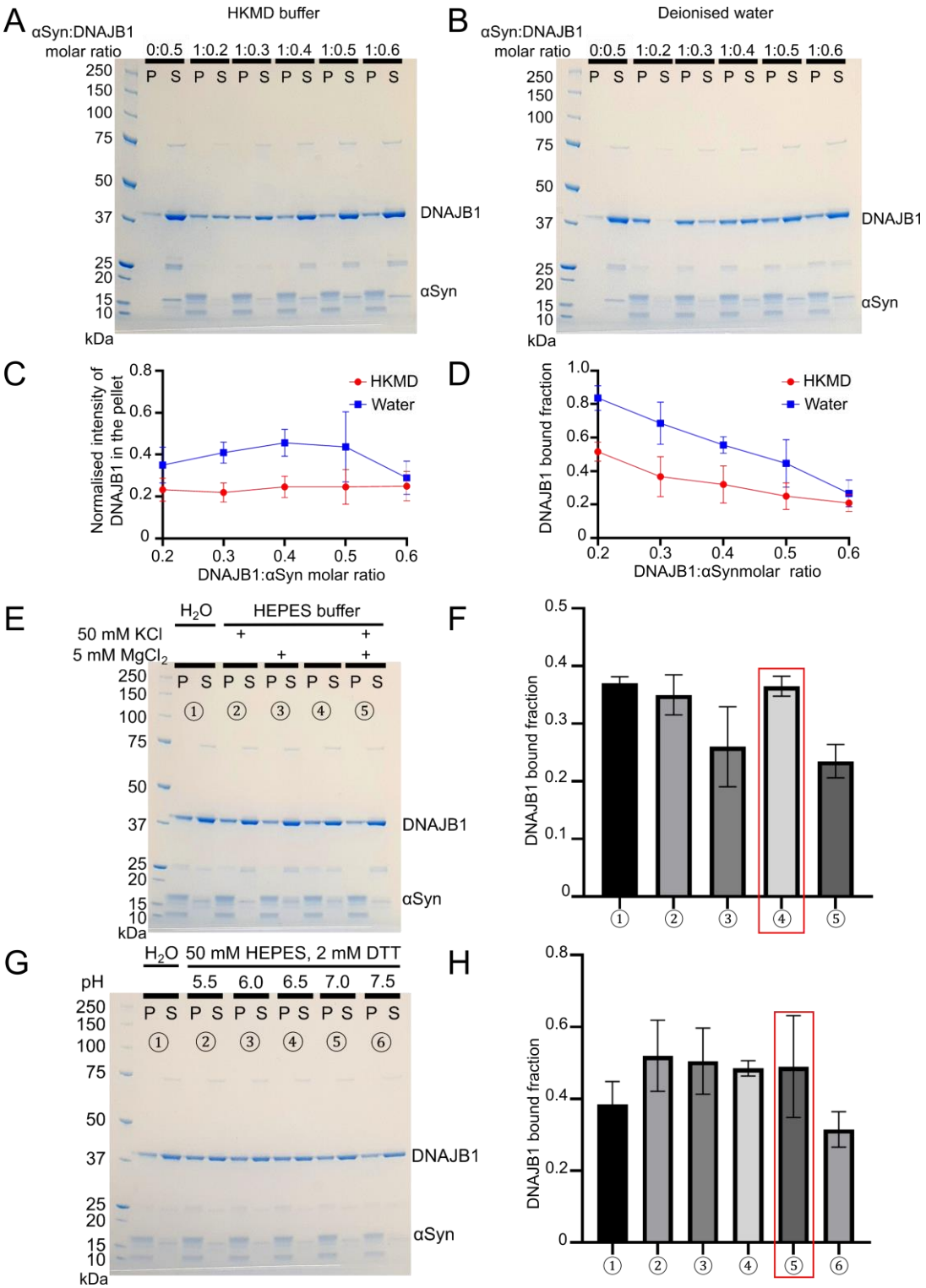

Figure 5.2: Buffer optimisation to promote DNAJB1 binding to αSyn fibres. (A-B) SDS-PAGE showing DNAJB1 binding to αSyn fibres in HKMD (A) or in deionised water (B). The band of DNAJB1 in the pellet is larger when DNAJB1 concentration increases. The concentrations are 20 µM αSyn (monomer concentration) and 4-12 µM DNAJB1. (C-D) Graphs showing the normalised intensity of DNAJB1 in

the pellet (C) and the bound fraction of DNAJB1 (D) in HKMD buffer and in deionised water. The intensity of DNAJB1 was normalised from the sum of the *band* intensities in the control (first condition, without αSyn fibres). (E) SDS-PAGE showing the influence of salts on DNAJB1 binding to fibres in 50 mM HEPES, 2 mM DTT, pH 7.5. The band of DNAJB1 in the pellet is larger when salts are depleted. The concentrations are 20 µM αSyn (monomer concentration) and 8 µM DNAJB1. (F) Histogram showing the bound fraction of DNAJB1 at different salt concentrations. (G) SDS-PAGE showing the DNAJB1 binding in 50 mM HEPES, 2 mM DTT at different pH. The band of DNAJB1 in the pellet is larger when the pH is between 5.5 and 7.0. The concentrations are 20 µM αSyn (monomer concentration) and 8 µM DNAJB1. (H) Histogram showing the influence of pH on the bound fraction of DNAJB1. The red boxes indicate the conditions selected for the cryo-EM experiments. The experiments assessing the influence of the salt concentration and the pH were repeated twice only. In the different gels, P: pellet; S: supernatant and the markers are noted as kDa in size.

This improvement of DNAJB1 binding to αSyn fibres was verified by cryo-EM (figure 5.3). In this new buffer, the fibres display a fuzzy decoration and the background is highly reduced without apparent DNAJB1 aggregates, showing that the αSyn:WT DNAJB1 complex is stabilised in this condition.

Before proceeding with cryo-EM analysis, it was necessary to check that: 1) the binding is reversible when the salts are added back and 2) DNAJB1 is not denatured in the HD buffer. Reversibility was assessed by performing the binding assay with 2 incubations. Three conditions were checked: 2 consecutive incubations in HD buffer (case 3 in figure 5.4A), incubation in HD buffer followed by incubation in HKMD buffer (case 4 in figure 5.4A) and 2 incubations in HKMD buffer (case 5 in figure 5.4A). The concentrations were 20 µM αSyn (monomer concentration) and 8 µM DNAJB1. Finally, two controls were added in which DNAJB1 alone was incubated in HD or HKMD buffer (cases 1 and 2 in figure 5.4A). The two controls display similar bands for

DNAJB1 in the pellet, showing that DNAJB1 does not form more aggregates in one of the buffers. Around 80% of DNAJB1 binds to the fibres in the HD buffer, while it is only 40% in the HKMD buffer (figure 5.4B). When the salts were added back for the second incubation, the final bound fraction of DNAJB1 returned to 40%, showing that the salt effect is fully reversible. Regarding DNAJB1 stability, DNAJB1 and αSyn fibres were pre-incubated for 30 minutes in either HD or HKMD buffer before running a ThT assay in the presence of Hsc70 and Apg2 in the disaggregation buffer (table 2.1, figure 5.4C). Fibres can be disassembled in both conditions. Therefore, the HD buffer does not inactivate DNAJB1 and this condition can be used for cryo-EM of the complex.

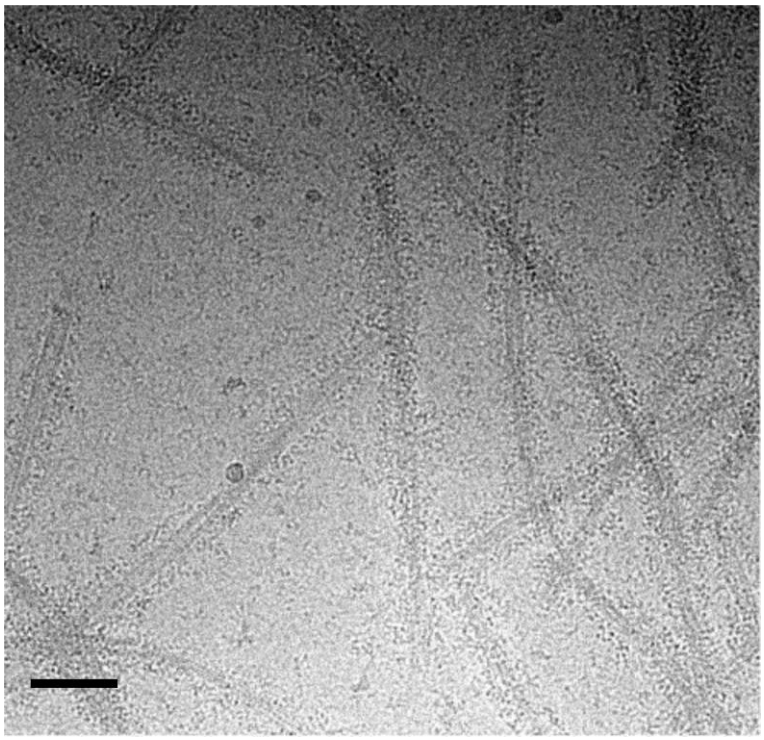

Figure 5.3: Cryo micrograph of αSyn amyloid fibres incubated with WT DNAJB1 in HD buffer.

The concentrations of αSyn fibres (monomer concentration) and DNAJB1 are 6 µM and 2.4 µM, respectively. The micrograph was collected by Dr Joe Beton. Scale bar, 50 nm.

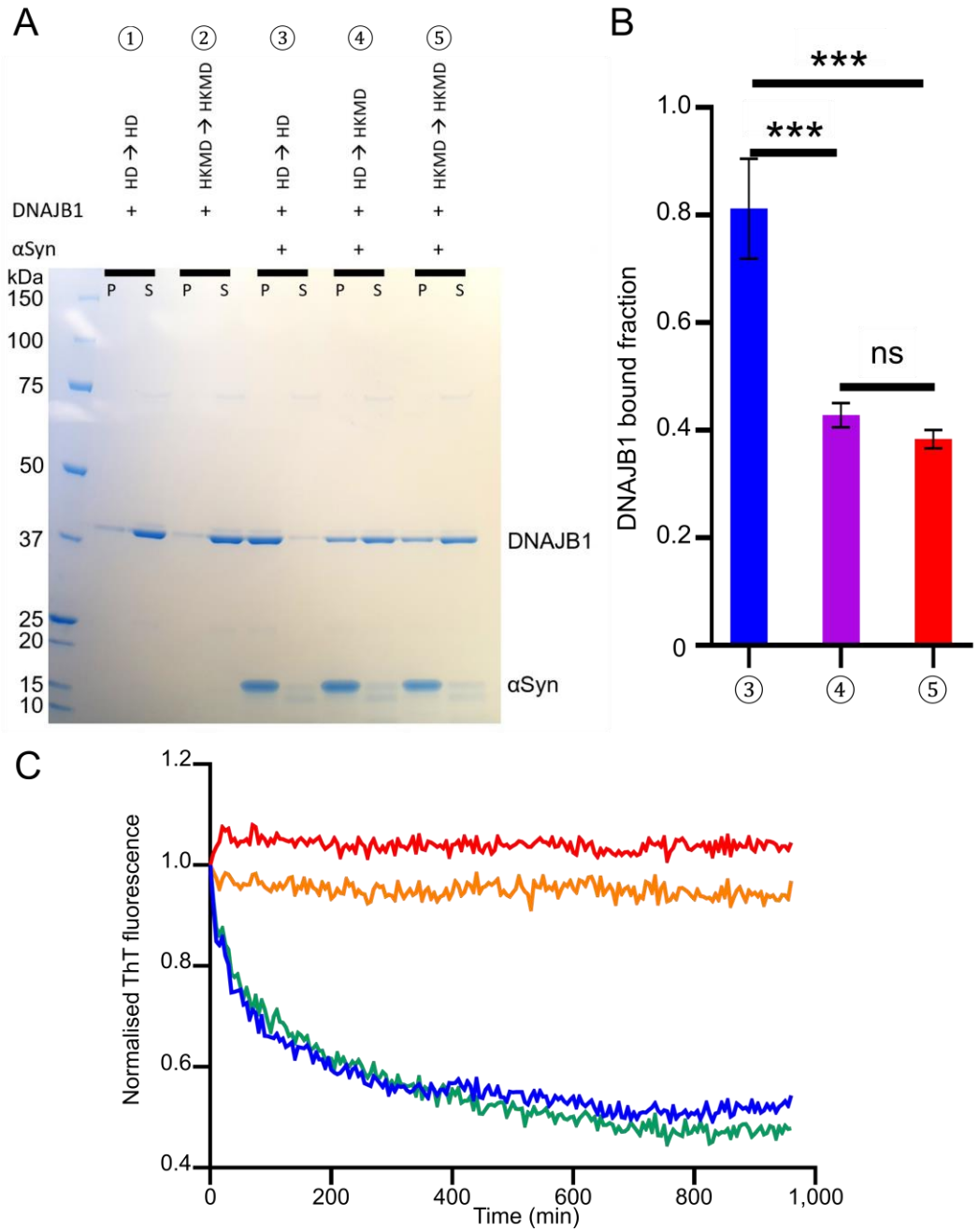

Figure 5.4: Verifications of the HD buffer on DNAJB1 binding and activity.
(A) SDS-PAGE of DNAJB1 binding: DNAJB1 was incubated with or without αSyn fibres, as marked, for 2 consecutive 30-min incubations in HD or HKMD buffer, as noted. The concentrations are 20 μM αSyn (monomer concentration) and 8 μM DNAJB1. The markers are noted as kDa in size. (B) Histogram showing DNAJB1 binding in cases ③, ④ and ⑤ of (A). When the salts are added back for the second incubation (case ④), 40% of DNAJB1 binds to the fibres. A similar fraction is obtained after two incubations in HKMD buffer (case ⑤) whereas 80% of DNAJB1 binds to the fibres after two incubations in HD buffer (case ③), showing that the binding is fully reversible. A one-way ANOVA was performed with Tukey's multiple comparisons

test (***:P<0.001, ns: not significant; N = 3 independent experiments). (C) Disaggregation curves comparing DNAJB1 and αSyn pre-incubated in HKMD (green curve) or HD (blue curve) buffer. Controls in the presence of chaperones without ATP (red curve) or in the presence of ATP without chaperones (orange curve) were also performed.

5.3 3D structure of αSyn:WT DNAJB1 complex

Dr Joe Beton prepared cryo-grids of αSyn amyloid fibres incubated with WT DNAJB1 in the HD buffer, collected ~13,000 movies on the Titan Krios microscope at Birkbeck College (figure 5.3) and processed the data using the helical reconstruction option in RELION 3.1 (Scheres, 2020; Zivanov et al., 2018).

First, Joe Beton reconstructed a high-resolution structure (~ 3.4 Å resolution) of the amyloid fibre without considering DNAJB1 decoration (figure 5.5A). This structure was almost identical to the reported polymorph 2b, with a few additional ordered densities (red circles in figure 5.5A, Guerrero-Ferreira et al., 2019).

Joe Beton also processed the data to study the DNAJB1 in the complex (figure 5.5B-D). The segments of αSyn fibres decorated by DNAJB1 obtained from the 2D classification display the 2 protofilament structure surrounded by an extra density (figure 5.5B). This extra density is characterised by two layers of dots (blue and purple arrows in figure 5.5B) with a ~40 Å repeat between equivalent dots and follows the helical twist of the fibre (figure 5.5B). A peak at ~40 Å is also observed in the power spectrum of 2D classes displaying a strong extra density (figure 5.5C). This extra density was considered as DNAJB1 decoration.

Joe Beton used the aforementioned 2D classes to generate a low-resolution structure of the αSyn fibres decorated by DNAJB1 along one protofilament (figure 5.5D). The DNAJB1 decoration displays a general horseshoe shape, which can be manually fitted

with the *T. thermophilus* DNAJ structure (PDB: 4J80, Barends et al., 2013). The DNAJB1 decoration was regular with a repeat of ~40 Å (figure 5.5B-D). Although DNAJB1 is asymmetrically positioned with one subunit closer to the fibre core, the two binding sites can interact with αSyn disordered C-terminus. Lastly, a gap is visible between the density of the fibre core and the DNAJB1 decoration and could be bridged by the 30 disordered residues, comprised between the fibre core and the binding site for DNAJB1. Indeed, DNAJB1 interacts with residues 123-129 of αSyn whereas the structured region ends at residue 94.

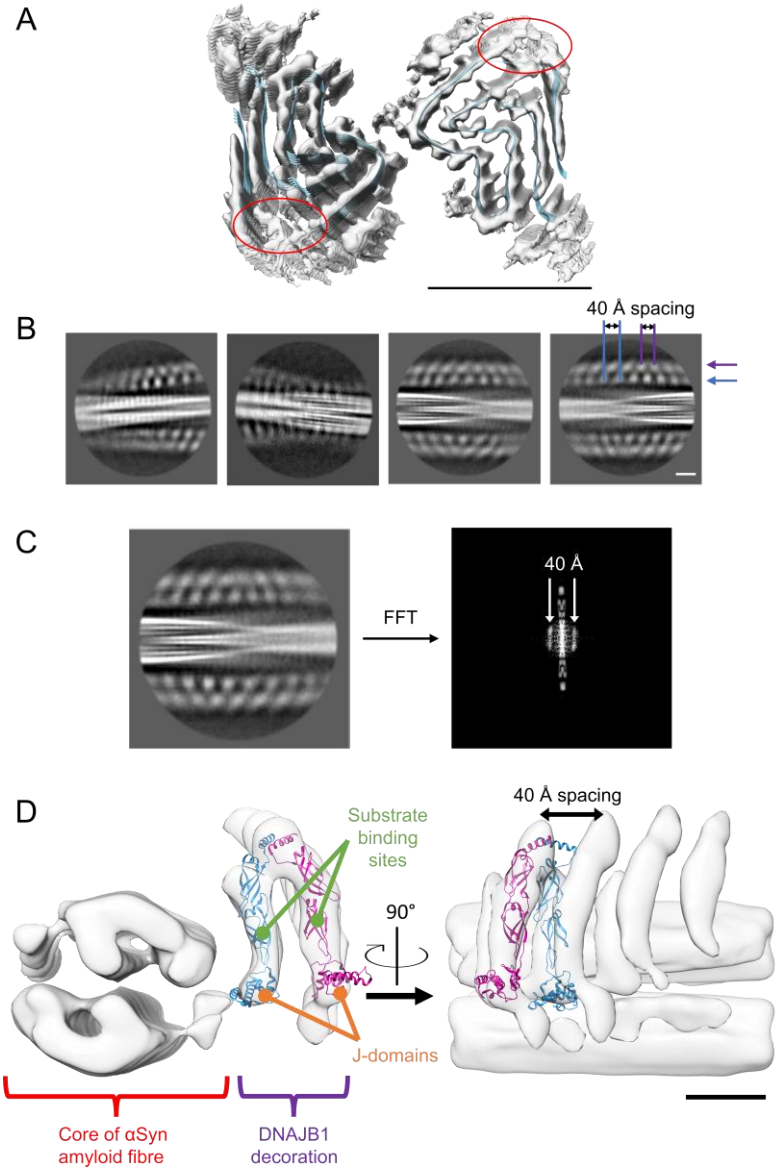

Figure 5.5: Reconstructions of αSyn fibre and αSyn:DNAJB1 complex.

(A) 3D reconstruction of WT αSyn fibre. The map was fitted with the reported polymorph 2b (PDB: 6SST, Guerrero-Ferreira et al., 2019). The red circles indicate the additional ordered densities which were not observed in polymorph 2b. (B) Representative 2D classes of αSyn fibres decorated by WT DNAJB1. The blue and purple arrows highlight the two layers of DNAJB1 features. (C) A representative 2D class and its corresponding power spectrum showing a peak at 40 Å. FFT: Fast Fourier Transformation (D) The refined structure of αSyn fibres decorated by WT DNAJB1. The density for DNAJB1 was manually fitted with the crystal structure of T. thermophilus DNAJ (PDB: 4J80, Barends et al., 2013). The DNAJ decoration shows the 40 Å periodicity. The processing summarised in this figure was performed by Joe Beton. Scale bars, 50 Å.

5.4 Optimising cryo grids for αSyn:ΔJ-DNAJB1 complex

The low resolution of the structure is attributed to the flexibility of the DNAJB1:αSyn complex. In an attempt to reduce the flexibility of the complex and in order to examine the influence of the J-domain, I studied the complex formed of αSyn amyloid fibres and ΔJ-DNAJB1.

As mentioned in the previous chapter, the purified protein of ΔJ-DNAJB1 mutant was provided by Dr Rina Rosenzweig's group.

Before making cryo grids of this sample, I checked that the optimised buffer also maximises ΔJ-DNAJB1 binding to the fibres without causing irreversible changes (figure 5.6). Two controls were carried out in which ΔJ-DNAJB1 alone was incubated in HD or HKMD buffer (cases 1 and 2 in figure 5.6, respectively). Again, ΔJ-DNAJB1 does not form more aggregates in one of the buffers. Three further conditions were tested: a first condition with 2 consecutive incubations in HD buffer (case 3 in figure 5.6A-B), a second condition in which the salts were added back for the second incubation (case 4 in figure 5.6A-B) and a third condition with 2 incubations in HKMD buffer (case 5 in figure 5.6A-B). The concentrations were 20 μM αSyn (monomer concentration) and 8 μM ΔJ-DNAJB1. In HD buffer, 92% of ΔJ-DNAJB1 is bound to the fibres (case 3 in figure 5.6A-B). The bound fraction drops to 50% when the salt are added back, a level similar to the two incubations in HKMD buffer (cases 4 and 5 in figure 5.6A-B, respectively), confirming the reversibility of the binding. Since the J-domain is missing in this mutant, ΔJ-DNAJB1 cannot stimulate the ATPase activity of Hsc70. Therefore, the activity assay could not be checked but it was assumed that ΔJ-DNAJB1 was not denatured in HD buffer since WT DNAJB1 is not. Lastly, cryo-grids of the ΔJ-DNAJB1:αSyn complex at a 1:0.4 molar ratio in HD buffer were imaged by

cryo-EM to confirm the formation of the complex (figure 5.6C). As for the αSyn:WT DNAJB1 complex, the fibres displayed a fuzzy decoration and the background was low.

Before collecting a data set of this complex, cryo grids had to be optimised, because αSyn fibres decorated by ΔJ-DNAJB1 tended to form large clusters composed of densely packed and tangled fibres (figure 5.7A). The presence of these clusters prevents the picking of isolated fibre segments required for image processing. The clusters also retain buffer, leading to thicker ice and lower contrast. The fibres were therefore sonicated before incubation with ΔJ-DNAJB1 to solve these two problems. This led to a more uniform distribution of the fibres on the grid and a significant reduction of cluster formation (figure 5.7B). The vitrification robot used for the grid preparation also strongly impacted the global quality of the ice thickness (figure 5.7C-D). The ice thickness was very variable when the grids were prepared using the Vitrobot (figure 5.7C). In contrast, the back-blotting option available of the Leica GP2 provided grids with a more consistent distribution of thin ice suitable for the acquisition of a large data set (figure 5.7D).

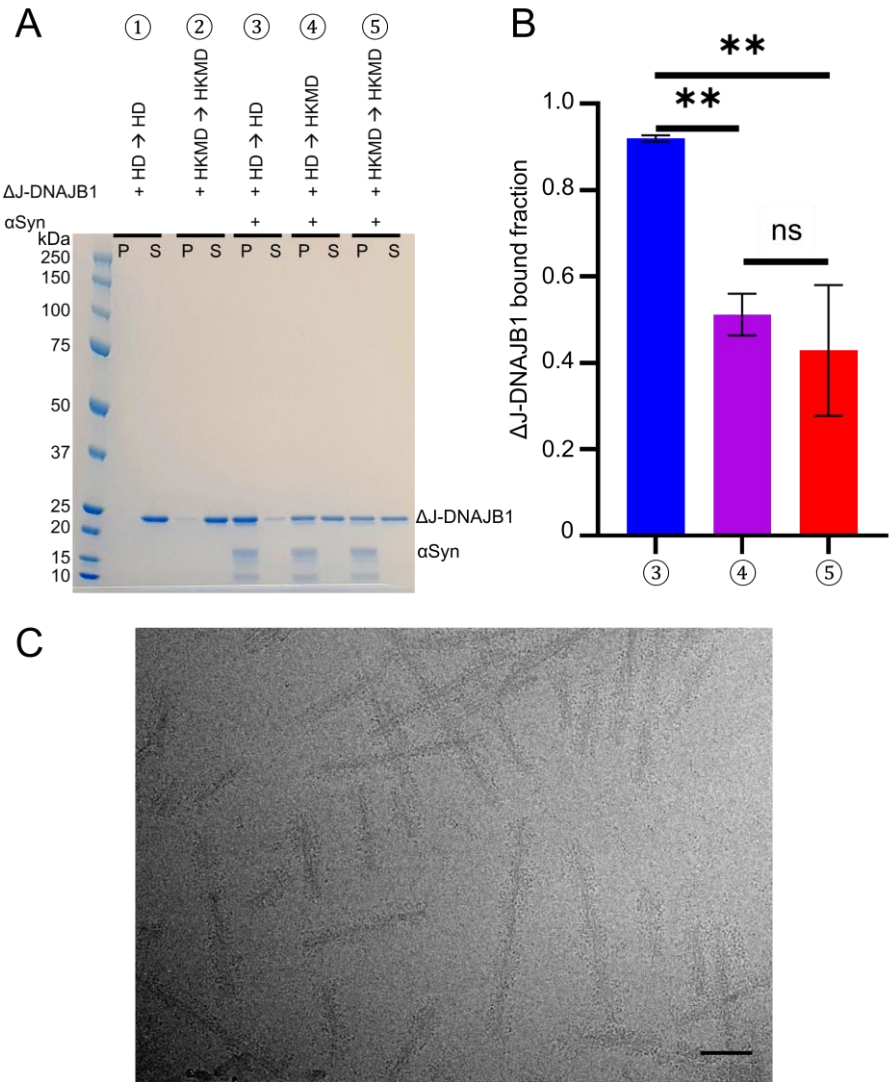

Figure 5.6: ΔJ-DNAJB1 binding to the fibres.

(A) SDS-PAGE of ΔJ-DNAJB1 binding: DNAJB1 was incubated with or without αSyn fibres, as marked, for 2 consecutive 30-min incubations in HD or HKMD buffer, as noted. The concentrations are 20 μM αSyn (monomer concentration) and 8 μM ΔJ-DNAJB1. The markers are noted as kDa in size. (B) Histogram showing ΔJ-DNAJB1 binding in cases ③, ④ and ⑤ of (A). When the salts are added back for the second incubation (case ④), 50% of ΔJ-DNAJB1 binds to the fibres. A similar fraction is obtained after two incubations in HKMD buffer (case ⑤) whereas 90% of ΔJ-DNAJB1 binds to the fibres after two incubations in HD buffer (case ③), showing that the binding is fully reversible. A 1-way ANOVA was performed with Tukey's multiple comparisons test (**:P<0.01, ns: not significant; N = 3 independent experiments). (C) Cryo micrograph of αSyn amyloid fibres incubated with ΔJ-DNAJB1 in HD buffer. The concentrations are 6 μM αSyn fibres (monomer concentration) and 2.4 μM ΔJ-DNAJB1. Scale bar, 50 nm.

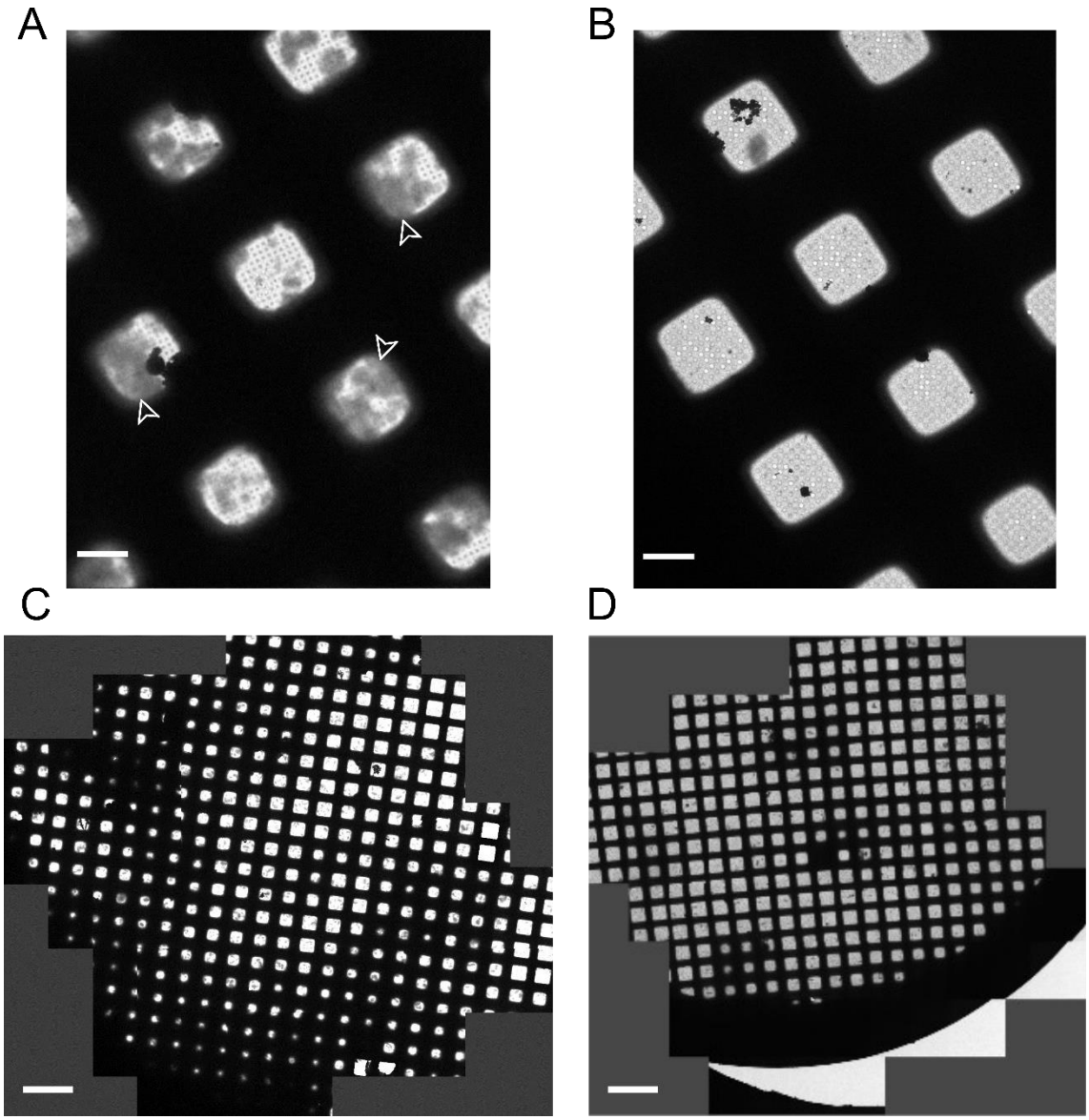

Figure 5.7: Optimisation of the cryo-grids.

(A) Low-magnification micrograph of non-sonicated αSyn amyloid fibres incubated with ΔJ-DNAJB1 in HD buffer. The white arrows highlight large aggregates of fibres. (B) As in (A) but with sonicated fibres. Scale bars, 50 µm. (C) Montage at low magnification of a grid prepared on the Vitrobot. (D) As in (C) but prepared on the Leica GP2. Scale bars, 150 µm.

5.5 Image processing of αSyn fibres

A data set of the optimised sample (αSyn:ΔJ-DNAJB1, 1:0.4 molar ratio in HD buffer) was collected using the Titan Krios microscope at Birkbeck college (figure 5.6C). The data set was pre-processed (motion correction, CTF estimation and manual inspection) as described in section 2.6.5.1 of the materials and methods chapter. The coordinates of decorated amyloid fibre segments were determined using SPHIRE-crYOLO and 911,478 particles were extracted in RELION 3.1 with a box size of 420^2 pixels (445^2 Å) and binned by a factor 3.3 to yield a box size of 128^2 pixels.

The particles were subjected to three consecutive rounds of reference-free 2D classification in RELION 3.1 to select the fibre segments displaying a regular ΔJ-DNAJB1 decoration (figure 5.8A). A first aim was to determine the fibre structure without resolving ΔJ-DNAJB1. Therefore, the corresponding particles (129,922 particles) were re-extracted without binning and subject to two additional reference-free 2D classifications with a regularisation parameter of 1 and then 8 and a cylindrical mask of 140 Å to exclude ΔJ-DNAJB1 density from the alignment (figure 5.8B). The regularisation parameter corresponds to the relative weights of experimental data and the prior information. By increasing the regularisation parameter, the 2D class averages display sharper features (Scheres, 2012b). In addition, using a higher regularisation parameter helps with alignment and separation of the cross-β repeats (helical rise) in amyloid fibres (Fitzpatrick et al., 2017). After the 2D classification with a regularisation parameter of 8, most of the 2D class averages displayed the cross-β repeat of 4.8 Å (figure 5.8B). A peak at 4.8 Å was also observed in the corresponding power spectra, confirming the accurate alignment of the particles (figure 5.8C).

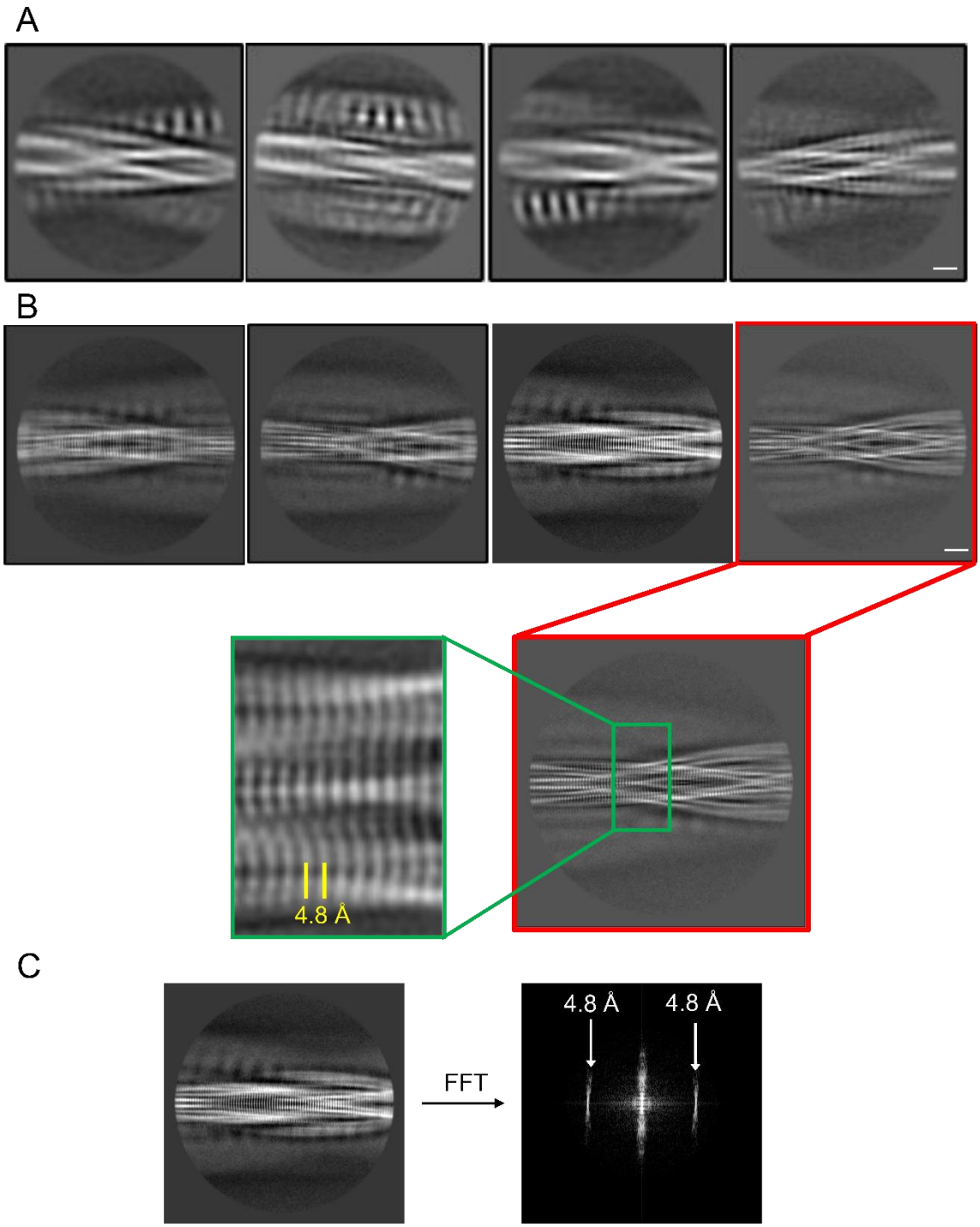

Figure 5.8: 2D classification of αSyn amyloid fibres decorated by ΔJ-DNAJB1.
(A) Representative 2D classes at low resolution displaying αSyn amyloid fibres and ΔJ-DNAJB1 decoration. (B) 2D classes of similar orientations at a higher resolution showing the cross-β repeat of 4.8 Å. (C) One 2D class at high resolution and its corresponding power spectrum showing a peak at 4.8 Å. FFT: Fast Fourier Transform. Scale bar, 50 Å.

An initial reprojection of the fibre was then calculated using the amyloid fibre reconstruction toolbox in RELION 3.1 (Scheres, 2020). Since all the *in vitro* reported structures of αSyn amyloid fibres have C2 helical symmetry, this symmetry was applied for this step. The pitch of the fibre, which is the distance corresponding to a 180° rotation of the fibre, is determined by trial and error during this step. With a pitch of 620 Å, the lateral reprojection of the fibre did not display missing segments or overlap (figure 5.9A). An initial cross section calculated at this stage shows that the secondary structure of the protofilaments can already be coarsely determined (figure 5.9B). Additional densities were also observed (white arrows in figure 5.9B).

Since the cross section was promising, 3D classification was omitted and the initial reprojection was directly used for 3D refinement followed by postprocessing and CTF refinement. This cycle (3D refinement, postprocessing and CTF refinement) was repeated a second time to yield the final postprocessed map.

After postprocessing, the final map displayed a left-handed fibre formed of 2 protofilaments characterised by a helical twist of -1.33° and a helical rise of 4.74 Å (figure 5.10A). The resolution was estimated at 3.2 Å using the 0.143 criterion for the FSC between corrected half-maps (figure 5.10B). The FSC of the phase randomised half-maps is very close to 0 at this resolution, indicating the absence of overfitting from noise (Scheres and Chen, 2012).

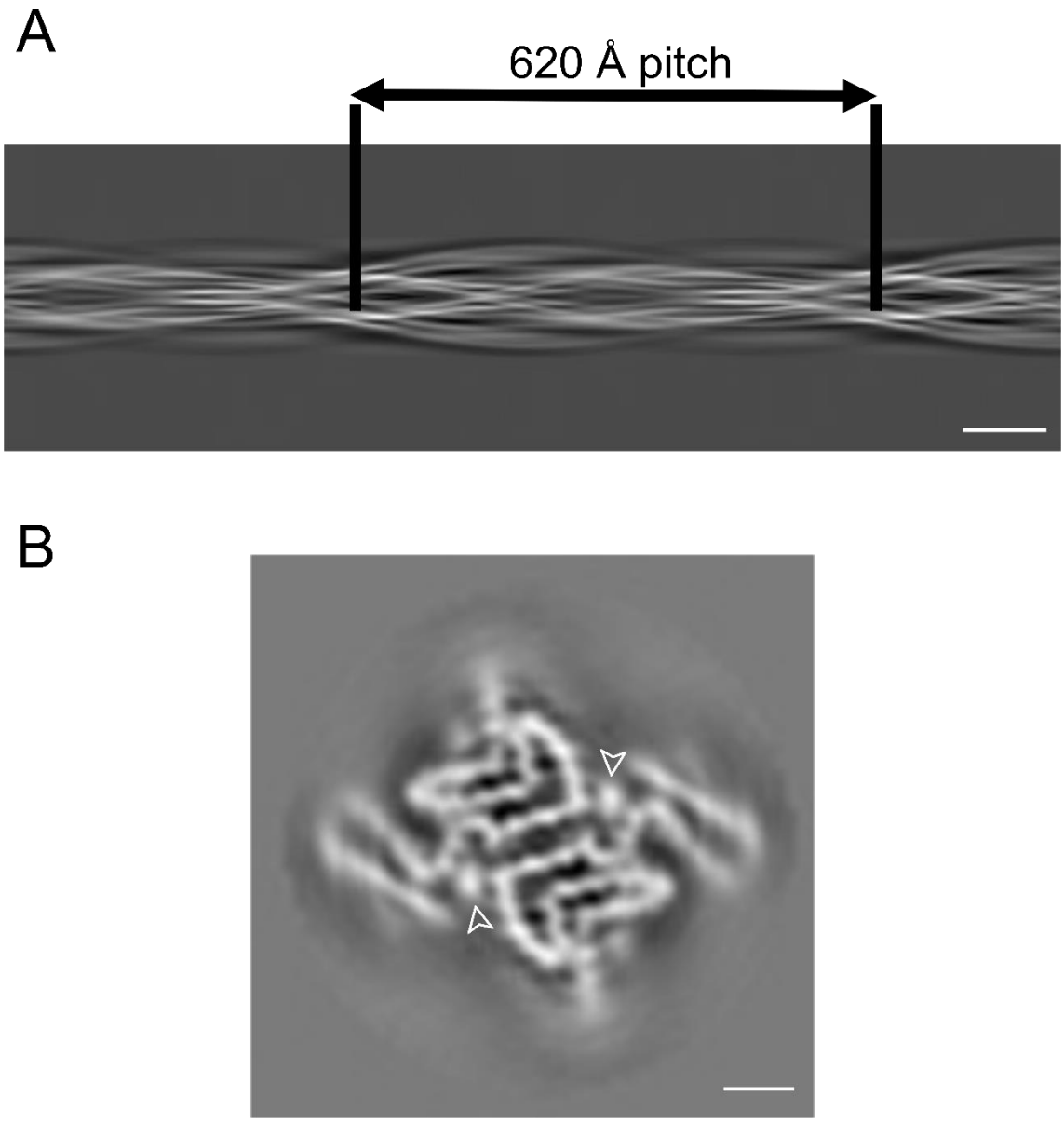

Figure 5.9: Initial reprojections of the αSyn amyloid fibre.

(A) Side view of the initial reprojection. The pitch (crossover repeat) was determined to be ~620 Å. Scale bar, 100 Å. (B) Initial reprojection of the cross section displaying the two protofilaments of the amyloid fibre. The secondary structure of αSyn is visible. The white arrows indicate the presence of an extra density. Scale bar, 20 Å.

One protofilament was fitted in COOT with the reported structure of the N-terminally acetylated WT αSyn structure (figure 5.10C, PDB: 6OSJ, Emsley and Cowtan, 2004; Ni et al., 2019). The protofilament appears to be composed of 8 β-strands (called β1 to β8 in figure 10.D) in the classical Greek key conformation which was previously observed in several *in vitro* αSyn fibre structures (figure 1.4). However, an additional hairpin is also partly ordered for the N-terminus of αSyn, a region that is usually disordered. In addition, an extra density seems to interact with the lysines at residues 43 and 45 (and the lysine at position 58 of the other protofilament, figure 5.10C). Interestingly, such an extra density has already been observed at the same position in reported structures which also had a partly ordered N-terminus (Guerrero-Ferreira et al., 2019, 2018; Schweighauser et al., 2020). It has been suggested that this extra density could correspond to phosphate ions based on their size and charge. This could also be the case here since the fibres were formed in a phosphate buffer, suggesting a possible role for phosphate ions in αSyn aggregation. Another possibility that could explain the density of the ordered N-terminus would be the binding of ΔJ-DNAJB1 to the C-terminus of αSyn amyloid fibres, preventing long-range interactions between the N- and C- termini. The N-terminus could then be partly folded. However, such an additional density for the N-terminus is not observed in the structure of αSyn fibres interacting with WT DNAJB1 (figure 5.5A). Therefore, this hypothesis seems unlikely.

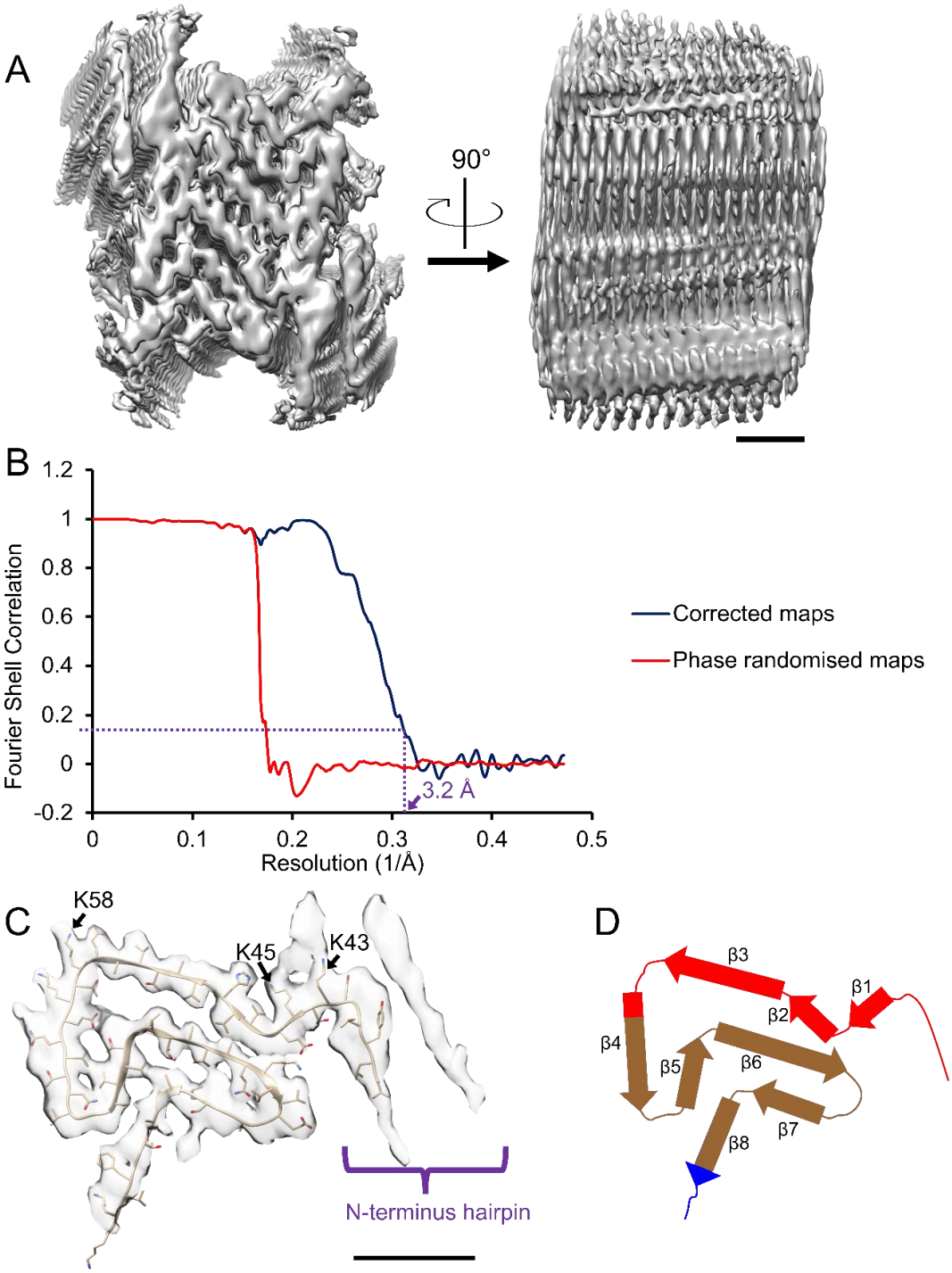

Figure 5.10: 3D structure of the αSyn fibre.

(A) The cross section and the side view of the final 3D reconstruction of the αSyn fibre. Scale bar, 20 Å. (B) The gold standard FSC curves of the reconstruction displayed in (A). The red and blue curves correspond to the phase randomised map and corrected map curves, respectively. (C) The reconstruction is fitted using the reported N-acetylated WT αSyn structure (PDB: 6OSJ, Ni et al., 2019). (D) Cartoon displaying the 8 fitted β-strands.

5.6 Image processing of αSyn:ΔJ-DNAJB1 complex

Unlike WT DNAJB1 whose decoration is characterised by two layers of dots in 2D class averages (figure 5.11A), ΔJ-DNAJB1 produces a projection with blurred radial stripes (figure 5.11B). This difference could arise from the absence of the J-domain, which is half the molecular weight of DNAJB1 subunit (~20 kDa). ΔJ-DNAJB1 features are blurred due to likely the flexibility of the complex and the heterogeneity of ΔJ-DNAJB1 binding to the fibres with a potential binding site every 4.8 Å, leading to an alignment which is dominated by αSyn fibre. This hypothesis was confirmed by comparing similar orientations of αSyn fibres at different resolutions (figure 5.12A). At a high resolution, the fibre is well aligned with a visible cross-β repeat of 4.8 Å. However, ΔJ-DNAJB1 density is very blurry and dim. Conversely, when the fibre alignment is only coarse, ΔJ-DNAJB1 decoration is more visible with a ~40 Å repeat (figure 5.12A). These observations were confirmed by power spectra of fine and coarse aligned 2D classes (figure 5.12B and C, respectively). A peak at ~40 Å was present only when the fibres were coarsely aligned with a loss of high-resolution features. To get enough orientations displaying ΔJ-DNAJB1 decoration, the particles were kept binned at a factor of 3.3 (figure 5.8A).

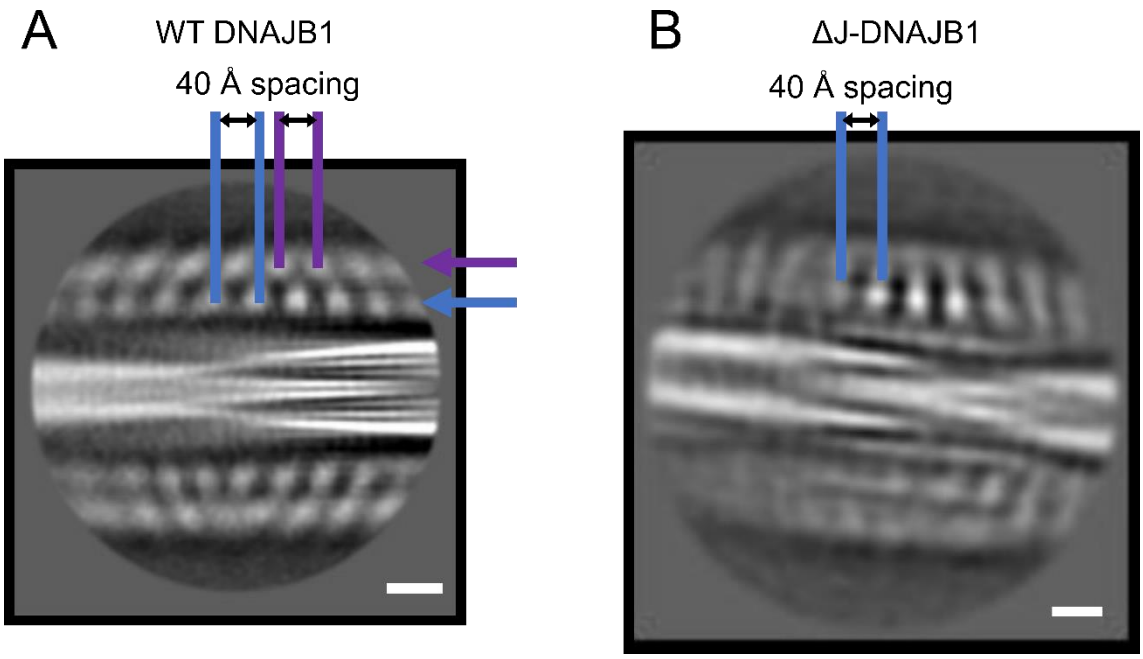

Figure 5.11: Representative 2D classes of WT αSyn fibre decorated with WT DNAJB1 (A) or ΔJ-DNAJB1 (B).

Scale bars, 50 Å.

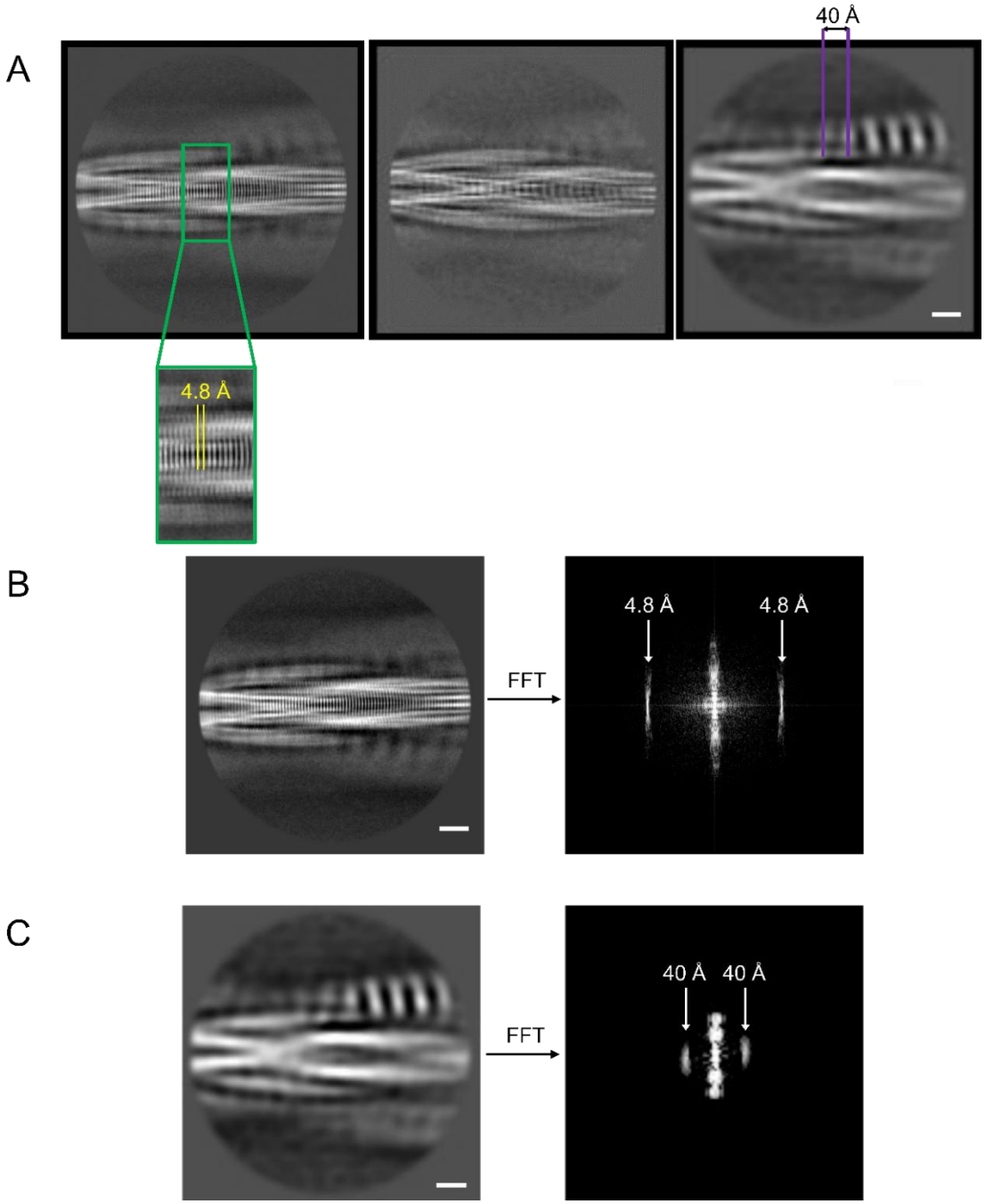

Figure 5.12: The compromise between resolution and ΔJ-DNAJB1 decoration in 2D classification.

(A) 2D classes of the same fibre orientation at three different resolutions. ΔJ-DNAJB1 repeat is only distinguishable when the fibre alignment is coarse. (B) A 2D class at high resolution and its corresponding power spectrum displaying the cross-β repeat at 4.8 Å. ΔJ-DNAJB1 feature at 40 Å is not visible. (C) As in (B) but with a coarser fibre alignment. The cross-β repeat is not visible but 40 Å ΔJ-DNAJB1 decoration is visible in the 2D class and in the corresponding power spectrum. FFT: Fast Fourier Transform. Scale bars, 50 Å.

An initial reprojection of the decorated fibres was calculated using the amyloid fibre reconstruction toolbox in RELION 3.1 (Scheres, 2020). The main advantage was that the pitch was already determined from the high-resolution structure of the fibres (~620 Å). A drawback is that the helical rise is set at 4.75 Å at this stage, which does not correspond to the ΔJ-DNAJB1 repeat. This leads to artefacts in the initial model (figure 5.13). In a first step, all the 2D classes are aligned to get the side view of the fibre (figure 5.13A). From this alignment, the initial side reprojection and cross section are calculated (figure 5.13B-C, respectively). ΔJ-DNAJB1 density was also considered as part of the fibre density, leading to the merging of DNAJB1 decoration and the disappearance of the ~40 Å ΔJ-DNAJB1 repeat (figure 5.13B in comparison to 5.13A). This also led to a very dim density of ΔJ-DNAJB1 in the cross section (figure 5.13C). Lastly these defects were also present in the initial model which is calculated from the initial reprojections (side view and cross section, figure 5.13D).

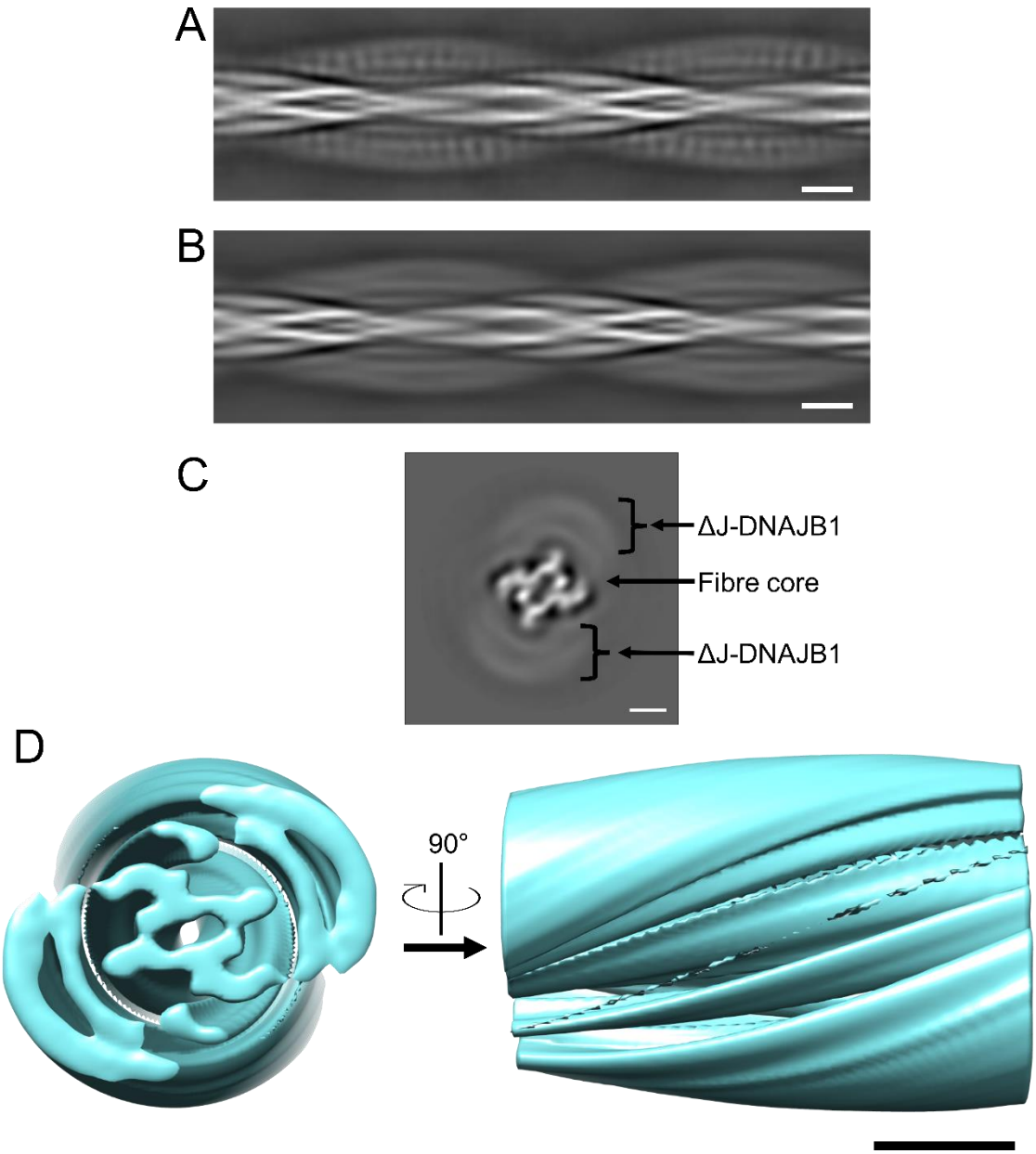

Figure 5.13: The initial reprojection and model of the αSyn:ΔJ-DNAJB1 complex. (A) The initial alignment of the 2D class averages performed by RELION. Scale bar, 100 Å. (B) The side view of the initial reprojection. Scale bar, 100 Å. (C) The initial cross section. Scale bar, 50 Å. (D) The resulting initial model. Scale bar, 100 Å.

The 3D classification was then performed with 4 classes to sort out different potential conformations of the complex (figure 5.14). The helical rise and twist were manually set to 40 Å and -11.6° and C2 symmetry was applied to favour the alignment of ΔJ-DNAJB1. It was not possible to refine these values because the density of ΔJ-DNAJB1 was not improved. Among the four classes, only two of them display a horseshoe-like shape for ΔJ-DNAJB1 density (classes 3 and 4 in figure 5.14). However, the fourth class also displays strong stripes connecting ΔJ-DNAJB1 repeats whereas this feature is more attenuated in the third class (side views in figure 5.14). Therefore, the third class was chosen for 3D auto refinement. No symmetry was imposed at this step. After refinement, there is decoration on the two protofilaments but only one side had a clearer density with a horseshoe-like shape (figure 5.15A). To check whether the subunit density is consistent with the structure of ΔJ-DNAJB1, the crystal structure of DNAJB1 lacking the J-domain and the G/F linker (figure 5.15B, PDB: 3AGY, Suzuki et al., 2010) was docked into the density and showed a reasonable match.

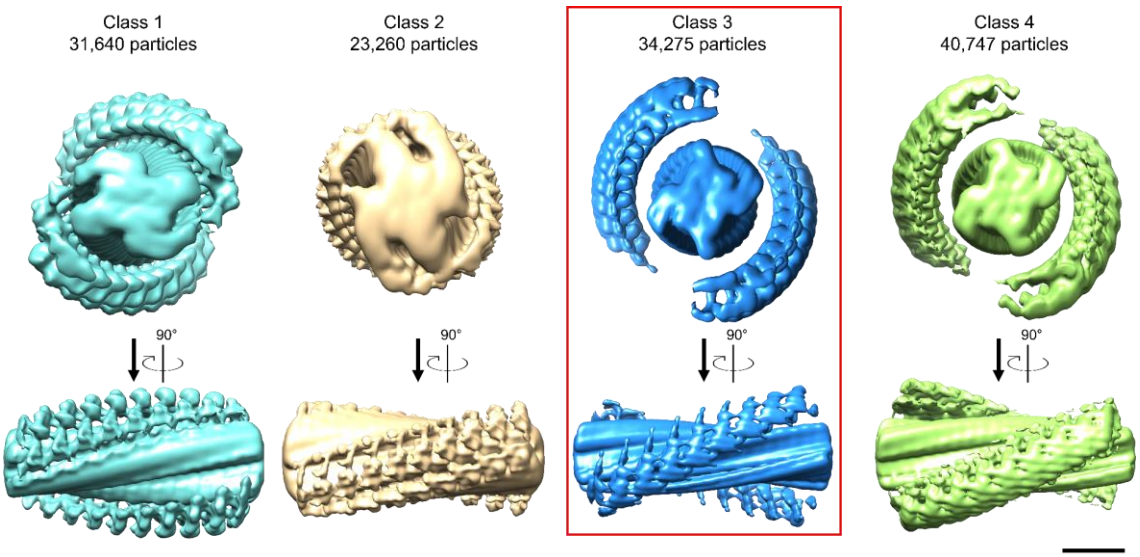

Figure 5.14: The 3D classification of the αSyn:ΔJ-DNAJB1 complex.
The red box indicates the 3D class which was chosen for 3D refinement. Scale bar, 100 Å.

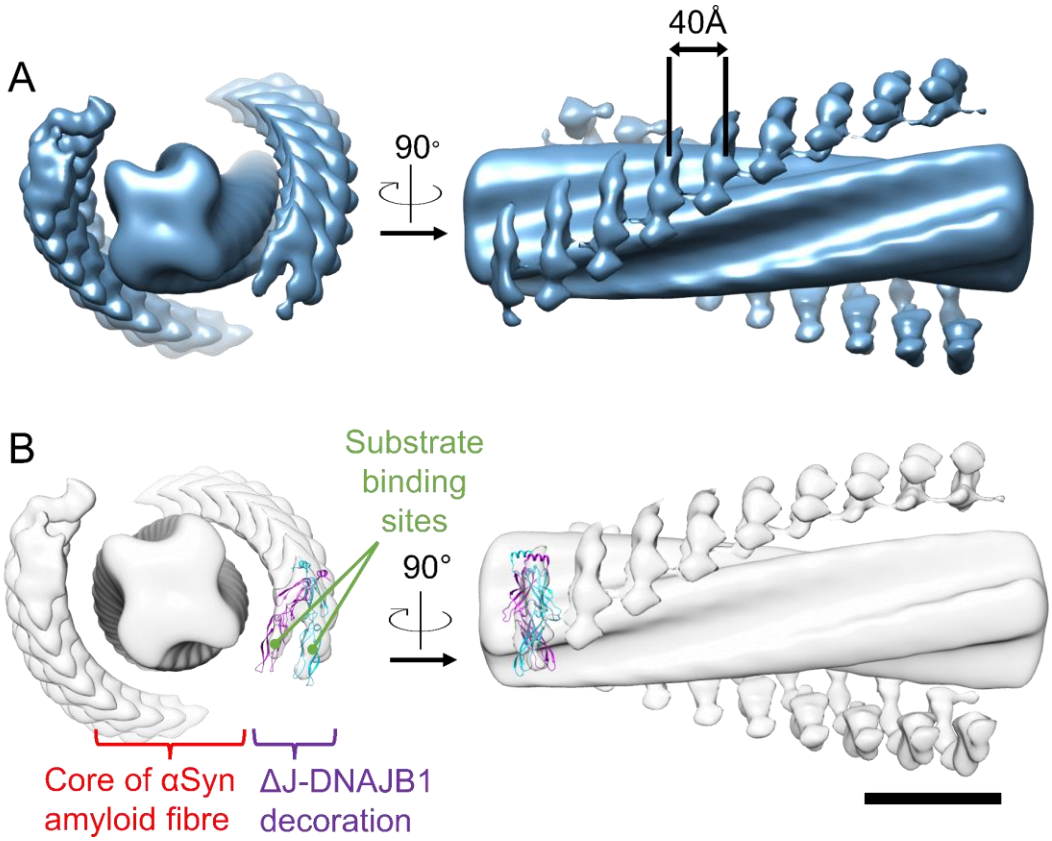

Figure 5.15: Final 3D reconstruction of the αSyn:ΔJ-DNAJB1 complex.
(A) Cross section and side view of the 3D refined reconstruction. The ΔJ-DNAJB1 repeat is ~40 Å. (B) The ΔJ-DNAJB1 decoration matches the shape and the size of the crystal structure of the human truncated DNAJB1 lacking the J-domain and the G/F linker (PDB: 3AGY, Suzuki et al., 2010). Scale bar, 100 Å.

5.7 Conclusion

In this chapter, I have explained how I optimised the buffer by reducing the salt concentration and pH to promote WT DNAJB1 or ΔJ-DNAJB1 binding to αSyn amyloid fibres. Joe Beton and I obtained cryo-EM reconstructions of these complexes, which give the first structural view of human DNAJ proteins bound to amyloid fibres. Although the information is limited due to the low resolution of the structures, the pattern of DNAJB1 binding can be identified. DNAJB1 binds to αSyn amyloid fibre with a ~40 Å repeat and its J-domain is not involved in this binding. This observation is consistent with previously reported decoration observed on negative stain tomograms

(figure 1.10D, Gao et al., 2015) Once bound, DNAJB1 is tilted and its orientation is unexpectedly not symmetrical to the fibre, with one subunit closer to the fibre. But both subunits of the dimer are close enough to interact with the flexible C-terminus of αSyn. Although the resolution is low, similar binding was observed with two different DNAJB1 proteins and two different polymorphs of αSyn amyloid fibres, supporting the reliability of the findings. In addition, a new conformation of WT αSyn amyloid has been identified. In this new fold, the N-terminus of αSyn is partly ordered and forms a hairpin. An extra density, which could correspond to phosphate ion, is also observed and could mediate αSyn aggregation via the folding of the N-terminus.

6. Discussion and future work

In this chapter, I will first discuss the main results presented in this thesis, their limits and their implications in the context of the current literature. Then, I will present some suggestions of future experiments that could be conducted in order to continue this work.

6.1 Insights into the aggregation of αSyn in yeast and its interactions with lipids

αSyn can adopt a broad range of aggregates *in vitro*, hindering identification of the toxic species. Moreover, cellular studies are often limited to fluorescence approaches (although recent EM studies are beginning to give structural information on αSyn inclusions in cells). The results presented in this thesis on the aggregation of αSyn in yeast cells using two complementary cryo-EM techniques (CEMOVIS and FIB-milling) provide new structural information which are consistent with reported observations.

6.1.1 The cytosolic inclusions are mainly composed of vesicles and lipid droplets

In our study, αSyn aggregation is associated with lipid membranes and vesicles. Initially, GFP-tagged αSyn colocalises at the plasma membrane with tubulated ER (figures 3.4 and 3.5). It has been shown that αSyn can block ER to Golgi vesicular trafficking in yeast, leading to ER stress (Cooper et al., 2006). But no direct association of αSyn with the ER has been observed. The *in vitro* experiments confirmed that αSyn can induce the tubulation of liposomes (figure 3.8), as previously reported (Varkey et al., 2010). Therefore, it is possible that αSyn also promotes ER tubulation at the plasma membrane in yeast. Cytosolic inclusions composed of vesicles and lipid droplets are

formed after a longer period of expression (figures 3.4 and 3.5). These observations are also consistent with reported studies. αSyn overexpression in yeast leads to the disruption of vesicle trafficking and the formation of vesicle clusters (Soper et al., 2008). The association of clustered vesicles with αSyn aggregates was also the most frequent type of cellular inclusion found in PD post-mortem patient brain sections (only 17% of the inclusions show filamentous aggregates, Shahmoradian et al., 2019). LBs are lipid-rich inclusions composed of amorphous aggregates surrounded by mitochondria. Interestingly, in our study, αSyn fluorescence frequently overlapped mitochondria found at the periphery of cytosolic inclusions in the FIB-milled lamellae but not in the vitreous sections because it has never been possible to clearly recognise mitochondria in the CEMOVIS data. Since the correlation between the fluorescence signal and the EM tomogram was more certain in the CEMOVIS data, the question remains whether αSyn aggregation is associated with its interactions with mitochondria in yeast. Lastly, lipid droplets were present in the cytosolic inclusions, in agreement with a previous report showing the accumulation of lipid droplets in the cytoplasm of yeast when αSyn is overexpressed (Outeiro and Lindquist, 2003). However, alternate theories could explain their accumulation. On one hand, the lipid droplets could play a role in the aggregation and toxicity of αSyn. Indeed, αSyn can interact with lipid droplets *in vitro* and in cells and these interactions can intervene in αSyn oligomerisation (Cole et al., 2002; Delacotte et al., 2013). On the other hand, the presence of lipid droplets in the inclusions could be the hallmark of a cell response. For instance, in yeast, lipid droplets can produce a sterol derivative which intervenes in the clearance of cytosolic inclusions (Moldavski et al., 2015). Lastly, the presence of lipid droplets could be the sign that the cellular response is overwhelmed. In mammalian cells, lipid droplets accumulates in the cytoplasm when chaperone-mediated autophagy

is blocked (Kaushik and Cuervo, 2015). Thus, although the observations provide new structural information about αSyn aggregation, their impact on understanding the aggregation process is limited. Distinguishing the features which are related to toxicity from the ones which are related to other cell responses is not currently possible.

6.1.2 Amyloid fibres are not present in the inclusions

A striking result in our study is the absence of amyloid fibres in the cytosolic inclusions (figures 3.4 and 3.5). Instead, amorphous aggregates are formed and yeast cells die 16h after αSyn induction (figure 3.1). This highlights an important detail about the αSyn toxicity which does not require the presence of amyloid fibres, although the toxic species remain unknown (small oligomer, transient species). Different hypotheses could explain the absence of amyloid fibres. The first reason is the construct used in our study, which had a GFP tag at the C-terminus of αSyn. However, it is known that amyloid fibre formation and structure are mediated by the C-terminus of αSyn (Ni et al., 2019; Van Der Wateren et al., 2018). Therefore, the GFP tag could block fibre formation in yeast. A structural study showing αSyn amyloid fibres in cytosolic bodies in neurons supports this hypothesis (Trinkaus et al., 2021). This study also showed that the inclusions contained clustered lipid membranes but there was no direct interaction between the membranes and the fibres. However, a few details limit the interpretation of these results. First, an EGFP tag was added to the N-terminus of αSyn. The addition of this tag could have prevented αSyn interaction with lipids since the N-terminus of αSyn is known to anchor to lipid membranes (Fusco et al., 2014). In addition, pre-formed fibres were used as seeds to trigger the fibril formation in neurons. The presence of fibres could have therefore been artificially promoted by the seeding. Lastly, as discussed above, cytosolic inclusions composed of crowded organelles and vesicles have been observed in yeast and human post-mortem brain sections (Shahmoradian et

al., 2019; Soper et al., 2008). Taken together, these findings support the results obtained in this thesis showing the absence of amyloid fibres as characteristic of αSyn aggregation in yeast.

Recent theories about the phenomenon of liquid-liquid phase separation involved in protein aggregation and protein physiological function could provide new perspectives on αSyn aggregation. Tau and huntingtin proteins can undergo liquid-liquid phase separation *in vitro* and in cells (Ambadipudi et al., 2017; Peskett et al., 2018). Huntingtin can undergo a liquid to solid conversion to form fibrillar assemblies from liquid droplets (Peskett et al., 2018). A similar mechanism has been observed *in vitro* and in mammalian cells for αSyn aggregation (Ray et al., 2020). Interestingly, the liquid droplets can have physiological functions. For instance, synapsin liquid droplets can mediate *in vitro* the clustering of synaptic vesicles (Milovanovic et al., 2017). It could be speculated that αSyn triggers the clustering of vesicles in yeast by a similar mechanism.

6.1.3 αSyn does not form assemblies larger than dimers on the surface of tubulated liposomes

Lastly, the *in vitro* cryo tomograms of tubulated liposomes did not reveal any density features at their surface (figure 3.9). Therefore, it is likely that αSyn does not adopt a defined globular conformation for these interactions. Since the lipid bilayer separation of 4 nm is visible, it can be assumed that if αSyn oligomers are formed, their diameter would be 4 nm or less. Assuming the largest entity would be a 4 nm-diameter sphere, the number of subunits can be determined using the following equations:

$$N = n \times N_A \qquad (equation\ 7)$$

Where N is the number of αSyn subunits, n is the number of moles of αSyn (mol) and N_A is Avogadro's constant (N_A = 6.022x10^{23} mol^{-1}).

$$n = \frac{m}{MW} \qquad (equation\ 8)$$

Where n is the number of moles of αSyn (mol), m is the mass of αSyn (g) and MW is the molecular weight of αSyn (MW = 14.4 kDa = 14.4x10^3 $g.mol^{-1}$).

$$m = d \times V = d \times \frac{4\pi r^3}{3} \qquad (equation\ 9)$$

Where m is the mass of αSyn (g), d is the density of αSyn and is assumed to be equal to the standard protein density (d = 1.35 $g.cm^{-3}$) and V is the volume of a 4 nm-diameter sphere (r = 2x10^{-9} m).

This corresponds to 1.89 subunits in a 4 nm sphere. Therefore, αSyn does not form assemblies larger than a dimer on the surface of tubulated liposomes. However, this result does not exclude a transient role of oligomers in fusion and tubulation of liposomes, or that αSyn molecules are extended on the membrane surface.

6.2 New structural details about the disaggregation of αSyn amyloid fibrils

6.2.1 Cryo-EM reveals a new conformer for *in vitro* WT αSyn amyloid fibres

To date, five different conformers of full-length WT αSyn amyloid fibres without post translational modifications have been reported by cryo-EM (Guerrero-Ferreira et al., 2019; B. Li et al., 2018; Y. Li et al., 2018). In this thesis, a new structure has been determined by cryo-EM at a resolution of 3.2 Å (figure 5.10). This new structure shares

the common Greek key fold comprising residues 43 to 93. The protofilament interface (residues 50 to 57) is also common to other structures. However, this unique conformer contains additional ordered density for the N-terminus which adopts a hairpin-like conformation. As discussed in the corresponding chapter, the presence of this partly ordered N-terminus could be due to the phosphate ions present in the buffer as it was already shown that the buffer conditions can influence fibre formation (de Oliveira and Silva, 2019; Guerrero-Ferreira et al., 2019). However, similar buffer conditions produced another structure, determined by Dr Joe Beton in the group, suggesting that unknown factors influence the fibre structure (figure 5.5). Another explanation for the extra N-terminal density would be that binding of ΔJ-DNAJB1 rearranges the fibre. But one observation argues against this hypothesis. As discussed in chapter 5, the structure of αSyn amyloid fibres in complex with WT DNAJB1 does not differ from a previously reported one (figure 5.5; Guerrero-Ferreira et al., 2019). Therefore, it can be speculated that the binding of ΔJ-DNAJB1 does not alter the fibre structure and the partly ordered N-terminus is a conformation that can be adopted by αSyn fibres, although it has not been previously reported.

6.2.2 Cryo-EM and Cryo-ET unveil structural details about the Hsp70 disaggregase machinery

So far, the Hsp70 disaggregase system has been studied by biochemical and biophysical techniques as well as negative stain electron microscopy and tomography (Beton et al., 2021; Franco et al., 2021; Gao et al., 2015; Schneider et al., 2021; Wentink et al., 2020). But structural details crucial to understand the mechanism of this system are unknown. In this study, I used cryo-EM to find the structure of the complex formed of WT αSyn fibres and ΔJ-DNAJB1 at low resolution. The decoration of ΔJ-DNAJB1 shows an expected horseshoe-like shape every 40 Å (figure 5.15). This observation is consistent

with the findings obtained by Dr Joe Beton on the complex of WT αSyn fibrils and WT DNAJB1 (figure 5.5). However, the low resolution of both structures limited the structural details about DNAJB1 binding to the fibres. A few factors can explain this limitation: 1) the complex is flexible since the binding site for DNAJB1 is localised in the disordered C-terminus of αSyn; 2) DNAJB1 is a small protein (80 kDa dimer; only 40 kDa for ΔJ-DNAJB1 dimer), rendering it difficult to solve by cryo-EM; 3) the amyloid reconstruction option in RELION is not currently suitable for decorated fibres whose decoration repeat does not match the 4.8 Å cross-β repeat.

It is unclear what determines the 40 Å repeat of DNAJB1 dimers. A potential explanation was an intermolecular interaction between the J-domain and G/F flexible linker between adjacent dimers. But a similar repeat is visible with the ΔJ-DNAJB1 mutant, ruling out the inhibitory interaction as the cause of the 40 Å repeat. Another potential explanation would be that long range interactions between the positively charged N-terminus and the acidic C-terminus of αSyn compete with the binding of DNAJB1 at the C-terminus. But this does not explain the regularity of the binding every 40 Å. Lastly, a similar pattern with a motif every ~50 Å was already observed by negative stain tomography where DNAJB1 was incubated with αSyn amyloid fibres in a physiological buffer before separation of the fibres from the free chaperones by sucrose gradient (Gao et al., 2015). This similarity suggests that the HD buffer did not alter the decoration pattern.

There are a few factors that may have introduced biases in the reconstruction. First, the inter-box distance between 2 adjacent particles was set to 42 pixels (44.5 Å) for the particle extraction. This chosen distance could have introduced biases in the reconstruction such as the regularity of the binding every 40 Å. Moreover, the helical symmetry parameters, such as a helical rise of 40 Å and a helical twist of -11.6°, which

were imposed at the different reconstruction steps (3D classification and 3D refinement), could have also led to an erroneous reconstruction of the complex. . However, the 40 Å repeat seems genuine because it is possible to see it in 2D class averages for which the helical rise was not restricted to 40 Å. Reconstructing the structure of the complex without imposing the helical symmetry parameters would reduce the risk of artefacts in the reconstruction. Moreover, collecting tilt series and reconstructing tomograms to generate an initial reference by subtomogram averaging are another approach to tackle this problem.

DNAJB1 dimers are oriented with one subunit closer to the fibre core in both complexes and the structure of the WT complex shows that both the J-domain and CTD-I of DNAJB1 in this orientation could be accessible to Hsc70 (figures 5.5 and 5.15). This shows how the tightly packed array of DNAJB1 could recruit many Hsc70 proteins to the fibres, as seen by cryo-electron tomography (figure 4.13). Densely packed chaperones are bound to the fibres in the presence of the full system (DNAJB1, Hsc70, Apg2, ATP) in the HKMD buffer which contains salts (50 mM KCl, 5 mM $MgCl_2$, table 2.1). This is the first direct observation of the full Hsc70 disaggregase system with a genuine substrate in a native-like environment. This dense decoration of chaperones supports the entropic pulling model which requires densely bound chaperones to generate the local pulling forces responsible for extraction of subunits from the fibres (Wentink et al., 2020).

6.3 A novel function of Apg2 is found

The last question of this study was to understand more precisely the function of Apg2 in the disaggregation, since its effects were inferred from indirect measurements (Wentink et al., 2020). Apg2 was considered as an enhancer of the disaggregation and a NEF

which triggered the selective release of non-clustered Hsc70 molecules bound to αSyn fibrils because of its large size. The current study extends these observations with new insights about the function of Apg2. Apg2 is involved in the formation of dense clusters of Hsc70 preferentially bound to one end of the fibres but does not change the nucleation of the decoration (figures 4.10 and 4.12). Apg2 mediates the disaggregation of the fibres in a concentration-dependent manner (figure 4.8).

But the most striking and surprising result revealed by biochemical assays and TIRF microscopy is that Apg2 stimulates the recruitment of Hsc70 (figure 4.7). On the face of it, this result seems to contradict the current model of the disaggregase system. But the different results can be reconciled. Apg2 has two main functions: an ATP-dependent holdase activity and an ATP-independent NEF activity (Mattoo et al., 2013). Wentink et al. showed that inhibiting the ATPase activity of Apg2 does not alter the disaggregation activity whereas inhibiting the NEF function does (Wentink et al., 2020). This result was confirmed by measuring the dissociation rate of Hsc70 which was 10-fold higher in the presence of Apg2 (Wentink et al., 2020). Therefore, Apg2 kinetically triggers the release of Hsc70 from the fibres. But counter intuitively, this leads to a net increase of Hsc70 recruitment. This suggests that there is a very rapid turnover of Hsc70 in the presence of Apg2 and that the association rate of Hsc70 must increase even more.

However, several points are still unclear about this mechanism. First, it was shown by NMR that Apg2 weakly interacts with monomeric αSyn (Wentink et al., 2020). Therefore, a transient binding of Apg2 SBD with the amyloid fibres may be required for the optimal recruitment of Hsc70. In addition, it has recently been found that a disordered C-terminal region which is highly conserved in metazoan Hsp110 proteins including Apg2, acts as a holdase and inhibits the formation of αβ-42 and αSyn amyloid

fibres *in vitro* (Yakubu and Morano, 2021). It is unknown if this region is also involved in the disaggregation process.

Another question raised by the results is why the dense chaperone decoration is localised at one fibre end. Hsc70 has 2 main binding sites on αSyn (residues 1-10 and 37-43; Wentink et al., 2020). The first binding site is disordered in the different αSyn fibre conformers. However, the second binding site is usually ordered. It is notable that the ordered binding site for Hsc70 exposes differences in charge between the two surfaces (figure 6.1), suggesting that Hsc70 could have a higher affinity for one surface. This could explain why Hsc70 decoration is localised at one end. Using truncated mutants of αSyn, Wentink et al. showed that the rigid binding site is essential for disaggregation whereas the flexible one is not (Wentink et al., 2020). Taken together, it could be speculated that initially, Hsc70 randomly binds to the flexible binding site on the fibre and destabilises the αSyn subunit, rendering the second binding site more accessible. Then, Apg2 releases the Hsc70 bound to the first binding site via its NEF activity and Hsc70 interacts with the second binding site (or a second Hsc70 binds to the second binding site). Because of the differences in charges between the two surfaces, Hsc70 has a higher affinity for the second binding site at one end of the fibre. This leads to the initiation of a dense decoration of Hsc70 at the exposed end of the fibre. Cooperativity between DNAJB1 and Hsc70 (and perhaps Apg2) would then be necessary for the formation of extended dense chaperone clusters. But what is the basis of this cooperativity? In the cryo tomograms of the full system, polymers of chaperones were visible (figure 4.13C). Their composition cannot be determined from the tomograms. However, comparisons provide useful information. In the absence of Apg2, the isolated polymers were rarer, shorter and thinner. Therefore, it seems that Apg2 can promote their formation, or at least their growth if a small oligomer is already formed

without Apg2. Since αSyn soluble monomers are extracted from the fibres (Schneider et al., 2021), these polymers of chaperones may form before interacting with the fibres rather than being composed of chaperones and disordered oligomers of αSyn (although there is no evidence for this hypothesis).

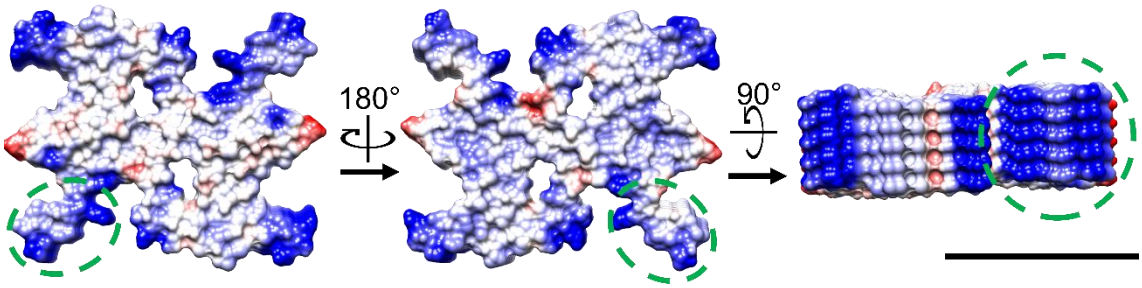

Figure 6.1: The polarity of Hsc70 binding site in αSyn amyloid fibre.
Top, bottom and side views of N-terminally acetylated WT αSyn fibre (PDB: 6OSJ, Ni et al., 2019) whose structure most closely resembles the structure found in chapter 5. The surfaces show the electrostatic surfaces of the different views: negatively charged residues are shown in red, positively charged residues in blue. The binding site for Hsc70 (residues 37-43) is indicated by a green dashed ellipse for one protofilament. The electrostatic surfaces show that the top and bottom surfaces have different charges for the binding site. The side view shows that the repeat of αSyn is not perfectly planar. Scale bar, 50 Å.

To conclude, the work presented in this thesis about the Hsc70 disaggregase system has brought new insights about the mechanism and is summarised in figure 6.2.

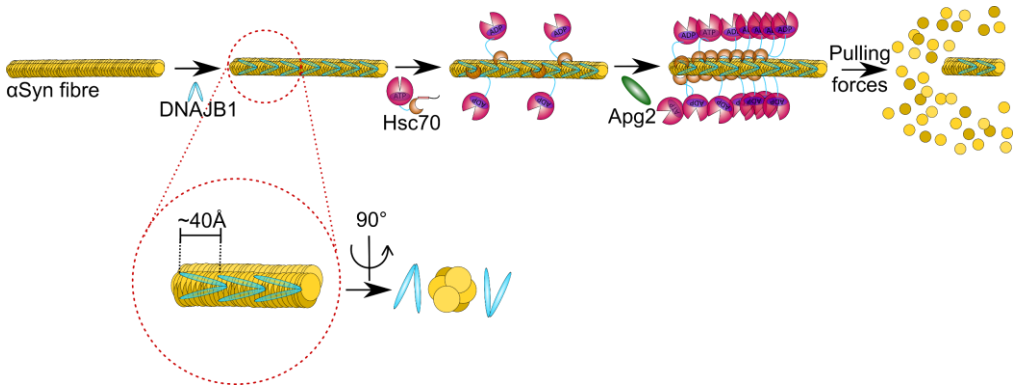

Figure 6.2: The new model of the tripartite disaggregase system.
Initially, DNAJB1 (blue) binds to the fibre (yellow) with a repeat of 40 Å. DNAJB1 is oriented sideways with one subunit closer to the fibril core. Hsc70 (purple and brown) is then recruited in a non-optimal manner displaying an irregular and sparse decoration. Apg2 (green) increases the net recruitment of Hsc70 to one end of the fibre, triggering the binding of dense clusters of Hsc70 which lead to depolymerisation from one end. It is still unclear whether Apg2 binds directly to the fibres or to the Hsc70s in complex with the fibres.

6.4 Future perspectives

6.4.1 Studying the aggregation of αSyn in cell models and the role of chaperones

The aggregation of αSyn in yeast in this study revealed features similar to the ones observed in LBs of PD patients. This model could therefore be used to study the aggregation of αSyn mutants and understand their specific properties in αSyn aggregation in future experiments. This yeast model could also be useful to investigate the effects of chaperones on αSyn aggregation and disaggregation by downregulating or upregulating them. However, yeast remains a simple model with a different disaggregase system because of the efficient Hsp104 which is absent in metazoa. Furthermore, protein aggregation depends on the precise cell or animal model. Consequently, structural studies on the aggregation of αSyn in a more sophisticated

model such as neurons or animal systems will be necessary to understand the properties of αSyn aggregation.

6.4.2 Defining the specificity of each protein in the *in vitro* Hsc70 disaggregase system

In future work, it will be important to address the following questions about the disaggregase machinery.

6.4.2.1 Determining the cause of enhanced Hsc70 recruitment

The optimal Hsc70 recruitment caused by Apg2 could be due to the presence of two main binding sites for Hsc70 in the αSyn sequence. Studying Hsc70 recruitment by tau or huntingtin amyloid fibres rather than αSyn ones could provide new information. This approach would need to combine biochemical assays and NMR experiments on WT and truncated mutants of tau or huntingtin as already performed for αSyn (Wentink et al., 2020). Another approach would be to create αSyn mutants that block Hsc70 interaction with one of the two binding sites. However, such an approach may also lead to the formation of new fibre structures and more complexity. Lastly, using ATP analogues to inhibit Hsc70 ATPase activity (or limit it to one cycle if ATP is already bound to Hsc70 with ATP analogues in the buffer) could also provide information about whether the ATPase cycle of Hsc70 is involved in its Apg2-mediated optimal recruitment.

6.4.2.2 Optimising the sample preparation for cryo-EM analysis

The structural information presented in this thesis was limited because of 1) the flexibility of the αSyn:DNAJB1 complexes and 2) the artefacts created by RELION because of the helical reconstruction. Franco et al. showed that the Hsc70 disaggregase system can also disassemble αSyn oligomers (Franco et al., 2021). Although the *in vivo*

relevance of these oligomers in αSyn cytotoxicity is unknown, using them as a substrate rather than amyloid fibres could provide crucial mechanistic details about the chaperone mechanism. Indeed, if micrographs of the complexes formed of αSyn oligomers with one, two or even three chaperones can be recorded, the image processing would be performed by single particle analysis without the helical reconstruction option and its constraints.

6.4.2.3 Identifying the specificity of DNAJB1

The reason for the specific requirement of DNAJB1 for disaggregation is still unknown. Faust et al. showed that the additional helix 5 found in members of class B DNAJ protein is necessary, but did not explain why (Faust et al., 2020). Looking at the effects of a mutant blocking the formation of helix 5 on the decoration of αSyn fibres by the chaperones could help to find an explanation.

Moreover, in mammalian cells, DNAJB6, but not DNAJB1, can trigger the degradation of αSyn aggregates (Deshayes et al., 2019) and can delay the aggregation of αSyn *in vitro*, in cooperation with Hsp70 (Aprile et al., 2017). However, there is no evidence that DNAJB6 is involved in the disaggregation of αSyn *in vitro* and *in vivo*. Therefore, studying whether the disaggregation can occur *in vitro* using DNAJB6 rather than DNAJB1 and comparing their activities would be interesting and could help understand the specificity of the J-domain protein in disaggregation.

Bibliography

Ambadipudi, S., Biernat, J., Riedel, D., Mandelkow, E., Zweckstetter, M., 2017. Liquid-liquid phase separation of the microtubule-binding repeats of the Alzheimer-related protein Tau. Nat. Commun. 8, 1–13. https://doi.org/10.1038/s41467-017-00480-0

Amo, T., Sato, S., Saiki, S., Wolf, A.M., Toyomizu, M., Gautier, C.A., Shen, J., Ohta, S., Hattori, N., 2011. Mitochondrial membrane potential decrease caused by loss of PINK1 is not due to proton leak, but to respiratory chain defects. Neurobiol. Dis. 41, 111–118. https://doi.org/10.1016/j.nbd.2010.08.027

Amor, S., Puentes, F., Baker, D., Van Der Valk, P., 2010. Inflammation in neurodegenerative diseases. Immunology 129, 154–169. https://doi.org/10.1111/j.1365-2567.2009.03225.x

Anfinsen, C.B., 1973. Principles that govern the Folding of Protein Chains. Science (80-.). 181, 223–230.

Appel-Cresswell, S., Vilarino-Guell, C., Encarnacion, M., Sherman, H., Yu, I., Shah, B., Weir, D., Thompson, C., Szu-Tu, C., Trinh, J., Aasly, J.O., Rajput, A., Rajput, A.H., Jon Stoessl, A., Farrer, M.J., 2013. Alpha-synuclein p.H50Q, a novel pathogenic mutation for Parkinson's disease. Mov. Disord. 28, 811–813. https://doi.org/10.1002/mds.25421

Aprile, F.A., Källstig, E., Limorenko, G., Vendruscolo, M., Ron, D., Hansen, C., 2017. The molecular chaperones DNAJB6 and Hsp70 cooperate to suppress α-synuclein aggregation. Sci. Rep. 7, 1–11. https://doi.org/10.1038/s41598-017-08324-z

Arosio, P., Knowles, T.P.J., Linse, S., 2015. On the lag phase in amyloid fibril formation. Phys. Chem. Chem. Phys. 17, 7606–7618. https://doi.org/10.1039/c4cp05563b

Auluck, P.K., Caraveo, G., Lindquist, S., 2010. α-Synuclein: Membrane Interactions and Toxicity in Parkinson's Disease. Annu. Rev. Cell Dev. Biol. 26, 211–233. https://doi.org/10.1146/annurev.cellbio.042308.113313

Baldwin, A.J., Knowles, T.P.J., Tartaglia, G.G., Fitzpatrick, A.W., Devlin, G.L., Shammas, S.L., Waudby, C.A., Mossuto, M.F., Meehan, S., Gras, S.L., Christodoulou, J., Anthony-Cahill, S.J., Barker, P.D., Vendruscolo, M., Dobson, C.M., 2011. Metastability of native proteins and the phenomenon of amyloid formation. J. Am. Chem. Soc. 133, 14160–14163. https://doi.org/10.1021/ja2017703

Barends, T.R.M., Brosi, R.W.W., Steinmetz, A., Scherer, A., Hartmann, E., Eschenbach, J., Lorenz, T., Seidel, R., Shoeman, R.L., Zimmermann, S., Bittl, R., Schlichting, I., Reinstein, J., 2013. Combining crystallography and EPR: Crystal and solution structures of the multidomain cochaperone DnaJ. Acta Crystallogr. Sect. D Biol. Crystallogr. 69, 1540–1552. https://doi.org/10.1107/S0907444913010640

Bepler, T., Kelley, K., Noble, A.J., Berger, B., 2020. Topaz-Denoise: general deep denoising models for cryoEM and cryoET. Nat. Commun. 11, 1–12. https://doi.org/10.1038/s41467-020-18952-1

Bepler, T., Morin, A., Rapp, M., Brasch, J., Shapiro, L., Noble, A.J., Berger, B., 2019. Positive-unlabeled convolutional neural networks for particle picking in cryo-electron micrographs. Nat. Methods 16, 1153–1160. https://doi.org/10.1038/s41592-019-0575-8

Beton, J.G., Monistrol, J., Wentink, A., Johnston, E.C., Roberts, An.J., Bukau, B., Hoogenboom, B.W., Saibil, H.R., 2021. Cooperative Amyloid Fibre Binding and Disassembly by the Hsp70 disaggregase. bioRxiv. https://doi.org/10.1101/2021.08.29.458036

Biancalana, M., Koide, S., 2010. Molecular mechanism of Thioflavin-T binding to amyloid fibrils. Biochim. Biophys. Acta - Proteins Proteomics 1804, 1405–1412. https://doi.org/10.1016/j.bbapap.2010.04.001

Boyer, D.R., Li, B., Sun, C., Fan, W., Sawaya, M.R., Jiang, L., Eisenberg, D.S., 2019. Structures of fibrils formed by α-synuclein hereditary disease mutant H50Q reveal new polymorphs. Nat. Struct. Mol. Biol. 26, 1044–1052. https://doi.org/10.1038/s41594-019-0322-y

Boyer, D.R., Li, B., Sun, C., Fan, W., Zhou, K., Hughes, M.P., Sawaya, M.R., Jiang, L., Eisenberg, D.S., 2020. The α-synuclein hereditary mutation E46K unlocks a more stable, pathogenic fibril structure. Proc. Natl. Acad. Sci. U. S. A. 117, 3592–3602. https://doi.org/10.1073/pnas.1917914117

Bracher, A., Verghese, J., 2015. The nucleotide exchange factors of Hsp70 molecular chaperones. Front. Mol. Biosci. 2, 1–9. https://doi.org/10.3389/fmolb.2015.00010

Brehmer, D., Rüdiger, S., Gässler, C.S., Klostermeier, D., Packschies, L., Reinstein, J., Mayer, M.P., Bukau, B., 2001. Tuning of chaperone activity of Hsp70 proteins by modulation of nucleotide exchange. Nat. Struct. Biol. 8, 427–432. https://doi.org/10.1038/87588

Bucciantini, M., Giannoni, E., Chiti, F., Baroni, F., Taddei, N., Ramponi, G., Dobson, C.M., Stefani, M., 2002. Inherent toxicity of aggregates implies a common mechanism for protein misfolding diseases. Nature 416, 507–511. https://doi.org/10.1038/416507a

Burré, J., Sharma, M., Tsetsenis, T., Buchman, V., Etherton, M.R., Südhof, T.C., 2010. α-Synuclein promotes SNARE-complex assembly in vivo and in vitro. Science (80-.). 329, 1663–1667. https://doi.org/10.1126/science.1195227

Burré, J., Vivona, S., Diao, J., Sharma, M., Brunger, A.T., Südhof, T.C., 2013. Properties of native brain α-synuclein. Nature 498, 107–110. https://doi.org/10.1038/nature12125

Chandra, S., Chen, X., Rizo, J., Jahn, R., Südhof, T.C., 2003. A broken α-helix in folded α-synuclein. J. Biol. Chem. 278, 15313–15318. https://doi.org/10.1074/jbc.M213128200

Chartier-Harlin, M., Kachergus, J., Roumier, C., Mouroux, V., Douay, X., Lincoln, S., Levecque, C., Larvor, L., Andrieux, J., Hulihan, M., Waucquier, N., Defebvre, L., P, A., Farrer, M., A, D., 2004. α-synuclein locus duplication as a cause of familial Parkinson's disease. Lancet 364, 1169–1171. https://doi.org/http://dx.doi.org/10.1016/S0140-6736(04)17104-3

Chen, S.W., Drakulic, S., Deas, E., Ouberai, M., Aprile, F.A., Arranz, R., Ness, S., Roodveldt, C., Guilliams, T., De-Genst, E.J., Klenerman, D., Wood, N.W., Knowles, T.P.J., Alfonso, C., Rivas, G., Abramov, A.Y., Valpuesta, J.M., Dobson, C.M., Cremades, N., 2015. Structural characterization of toxic oligomers that are kinetically trapped during α-synuclein fibril formation. Proc. Natl. Acad. Sci. U. S. A. 112, E1994–E2003. https://doi.org/10.1073/pnas.1421204112

Choi, W., Zibaee, S., Jakes, R., Serpell, L.C., Davletov, B., Anthony Crowther, R., Goedert, M., 2004. Mutation E46K increases phospholipid binding and assembly into filaments of human α-synuclein. FEBS Lett. 576, 363–368. https://doi.org/10.1016/j.febslet.2004.09.038

Cole, N.B., Murphy, D.D., Grider, T., Rueter, S., Brasaemle, D., Nussbaum, R.L., 2002. Lipid droplet binding and oligomerization properties of the Parkinson's disease protein α-synuclein. J. Biol. Chem. 277, 6344–6352. https://doi.org/10.1074/jbc.M108414200

Cooper, A.A., Gitler, A.D., Cashikar, A., Haynes, C.M., Hill, K.J., Bhullar, B., Liu, K., Xu, K., Strathearn, K.E., Liu, F., Cao, S., Caldwell, K.A., Caldwell, G.A., Marsischky, G., Kolodner, R.D., Labaer, J., Rochet, J., Bonini, N.M., Lindquist, S., 2006. α-Synuclein Blocks ER-Golgi Traffic and Rab1 Rescues Neuron Loss in Parkinson's Models. Science (80-.). 313, 324–329.

Danev, R., Buijsse, B., Khoshouei, M., Plitzko, J.M., Baumeister, W., 2014. Volta potential phase plate for in-focus phase contrast transmission electron microscopy. Proc. Natl. Acad. Sci. U. S. A. 111, 15635–15640. https://doi.org/10.1073/pnas.1418377111

de Oliveira, G.A.P., Silva, J.L., 2019. Alpha-synuclein stepwise aggregation reveals features of an early onset mutation in Parkinson's disease. Commun. Biol. 2. https://doi.org/10.1038/s42003-019-0598-9

Delacotte, J., Thiam, A.R., Rothman, J.E., Antonny, B., Pincet, F., Walther, T.C., Wilfling, F., Wang, J., Beck, R., 2013. COPI buds 60-nm lipid droplets from reconstituted water-phospholipid-triacylglyceride interfaces, suggesting a tension clamp function. Proc. Natl. Acad. Sci. 110, 13244–13249. https://doi.org/10.1073/pnas.1307685110

Deshayes, N., Arkan, S., Hansen, C., 2019. The molecular chaperone DNAJB6, but Not DNAJB1, suppresses the seeded aggregation of alpha-synuclein in cells. Int. J. Mol. Sci. 20, 1–13. https://doi.org/10.3390/ijms20184495

Desplats, P., Lee, H.-J., Bae, E.-J., Patrick, C., Rockenstein, E., Crews, L., Spencer, B., Masliah, E., Lee, S.-J., 2009. Inclusion formation and neuronal cell death through neuron-to-neuron transmission of alpha-synuclein. Proc. Natl. Acad. Sci. 106, 13010–13015. https://doi.org/10.1073/pnas.0903691106

Deville, C., Carroni, M., Franke, K.B., Topf, M., Bukau, B., Mogk, A., Saibil, H.R., 2017. Structural pathway of regulated substrate transfer and threading through an Hsp100 disaggregase. Sci. Adv. 3, 1–8. https://doi.org/10.1126/sciadv.1701726

Deville, C., Franke, K., Mogk, A., Bukau, B., Saibil, H.R., 2019. Two-Step Activation Mechanism of the ClpB Disaggregase for Sequential Substrate Threading by the Main ATPase Motor. Cell Rep. 27, 3433-3446.e4.

https://doi.org/10.1016/j.celrep.2019.05.075

Diao, J., Burré, J., Vivona, S., Cipriano, D.J., Sharma, M., Kyoung, M., Südhof, T.C., Brunger, A.T., 2013. Native α-synuclein induces clustering of synaptic-vesicle mimics via binding to phospholipids and synaptobrevin-2/VAMP2. Elife 2013, 1–17. https://doi.org/10.7554/eLife.00592

Doherty, C.P.A., Ulamec, S.M., Maya-Martinez, R., Good, S.C., Makepeace, J., Khan, G.N., van Oosten-Hawle, P., Radford, S.E., Brockwell, D.J., 2020. A short motif in the N-terminal region of α-synuclein is critical for both aggregation and function. Nat. Struct. Mol. Biol. 27, 249–259. https://doi.org/10.1038/s41594-020-0384-x

Doyle, S.M., Wickner, S., 2009. Hsp104 and ClpB: protein disaggregating machines. Trends Biochem. Sci. 34, 40–48. https://doi.org/10.1016/j.tibs.2008.09.010

Dragovic, Z., Broadley, S.A., Shomura, Y., Bracher, A., Hartl, F.U., 2006. Molecular chaperones of the Hsp110 family act as nucleotide exchange factors of Hsp70s. EMBO J. 25, 2519–2528. https://doi.org/10.1038/sj.emboj.7601138

Dubochet, J., Adrian, M., Chang, J.-J., Homo, J.-C., Jean, L., McDowall, A.W., Schultz, P., 1988. Cryo-electron microscopy of vitrified specimens. Q. Rev. Biophys. 21, 129–228. https://doi.org/10.1017/S0033583500004297

Emsley, P., Cowtan, K., 2004. Coot: Model-building tools for molecular graphics. Acta Crystallogr. Sect. D Biol. Crystallogr. 60, 2126–2132. https://doi.org/10.1107/S0907444904019158

Fares, M.-B., Maco, B., Oueslati, A., Rockenstein, E., Lashuel, H.A., Ninkina, N., Buchman, V.L., Masliah, E., 2016. Induction of de novo α-synuclein fibrillization in a neuronal model for Parkinson's disease. Proc. Natl. Acad. Sci. 113, E912–E921. https://doi.org/10.1073/pnas.1512876113

Faust, O., Abayev-Avraham, M., Wentink, A.S., Maurer, M., Nillegoda, N.B., London, N., Bukau, B., Rosenzweig, R., 2020. HSP40 proteins use class-specific regulation to drive HSP70 functional diversity. Nature 587, 489–494. https://doi.org/10.1038/s41586-020-2906-4

Feany, M.B., Bender, W.W., 2000. A Drosophila model of Parkinson's disease. Nature 404, 47405. https://doi.org/10.1038/35006074

Feifel, B., Scho, H., Christen, P., Zu, C.-, 1998. D-Peptide Ligands for the Co-chaperone DnaJ. J. Biol. Chem. 273, 11999–12002. https://doi.org/10.1074/jbc.273.20.11999

Fish, K.N., 2009. Total Internal Reflection Fluorescence (TIRF) Microscopy. Curr. Protoc. Cytom. https://doi.org/10.1002/0471142956.cy1218s50.

Fitzpatrick, A.W.P., Falcon, B., He, S., Murzin, A.G., Murshudov, G., Garringer, H.J., Crowther, R.A., Ghetti, B., Goedert, M., Scheres, S.H.W., 2017. Cryo-EM structures of tau filaments from Alzheimer's disease. Nature 547, 185–190. https://doi.org/10.1038/nature23002

Flaherty, K.M., DeLuca-Flaherty, C., McKay, D.B., 1990. Three-dimensional structure of the ATPase fragment of a 70K heat-shock cognate protein. Nature 346, 623–628. https://doi.org/10.1038/346623a0

Flynn, J.D., Jiang, Z., Lee, J.C., 2018a. Segmental 13C-Labeling and Raman Microspectroscopy of α-Synuclein Amyloid Formation. Angew. Chemie - Int. Ed. 57, 17069–17072. https://doi.org/10.1002/anie.201809865

Flynn, J.D., McGlinchey, R.P., Walker, R.L., Lee, J.C., 2018b. Structural features of alpha-synuclein amyloid fibrils revealed by raman spectroscopy. J. Biol. Chem. 293, 767–776. https://doi.org/10.1074/jbc.M117.812388

Franco, A., Gracia, P., Colom, A., Camino, J.D., Fernández-higuero, J.Á., 2021. All-or-none disassembly via chaperone-triggered fibril unzipping favors clearance of α -synuclein toxic species. Proc. Natl. Acad. Sci. 118, 1–11. https://doi.org/10.1073/pnas.2105548118/-/DCSupplemental.Published

Frangakis, A.S., Hegerl, R., 2001. Noise reduction in electron tomographic reconstructions using nonlinear anisotropic diffusion. J. Struct. Biol. 135, 239–250. https://doi.org/10.1006/jsbi.2001.4406

Fusco, G., Chen, S.W., Williamson, P.T.F., Cascella, R., Perni, M., Jarvis, J.A., Cecchi, C., Vendruscolo, M., Chiti, F., Cremades, N., Ying, L., Dobson, C.M., Simone, A. De, 2017. Structural basis of membrane disruption and cellular toxicity by α-synuclein oligomers. Science (80-.). 1440, 1–30. https://doi.org/10.1126/science.aan6160

Fusco, G., De Simone, A., Gopinath, T., Vostrikov, V., Vendruscolo, M., Dobson, C.M., Veglia, G., 2014. Direct observation of the three regions in α-synuclein that determine its membrane-bound behaviour. Nat. Commun. 5, 1–17. https://doi.org/10.1038/ncomms4827

Fusco, G., Pape, T., Stephens, A.D., Mahou, P., Costa, A.R., Kaminski, C.F., Kaminski Schierle, G.S., Vendruscolo, M., Veglia, G., Dobson, C.M., De Simone, A., 2016. Structural basis of synaptic vesicle assembly promoted by α-synuclein. Nat. Commun. 7, 1–11. https://doi.org/10.1038/ncomms12563

Galvagnion, C., Brown, J.W.P., Ouberai, M.M., Flagmeier, P., Vendruscolo, M., Buell, A.K., Sparr, E., Dobson, C.M., 2016. Chemical properties of lipids strongly affect the kinetics of the membrane-induced aggregation of α-synuclein. Proc. Natl. Acad. Sci. 113, 7065–7070. https://doi.org/10.1073/pnas.1601899113

Gao, X., Carroni, M., Nussbaum-Krammer, C., Mogk, A., Nillegoda, N.B., Szlachcic, A., Guilbride, D.L., Saibil, H.R., Mayer, M.P., Bukau, B., 2015a. Human Hsp70 Disaggregase Reverses Parkinson's-Linked alpha-Synuclein Amyloid Fibrils. Mol. Cell 59, 781–793. https://doi.org/10.1016/j.molcel.2015.07.012

Gasteiger, E., Hoogland, C., Gattiker, A., Duvaud, S., Wilkins, M.R., Appel, R.D., Bairoch, A., 2005. Protein Identification and Analysis Tools on the ExPASy Server. Proteomics Protoc. Handb. 571–608. https://doi.org/10.1385/1592598900

Georgieva, E., Ramlall, T., Borbat, P., Freed, J., Eliezer, D., 2008. Membrane-bound α-synuclein forms an extended helix: Long-distance pulsed ESR measurements using vesicles, bicelles, and rodlike micelles. J. Am. Chem. Soc. 130, 12856–12857. https://doi.org/10.1021/ja804517m

Giasson, B.I., Murray, I.V.J., Trojanowski, J.Q., Lee, V.M.Y., 2001. A Hydrophobic Stretch of 12 Amino Acid Residues in the Middle of α-Synuclein Is Essential for Filament Assembly. J. Biol. Chem. 276, 2380–2386.

https://doi.org/10.1074/jbc.M008919200

Glover, J.R., Lindquist, S., 1998. Hsp104, Hsp70, and Hsp40: A novel chaperone system that rescues previously aggregated proteins. Cell 94, 73–82. https://doi.org/10.1016/S0092-8674(00)81223-4

Goloubinoff, P., Mogk, A., Ben Zvi, A.P., Tomoyasu, T., Bukau, B., 1999. Sequential mechanism of solubilization and refolding of stable protein aggregates by a bichaperone network. Proc. Natl. Acad. Sci. U. S. A. 96, 13732–13737. https://doi.org/10.1073/pnas.96.24.13732

Greene, M.K., Maskos, K., Landry, S.J., 1998. Role of the J-domain in the cooperation of Hsp40 with Hsp70. Proc. Natl. Acad. Sci. U. S. A. 95, 6108–6113. https://doi.org/10.1073/pnas.95.11.6108

Guerrero-Ferreira, R., Taylor, N.M.I., Arteni, A.-A., Kumari, P., Mona, D., Ringler, P., Britschgi, M., Lauer, M.E., Verasdock, J., Riek, R., Melki, R., Meier, B.H., Böckmann, A., Bousset, L., Stahlberg, H., 2019. Two new polymorphic structures of alpha-synuclein solved by cryo-electron microscopy. Elife. https://doi.org/10.1101/654582

Guerrero-Ferreira, R., Taylor, N.M.I., Mona, D., Ringler, P., Lauer, M.E., Riek, R., Britschgi, M., Stahlberg, H., 2018. Cryo-EM structure of alpha-synuclein fibrils. Elife 7, 1–18. https://doi.org/10.7554/eLife.36402

Iadanza, M.G., Jackson, M.P., Hewitt, E.W., Ranson, N.A., Radford, S.E., 2018. A new era for understanding amyloid structures and disease. Nat. Rev. Mol. Cell Biol. https://doi.org/10.1038/s41580-018-0060-8

Jahn, T.R., Radford, S.E., 2005. The Yin and Yang of protein folding. FEBS J. 272, 5962–5970. https://doi.org/10.1111/j.1742-4658.2005.05021.x

Jiang, Y., Rossi, P., Kalodimos, C.G., 2019. Structural basis for client recognition and activity of Hsp40 chaperones. Science (80-.). 365, 1313–1319. https://doi.org/10.1126/science.aax1280

Jin, T., Gu, Y., Zanusso, G., Sy, M.S., Kumar, A., Cohen, M., Gambetti, P., Singh, N., 2000. The chaperone protein BiP binds to a mutant prion protein and mediates its degradation by the proteasome. J. Biol. Chem. 275, 38699–38704. https://doi.org/10.1074/jbc.M005543200

Jordan, R., McMacken, R., 1995. Modulation of the ATPase activity of the molecular chaperone DnaK by peptides and the DnaJ and GrpE heat shock proteins. J. Biol. Chem. 270, 4563–4569. https://doi.org/10.1074/jbc.270.9.4563

Kaku, H., Ludlow, A. V., Gutknecht, M.F., Rothstein, T.L., 2020. FAIM Opposes Aggregation of Mutant SOD1 That Typifies Some Forms of Familial Amyotrophic Lateral Sclerosis. Front. Neurosci. 14, 1–8. https://doi.org/10.3389/fnins.2020.00110

Kampinga, H.H., Craig, E.A., 2010. The HSP70 chaperone machinery: J proteins as drivers of functional specificity. Nat. Rev. Mol. Cell Biol. 11, 579–592. https://doi.org/10.1038/nrm2941

Kampinga, H.H., Hageman, J., Vos, M.J., Kubota, H., Tanguay, R.M., Bruford, E.A., Cheetham, M.E., Chen, B., Hightower, L.E., 2009. Guidelines for the

nomenclature of the human heat shock proteins. Cell Stress Chaperones 14, 105–111. https://doi.org/10.1007/s12192-008-0068-7

Kaushik, S., Cuervo, A.M., 2015. Degradation of lipid droplet-associated proteins by chaperone-mediated autophagy facilitates lipolysis. Nat. Cell Biol. 17, 759–770. https://doi.org/10.1038/ncb3166

Kayed, R., Head, E., Thompson, J.L., McIntire, T.M., Milton, S.C., Cotman, C.W., Glabel, C.G., 2003. Common structure of soluble amyloid oligomers implies common mechanism of pathogenesis. Science (80-.). 300, 486–489. https://doi.org/10.1126/science.1079469

Kayed, R., Sokolov, Y., Edmonds, B., McIntire, T.M., Milton, S.C., Hall, J.E., Glabe, C.G., 2004. Permeabilization of lipid bilayers is a common conformation-dependent activity of soluble amyloid oligomers in protein misfolding diseases. J. Biol. Chem. 279, 46363–46366. https://doi.org/10.1074/jbc.C400260200

Kelley, W.L., 1998. The J-domain family and the recruitment of chaperone power. Trends Biochem. Sci. 23, 222–227. https://doi.org/10.1016/S0968-0004(98)01215-8

Kellie, J.F., Higgs, R.E., Ryder, J.W., Major, A., Beach, T.G., Adler, C.H., Merchant, K., Knierman, M.D., 2014. Quantitative measurement of intact alpha-synuclein proteoforms from post-mortem control and parkinson's disease brain tissue by intact protein mass spectrometry. Sci. Rep. 4. https://doi.org/10.1038/srep05797

Khalaf, O., Fauvet, B., Oueslati, A., Dikiy, I., Mahul-Mellier, A.L., Ruggeri, F.S., Mbefo, M.K., Vercruysse, F., Dietler, G., Lee, S.J., Eliezer, D., Lashuel, H.A., 2014. The H50Q mutation enhances α-synuclein aggregation, secretion, and toxicity. J. Biol. Chem. 289, 21856–21876. https://doi.org/10.1074/jbc.M114.553297

Killinger, B.A., Madaj, Z., Sikora, J.W., Rey, N., Haas, A.J., Vepa, Y., Lindqvist, D., Chen, H., Thomas, P.M., Brundin, P., Brundin, L., Labrie, V., 2018. The vermiform appendix impacts the risk of developing Parkinson's disease. Sci. Transl. Med. 10. https://doi.org/10.1126/scitranslmed.aar5280

Kim, S., Kwon, S.H., Kam, T.I., Panicker, N., Karuppagounder, S.S., Lee, S., Lee, J.H., Kim, W.R., Kook, M., Foss, C.A., Shen, C., Lee, H., Kulkarni, S., Pasricha, P.J., Lee, G., Pomper, M.G., Dawson, V.L., Dawson, T.M., Ko, H.S., 2019. Transneuronal Propagation of Pathologic α-Synuclein from the Gut to the Brain Models Parkinson's Disease. Neuron 103, 627-641.e7. https://doi.org/10.1016/j.neuron.2019.05.035

Kitada, T., Aakawa, S., Hattori, N., Matsumine, H., Yokochi, M., Mizuno, Y., Shimizu, N., 1998. Mutations in the parkin gene cause autosomal recessive juvenile parkinsonism. Nat. Lett. 169, 166–169.

Kityk, R., Kopp, J., Mayer, M.P., 2018. Molecular Mechanism of J-Domain-Triggered ATP Hydrolysis by Hsp70 Chaperones. Mol. Cell 69, 227-237.e4. https://doi.org/10.1016/j.molcel.2017.12.003

Kityk, R., Kopp, J., Sinning, I., Mayer, M.P., 2012. Structure and Dynamics of the ATP-Bound Open Conformation of Hsp70 Chaperones. Mol. Cell 48, 863–874. https://doi.org/10.1016/j.molcel.2012.09.023

Kityk, R., Vogel, M., Schlecht, R., Bukau, B., Mayer, M.P., 2015. Pathways of allosteric regulation in Hsp70 chaperones. Nat. Commun. 6. https://doi.org/10.1038/ncomms9308

Kjaer, L., Giehm, L., Heimburg, T., Otzen, D., 2009. The influence of vesicle size and composition on α-synuclein structure and stability. Biophys. J. 96, 2857–2870. https://doi.org/10.1016/j.bpj.2008.12.3940

Kremer, J.R., Mastronarde, D.N., McIntosh, J.R., 1996. Computer visualization of three-dimensional image data using IMOD. J. Struct. Biol. 116, 71–76. https://doi.org/10.1006/jsbi.1996.0013

Kruger, R., Kuhn, W., Muller, T., Woitalla, D., Graeber, M., Kosel, S., Przuntek, H., Epplen, J.T., Schols, L., Riess, O., 1998. Ala30Pro mutation in the gene encoding a-synuclein in Parkinson's disease. Nat. Genet. 18, 231–236.

Kühlbrandt, W., 2014. The Resolution Revolution. Science (80-.). 343, 1443–1444. https://doi.org/10.1126/science.1251652

Lautenschläger, J., Kaminski, C.F., Kaminski Schierle, G.S., 2017. α-Synuclein – Regulator of Exocytosis, Endocytosis, or Both? Trends Cell Biol. 27, 468–479. https://doi.org/10.1016/j.tcb.2017.02.002

Lautenschläger, J., Stephens, A.D., Fusco, G., Ströhl, F., Curry, N., Zacharopoulou, M., Michel, C.H., Laine, R., Nespovitaya, N., Fantham, M., Pinotsi, D., Zago, W., Fraser, P., Tandon, A., St George-Hyslop, P., Rees, E., Phillips, J.J., De Simone, A., Kaminski, C.F., Schierle, G.S.K., 2018. C-terminal calcium binding of α-synuclein modulates synaptic vesicle interaction. Nat. Commun. 9. https://doi.org/10.1038/s41467-018-03111-4

Lesage, S., Anheim, M., Letournel, F., Bousset, L., Honoré, A., Rozas, N., Pieri, L., Madiona, K., Dürr, A., Melki, R., Verny, C., Brice, A., 2013. G51D α-synuclein mutation causes a novel Parkinsonian-pyramidal syndrome. Ann. Neurol. 73, 459–471. https://doi.org/10.1002/ana.23894

Li, B., Ge, P., Murray, K.A., Sheth, P., Zhang, M., Nair, G., Sawaya, M.R., Shin, W.S., Boyer, D.R., Ye, S., Eisenberg, D.S., Zhou, Z.H., Jiang, L., 2018. Cryo-EM of full-length α-synuclein reveals fibril polymorphs with a common structural kernel. Nat. Commun. 9, 1–10. https://doi.org/10.1038/s41467-018-05971-2

Li, W., West, N., Colla, E., Pletnikova, O., Troncoso, J.C., Marsh, L., Dawson, T.M., Jäkälä, P., Hartmann, T., Price, D.L., Lee, M.K., 2005. Aggregation promoting C-terminal truncation of α-synuclein is a normal cellular process and is enhanced by the familial Parkinson's disease-linked mutations. Proc. Natl. Acad. Sci. U. S. A. 102, 2162–2167. https://doi.org/10.1073/pnas.0406976102

Li, Y., Zhao, C., Luo, F., Liu, Z., Gui, X., Luo, Z., Zhang, X., Li, D., Liu, C., Li, X., 2018. Amyloid fibril structure of α-synuclein determined by cryo-electron microscopy. Cell Res. 28, 897–903. https://doi.org/10.1038/s41422-018-0075-x

Liu, Q., Hendrickson, W.A., 2007. Insights into Hsp70 Chaperone Activity from a Crystal Structure of the Yeast Hsp110 Sse1. Cell 131, 106–120. https://doi.org/10.1016/j.cell.2007.08.039

Lu, Z., Cyr, D.M., 1998. The conserved carboxyl terminus and zinc finger-like domain

of the co-chaperone Ydj1 assist Hsp70 in protein folding. J. Biol. Chem. 273, 5970–5978. https://doi.org/10.1074/jbc.273.10.5970

Man, W.K., Tahirbegi, B., Vrettas, M.D., Preet, S., Ying, L., Vendruscolo, M., De Simone, A., Fusco, G., 2021. The docking of synaptic vesicles on the presynaptic membrane induced by α-synuclein is modulated by lipid composition. Nat. Commun. 12. https://doi.org/10.1038/s41467-021-21027-4

Maroteaux, L., Campanelli, J., Scheller, R., 1988. Synuclein: a neuron-specific protein localized to the nucleus and presynaptic nerve terminal. J. Neurosci. 8, 2804–2815. https://doi.org/10.1523/jneurosci.08-08-02804.1988

Matheoud, D., Cannon, T., Voisin, A., Penttinen, A.-M., Ramet, L., Fahmy, A.M., Ducrot, C., Laplante, A., Bourque, M.-J., Zhu, L., Cayrol, R., Le Campion, A., McBride, H.M., Gruenheid, S., Trudeau, L.-E., Desjardins, M., 2019. Intestinal infection triggers Parkinson's disease-like symptoms in Pink1−/− mice. Nature 571, 565–569. https://doi.org/10.1038/s41586-019-1405-y

Mattoo, R.U.H., Sharma, S.K., Priya, S., Finka, A., Goloubinoff, P., 2013. Hsp110 is a bona fide chaperone using ATP to unfold stable misfolded polypeptides and reciprocally collaborate with Hsp70 to solubilize protein aggregates. J. Biol. Chem. 288, 21399–411. https://doi.org/10.1074/jbc.M113.479253

Mayer, M.P., Bukau, B., 2005. Hsp70 chaperones: Cellular functions and molecular mechanism. Cell. Mol. Life Sci. 62, 670–684. https://doi.org/10.1007/s00018-004-4464-6

McGlinchey, R.P., Ni, X., Shadish, J.A., Jiang, J., Lee, J.C., 2021. The N terminus of α-synuclein dictates fibril formation. Proc. Natl. Acad. Sci. U. S. A. 118, 1–7. https://doi.org/10.1073/pnas.2023487118

McMullan, G., Chen, S., Henderson, R., Faruqi, A.R., 2009. Detective quantum efficiency of electron area detectors in electron microscopy. Ultramicroscopy 109, 1126–1143. https://doi.org/10.1016/j.ultramic.2009.04.002

Meade, R.M., Fairlie, D.P., Mason, J.M., 2019. Alpha-synuclein structure and Parkinson's disease – lessons and emerging principles. Mol. Neurodegener. 14, 1–14. https://doi.org/10.1186/s13024-019-0329-1

Middleton, E.R., Rhoades, E., 2010. Effects of curvature and composition on α-synuclein binding to lipid vesicles. Biophys. J. 99, 2279–2288. https://doi.org/10.1016/j.bpj.2010.07.056

Milovanovic, D., Wu, Y., Bian, X., De Camilli, P., 2017. A Liquid Phase of Synapsin and Lipid Vesicles. Science (80-.). 20, 48–55. https://doi.org/10.1007/s10995-015-1800-4.Alcohol

Mogk, A., Bukau, B., Kampinga, H.H., 2018. Cellular Handling of Protein Aggregates by Disaggregation Machines. Mol. Cell 69, 214–226. https://doi.org/10.1016/j.molcel.2018.01.004

Mok, S.A., Condello, C., Freilich, R., Gillies, A., Arhar, T., Oroz, J., Kadavath, H., Julien, O., Assimon, V.A., Rauch, J.N., Dunyak, B.M., Lee, J., Tsai, F.T.F., Wilson, M.R., Zweckstetter, M., Dickey, C.A., Gestwicki, J.E., 2018. Mapping interactions with the chaperone network reveals factors that protect against tau

aggregation. Nat. Struct. Mol. Biol. 25, 384–393. https://doi.org/10.1038/s41594-018-0057-1

Moldavski, O., Amen, T., Levin-Zaidman, S., Eisenstein, M., Rogachev, I., Brandis, A., Kaganovich, D., Schuldiner, M., 2015. Lipid Droplets Are Essential for Efficient Clearance of Cytosolic Inclusion Bodies. Dev. Cell 33, 603–610. https://doi.org/10.1016/j.devcel.2015.04.015

Murphy, D.D., Rueter, S.M., Trojanowski, J.Q., Lee, V.M., 2000. Synucleins are developmentally expressed, and alpha-synuclein regulates the size of the presynaptic vesicular pool in primary hippocampal neurons. J. Neurosci. 20, 3214–3220. https://doi.org/10.1016/S0165-3806(96)00210-6

Nachman, E., Wentink, A.S., Madiona, K., Bousset, L., Katsinelos, T., Allinson, K., Kampinga, H., McEwan, W.A., Jahn, T.R., Melki, R., Mogk, A., Bukau, B., Nussbaum-Krammer, C., 2020. Disassembly of Tau fibrils by the human Hsp70 disaggregation machinery generates small seeding-competent species. J. Biol. Chem. 295, 9676–9690. https://doi.org/10.1074/jbc.RA120.013478

Naiki, H., Higuchi, K., Hosokawa, M., Takeda, T., 1989. Fluorometric determination of amyloid fibrils in vitro using the fluorescent dye, thioflavine T. Anal. Biochem. 177, 244–249. https://doi.org/10.1016/0003-2697(89)90046-8

Ni, X., McGlinchey, R.P., Jiang, J., Lee, J.C., 2019. Structural Insights into α-Synuclein Fibril Polymorphism: Effects of Parkinson's Disease-Related C-Terminal Truncations. J. Mol. Biol. 431, 3913–3919. https://doi.org/10.1016/j.jmb.2019.07.001

Nillegoda, N.B., Bukau, B., 2015. Metazoan Hsp70-based protein disaggregases: Emergence and mechanisms. Front. Mol. Biosci. 2. https://doi.org/10.3389/fmolb.2015.00057

Nillegoda, Nadinath B, Kirstein, J., Szlachcic, A., Berynskyy, M., Stank, A., Stengel, F., Arnsburg, K., Gao, X., Scior, A., Aebersold, R., Guilbride, D.L., Wade, R.C., Morimoto, R.I., Mayer, M.P., Bukau, B., 2015. Crucial HSP70 co-chaperone complex unlocks metazoan protein disaggregation. Nature 524, 247–251.

Nillegoda, Nadinath B., Kirstein, J., Szlachcic, A., Berynskyy, M., Stank, A., Stengel, F., Arnsburg, K., Gao, X., Scior, A., Aebersold, R., Guilbride, D.L., Wade, R.C., Morimoto, R.I., Mayer, M.P., Bukau, B., 2015. Crucial HSP70 co-chaperone complex unlocks metazoan protein disaggregation. Nature 524, 247–251. https://doi.org/10.1038/nature14884

Ojha, J., Masilamoni, G., Dunlap, D., Udoff, R.A., Cashikar, A.G., 2011. Sequestration of Toxic Oligomers by HspB1 as a Cytoprotective Mechanism. Mol. Cell. Biol. 31, 3146–3157. https://doi.org/10.1128/mcb.01187-10

Orlova, E. V., Saibil, H.R., 2011. Structural Analysis of Macromolecular Assemblies by Electron Microscopy. Chem. Rev. 111, 7710–7748. https://doi.org/10.1021/cr100353t

Outeiro, T.F., Lindquist, S., 2003. Yeast Cells Provide Insight into Alpha-Synuclein Biology and Pathobiology. Science (80-.). 302, 1772–1775. https://doi.org/10.1126/science.1090439

Pandey, N., Schmidt, R.E., Galvin, J.E., 2006. The alpha-synuclein mutation E46K promotes aggregation in cultured cells. Exp. Neurol. 197, 515–520. https://doi.org/10.1016/j.expneurol.2005.10.019

Pasanen, P., Myllykangas, L., Siitonen, M., Raunio, A., Kaakkola, S., Lyytinen, J., Tienari, P.J., Pöyhönen, M., Paetau, A., 2014. A novel α-synuclein mutation A53E associated with atypical multiple system atrophy and Parkinson's disease-type pathology. Neurobiol. Aging 35, 2180.e1-2180.e5. https://doi.org/10.1016/j.neurobiolaging.2014.03.024

Peskett, T.R., Rau, F., O'Driscoll, J., Patani, R., Lowe, A.R., Saibil, H.R., 2018. A Liquid to Solid Phase Transition Underlying Pathological Huntingtin Exon1 Aggregation. Mol. Cell 70, 588-601.e6. https://doi.org/10.1016/j.molcel.2018.04.007

Petroi, D., Popova, B., Taheri-Talesh, N., Irniger, S., Shahpasandzadeh, H., Zweckstetters, M., Outeiro, T.F., Braus, G.H., 2012. Aggregate clearance of α-synuclein in Saccharomyces cerevisiae depends more on autophagosome and vacuole function than on the proteasome. J. Biol. Chem. 287, 27567–27579. https://doi.org/10.1074/jbc.M112.361865

Pickrell, A.M., Youle, R.J., 2015. The roles of PINK1, Parkin, and mitochondrial fidelity in parkinson's disease. Neuron 85, 257–273. https://doi.org/10.1016/j.neuron.2014.12.007

Poepsel, S., Sprengel, A., Sacca, B., Kaschani, F., Kaiser, M., Gatsogiannis, C., Raunser, S., Clausen, T., Ehrmann, M., 2015. Determinants of amyloid fibril degradation by the PDZ protease HTRA1. Nat. Chem. Biol. 11, 862–869. https://doi.org/10.1038/nchembio.1931

Polier, S., Dragovic, Z., Hartl, F.U., Bracher, A., 2008. Structural Basis for the Cooperation of Hsp70 and Hsp110 Chaperones in Protein Folding. Cell 133, 1068–1079. https://doi.org/10.1016/j.cell.2008.05.022

Polymeropoulos, M.H., Lavedan, C., Leroy, E., Ide, S.E., Dehejia, A., Dutra, A., Pike, B., Root, H., Rubenstein, J., Boyer, R., Stenroos, E.S., Chandrasekharappa, S., Athanassiadou, A., Papapetropoulos, T., Johnson, W.G., Lazzarini, A.M., Duvoisin, R.C., Iorio, G. Di, Golbe, L.I., Nussbaum, R.L., 1997. Mutation in the α-Synuclein Gene Identified in Families with Parkinson's Disease. Science (80-.). 276, 2045–2047. https://doi.org/10.1126/science.276.5321.2045

Queitsch, C., Hong, S.W., Vierling, E., Lindquist, S., 2000. Heat shock protein 101 plays a crucial role in thermotolerance in Arabidopsis. Plant Cell 12, 479–492. https://doi.org/10.1105/tpc.12.4.479

Ramezani, M., Wilkes, M.M., Das, T., Holowka, D., Eliezer, D., Baird, B., 2019. Regulation of exocytosis and mitochondrial relocalization by Alpha-synuclein in a mammalian cell model. npj Park. Dis. 5, 1–17. https://doi.org/10.1038/s41531-019-0084-6

Rampelt, H., Kirstein-Miles, J., Nillegoda, N.B., Chi, K., Scholz, S.R., Morimoto, R.I., Bukau, B., 2012. Metazoan Hsp70 machines use Hsp110 to power protein disaggregation. EMBO J. 31, 4221–4235. https://doi.org/10.1038/emboj.2012.264

Ray, S., Singh, N., Kumar, R., Patel, K., Pandey, S., Datta, D., Mahato, J., Panigrahi,

R., Navalkar, A., Mehra, S., Gadhe, L., Chatterjee, D., Sawner, A.S., Maiti, S., Bhatia, S., Gerez, J.A., Chowdhury, A., Kumar, A., Padinhateeri, R., Riek, R., Krishnamoorthy, G., Maji, S.K., 2020. α-Synuclein aggregation nucleates through liquid–liquid phase separation. Nat. Chem. 12, 705–716. https://doi.org/10.1038/s41557-020-0465-9

Rohou, A., Grigorieff, N., 2015. CTFFIND4: Fast and accurate defocus estimation from electron micrographs. J. Struct. Biol. 192, 216–221. https://doi.org/10.1016/j.jsb.2015.08.008

Rosenthal, P.B., Henderson, R., 2003. Optimal determination of particle orientation, absolute hand, and contrast loss in single-particle electron cryomicroscopy. J. Mol. Biol. 333, 721–745. https://doi.org/10.1016/j.jmb.2003.07.013

Rosenzweig, R., Nillegoda, N.B., Mayer, M.P., Bukau, B., 2019. The Hsp70 chaperone network. Nat. Rev. Mol. Cell Biol. https://doi.org/10.1038/s41580-019-0133-3

Roy, S., Wolman, L., 1969. Ultrastructural observations in Parkinsonism. J. Pathol. 99. https://doi.org/https://doi.org/10.1002/path.1710990106

Roy, S, Wolman, L., 1969. Ultrastructural observations in Parkinsonism. J. Pathol. 99.

Rüdiger, S., Germeroth, L., Schneider-Mergener, J., Bukau, B., 1997. Substrate specificity of the DnaK chaperone determined by screening cellulose-bound peptide libraries respect to the bound folding conformer are only partly. EMBO J. 16, 1501–1507.

Rüdiger, S., Schneider-Mergener, J., Bukau, B., 2001. Its substrate specificity characterizes the DnaJ co-chaperone as a scanning factor for the DnaK chaperone. EMBO J. 20, 1042–1050. https://doi.org/10.1093/emboj/20.5.1042

Ruskin, R.S., Yu, Z., Grigorieff, N., 2013. Quantitative characterization of electron detectors for transmission electron microscopy. J. Struct. Biol. 184, 385–393. https://doi.org/10.1016/j.jsb.2013.10.016

Saibil, H., 2013. Chaperone machines for protein folding, unfolding and disaggregation. Nat. Rev. Mol. Cell Biol. 14, 630–642. https://doi.org/10.1038/nrm3658

Sawaya, M.R., Sambashivan, S., Nelson, R., Ivanova, M.I., Sievers, S.A., Apostol, M.I., Thompson, M.J., Balbirnie, M., Wiltzius, J.J.W., McFarlane, H.T., Madsen, A., Riekel, C., Eisenberg, D., 2007. Atomic structures of amyloid cross-β spines reveal varied steric zippers. Nature 447, 453–457. https://doi.org/10.1038/nature05695

Scheres, S.H.W., 2020. Amyloid structure determination in RELION-3.1. Acta Crystallogr. Sect. D Struct. Biol. 76, 94–101. https://doi.org/10.1107/S2059798319016577

Scheres, S.H.W., 2012a. RELION: Implementation of a Bayesian approach to cryo-EM structure determination. J. Struct. Biol. 180, 519–530. https://doi.org/10.1016/j.jsb.2012.09.006

Scheres, S.H.W., 2012b. A bayesian view on cryo-EM structure determination. J. Mol. Biol. 415, 406–418. https://doi.org/10.1016/j.jmb.2011.11.010

Scheres, S.H.W., Chen, S., 2012. Prevention of overfitting in cryo-EM structure determination. Nat. Methods 9, 853–854. https://doi.org/10.1038/nmeth.2115

Schindelin, J., Arganda-Carreras, I., Frise, E., Kaynig, V., Longair, M., Pietzsch, T., Preibisch, S., Rueden, C., Saalfeld, S., Schmid, B., Tinevez, J.Y., White, D.J., Hartenstein, V., Eliceiri, K., Tomancak, P., Cardona, A., 2012. Fiji: An open-source platform for biological-image analysis. Nat. Methods 9, 676–682. https://doi.org/10.1038/nmeth.2019

Schneider, M.M., Gautam, S., Herling, T.W., Andrzejewska, E., Krainer, G., Miller, A.M., Trinkaus, V.A., Peter, Q.A.E., Ruggeri, F.S., Vendruscolo, M., Bracher, A., Dobson, C.M., Hartl, F.U., Knowles, T.P.J., 2021. The Hsc70 disaggregation machinery removes monomer units directly from α-synuclein fibril ends. Nat. Commun. 12, 1–11. https://doi.org/10.1038/s41467-021-25966-w

Schuermann, J.P., Jiang, J., Cuellar, J., Llorca, O., Wang, L., Gimenez, L.E., Jin, S., Taylor, A.B., Demeler, B., Morano, K.A., Hart, P.J., Valpuesta, J.M., Lafer, E.M., Sousa, R., 2008. Structure of the Hsp110:Hsc70 Nucleotide Exchange Machine. Mol. Cell 31, 232–243. https://doi.org/10.1016/j.molcel.2008.05.006

Schweighauser, M., Shi, Y., Tarutani, A., Kametani, F., Murzin, A.G., Ghetti, B., Matsubara, T., Tomita, T., Ando, T., Hasegawa, K., Murayama, S., Yoshida, M., Hasegawa, M., Scheres, S.H.W., Goedert, M., 2020. Structures of α-synuclein filaments from multiple system atrophy. Nature 585, 464–469. https://doi.org/10.1038/s41586-020-2317-6

Scior, A., Arnsburg, K., Iburg, M., Juenemann, K., Lucia Pigazzini, M., Mlody, B., Puchkov, D., Ast, A., Buntru, A., Priller, J., Wanker, E.E., Prigione, A., Kirstein, J., 2021. Complete suppression of Htt fibrillization and disaggregation of Htt fibrils by a trimeric chaperone complex. EMBO J. 40. https://doi.org/10.15252/embj.2021109413

Sekhar, A., Rosenzweig, R., Bouvignies, G., Kay, L.E., 2016. Hsp70 biases the folding pathways of client proteins. Proc. Natl. Acad. Sci. U. S. A. 113, E2794-2801. https://doi.org/10.1073/pnas.1601846113

Sekhar, A., Rosenzweig, R., Bouvignies, G., Kay, L.E., 2015. Mapping the conformation of a client protein through the Hsp70 functional cycle. Proc. Natl. Acad. Sci. U. S. A. 112, 10395–10400. https://doi.org/10.1073/pnas.1508504112

Shahmoradian, S.H., Lewis, A.J., Genoud, C., Hench, J., Moors, T.E., Navarro, P.P., Castaño-Díez, D., Schweighauser, G., Graff-Meyer, A., Goldie, K.N., Sütterlin, R., Huisman, E., Ingrassia, A., Gier, Y. de, Rozemuller, A.J.M., Wang, J., Paepe, A. De, Erny, J., Staempfli, A., Hoernschemeyer, J., Großerüschkamp, F., Niedieker, D., El-Mashtoly, S.F., Quadri, M., Van IJcken, W.F.J., Bonifati, V., Gerwert, K., Bohrmann, B., Frank, S., Britschgi, M., Stahlberg, H., Van de Berg, W.D.J., Lauer, M.E., 2019. Lewy pathology in Parkinson's disease consists of crowded organelles and lipid membranes. Nat. Neurosci. 22, 1099–1109. https://doi.org/10.1038/s41593-019-0423-2

Shaner, L., Trott, A., Goeckeler, J.L., Brodsky, J.L., Morano, K.A., 2004. The function of the yeast molecular chaperone Sse1 is mechanistically distinct from the closely related Hsp70 family. J. Biol. Chem. 279, 21992–22001. https://doi.org/10.1074/jbc.M313739200

Shannon, K.M., Keshavarzian, A., Dodiya, H.B., Jakate, S., Kordower, J.H., 2012. Is alpha-synuclein in the colon a biomarker for premotor Parkinson's Disease?

Evidence from 3 cases. Mov. Disord. 27, 716–719. https://doi.org/10.1002/mds.25020

Singh, Y., Sharpe, P.C., Hoang, H.N., Lucke, A.J., McDowall, A.W., Bottomley, S.P., Fairlie, D.P., 2011. Amyloid formation from an α-helix peptide bundle is seeded by 3 10-helix aggregates. Chem. - A Eur. J. 17, 151–160. https://doi.org/10.1002/chem.201002500

Singleton, A.B., Farrer, M., Johnson, J., Singleton, A., Hague, S., Kachergus, J., Hulihan, M., Peuralinna, T., Dutra, A., Nussbaum, R., Lincoln, S., Crawley, A., Hanson, M., Maraganore, D., Adler, C., Cookson, M.R., Muenter, M., Baptista, M., Miller, D., Blancato, J., Hardy, J., Gwinn-Hardy, K., 2003. α-Synuclein Locus Triplication Causes Parkinson's Disease. Science (80-.). 302, 841. https://doi.org/10.1126/science.1090278

Sipe, J.D., Benson, M.D., Buxbaum, J.N., Ikeda, S.I., Merlini, G., Saraiva, M.J.M., Westermark, P., 2016. Amyloid fibril proteins and amyloidosis: chemical identification and clinical classification International Society of Amyloidosis 2016 Nomenclature Guidelines. Amyloid 23, 209–213. https://doi.org/10.1080/13506129.2016.1257986

Soper, J.H., Roy, S., Stieber, S., Lee, E., Wilson, R.B., Trojanowski, J.Q., Burd, C.G., Lee, V.M.-Y., 2008. Alpha-Synuclein–induced Aggregation of Cytoplasmic Vesicles in Saccharomyces cerevisiae. Mol. Biol. Cell 19, 1093–1103. https://doi.org/10.1091/mbc.E07

Soto, C., Pritzkow, S., 2018. Protein misfolding, aggregation, and conformational strains in neurodegenerative diseases. Nat. Neurosci. 21, 1332–1340. https://doi.org/10.1038/s41593-018-0235-9

Spillantini, M.G., Schmidt, M.L., Lee, V.M.-Y., Trojanowski, J.Q., Jakes, R., Goedert, M., 1997. alpha-Synuclein in Lewy bodies. Nature 388, 839–840. https://doi.org/10.1038/42166

Sun, Y., Hou, S., Zhao, K., Long, H., Liu, Z., Gao, J., Zhang, Y., Su, X.D., Li, D., Liu, C., 2020. Cryo-EM structure of full-length α-synuclein amyloid fibril with Parkinson's disease familial A53T mutation. Cell Res. 30, 360–362. https://doi.org/10.1038/s41422-020-0299-4

Sun, Y., Long, H., Xia, W., Wang, K., Zhang, X., Sun, B., Cao, Q., Zhang, Y., Dai, B., Li, D., Liu, C., 2021. The hereditary mutation G51D unlocks a distinct fibril strain transmissible to wild-type α-synuclein. Nat. Commun. 12, 1–10. https://doi.org/10.1038/s41467-021-26433-2

Suzuki, H., Noguchi, S., Arakawa, H., Tokida, T., Hashimoto, M., Satow, Y., 2010. Peptide-binding sites as revealed by the crystal structures of the human Hsp40 Hdj1 c-terminal domain in complex with the octapeptide from human Hsp70. Biochemistry 49, 8577–8584. https://doi.org/10.1021/bi100876n

Szyperski, T., Pellecchia, M., Wall, D., Georgopoulos, C., Wothrich, K., 1994. NMR structure determination of the Escherichia coli DnaJ molecular chaperone: Secondary structure and backbone fold of the N-terminal region (residues 2-108) containing the highly conserved J domain. Encycl. Food Microbiol. Second Ed. 91, 11343–11347. https://doi.org/10.1016/B978-0-12-384730-0.00100-2

Takamori, S., Holt, M., Stenius, K., Lemke, E.A., Grønborg, M., Riedel, D., Urlaub, H., Schenck, S., Brügger, B., Ringler, P., Müller, S.A., Rammner, B., Gräter, F., Hub, J.S., De Groot, B.L., Mieskes, G., Moriyama, Y., Klingauf, J., Grubmüller, H., Heuser, J., Wieland, F., Jahn, R., 2006. Molecular Anatomy of a Trafficking Organelle. Cell 127, 831–846. https://doi.org/10.1016/j.cell.2006.10.030

Tennstaedt, A., Pöpsel, S., Truebestein, L., Hauske, P., Brockmann, A., Schmidt, N., Irle, I., Sacca, B., Niemeyer, C.M., Brandt, R., Ksiezak-Reding, H., Tirniceriu, A.L., Egensperger, R., Baldi, A., Dehmelt, L., Kaiser, M., Huber, R., Clausen, T., Ehrmanna, M., 2012. Human high temperature requirement serine protease A1 (HTRA1) degrades tau protein aggregates. J. Biol. Chem. 287, 20931–20941. https://doi.org/10.1074/jbc.M111.316232

Thevenaz, P., Ruttimann, U.E., Unser, M., 1998. A pyramid approach to subpixel registration based on intensity. IEEE Trans. Image Process. 7, 27–41. https://doi.org/10.1109/83.650848

Trinkaus, V.A., Riera-Tur, I., Martínez-Sánchez, A., Bäuerlein, F.J.B., Guo, Q., Arzberger, T., Baumeister, W., Dudanova, I., Hipp, M.S., Hartl, F.U., Fernández-Busnadiego, R., 2021. In situ architecture of neuronal α-Synuclein inclusions. Nat. Commun. 12, 1–10. https://doi.org/10.1038/s41467-021-22108-0

Tsai, J., Douglas, M.G., 1996. A conserved HPD sequence of the J-domain is necessary for YDJ1 stimulation of Hsp70 ATPase activity at a site distinct from substrate binding. J. Biol. Chem. 271, 9347–9354.

Tuttle, M.D., Comellas, G., Nieuwkoop, A.J., Covell, D.J., Berthold, D.A., Kloepper, K.D., Courtney, J.M., Kim, J.K., Barclay, A.M., Kendall, A., Wan, W., Stubbs, G., Schwieters, C.D., Lee, V.M.Y., George, J.M., Rienstra, C.M., 2016. Solid-state NMR structure of a pathogenic fibril of full-length human α-synuclein. Nat. Struct. Mol. Biol. 23, 409–415. https://doi.org/10.1038/nsmb.3194

Tzankov, S., Wong, M.J.H., Shi, K., Nassif, C., Young, J.C., 2008. Functional divergence between Co-chaperones of Hsc70. J. Biol. Chem. 283, 27100–27109. https://doi.org/10.1074/jbc.M803923200

Ulmer, T.S., Bax, A., 2005. Comparison of structure and dynamics of micelle-bound human α-synuclein and Parkinson disease variants. J. Biol. Chem. 280, 43179–43187. https://doi.org/10.1074/jbc.M507624200

Valente, E.M., Abou-Sleiman, P.M., Caputo, V., Muqit, M.M.K., Harvey, K., Gispert, S., Ali, Z., Del Turco, D., Bentivoglio, A.R., Healy, D.G., Albanese, A., Nussbaum, R., González-Maldonado, R., Deller, T., Salvi, S., Cortelli, P., Gilks, W.P., Latchman, D.S., Harvey, R.J., Dallapiccola, B., Auburger, G., Wood, N.W., 2004. Hereditary early-onset Parkinson's disease caused by mutations in PINK1. Science (80-.). 304, 1158–1160. https://doi.org/10.1126/science.1096284

Van Der Wateren, I.M., Knowles, T.P.J., Buell, A.K., Dobson, C.M., Galvagnion, C., 2018. C-terminal truncation of α-synuclein promotes amyloid fibril amplification at physiological pH. Chem. Sci. 9, 5506–5516. https://doi.org/10.1039/c8sc01109e

Varkey, J., Isas, J.M., Mizuno, N., Jensen, M.B., Bhatia, V.K., Jao, C.C., Petrlova, J., Voss, J.C., Stamou, D.G., Steven, A.C., Langen, R., 2010. Membrane curvature induction and tubulation are common features of synucleins and apolipoproteins. J.

Biol. Chem. 285, 32486–32493. https://doi.org/10.1074/jbc.M110.139576

Wagner, T., Merino, F., Stabrin, M., Moriya, T., Antoni, C., Apelbaum, A., Hagel, P., Sitsel, O., Raisch, T., Prumbaum, D., Quentin, D., Roderer, D., Tacke, S., Siebolds, B., Schubert, E., Shaikh, T.R., Lill, P., Gatsogiannis, C., Raunser, S., 2019. SPHIRE-crYOLO is a fast and accurate fully automated particle picker for cryo-EM. Commun. Biol. 2, 1–13. https://doi.org/10.1038/s42003-019-0437-z

Walsh, P., Bursać, D., Law, Y.C., Cyr, D., Lithgow, T., 2004. The J-protein family: Modulating protein assembly, disassembly and translocation. EMBO Rep. 5, 567–571. https://doi.org/10.1038/sj.embor.7400172

Wan, W., Briggs, J.A.G., 2016. Cryo-Electron Tomography and Subtomogram Averaging, 1st ed, Methods in Enzymology. Elsevier Inc. https://doi.org/10.1016/bs.mie.2016.04.014

Wang, X., Winter, D., Ashrafi, G., Schlehe, J., Wong, Y.L., Selkoe, D., Rice, S., Steen, J., Lavoie, M.J., Schwarz, T.L., 2011. PINK1 and Parkin target miro for phosphorylation and degradation to arrest mitochondrial motility. Cell 147, 893–906. https://doi.org/10.1016/j.cell.2011.10.018

Wentink, A., Nussbaum-Krammer, C., Bukau, B., 2019. Modulation of amyloid states by molecular chaperones. Cold Spring Harb. Perspect. Biol. 11. https://doi.org/10.1101/cshperspect.a033969

Wentink, A.S., Nillegoda, N.B., Feufel, J., Ubartaitė, G., Schneider, C.P., De Los Rios, P., Hennig, J., Barducci, A., Bukau, B., 2020. Molecular dissection of amyloid disaggregation by human HSP70. Nature 587, 483–488. https://doi.org/10.1038/s41586-020-2904-6

Winner, B., Jappelli, R., Maji, S.K., Desplats, P.A., Boyer, L., Aigner, S., Hetzer, C., Loher, T., Vilar, M., Campioni, S., Tzitzilonis, C., Soragni, A., Jessberger, S., Mira, H., Consiglio, A., Pham, E., Masliah, E., Gage, F.H., Riek, R., 2011. In vivo demonstration that alpha-synuclein oligomers are toxic. Proc. Natl. Acad. Sci. 108, 4194–4199. https://doi.org/10.1073/pnas.1100976108

Xue, W.F., Hellewell, A.L., Gosal, W.S., Homans, S.W., Hewitt, E.W., Radford, S.E., 2009. Fibril fragmentation enhances amyloid cytotoxicity. J. Biol. Chem. 284, 34272–34282. https://doi.org/10.1074/jbc.M109.049809

Yakubu, U.M., Morano, K.A., 2021. Suppression of aggregate and amyloid formation by a novel intrinsically disordered region in metazoan Hsp110 chaperones. J. Biol. Chem. 296, 100567. https://doi.org/10.1016/j.jbc.2021.100567

Yamamoto, N., Matsubara, T., Sato, T., Yanagisawa, K., 2008. Age-dependent high-density clustering of GM1 ganglioside at presynaptic neuritic terminals promotes amyloid β-protein fibrillogenesis. Biochim. Biophys. Acta - Biomembr. 1778, 2717–2726. https://doi.org/10.1016/j.bbamem.2008.07.028

Yap, T.L., Pfefferkorn, C.M., Lee, J.C., 2011. Residue-specific fluorescent probes of α-synuclein: Detection of early events at the N- and C-termini during fibril assembly. Biochemistry 50, 1963–1965. https://doi.org/10.1021/bi2000824

Yoshino, H., Hirano, M., Stoessl, A.J., Imamichi, Y., Ikeda, A., Li, Y., Funayama, M., Yamada, I., Nakamura, Y., Sossi, V., Farrer, M.J., Nishioka, K., Hattori, N., 2017.

Homozygous alpha-synuclein p.A53V in familial Parkinson's disease. Neurobiol. Aging 57, 248.e7-248.e12. https://doi.org/10.1016/j.neurobiolaging.2017.05.022

Yu, H.Y., Ziegelhoffer, T., Craig, E.A., 2015. Functionality of Class A and Class B J-protein Co-chaperones with Hsp70. FEBS Lett. 589, 2825–2830. https://doi.org/10.1016/j.physbeh.2017.03.040

Zarranz, J.J., Alegre, J., Gómez-Esteban, J.C., Lezcano, E., Ros, R., Ampuero, I., Vidal, L., Hoenicka, J., Rodriguez, O., Atarés, B., Llorens, V., Gomez Tortosa, E., Del Ser, T., Muñoz, D.G., De Yebenes, J.G., 2004. The New Mutation, E46K, of α-Synuclein Causes Parkinson and Lewy Body Dementia. Ann. Neurol. 55, 164–173. https://doi.org/10.1002/ana.10795

Zhang, W., Falcon, B., Murzin, A.G., Fan, J., Crowther, R.A., Goedert, M., Scheres, S.H.W., 2019. Heparin-induced tau filaments are polymorphic and differ from those in alzheimer's and pick's diseases. Elife 8, 1–24. https://doi.org/10.7554/eLife.43584

Zhao, K., Li, Y., Liu, Z., Long, H., Zhao, C., Luo, F., Sun, Y., Tao, Y., Su, X. dong, Li, D., Li, X., Liu, C., 2020a. Parkinson's disease associated mutation E46K of α-synuclein triggers the formation of a distinct fibril structure. Nat. Commun. 11. https://doi.org/10.1038/s41467-020-16386-3

Zhao, K., Lim, Y.J., Liu, Z., Long, H., Sun, Y., Hu, J.J., Zhao, C., Tao, Y., Zhang, X., Li, D., Li, Y.M., Liu, C., 2020b. Parkinson's disease-related phosphorylation at Tyr39 rearranges α-synuclein amyloid fibril structure revealed by cryo-EM. Proc. Natl. Acad. Sci. U. S. A. 117, 20305–20315. https://doi.org/10.1073/PNAS.1922741117

Zheng, S.Q., Palovcak, E., Armache, J.P., Verba, K.A., Cheng, Y., Agard, D.A., 2017. MotionCor2: Anisotropic correction of beam-induced motion for improved cryo-electron microscopy. Nat. Methods 14, 331–332. https://doi.org/10.1038/nmeth.4193

Zhu, X., Zhao, X., Burkholder, W., Gragerov, A., Ogata, C., Gottesman, M., Hendrickson, W., 1996. Structural Analysis of Substrate Binding by the Molecular Chaperone DnaK. Science (80-.). 272, 1606–1614.

Zivanov, J., Nakane, T., Forsberg, B.O., Kimanius, D., Hagen, W.J.H., Lindahl, E., Scheres, S.H.W., 2018a. New tools for automated high-resolution cryo-EM structure determination in RELION-3. Elife 7, 1–22. https://doi.org/10.7554/eLife.42166

Zivanov, J., Nakane, T., Scheres, S.H.W., 2018b. A Bayesian approach to beam-induced motion correction in cryo-EM single-particle analysis. IUCrJ 6, 5–17. https://doi.org/10.1107/S205225251801463X

Zuiderweg, E.R.P., Bertelsen, E.B., Rousaki, A., Mayer, M.P., Gestwicki, J.E., AHmad, A., 2013. Allostery in the Hsp70 chaperone proteins. Top. Curr. Chem 328, 99–153. https://doi.org/10.1007/128